2017-03

Spectral LiDAR analysis and terrain classification in a semi-urban environment

McIver, Charles A.

Monterey, California: Naval Postgraduate School

http://hdl.handle.net/10945/53017

NAVAL POSTGRADUATE SCHOOL

MONTEREY, CALIFORNIA

THESIS

SPECTRAL LiDAR ANALYSIS AND TERRAIN CLASSIFICATION IN A SEMI-URBAN ENVIRONMENT

by

Charles A. McIver

March 2017

Thesis Advisor:	Richard Olsen
Co-Advisor:	Marcus Stefanou

Approved for public release. Distribution is unlimited.

THIS PAGE INTENTIONALLY LEFT BLANK

REPORT DOCUMENTATION PAGE	*Form Approved OMB No. 0704-0188*

1. AGENCY USE ONLY ***(Leave blank)***	**2. REPORT DATE** March 2017	**3. REPORT TYPE AND DATES COVERED** Master's Thesis Feb 2016—Mar 2017

4. TITLE AND SUBTITLE SPECTRAL LiDAR ANALYSIS AND TERRAIN CLASSIFICATION IN A SEMI-URBAN ENVIRONMENT	**5. FUNDING NUMBERS**
6. AUTHOR(S), Charles A. McIver	
7. PERFORMING ORGANIZATION NAME(S) AND ADDRESS(ES) Naval Postgraduate School Monterey, CA 93943-5000	**8. PERFORMING ORGANIZATION REPORT NUMBER**
9. SPONSORING/MONITORING AGENCY NAME(S) AND ADDRESS(ES) N/A	**10. SPONSORING/ MONITORING AGENCY REPORT NUMBER**

11. SUPPLEMENTARY NOTES The views expressed in this thesis are those of the author and do not reflect the official policy or position of the Department of Defense or the U.S. Government. IRB Protocol number ____N/A____.

12a. DISTRIBUTION/AVAILABILITY STATEMENT Approved for public release. Distribution is unlimited.	**12b. DISTRIBUTION CODE**

13. ABSTRACT (maximum 200 words)

Remote-sensing analysis is conducted for the Naval Postgraduate School campus, containing buildings, impervious surfaces (asphalt and concrete), natural ground, and vegetation. Data is from the Optech Titan, providing three-wavelength laser data (532, 1064, and 1550 nm) at 10–15 points/m^2. Analysis techniques for laser-scanner (LiDAR) data traditionally use only x, y, z coordinate information. The traditional approach is used to initialize the classification process into broad-spatial classes (unclassified, ground, vegetation, and buildings).

Spectral analysis contributes a unique approach to the classification process. Tools and techniques designed for multispectral imagery are adapted to the LiDAR analysis herein. ENVI's N-Dimensional Visualizer is employed to develop training sets for supervised classification techniques, primarily Maximum Likelihood. Unsupervised classification for the combined spatial/spectral data is accomplished using a K-means classifier for comparison.

The campus is classified into 10 and 16 classes, compared to the four from traditional methods. Addition of the spectral component improves the discrimination among impervious surfaces, other ground elements, and building materials. Maximum Likelihood demonstrates 75% overall classification accuracy, with grass (99.9%), turf (95%), asphalt shingles (94%), light-building concrete (89%), sand (88%), shrubs (85%), asphalt (84%), trees (80%), and clay-tile shingles (77%). Post-process filtering by "number of returns" increases overall accuracy to 82%.

14. SUBJECT TERMS remote sensing, space systems operations, LiDAR, satellite laser altimetry, Optech Titan, multi-wavelength LiDAR, spectral LiDAR, terrain and building classification	**15. NUMBER OF PAGES** 181
	16. PRICE CODE

17. SECURITY CLASSIFICATION OF REPORT Unclassified	**18. SECURITY CLASSIFICATION OF THIS PAGE** Unclassified	**19. SECURITY CLASSIFICATION OF ABSTRACT** Unclassified	**20. LIMITATION OF ABSTRACT** UU

NSN 7540-01-280-5500

Standard Form 298 (Rev. 2-89)
Prescribed by ANSI Std. 239-18

SPECTRAL LiDAR ANALYSIS AND TERRAIN CLASSIFICATION IN A SEMI-URBAN ENVIRONMENT

Charles A. McIver
Lieutenant, United States Navy
B.S., University of North Carolina at Greensboro, 2007

Submitted in partial fulfillment of the
requirements for the degrees of

MASTER OF SCIENCE IN SPACE SYSTEMS OPERATIONS

and

MASTER OF SCIENCE IN REMOTE SENSING INTELLIGENCE

from the

NAVAL POSTGRADUATE SCHOOL
March 2017

Approved by: Richard Olsen
Thesis Advisor

Marcus Stefanou
Co-Advisor

James Newman
Chair, Space Systems Academic Group

Dan Boger
Chair, Department of Information Sciences

THIS PAGE INTENTIONALLY LEFT BLANK

ABSTRACT

Remote-sensing analysis is conducted for the Naval Postgraduate School campus, containing buildings, impervious surfaces (asphalt and concrete), natural ground, and vegetation. Data is from the Optech Titan, providing three-wavelength laser data (532, 1064, and 1550 nm) at 10–15 points/m^2. Analysis techniques for laser-scanner (LiDAR) data traditionally use only x, y, z coordinate information. The traditional approach is used to initialize the classification process into broad-spatial classes (unclassified, ground, vegetation, and buildings).

Spectral analysis contributes a unique approach to the classification process. Tools and techniques designed for multispectral imagery are adapted to the LiDAR analysis herein. ENVI's N-Dimensional Visualizer is employed to develop training sets for supervised classification techniques, primarily Maximum Likelihood. Unsupervised classification for the combined spatial/spectral data is accomplished using a K-means classifier for comparison.

The campus is classified into 10 and 16 classes, compared to the four from traditional methods. Addition of the spectral component improves the discrimination among impervious surfaces, other ground elements, and building materials. Maximum Likelihood demonstrates 75% overall classification accuracy, with grass (99.9%), turf (95%), asphalt shingles (94%), light-building concrete (89%), sand (88%), shrubs (85%), asphalt (84%), trees (80%), and clay-tile shingles (77%). Post-process filtering by "number of returns" increases overall accuracy to 82%.

THIS PAGE INTENTIONALLY LEFT BLANK

TABLE OF CONTENTS

LIST OF FIGURES

THIS PAGE INTENTIONALLY LEFT BLANK

LIST OF TABLES

THIS PAGE INTENTIONALLY LEFT BLANK

LIST OF ACRONYMS AND ABBREVIATIONS

2D	Two-Dimensional
3D	Three-Dimensional
A2AD	Anti-access Area Denial
AEDR	Aggregated Experiment Data Records
AGL	Above Ground Level
ALHAT	Autonomous Landing and Hazard Avoidance Technology
ALISSA	l’Atmosphere Par LiDAR Sur Saliout
ASCII	American Standard Code for Information Interchange
ATLAS	Advanced Topographic Laser Altimeter System
BE	Beacon Explorer
CALIOP	Cloud-Aerosol LiDAR with Orthogonal Polarization
CALIPSO	Cloud-Aerosol LiDAR and Infrared Pathfinder Satellite Observations
CC	Cloud Compare Software
Cr:Nd:YAG	Chromium Neodymium-doped Yttrium Aluminum Garnet
CLC	CORINE Land Cover
CSRMSS95	University of Texas Mean Sea Surface Model
CSV	Comma Delimited Text File Format
DEM	Digital Elevation Model
DSM	Digital Surface Model
EDR	Experiment Data Record
EGM96	Earth Gravitational Model 1996 Geoid
ENVI	ENvironment for Visualizing Images
EO	Electro-optical
FTP	File Transfer Protocol
GDVI	Green Difference Vegetation Index
GEDI	Global Ecosystem Dynamics Investigation LiDAR
GLAS	Geoscience Laser Altimeter System
GNDVI	Green Normalized Difference Vegetation Index
GODLAS	Goddard Laser

GPS	Global Positioning System
GRVI	Green Ratio Vegetation Index
GSFC	Goddard Space Flight Center
GTOPO30	Global 30 Arc-Second Elevation Dataset
HAL	High Altitude LiDAR
HRQLS	High Resolution Quantum LiDAR System
IAU	International Astronomical Union
ICESat	Ice, Cloud, and Land Elevation Satellite
IDL	Interactive Data Language
IED	Improvised Explosive Device
IR	Infrared
ISR	Intelligence, Surveillance, Reconnaissance
ISS	International Space Station
JAXA	Japan Aerospace Exploration Agency
LAS	Laser File Format
LiDAR	Light Detection and Ranging
LIST	LiDAR Surface Topography Mission
LITE	LiDAR In-space Technology Experiment
LOLA	Lunar Reconnaissance Orbiter Laser Altimeter
LRO	Lunar Reconnaissance Orbiter
MATLAB	Matrix Laboratory
MEGR	Mission Experiment Gridded Data Records
MESSENGER	Mercury Surface, Space Environment, Geochemistry, and Ranging Orbiter
MGS	Mars Global Surveyor
Mir	Мир "Peace"
ML	Maximum Likelihood
MLA	Mercury Laser Altimeter
MODIS	Moderate Resolution Imaging Spectroradiometer
MOLA	Mars Orbiter Laser Altimeter
NAD83	North American Datum of 1983
NASA	National Aeronautics and Space Administration

NAVD 88	North American Vertical Datum of 1988
NCALM	National Center for Airborne Laser Mapping
NDFI	Normalized Difference Feature Index
N-D VIS	N-Dimension Visualizer
NEAR	Near Earth Asteroid Rendezvous Spacecraft
NEX	Naval Exchange
NIR	Near-Infrared
NLR	NEAR Laser Rangefinder
NSSDC	National Space Science Data Center
NSSDCA	NASA Space Science Data Coordinated Archive
PEDR	Precision Experiment Data Record
PDS	NASA Planetary Data System
QTM	Quick Terrain Modeler Software
QTT	Quick Terrain Modeler Gridded Surface
RDR	Reduced Data Record
RGB	Red-Green-Blue
ROI	Region of Interest
SAM	Spectral Angle Mapper
SAR	Synthetic Aperture Radar
SID	Spectral Information Divergence
SIMPL	Swath/Slope Imaging Multi-polarization Photon-counting LiDAR
SLA	Shuttle Laser Altimetry
SRTM	Shuttle Radar Topography Mission
SWIR	Shortwave-Infrared
STS	Space Transportation System (Space Shuttle)
TAB	Tab Delimited Text File Format
TOF	Time-of-flight
TriDAR	Triangulation and LiDAR Automated Rendezvous and Docking
UAV	Unmanned Aerial Vehicle
UTM	Universal Transverse Mercator

THIS PAGE INTENTIONALLY LEFT BLANK

I. INTRODUCTION

A. PURPOSE OF RESEARCH

Remote sensing from the air and space contributes invaluable tactical-, operational-, and strategic-level intelligence for military commanders and national leaders. This is especially true for areas that are becoming increasingly difficult for United States' land- and sea-based platforms to access. Remote-sensing technologies must continue to evolve in order to maintain dominance over our adversaries' expanding methods of anti-access area denial (A2AD) and deception tactics.

This research is devoted to the expanding use of the laser for remote-sensing purposes by analyzing a new and different approach for terrain classification using data from an aerial laser scanner. Modern-day light detection and ranging (LiDAR) systems offer more than traditional laser detection and ranging. Aerial LiDAR platforms are now capable of high resolution, three-dimensional (3D), spatial and spectral imaging from ever-increasing altitudes. In addition to active nighttime imaging, LiDAR gives us exceptional tree canopy and vegetation penetration at substantially better resolutions than synthetic aperture radar (SAR). This helps negate adversarial attempts to disguise buildings and vehicles under dense foliage, and it provides a means to detect hidden roads and trails, even in jungles. LiDAR is the only remote-sensing technology that can regularly detect powerlines and cables, a necessity for safe helicopter and unmanned aerial vehicle (UAV) operations in hostile and unfamiliar terrains. It may even be able to detect the thin trip wires used for some improvised explosive devices (IED).

Currently, the majority of terrain classification within LiDAR point clouds is accomplished using spatial attributes, such as point position (the physical x, y, z coordinates), height above the calculated ground level, and the apparent surface roughness. Intensity is rarely included, and typically it is only available for a single wavelength. This results in a limited number of generalized classification categories, approximately two to four. Additional research needs to analyze the conjoined spectral intensities of a multi-wavelength LiDAR system to determine if the additional spectral information collected from this sensor lends itself to producing a greater variety of classification results over purely spatial and single-intensity methods.

B. OBJECTIVE

The primary objective of this thesis is to determine if a multi-wavelength (spectral) LiDAR system, such as the Optech Titan, can generate more accurate and diverse results in the process of terrain, building, and vegetation classification within the LiDAR point cloud. The goal is to expand upon the output of a popular spatial classifier (LASclassify) that only considers the geometric attributes of points, resulting in four generalized classes: unclassified, ground, buildings, and vegetation. Herein, we will analyze three-wavelength intensity values for a 5% random subset of the point cloud to distinguish subclasses that correspond to specific manmade materials and terrain types, such as asphalt, concrete, clay/brick, turf (fake grass), dirt, sand, and lawn grass. Then, we compare the effectiveness of the Maximum Likelihood (ML), Spectral Angle Mapper (SAM), and K-means (Bayesian) classifiers in classifying the remaining 95% of the data. To meet this objective in a well-understood environment, we select Optech Titan data collected in three wavelengths simultaneously over the campus of the Naval Postgraduate School in Monterey, California—a semi-urban (urban forest) environment.

The secondary objective of this thesis is to provide a detailed historical and contemporary account of LiDAR systems in space and a thorough review of the accompanying scientific literature. One will see that remote-sensing laser systems have been an integral part of space operations since the mid-1960s. This secondary objective culminates in the Appendix where three NASA-released datasets are adapted to produce intriguing LiDAR point clouds of the Moon and Mars. Also, the work detailed in the Appendix predates the primary thesis effort and represents important practice with LiDAR data in American Standard Code for Information Interchange (ASCII) format using two fundamental software programs for point cloud modeling.

II. HISTORICAL AND LITERARY REVIEW OF SPACEBORNE LiDAR SYSTEMS

A. BACKGROUND

The National Aeronautics and Space Administration (NASA) maintains a robust resume of space-based LiDAR that spans over five decades. Appropriately, Section B reviews the prominent LiDAR-wielding space platforms designed, launched, and operated by NASA; Section B also includes systems designed, launched, and operated by other agencies that partnered with NASA during their endeavors. Thirteen systems are presented in a roughly chronological order from simple satellites bearing only laser reflectors to complex explorer probes still operational at the time of writing.

Section C reviews two space-based LiDAR systems designed, launched, and operated by nations other than the United States (U.S.): the Russian Space Program and the Japan Aerospace Exploration Agency (JAXA). In Section D, this review concludes with a look at four new technologies and their implications on the future of LiDAR in space. Overall, the author located 22 LiDAR-satellite platforms, including the 14 U.S., one French/Russian, and the one Japanese sensors discussed herein. Although not covered further, additional noteworthy space LiDAR systems are listed, with red indicating an early mission failure:

U.S.	Mars Polar Lander (Atmospheric LiDAR for ice and aerosols)
	Mars Observer Laser Altimeter (Topographic LiDAR)
Russia	BALKAN-1 (Atmospheric LiDAR on the MIR space station)
	BALKAN-2 (Atmospheric LiDAR on the ALMAZ-1B satellite)
China	Chang'e Lunar Orbiter (Laser Altimeter)
Japan	Selenological and Engineering Explorer/Lunar Orbiter "SELENE aka Kaguya" (Laser Altimeter)

Table 1 offers a comprehensive list of the upcoming laser systems and some important facts for a comparison on the evolution of space-based LiDAR. **The sources of platform and orbital characteristics are cited in the narrative section for each listed LiDAR system**. The past, present, and future trends are the author's interpretations based on the information in Table 1.

Table 1. Summary of Space-based LiDAR Systems in Chapter II.

<table>
<tr><th colspan="6">Past (Systems no longer in operation)</th></tr>
<tr><th>Name</th><th>Purpose</th><th>Operating λ</th><th>Beams</th><th>Type</th><th>Orbit</th></tr>
<tr><td>Beacon Explorer- B/C</td><td>Ground laser tracking on satellite target</td><td>694 nm (red)</td><td>1</td><td>Ruby</td><td>Elliptical, low-Earth, 79.7°</td></tr>
<tr><td>Apollo 15 - 17</td><td>Lunar laser altimeter</td><td>Unsure - maybe 694 nm</td><td>1</td><td>Q-switch Ruby</td><td>Circular lunar</td></tr>
<tr><td>ALISSA</td><td>Cloud-profile LiDAR on Mir station</td><td>532 nm (green)</td><td>1 (4 combined)</td><td>4 Nd:YAG</td><td>Circular, low-Earth, 52°</td></tr>
<tr><td>Clementine</td><td>Lunar laser mapping—low quality</td><td>532, 1064 nm (IR)</td><td>1—Either separately</td><td>Cr:Nd:YAG</td><td>Circular lunar & Earth transfer</td></tr>
<tr><td>Shuttle LITE</td><td>Cloud profile, atmospheric particles</td><td>355 (UV), 532, 1064 nm</td><td>1—3 λ’s combined</td><td>2 Nd:YAG</td><td>Shuttle STS-64, near-Earth</td></tr>
<tr><td>Shuttle Laser Altimetry</td><td>Earth laser topography</td><td>1064 nm</td><td>1</td><td>Cr:Nd:YAG</td><td>Shuttle STS-72, 85 near-Earth, 57°</td></tr>
<tr><td>Mars Orbiter Laser Altimeter</td><td>Mars laser topography</td><td>1064 nm</td><td>1</td><td>Nd:YAG</td><td>Mars retrograde ~93°, near-polar</td></tr>
<tr><td>NEAR Probe</td><td>Earth–Asteroid rendezvous</td><td>1064 nm</td><td>1</td><td>Nd:YAG</td><td>433 Eros proximity ops</td></tr>
<tr><td>Phoenix Lander</td><td>Mars surface probe & atmospheric LiDAR</td><td>532, 1064 nm</td><td>1—2 λ’s combined</td><td>Nd:YAG</td><td>N/A</td></tr>
<tr><td>Shuttle TriDAR</td><td>Laser docking & proximity ops</td><td>Unsure—likely 1400 or 1550 nm</td><td>1</td><td>Probably Nd:YAG</td><td>Shuttle proximity ops with ISS</td></tr>
<tr><td>ICESat/GLAS</td><td>Clouds/aerosols, forest structure, biomass, ice sheets</td><td>532, 1064 nm</td><td>1—2 λ’s Combined</td><td>3 Nd:YAG</td><td>Circular, low-Earth, near-polar</td></tr>
<tr><td>MESSENGER</td><td>Mercury topography</td><td>1064 nm</td><td>1</td><td>Nd:YAG</td><td>Highly elliptical, sun-shielded</td></tr>
<tr><td>Hayabusa</td><td>Asteroid probe</td><td>1064 nm</td><td>1</td><td>Nd:YAG</td><td>Asteroid rndv</td></tr>
<tr><td colspan="6">**Past Trend**: Diode-pumped, Q-switched, Nd:YAG lasers; 1 - 1064 nm beam; planetary/lunar orbits less than 1000 km</td></tr>
<tr><th colspan="6">Present (Systems in operation at the time of writing)</th></tr>
<tr><td>CALIPSO</td><td>Cloud-aerosol, polarization</td><td>532, 1064 nm</td><td>1—2 λ’s Combined</td><td>2 Nd:YAG</td><td>Sun-synch 98°, low-Earth</td></tr>
<tr><td>Lunar Orbiter Laser Altimeter</td><td>High quality lunar mapping and topography</td><td>1064 nm</td><td>5</td><td>1 Nd:YAG w/ split optics</td><td>Elliptical, near-lunar</td></tr>
<tr><th colspan="6">Future (System concepts in various stages of development and testing)</th></tr>
<tr><td>Next Gen. Integrated Landing (ALHAT)</td><td>Spacecraft autonomous landing</td><td colspan="4">Laser Altimeter—1570 nm Ranges > 2km
Doppler LiDAR—1550 nm (pre-chirp) Ranges < 2km
Flash Imaging LiDAR –1060 nm Direct hazard avoidance</td></tr>
<tr><td>ICESat-2/A TLAS</td><td>ICESat follow-on</td><td>532 nm (micro-pulsed)</td><td>6—in 3 pairs</td><td>Probably Nd:YAG</td><td>Circular, low-Earth, near-polar</td></tr>
<tr><td>GEDI</td><td>Large area forest structure/biomass</td><td>1064 nm</td><td>14</td><td>Nd:YAG</td><td>ISS attachment</td></tr>
<tr><td>High Altitude LiDAR</td><td>Aerial single photon: wide swath/high res.</td><td>532 nm</td><td>~100 pulselets</td><td>Nd:YAG</td><td>8-10 km altitude - not yet space cap.</td></tr>
<tr><td colspan="6">**Present/Future Trend**: Multi-beam (or combination) LiDAR systems, micro-pulsed (high Hz), large area coverage, and high point density (spatial resolution)</td></tr>
</table>

B. U.S./NASA PLATFORMS

1. Beacon Explorer—B and C and the Goddard Laser

The history of LiDAR in space began in October 1964 with ground-based lasers and satellites carrying cube-corner reflectors (Abshire 2011). Zubritsky explained that, almost immediately, satellite laser tracking demonstrated a vast improvement over the current method of tracking with microwave radars; radar satellite tracking contributed accuracies of approximately 75 meters (m) (Zubritsky 2014). The same document makes an important comparison, that the first successful tracking tests with lasers "reported a range accuracy up to about three meters—about 25 times better" (Zubritsky 2014, 1).

Figure 1 shows the Goddard laser (GODLAS) with receiving telescope (left) and the Beacon Explorer-B (BE-B) satellite with its array of cube-corner reflectors circled (right). The GODLAS was a rotating-mirror, Q-switched, ruby laser mounted on a NIKE-AJAX radar pedestal; it functioned at a wavelength of 694 nanometers (nm) (red) with 20 nanosecond (ns) pulses of approximately 0.8 joules (J) and a repetition rate of 1 Hertz (Hz) (Degnan 2014). Separate elevation and azimuth joysticks moved the 16-inch telescope and the corresponding 9558A photomultiplier detector (Degnan 2014).

Figure 1. Goddard Laser and BE-B Satellite. Adapted from Abshire (2011).

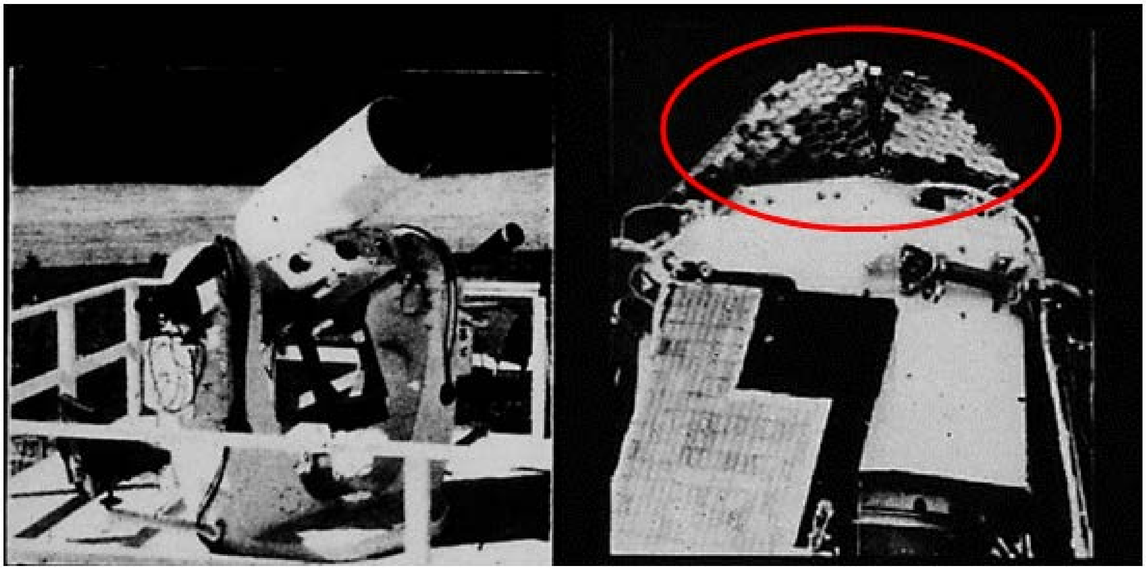

The BE-B satellite (Explorer 22) was a 52.6 kilogram (kg) ionospheric-research satellite tasked with measuring worldwide electron content (NASA Space Science Data Coordinated Archive [NSSDCA] 2016b). The NSSDCA page stated that in addition to the laser reflectors, BE-B carried an electrostatic probe, radio beacons, and a Doppler-navigation system (2016b). This source confirmed that with no onboard storage capacity, data collection could occur only when the satellite was in view of a ground station (2016b). BE-B's elliptical orbit parameters included an 889 kilometer (km) perigee, 1,081 km apogee, 79.7° inclination, and 104.8 minute period (NSSDCA 2016b). Its cube-corner reflectors returned a high percentage of incident light directly back to the source (Degnan 2014). BE-B's specifically designed array of such reflectors ensured adequate strength of the returned signal by accounting for beam divergence (Degnan 2014).

In the first five years, the GODLAS, BE-B/BE-C, other reflector satellites, and the deposited lunar retroreflectors of the early Apollo missions proved the ability of the laser to operate within the space environment (Abshire 2011). This set the stage for a critical transformation: The spacecraft would become the source of the laser pulse instead of the target. Over subsequent decades, LiDAR technology would expand from its humble beginnings into advanced laser altimeters, precision docking instruments, and tools for atmospheric-constituent measurements.

2. Apollo 15, 16, 17 Laser Altimeters

The last three Apollo missions carried a flash-lamp pumped, mechanically Q-switched, ruby laser designed by RCA Aerospace (Abshire 2011). In the same presentation, it is mentioned how the Apollo laser altimeter came into existence adapted from a tank rangefinder (2011). It weighed 23 kg, dissipated 60 watts of power, had a firing rate of 0.05 Hz, and possessed 10 centimeter (cm) transmit and receive apertures (Abshire 2011).

During Apollo 15, 16, and 17, the laser altimeter performed an integral role in the service module's mission "to obtain high-resolution panoramic and high-quality metric lunar-surface photographs and altitude data from lunar orbit" (Baldwin 1972, 1–10). Baldwin announced that the laser altimeter could work in one of two modes, either in conjunction with or independently of the metric camera system (1972). In the first mode, the laser altimeter provided a corresponding altitude measurement for each photographic exposure (Baldwin 1972). Later, Roberson and Kaula derived an iterative least-squares triangulation process that used exposure times, altitude measurements, and orbital data in order to construct properly georeferenced maps from the overlapping lunar photographs (Roberson and Kaula 1972).

Figure 2 demonstrates the laser altimeter's second mode of operation during orbits 15 and 16, independent of the cameras. Roberson and Kaula combined altimetry measurements with orbital data to create graphs of the lunar surface height relative to a sphere situated at the Moon's center of mass (1972). The sphere's radius is 1,738 km, and surface elevation is represented on the y-axis in km above spheroid (Roberson and Kaula 1972).

Figure 2. Reduced Laser Altimetry for Orbits 15/16 of Apollo 15. Source: Roberson and Kaula (1972, 25–49).

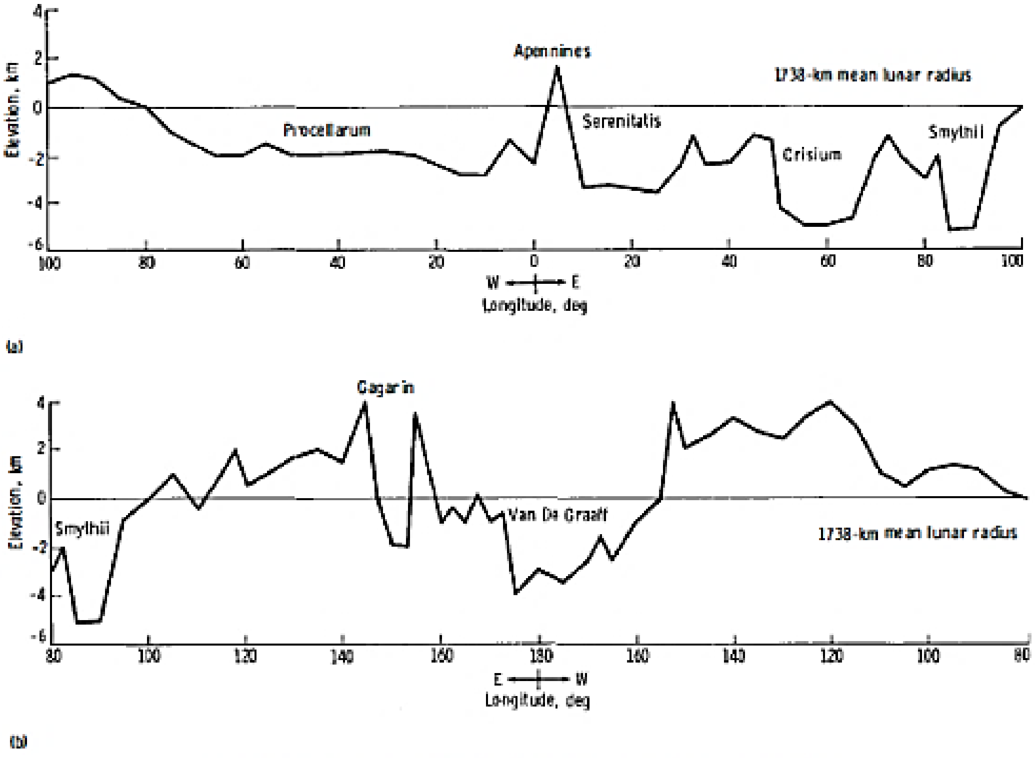

FIGURE 25-41.—Apollo 15 laser altimeter data. (a) Near side. (b) Far side.

On orbit 27, the Apollo 15 laser altimeter began malfunctioning, and its performance worsened due to decreased laser output power until orbit 38, when a different anomaly permanently ceased laser-altimetry operations (National Aeronautics and Space Administration [NASA] 1971). According to the *Apollo 15 Mission Report*, NASA never fully determined the exact cause of the degraded output power anomaly, but it attributed the fault to the laser module (1971). Consequently, future flight units included an automatic power compensation circuit with a photodiode sensor (1971). NASA concluded that the final anomaly likely resulted from electromagnetic interference due to a malfunctioning ground-testing safety relay that interrupted the proper operation of the laser receiver’s video amplifier (1971). As a result, the power supply to the photomultiplier tube held the system at idle voltage for too long (NASA 1971).

Figure 3 shows the receiver missing the return pulse as a consequence of the photomultiplier remaining at idle voltage after laser firing. NASA would remove the safety relay from future units, however this marked the end of Apollo 15 laser altimetry operations (NASA 1971).

Figure 3. The Final Apollo 15 Laser Altimeter Anomaly on Orbit 38. Source: National Aeronautics and Space Administration [NASA] (1971, 213).

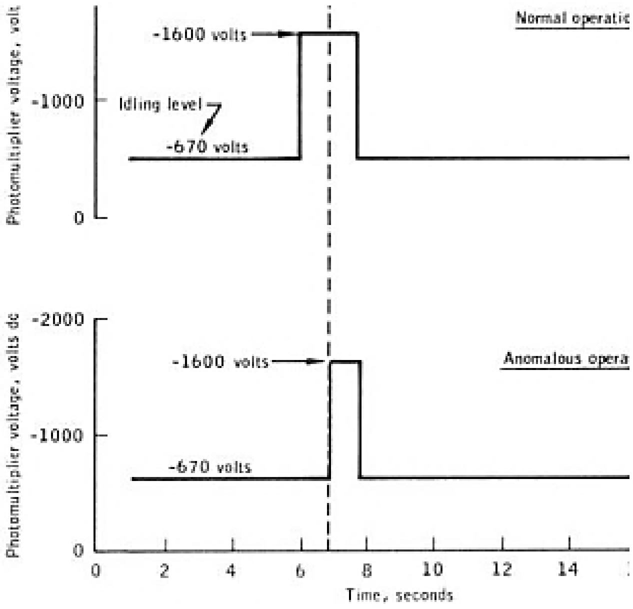

The Apollo 16 laser altimeter fared somewhat better than its predecessor (NSSDCA 2016a). Per NSSDCA, the system's average reliability had decreased by orbit 60 to approximately 50% (2016a). Unfortunately, the laser altimeter failed three orbits later during the final run of photograph collection (NSSDCA 2016a).

The Apollo 17 laser altimeter operated successfully for the duration of the mission (Kaula et al. 1974). Kaula et al. stated that concern about the prior failures caused the astronauts of Apollo 17 to avoid excessive use of the laser altimeter early in the mission to ensure its later availability to support photographic-mapping operations (1974). Figure 4 indicates the position of the laser altimeter on the Apollo 17 Scientific Instrument Module. The photograph is from the Command Module in lunar orbit.

Figure 4. Apollo 17 Scientific Instrument Module and Layout Diagram. Adapted from Lunar and Planetary Institute and Universities Space Research Association (2016).

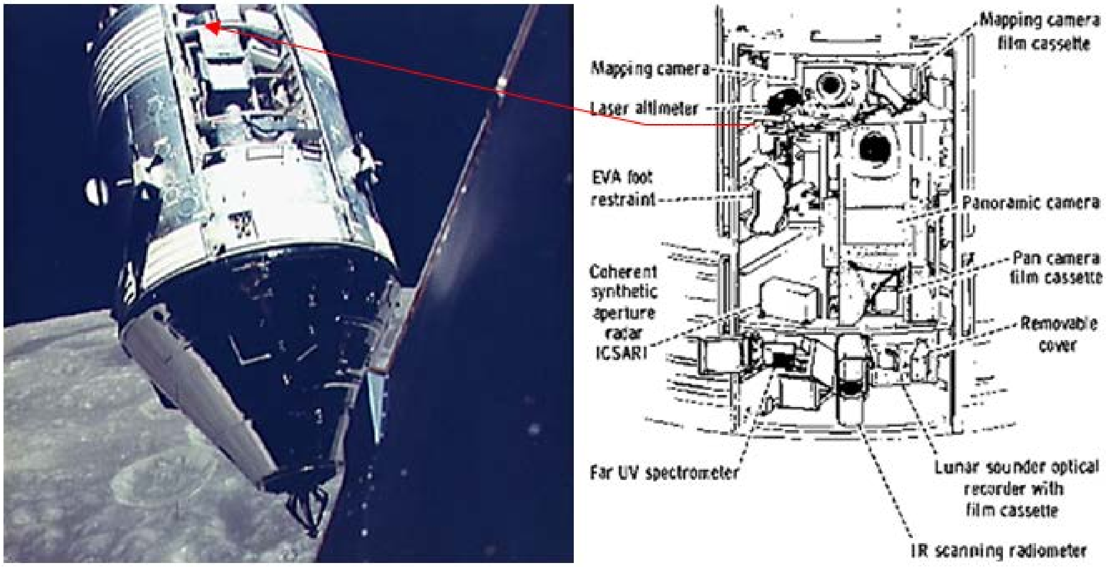

Kaula et al. combined laser altimetry data from the Apollo 15, 16, and 17 missions to derive average elevations for important lunar terrains in relation to the 1,738 km (mean radius) spheroid: "farside terrae +1.8 km, nearside terrae -1.4 km, ringed maria -4.0 km, and other maria -2.3 km" (Kaula et al. 1974, 3049). Their analyses of these laser-derived elevation differences, along with gravitational and surface density measurements, led them to conclusions about the composition and density of the lunar core: "It is unlikely that any iron core is greater than 400 km in radius. A more likely model is a gradual increase in density from 3.33 g/cm-3 to 3.46 g/cm-3 at 1,000 km depth, compatible with Mg/Fe ratios plausible for mare basalt parent material" (Kaula et al. 1974, 3049).

3. Clementine

Launched 25 January 1994, the Clementine lunar probe originated from a NASA/ Ballistic Missile Defense Organization partnership. According to the National Space Science Data Center (NSSDC), Clementine's mission was "to test sensors and spacecraft components under extended exposure…and to observe the Moon and near-Earth asteroid 1620 Geographos" (National Space Science Data Center [NSSDC] 1994, 1). NSSDC claimed that after completing two months of lunar mapping operations and an Earth transfer orbit, Clementine suffered from an attitude control thruster malfunction that exhausted the thruster's remaining hydrazine fuel supply and spun the spacecraft at 80 revolutions per minute (1994). Therefore, NASA scrapped the asteroid rendezvous portion of the mission, and Clementine headed into the Van Allen radiation belts to test its remaining functional components (1994). The mission ended in June 1994 when intelligible transmissions from Clementine to Earth ceased (NSSDC 1994).

Figure 5 provides a drawing of the 1.88 m by 1.14 m (main-body dimensions), 227 kg Clementine spacecraft and its diode-pumped chromium neodymium-doped yttrium aluminum garnet (Cr:Nd:YAG) solid-state compact LiDAR (NSSDC 1994). The NSSDC details page informed us that the Clementine LiDAR functioned at 532 nm and 1064 nm wavelengths (green and infrared) with pulse energies of nine and 180 milli-joules (mJ), respectively (1994). Both the infrared ranging and green active-imaging wavelengths had a pulse-width of less than 10 ns (NSSDC 1994). During lunar-mapping, Clementine's LiDAR frequently outperformed its maximum effective range of 500 km (NSSDC 1994). The Clementine project represented a vast improvement over the Apollo laser altimeters. Researchers geolocated 72,300 of Clementine's 600,000 total laser shots, and accuracy averaged 90 m vertically and 3 km horizontally (Neumann 2001).

Figure 5. Drawing of the Clementine Spacecraft and its LiDAR System. Source: Williams (2011).

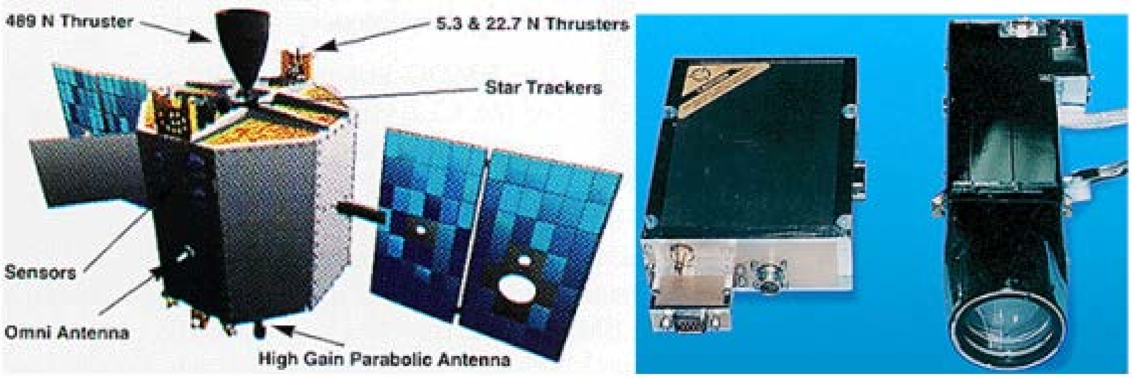

Figure 6 is an equal-area projection topographic map of the Moon derived from Clementine LiDAR data. Elevations range from about -8 km (purple) to +4 km (pink/ white). Also, the Lunar and Planetary Institute informs us that the farside image is tilted in order to show the low-lying, 2,500 km wide, Aitken Basin near the lunar south pole (Lunar and Planetary Institute 2016).

Figure 6. Clementine Topographic Map of the Moon. Source: Lunar and Planetary Institute (2016).

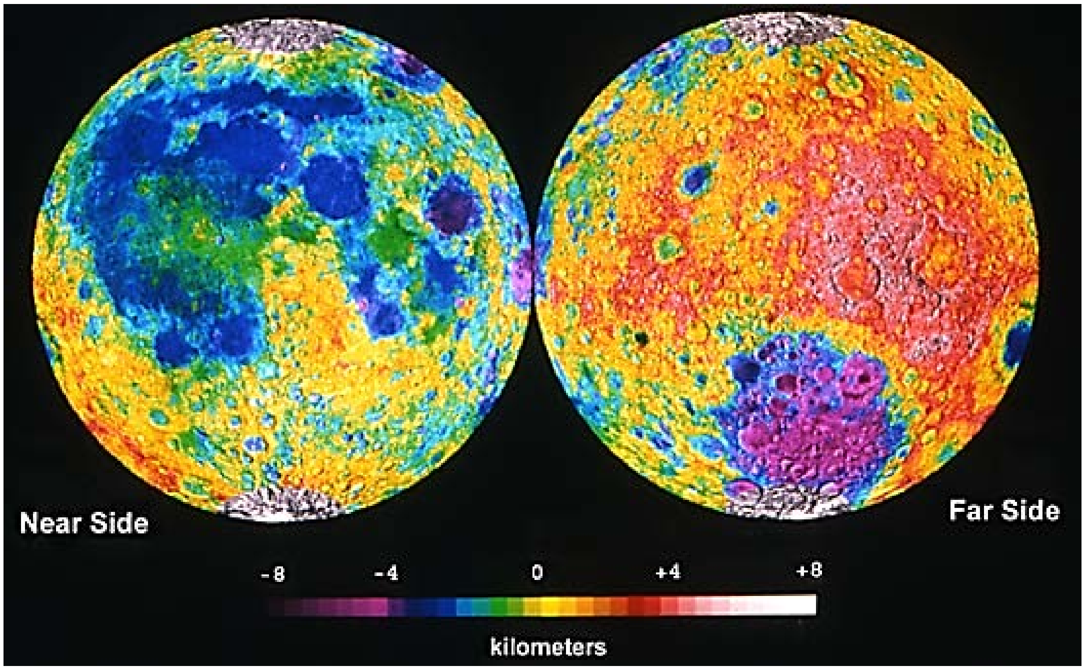

4. Space Shuttle LiDAR In-space Technology Experiment and Laser Altimeter Experiments

In 1994, NASA released a factsheet that contained an interesting eye-safety laser disclaimer and a warning to the international science community to avoid using a medium-plus sized telescope to view the Space Shuttle Discovery during STS-64 (McCormick et al. 1994). The Space Shuttle LiDAR In-space Technology Experiment (LITE) was a first: an atmospheric LiDAR survey conducted by an Earth-orbiting spacecraft (Abshire 2011). Figure 7 provides an illustrated diagram of the payload bay apparatus and the LITE mission concept.

According to Abshire, Discovery maintained a circular low-Earth orbit at 206 km for nine days of data collection (2011). He explained how the thin laser pulses traveled downward through the mid-stratosphere and the troposphere, diverging into 300 m ground spots spaced 740 m along-track (2011). Overall, LITE collected 53 hours of near-nadir atmospheric backscatter profiles on the order of 10 seconds each (Abshire 2011).

Figure 7. LITE Sample Mission and Laser Apparatus Cartoons. Adapted from McCormick et al. (1994).

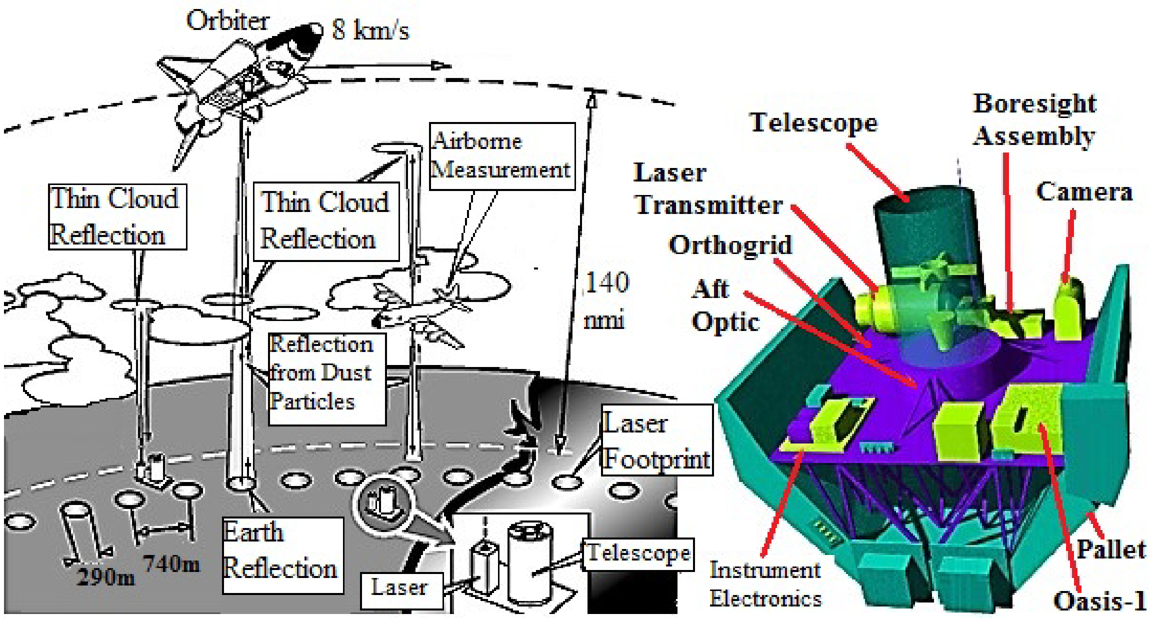

Altogether, the LITE transmitter apparatus, boresight assembly, telescope receiver, camera, and system electronics weighted 1,304 kg and consumed 3,030 watts (McCormick et al. 1994). McCormick commented that the pressurized and thermal-controlled laser transmitter module encased two identical, flash-lamp pumped, Q-switched Nd:YAG lasers (1994). He added that the two lasers never fired simultaneously to ensure redundancy, and the initial laser pulse created was a 1064 nm (infrared) beam (1994). McCormick went on to say that this pulse was temporarily split and then recombined into one beam containing three wavelengths—harmonic generators converted two of the three split-beams into the additional 532 nm (green) and 355 nm (ultraviolet) wavelengths (1994). Additionally, LITE used gimballed turning prisms to point the laser boresight at the Earth, and the receiver encased a Ritchey-Chretien Cassegrain telescope with beryllium as the primary mirror and quartz as the secondary mirror (McCormick et al. 1994). The aft optics assembly contained photomultiplier tubes for detecting the ultraviolet and green ground/atmospheric returns and a silicon avalanche photodiode for the infrared signal (McCormick et al. 1994).

Almost 10 years after program commencement, LITE accomplished the goals of its creators and the LITE Science Steering Group "to demonstrate operation of a LiDAR in space and the maturation of LiDAR technology toward the development of future systems on free-flying satellite platforms" (Winker, Couch, and McCormick 1996, 1). Winker, Couch, and McCormick claimed that LITE would pave the way for future longer-term atmospheric and climate-monitoring satellites, and they were right: ICESat, CALIPSO, and the upcoming ICESat-2 (Winker, Couch, and McCormick 1996).

Within three years of LITE, shuttle-based LiDAR would conduct two additional missions, albeit for a traditional topographic purpose. Shuttle Laser Altimetry (SLA) Missions 1 and 2 "demonstrated the effectiveness of orbital laser altimeters for terrestrial geodesy despite the inconvenience of using the shuttles as an orbital platform" (Neumann 2001, 73). Furthermore, in the publication "Some Aspects of Processing Extraterrestrial LiDAR Data—Clementine, NEAR, MOLA," Neumann mentioned that left-over spares from the Mars Orbiter Laser Altimeter (MOLA) project plus additional components gave rise to the SLA (2001). Although, Neumann did not disclose much further, he did provide some statistics (listed in Table 2) on the MOLA-offshoot that became the LiDAR system for the SLA-01 and SLA-02 missions.

Table 2. SLA Mission Quick Stats. Adapted from Neumann (2001).

Mission	STS	Date	Laser	Shots Fired	Shots Geolocated	Horizontal Accuracy	Vertical Accuracy
SLA-01	STS-72	Jan 1996	Cr:Nd:YAG at 10 Hz	3 Million	1,203,000	40 m	2.78 m
SLA-02	STS-85	Aug 1997	Cr:Nd:YAG at 10 Hz	3 Million	2,090,000	40 m	6.74 m

Unlike the atmospheric-sensing LITE, SLA only needed one 40 mJ, 1064 nm (infrared) laser beam (Bufton et al. 1995). Bufton et al. described that the SLA pulse-width was 10 ns, and the resulting terrestrial footprint was 100 m in diameter (1995). A silicon avalanche diode detected the echoed waveforms (1995). Next, they stated that a pulse waveform digitalizer interpreted the return signal in order to resolve the terrain topography and vegetation height-above-ground profiles within each laser footprint (1995). Furthermore, reducing the waveform resolution and sampling for a longer duration enabled the SLA to function as an atmospheric and cloud-aerosol LiDAR (Bufton et al. 1995). Attached as a Hitchhiker payload, the SLA transmitted its pulses directly along nadir while the Shuttle orbited at around 300 km; along-track sampling was similar to LITE, approximately 740–750 m (Sun et al. 2003).

Figure 8 shows a composite map of the mostly tropical (28.45° N and S) SLA-01 ground tracks and the 57° inclination SLA-02 tracks. Harding et al. used data collected from the SLA-01 mission over “Africa, southern Asia, central South America, and Australia” to test the vertical accuracy of the U.S. Geological Survey’s Global 30 Arc-second Digital Elevation Model (DEM) Dataset (GTOPO30), a DEM with 30 arc-second (~1 km) grid spacing (Harding et al. 1998, 1). For example, Australia had 29,139 discrepancies between SLA-01 measurements and the GTOPO30, with an average error of -21.72 m and a standard deviation of 48.92 m; Africa’s discrepancies totaled 244,640, with a mean error of -1.40 m and a standard deviation of 44.75 m (1998). Additionally, Harding et al. realized that the SLA’s ability to achieve an accurate ground return in a forested area depended significantly on the density of the vegetation (1998). Also, they noted that the SLA mapped only the cloud-top layer when it operated above opaque clouds (Harding et al. 1998).

Figure 8. Earth Surface Coverage for Both Shuttle Laser Altimetry Missions. Source: Carabajal et al. (2000, 2).

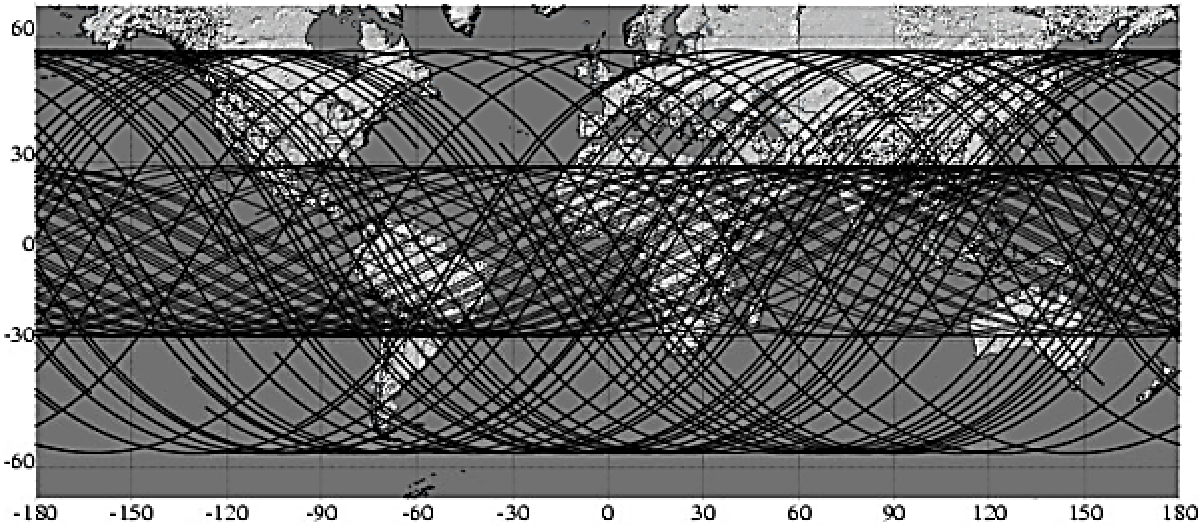

Behn and Zuber combined SLA-01 LiDAR data and TOPEX/POSEIDON radar altimetry to study ocean topography (Behn and Zuber 2000). They discovered a 2.33 m difference (root mean square) between the University of Texas Mean Sea Surface Model (CSRMSS95) and the more than one million SLA-01 sea surface measurements (2000). Moreover, Figure 9 illustrates that the SLA LiDAR could successfully maintain track even when crossing the land-sea threshold in coastal areas with drastically varying elevations (Behn and Zuber 2000). The top region presented in Figure 9 is a selection of the South American coast and the bottom region is a segment of the Red Sea. Also, the laser points are represented by red dots, and the land outline is a conjunction of National Geophysical Data Center Terrain Base elevations and over-ocean segments of the Earth Gravitational Model 1996 (EGM96) geoid (Behn and Zuber 2000).

Sun et al. compared SLA-02 altimetry data to the corresponding surface heights from the year 2000 Shuttle Radar Topography Mission (SRTM) to create a highly accurate and digital global-topographic database (Sun et al. 2003). Their first step was filtering out cloud returns by eliminating any point with an elevation above 3 km (2003). Their follow-on tasks involved analyzing all waveforms and terrain returns, then associating them to Landsat imagery (2003). The LiDAR data was instrumental in validating the radar data and led to their strong conclusion: “The SRTM DEM proves to be the best-known DEM ever generated at the global scale with its consistency and overall accuracy” (Sun et al. 2003, 410).

Figure 9. Two SLA-01 Profiles Illustrating the Ability to Track Across the Land-Sea Interface. Source: Behn and Zuber (2000, 1436).

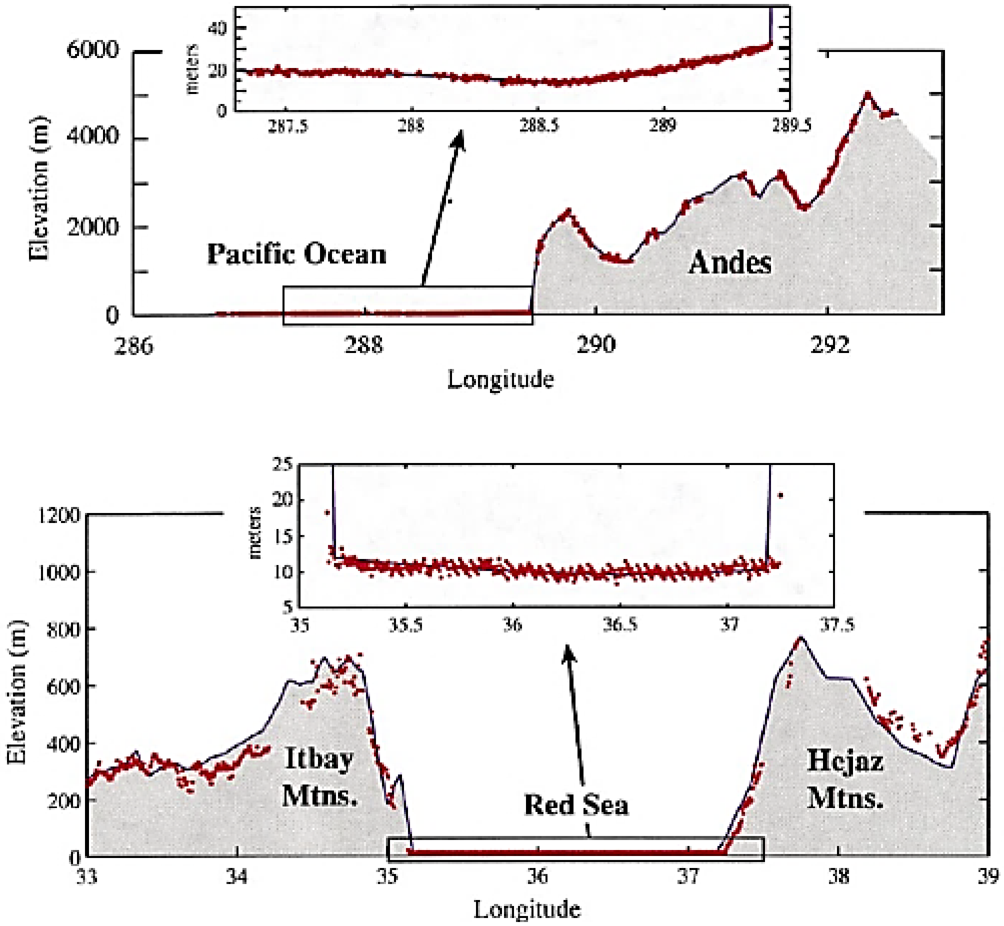

Only two of the four originally planned SLA missions occurred, nevertheless Bufton et al. correctly predicted that the SLA would serve as an important precursor for future space-based LiDAR systems, including the Geoscience Laser Altimeter System (GLAS)—eventually to fly onboard ICESat (Bufton et al. 1995). Indeed, LITE and SLA marked the beginning of an ongoing NASA Goddard endeavor to transcend aircraft LiDAR systems into “space-based laser remote sensing devices” (Bufton et al. 1995, 1).

5. Mars Global Surveyor/Mars Orbiter Laser Altimeter

Over the course of its decade-long mission from November 1996–2006, the Mars Global Surveyor (MGS) spacecraft and its LiDAR, the Mars Orbiter Laser Altimeter (MOLA), provided laser topographic mapping across the entire surface of the red planet (NASA 2007b). Figure 10 offers a rendition of the MGS and a photograph of MOLA.

Figure 10. Mars Global Surveyor and MOLA. Left Source: NASA Jet Propulsion Laboratory [JPL]/California Institute of Technology [Caltech] (2012). Right Source: Smith, David, and Zuber (2007).

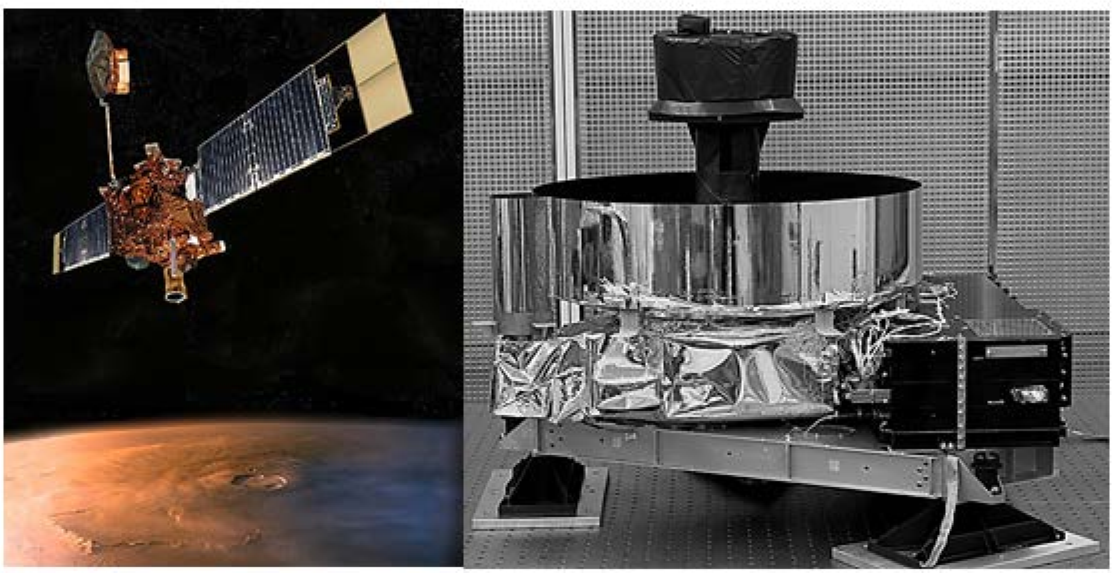

According to Smith, the 25.9 kg and 30.9 watt MOLA was nearly identical to the Mars Observer Laser Altimeter (same acronym) that had flown onboard the ill-fated Mars Observer Probe three years prior (Smith 1996). He mentioned that MOLA’s non-topographic objectives included measuring the vertical profiles of carbon dioxide and water clouds in the Martian atmosphere (1996). Furthermore, Smith and other scientists combined MOLA LiDAR data with measurements from the spacecraft’s other instruments, such as the thermal emission spectrometer and the magnetometer, to study the internal compositions of the two polar caps and the other planetary structures on Mars (Smith 1996).

Figure 11 shows a diagram of the laser waveform produced by MOLA's Q-switched, diode-pumped, Nd:YAG laser that operated at 10 Hz, 40 to 45 mJ, 8 ns pulse-widths, and a 1064 nm (infrared) wavelength (Abshire 2011). Abshire stated that the silicon avalanche photodiode analog detector was effective at catching a minimum return signal of 230 photons (represented by the line labelled detection threshold); pulse round-trip travel time and the corresponding laser-derived ranges enabled the calculation of surface elevation (2011). The shape of the returned laser waveform described terrain roughness, and a comparison of the transmitted versus received pulse energies yielded a means to predict surface reflectance (Abshire 2011). MOLA's horizontal and absolute vertical resolutions were 160 m and 30 m, respectively (Smith 1996).

Figure 11. Sample MOLA Measurement. Source: Abshire (2011, 11).

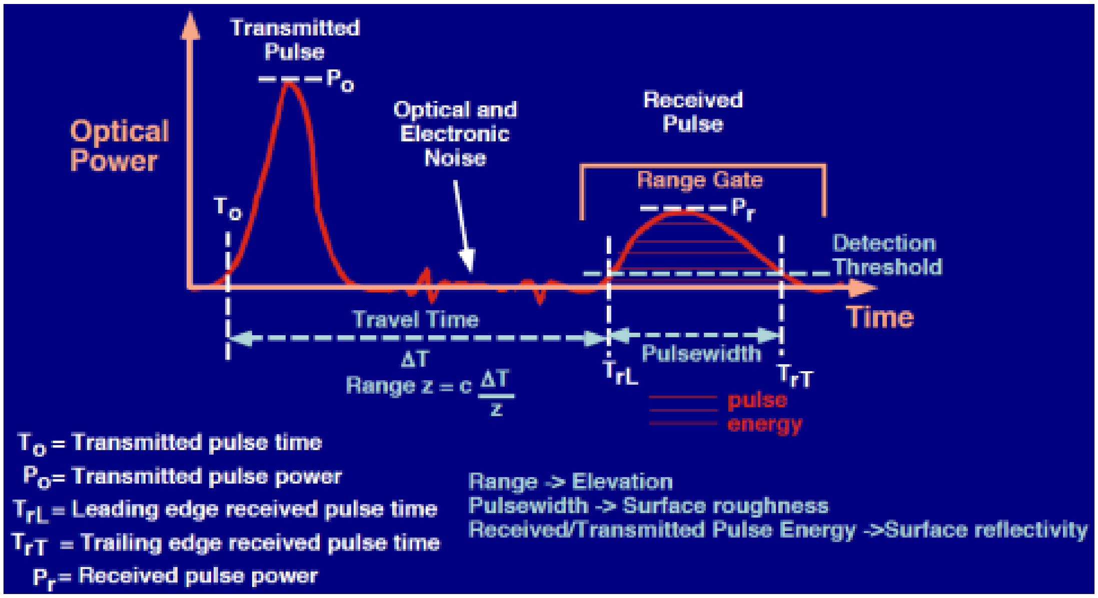

An example of one of about 671 million MOLA laser shots.

The MGS mission represents a historic success. MOLA data vastly improved the scientific community's overall understanding of Mars (NASA JPL/Caltech 2016). Prior knowledge about the red planet came almost exclusively from less accurate and outdated

Mariner, Viking, and Earth-based radar measurements (Smith et al. 2001). Per Smith et al., after spending the first two years on station in capture and aerobrake testing orbits, the MGS spacecraft commenced its LiDAR-mapping mission in February of 1999 from a 400 km circular, near-polar, orbit at 92.8° inclination (2001). Figure 12 provides topographic maps of the Martian north and south poles (elevations in m). Figure 13 is a side-by-side topographic map of the eastern and western hemispheres (elevations in km).

Figure 12. MOLA LiDAR Elevation Maps of Mars' North and South Poles.
Source: NASA JPL/Caltech (2016).

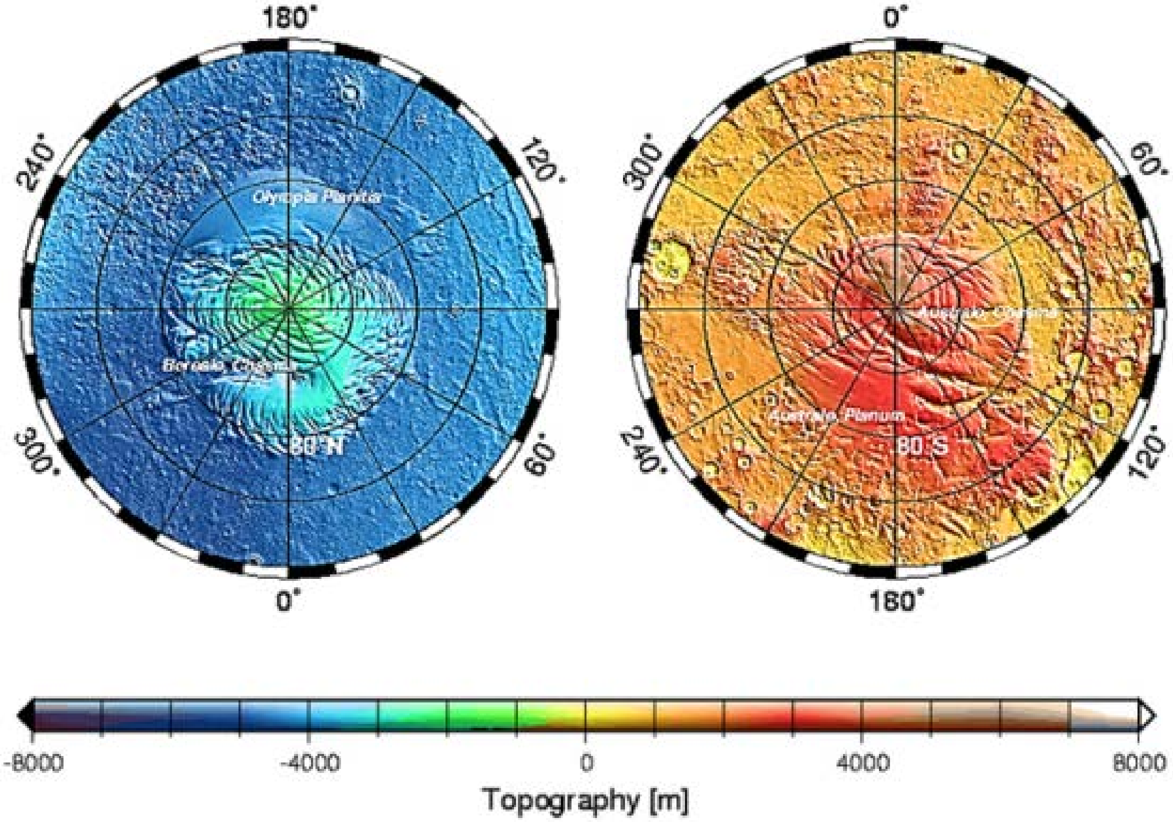

North pole (Left) labels: Olympia Planum—Icecap plateau at (180º E, 80º N). Boreale, Chasma—The deep trench in the ice cap at (330º E, 85º N).

South pole (Right) labels: Australe, Planum—Southern plain that coincides with part of the southern icecap. Australe, Chasma—A canyon near (90º E, 85º S).

Figure 13. MOLA LiDAR Elevation Map of Mars' Eastern and Western Hemispheres. Source: NASA JPL/Caltech (2016).

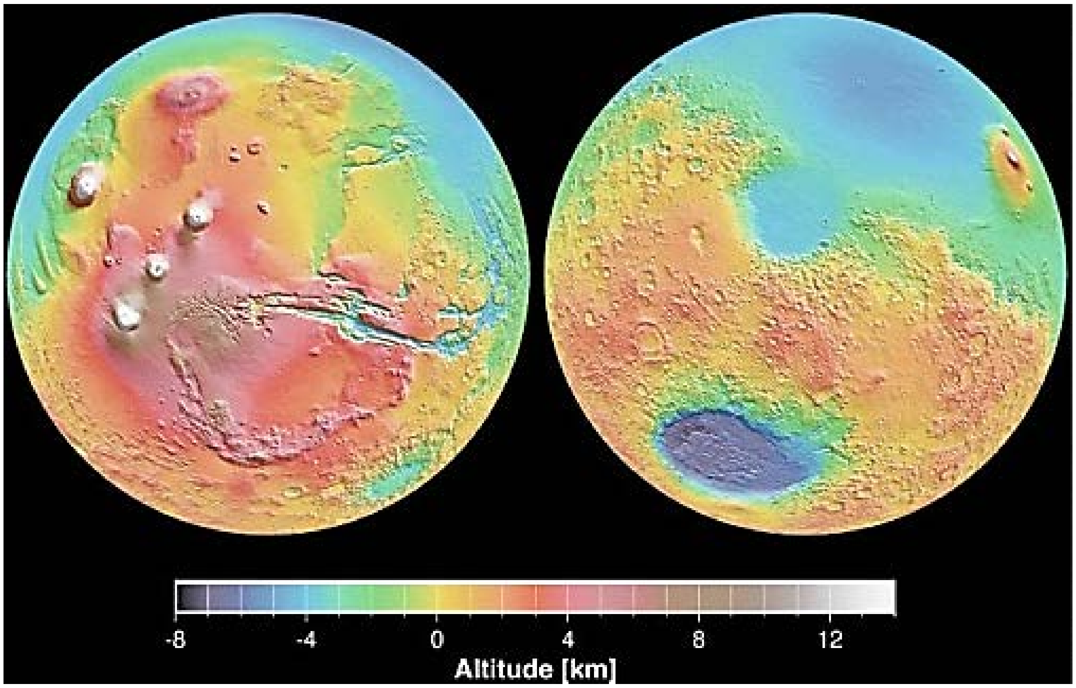

6. Near Earth Asteroid Rendezvous Spacecraft—Asteroid 433 Eros

From 2000 to 2001, NASA's Near Earth Asteroid Rendezvous (NEAR) spacecraft, nicknamed Shoemaker, performed a scientific study of the asteroid 433 Eros from a predominantly 35 km orbit (Cole 1998). Cole explained that the NEAR Laser Rangefinder's (NLR) mission was to collect precise laser altimetry measurements that would supply scientists with high quality data products unobtainable from Earth-based asteroid research (1998). Also, he revealed that in order to carry out its extended deep-space tasking, NEAR maintained orbital trajectories which kept its LiDAR and other instruments directed at 433 Eros while simultaneously pointing the topside communications antenna and solar arrays at the Earth and Sun, respectively (1998). Figure 14 demonstrates this feat of spacecraft attitude control, and it also shows a single NLR footprint of 12 m—not to scale on the estimated 36 km x 15 km x 13 km (length, width, height) asteroid.

Figure 14. Drawing of Orbital Requirements for NEAR and Photograph of Its Laser Rangefinder. Source: Cole (1998, 143, 145).

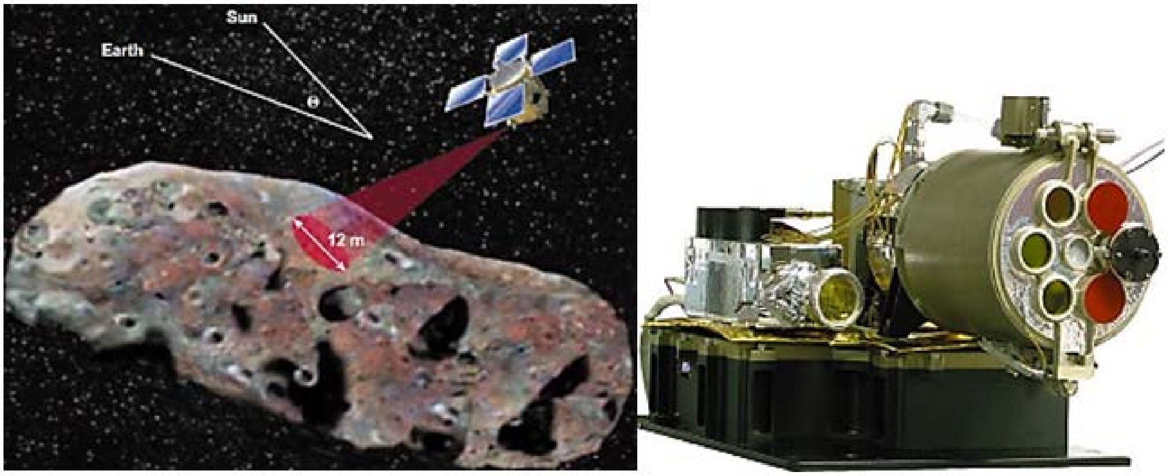

Figure 14 also provides a picture of the LiDAR device that successfully mapped 433 Eros from ranges up to 100 km (Cole 1998). Cole commented that pre-launch testing of the NLR yielded an average range accuracy of 32 cm and a beam divergence of 235 micro-radians (Cole 1998). Per Abshire, the 4.9 kg NLR operated at 1 Hz, 16.5 watts of power (average), 15 mJ pulse energies, 12 to 15 ns pulse-widths, and a wavelength of 1064 nm (infrared) (Abshire 2011). Also, the laser transmitter was a Q-switched, diode-pumped, Nd:YAG system (Abshire 2011). Cole mentioned that the NLR's avalanche photodiode detector employed advanced timing electronics for time-of-flight (TOF) calibrations and for accurate detection of the laser backscatter from the asteroid's surface (Cole 1998).

In their report titled "The Shape of 433 Eros from the NEAR-Shoemaker Laser Rangefinder," Zuber et al. presented topographic findings and diagrams based on the NLR-collected data (Zuber et al. 2000). Figure 15 is a radius map of the asteroid using a cylindrical projection; longitude is positive in the easterly direction from 0° to 360°, and latitude ranges from -90° to 90°. Zuber et al. indicated that latitude separation is approximately 54 m at the asteroid's poles, expanding to 307 m at the equator (2000). Of note, the low regions named Himeros and Psyche center themselves at 75° East and 270° East, respectively.

Figure 15. Radius Map of 433 Eros in Cylindrical Projection.
Source: Zuber et al. (2000, 2098).

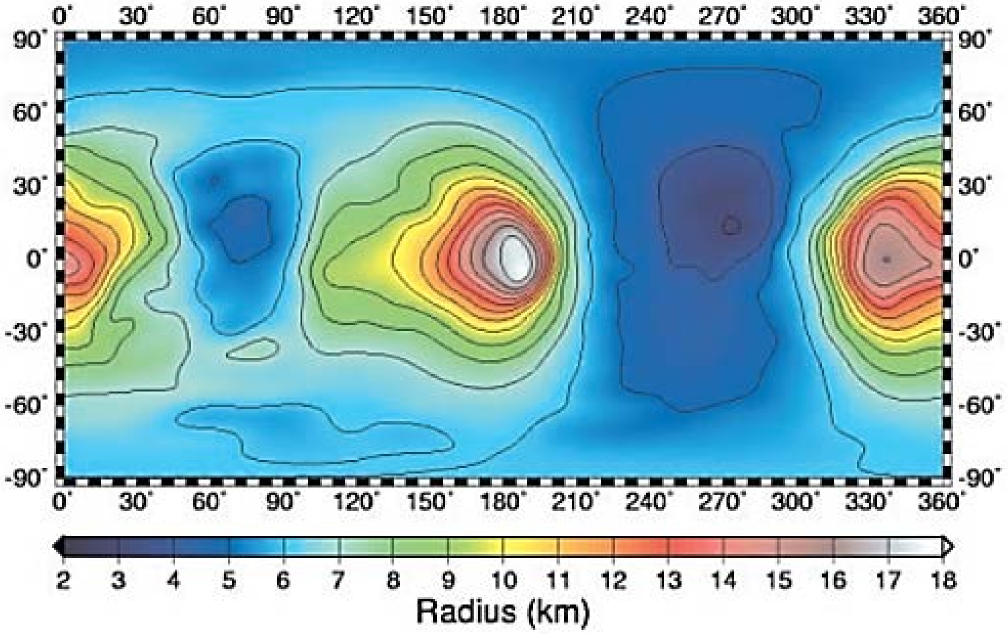

Furthermore, the NLR enabled Zuber et al. to determine the overall shape and slopes of 433 Eros (2000). They concluded that the asteroid generally slopes between five and 15 degrees with exception of the two sharply concave regions Himeros and Psyche that together form a wide depression running north to south, slightly offset toward the positive x-direction (Zuber et al. 2000). Figure 16 provides two 3D views of 433 Eros with slopes color-scaled from a 0° low (purple) to a 40° high (white). The left view is from (300°E, 30°S), and the right view is from (0°E, 30°S).

Figure 16. Two Views of a 3D Shape Model of 433 Eros from the NLR. Source: Zuber et al. (2000, 2099).

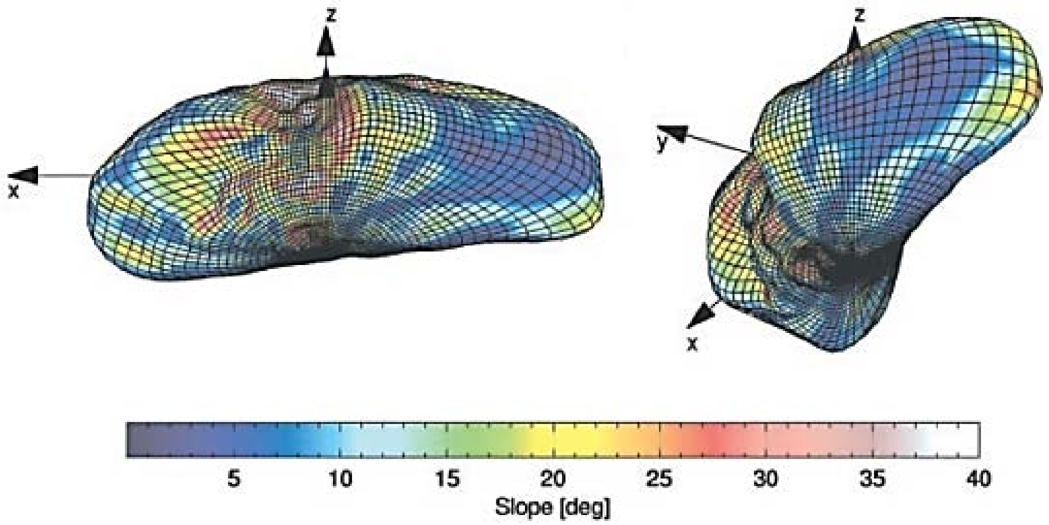

7. Phoenix Mars Lander

Landing on the red planet in May 2008, the mission of Phoenix Mars Lander was to investigate a region on Mars where scientists expected the topsoil to contain a significant amount of frozen water (NASA 2008).[1] NASA explained that Phoenix would conduct ground-based weather research near the Martian north pole, specifically focusing on the seasonal water cycle where ground-ice sublimes into atmospheric water vapor and later depositions back into solid form (2008). Phoenix's meteorological LiDAR measured the downward-reflected laser backscatter in order to collect altitude, abundancy, and sizing data for particles of dust and ice in the atmosphere (NASA 2008).

Figure 17 presents an artistic rendition of the probe's robotic arm hard at work collecting soil samples for onboard testing. Meanwhile, its top-mounted LiDAR conducts laser measurements of the Martian atmosphere. Figure 17 also displays a true-color surface stereo photograph taken by Phoenix on 25 June 2008.

---

[1] Earlier gamma-ray spectrometer observations by the Mars Odyssey Orbiter aided in selection of the Phoenix landing site; Odyssey measurements suggested that permafrost soil existed near the planet's poles (NASA, 2008).

Figure 17. The Phoenix Mars Lander. Source: NASA (2015).

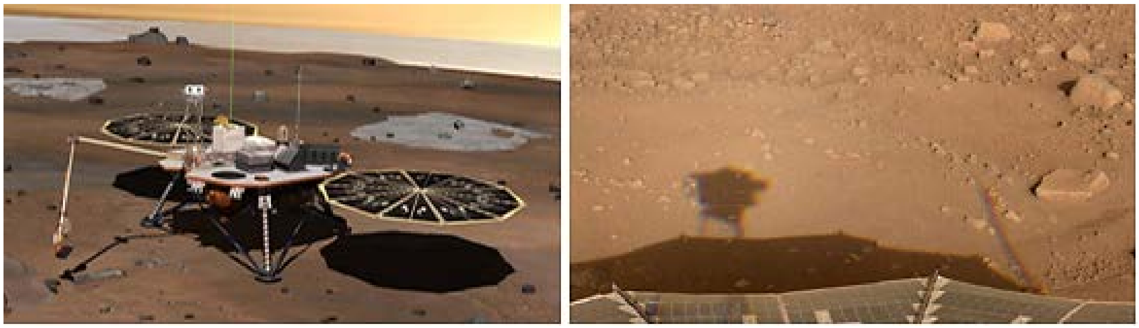

The Canadian Space Agency contributed the Phoenix weather instrument suite, and the LiDAR came courtesy of MDA Space Systems, Ontario and Optech Inc., Toronto. Whiteway et al. remarked that the laser transmitted at 100 Hz via a passively Q-switched, diode-pumped, Nd:YAG assembly that produced a pulse-width of 10 ns and a total pulse energy of 0.7 mJ: 0.3 mJ at 1064 nm (infrared) and 0.4 mJ at 532 nm (green) (Whiteway et al. 2008). They stated that a potassium-titanyl phosphate crystal created the visible green wavelength from part of the original infrared beam through frequency doubling (2008). Additionally, the 10 cm diameter receiver employed a silicon avalanche photodiode detector that recorded the return signals via 14-bit analog and photon-counting methods (Whiteway et al. 2008).

Overall, Phoenix exceeded expectations by significantly outlasting its intended mission duration of 90 Martian solar days (sols) (Whiteway et al. 2008). A sol is approximately 24 hr 39 min 35 sec. Figure 18 provides a LiDAR-derived vertical profile, local time versus altitude, of the Martian clouds directly above the probe on sol 99 (3 September 2008); starting at 0500 local, ice crystals are detected falling from the clouds at an altitude of about 3.25 km (NASA/JPL-Caltech 2016).

Figure 18. Phoenix LiDAR Profile of Martian Clouds with Falling Ice Crystals. Source: NASA/JPL-Caltech (2016).

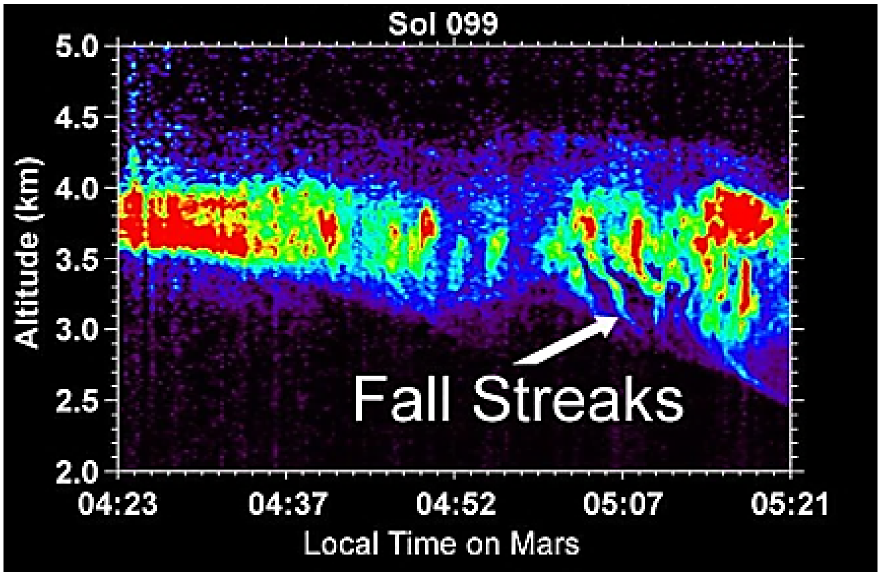

Collected on 3 September 2008.

8. Space Shuttle Triangulation + LiDAR Automated Rendezvous and Docking

Although the purpose of the LiDAR system discussed here differs substantially from nearly all of the others, it is nonetheless worthy of inclusion as a two-fold testament to the future of precision spacecraft rendezvous and to the honored memory of the Space Shuttle. Figure 19 is a photograph taken from the International Space Station (ISS) of the Space Shuttle Discovery testing the Triangulation + LiDAR (TriDAR) spacecraft precision docking system during STS-131 in April 2010 (NASA Human Space Flight 2014). Neptec Design Groups' TriDAR is a self-sufficient "vision" laser system that applies its own models and protocols during proximity operations without the assistance of retroreflectors or other inputs from the rendezvous target (Ruel, Luu, and Berube 2010, 15). Representing another international endeavor between NASA and the Canadian Space Agency, the TriDAR completed three space-testing flights on STS-128, STS-131, and STS-135 (Christian and Cryan 2013).

Figure 19. Discovery Docking with the ISS Using TriDAR. Adapted from NASA Human Space Flight (2014).

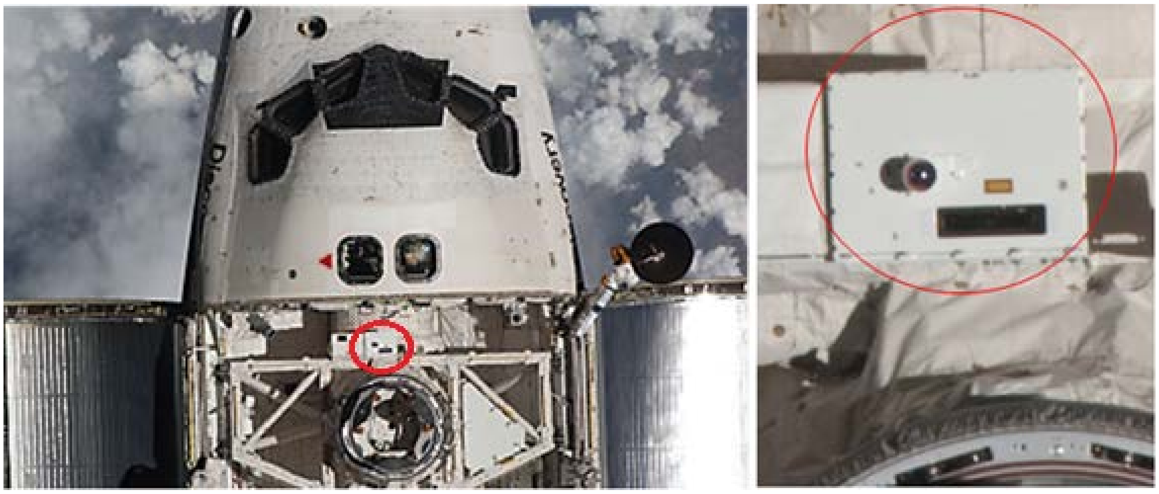

STS-131, April 2010. TriDAR is circled.

On these STS missions, TriDAR demonstrated the ability to derive the target spacecraft’s shape, proximity, and relative velocity from its analyses of successive 3D point clouds (Christian and Cryan 2013). Furthermore, starting with STS-131, TriDAR successfully maintained a real-time track on the ISS during a 360-degree circumnavigation without any external automation or human-controlled inputs (Ruel, Luu, and Berube 2010).

Figure 20 graphs the three-axis docking approach of Discovery with the ISS during the first TriDAR space-test in August 2009. Relative distances on all y-axes are in feet, and each graph includes three vertical lines to distinguish among the final approach, triangulation transition, and capture phases. Ruel, Luu, and Berube noted that the total process took approximately 30 minutes from the go-for-dock command (2010). Moreover, the TriDAR system continuously fed the Space Shuttle’s pilots highly accurate closing data, including automatically updated state vectors giving the relative position of the ISS throughout docking and undocking operations (Ruel, Luu, and Berube 2010).

Figure 20. Three-Axis Docking Distances from Discovery (STS-128) to ISS. Source: Ruel, Luu, and Berube (2010, 18).

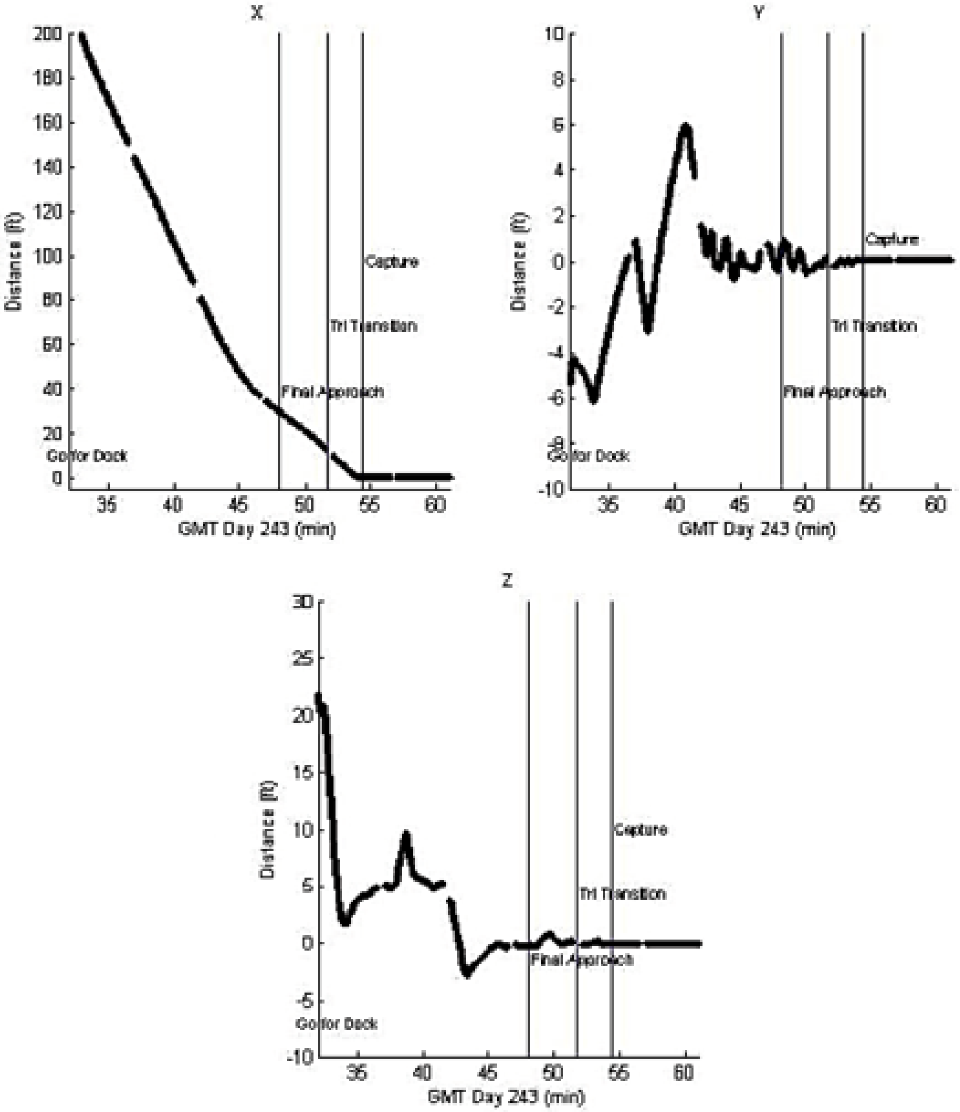

According to Neptec, the TriDAR system uses laser-triangulation methods similar to those applied by the Space Shuttle's Laser Camera System (Ruel, Luu, and Berube 2010). Ruel, Luu, and Berube mentioned that a single laser optic conducted both triangulation and LiDAR functions to collectively improve the system's capability to accurately detect objects in space (2010). Additionally, the system employs a thermal detector to extend initial target detection and subsequent rendezvous guidance beyond the maximum range of the laser component alone (a few km) (2010). With the thermal imager operational, the TriDAR system successfully detected the ISS at a range of just over 43 km (Ruel, Luu, and Berube 2010).

Lastly, Figure 21 is a 3D TriDAR-generated laser image of the ISS. Space Shuttle Discovery compiled the image during undocking operations and throughout the shuttle’s subsequent circumnavigation of the station (Ruel, Luu, and Berube 2010). The image is colored by relative ranges from near to far: red, yellow, green, and blue. Despite Discovery passing behind the ISS while mapping, the opposite side is still represented in the TriDAR point cloud as farther-away (blue) due to the outward spiral-type maneuver taken by the Shuttle around the station (Ruel, Luu, and Berube 2010).

Figure 21. TriDAR 3D Mapping of ISS During STS-128 Undocking Operations.
Source: Ruel, Luu, and Berube (2010, 19).

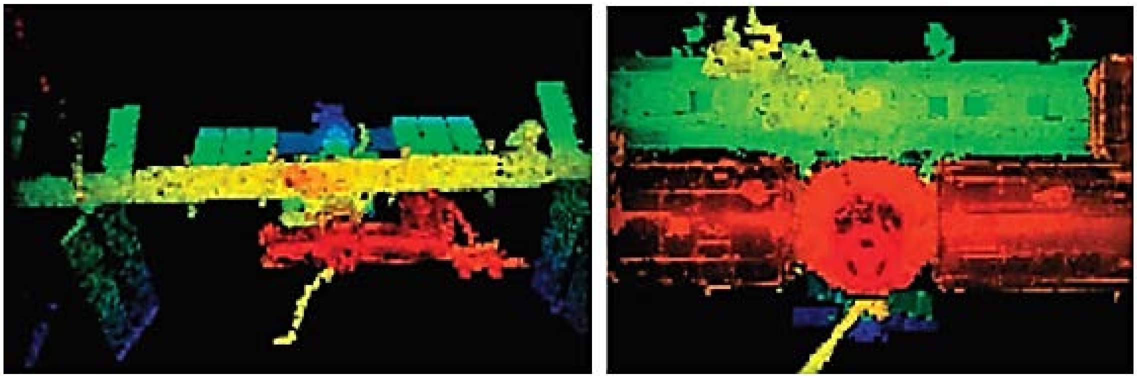

9. Ice, Cloud, and Land Elevation Satellite/Geoscience Laser Altimeter System

In the early 2000s, the Shuttle’s LITE and Laser Altimetry missions of the 1990s became surpassed in duration, scope, and magnitude. NASA’s Ice, Cloud, and Land Elevation Satellite (ICESat) carried one scientific instrument, the Geoscience Laser Altimeter System (GLAS); the final stats are seven years in operation (2003–2010) and 1.98 billion laser shots (Abshire 2011). ICESat had numerous objectives, but the principle ones involved measuring the changing elevations and mass balances of the ice sheets and landmasses located at the Earth’s Arctic and Antarctic regions (NSSDC 2003). NASA scientists would use this data to calculate the current and estimated-future effects of climate change on global sea levels and polar sea-ice volumes (2003). ICESat's secondary missions included additional LiDAR-specialized tasks, such as measuring the vertical structures and heights of clouds and aerosols; mapping terrain topography, reflectivity, and roughness (outside of the polar regions); and analyzing forest structures and biomass, vegetation heights, and snow patterns (NSSDC 2003). Figure 22 provides a rendition of ICESat and a photograph of GLAS under construction.

Figure 22. Artist Rendition of ICESat on Orbit and Boresight View of GLAS. Adapted from NASA Goddard (2015).

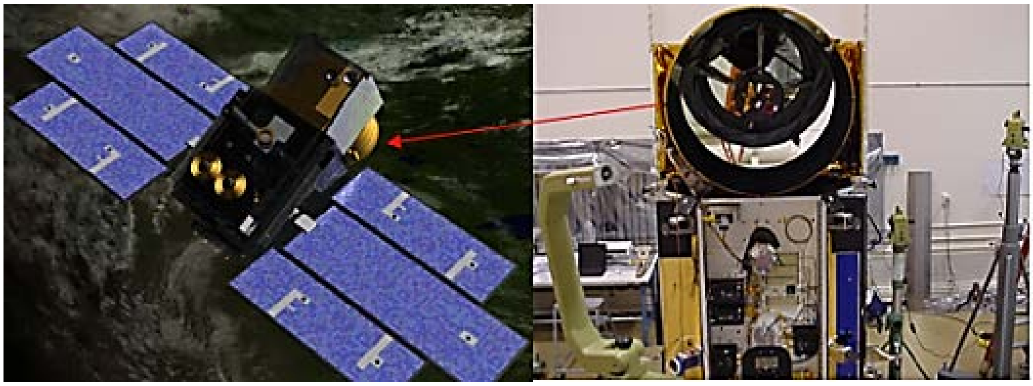

After initial on-orbit testing, ICESat repositioned into its 94° low-earth, nearly circular, orbit with an apogee of 594 km and a perigee of 586 km (NSSDC 2003). Figure 23 demonstrates ICESat using Global Positioning System (GPS) receivers to maintain accurate orbital timing and positioning. Additionally, it shows ICESat employing star trackers for precision spacecraft attitude control and laser boresight pointing. The ground tracks, transmitted along nadir, are spaced 170 m apart with each laser footprint measuring 70 m in diameter (Abshire 2011).

Figure 23. GLAS Measurement Approach. Source: Abshire (2011, 24).

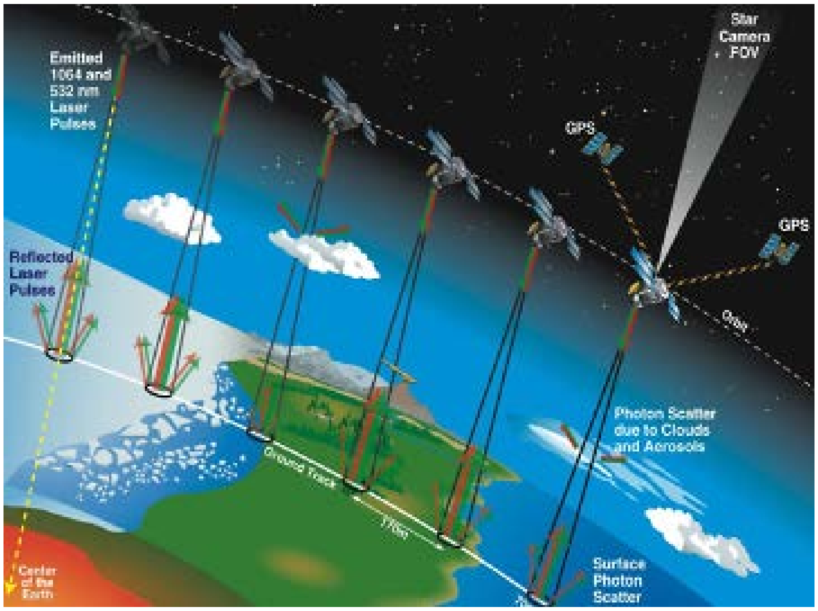

To achieve the intended three- to five- year data collection period, GLAS carried three transmitter modules, and each one had a 40 Hz Nd:YAG laser that produced a combined 1064 nm (infrared) and 532 nm (green) pulse (Abshire 2011). Abshire stated that pulse-widths were 4 ns in duration (2011). Additionally, he specified that a silicon avalanche photodiode served as the infrared detector capable of recording the return signal at 1 Gigahertz (GHz) (2011). Photon-counting detectors captured the green ground-return pulses and atmospheric backscatter (Abshire 2011). The infrared component measured surface altimetry and thick-cloud elevation data at accuracies of 15 cm, and the green component measured thin-cloud and atmospheric-aerosol distributions (Zwally et al. 2002).

The literature-base of research conducted from ICESat/GLAS measurements is as extensive as the numerous raw and processed data products themselves. The author discovered more scientific publications hereunto pertaining than for any of the other systems discussed in this review. Hieu van Duong analyzed the quality of large-footprint full waveforms and elevation data for selected areas in Europe, discovering that the available ICESat data conformed reasonably well to a Gaussian decomposition approach for waveform analysis despite the low number of identical-repeat footprints across the

European continent (Duong 2010). Likewise, Yadav's study of the complex, multi-peaked, ICESat waveforms from ravines and other areas of rough terrain created improved DEMs for those areas as compared to DEMs generated exclusively from the Earth Observing Cartosat satellites (Yadav 2010).

Figure 24 provides examples of Duong's Gaussian decomposition approach for land-cover classification. Two ICESat tracks are aligned to the right of their respective CORINE Land Cover (CLC) 2000 database tracks. All tracks are colored by coverage classification: high vegetation (green), urban (red), bare/low vegetation (white), or water (blue). Overall, Duong's classification results matched well with the CLC2000 data, with general exceptions in three small areas (labelled one through three with zoomed in views to the left). Area one represents bare ground misclassified as urban; Area two is water misclassified as bare ground; Area three is urban misclassified as forest. In each area of misclassification, the waveform for one return is illustrated, it corresponds to the location marked by the white arrows. The black waveform is the ICESat data, and the yellow its Gaussian decomposition.

Figure 24. Classification Based on Waveform Gaussian Decomposition for Two ICESat Tracks Superimposed on Landsat-7 Imagery.
Source: Duong (2010, 140).

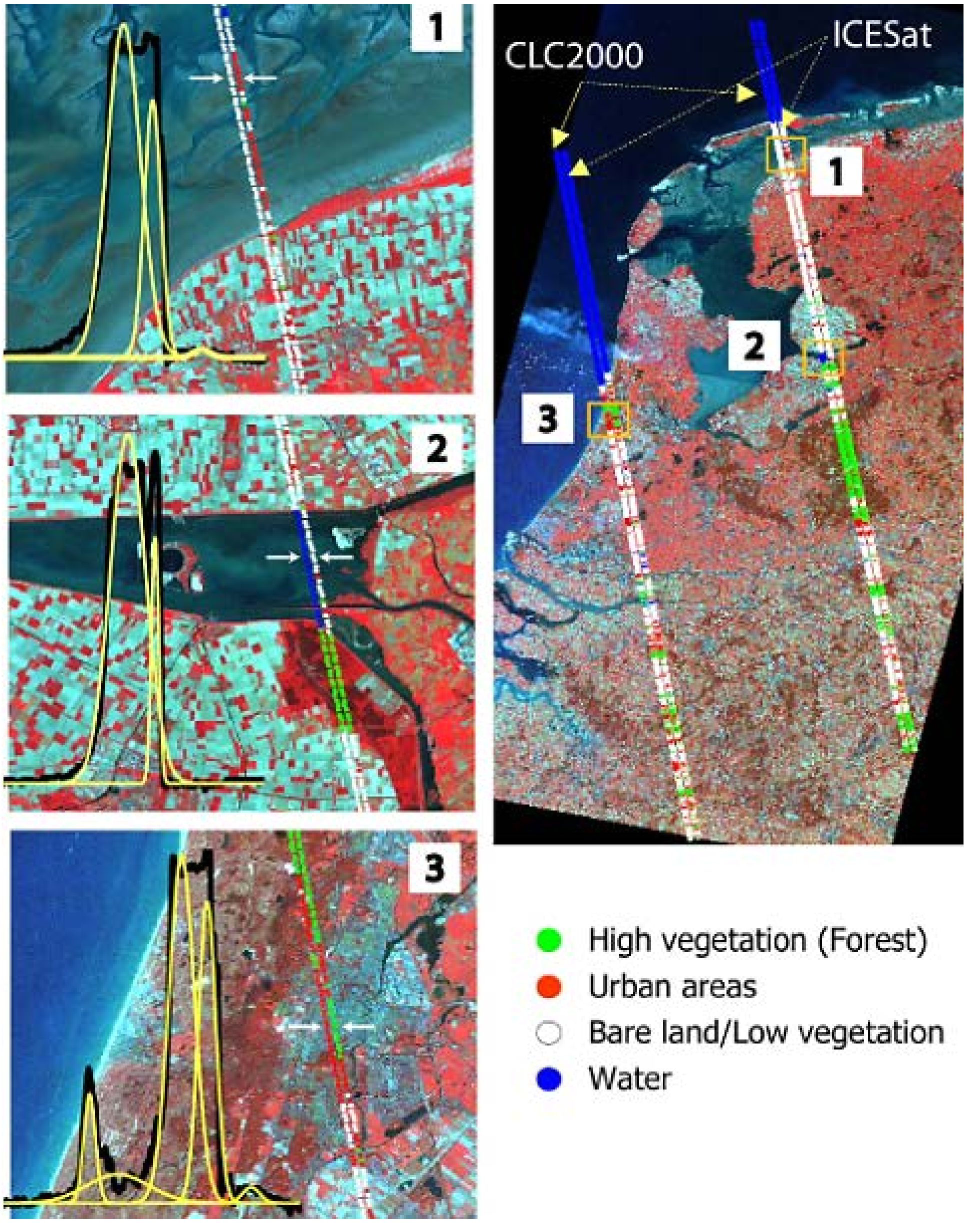

Research studies which derive an understanding of Arctic and Antarctic landmass elevations, sea-ice thickness, subglacial features, and climate changes are even more impressive. Kurtz et al. merged snow depth models with ICESat data for the winter and fall seasons from 2003 to 2008 (Kurtz et al. 2011). Their results indicated that the warmer ocean is contributing an ever-increasing effect on Artic land temperatures due to the shrinking volume of sea-ice, which acts as an insulator between land and sea (Kurtz et al. 2011). Sorensen et al. used an ICESat measurement-based procedure to predict the changing mass distribution of the Greenland ice sheet, concluding that annual losses ranged from between 191 ± 23 to 240 ± 28 billion tons of ice (Sorensen et al. 2011). More recently, Howat et al. combined ICESat elevation data, Worldview stereopair imagery, Landsat imagery, and ice-penetrating radar measurements to expose the sudden and unexpected drainage of a subglacial lake in Greenland (Howat et al. 2015).

Figure 25 provides an elevation map of Antarctica derived by Shuman from ICESat/GLAS collections over approximately one month: 3 October to 8 November 2004 (Shuman 2016). The dark blue areas at 0 m above sea level are the ice sheets. The maximum elevation, about 4 km, defines the majority of Antarctica's eastern region. The crisscrossing lines show the satellite's ground tracks over time.

Figure 25. Antarctica Elevation Model from GLAS Collections. Source: Shuman (2016).

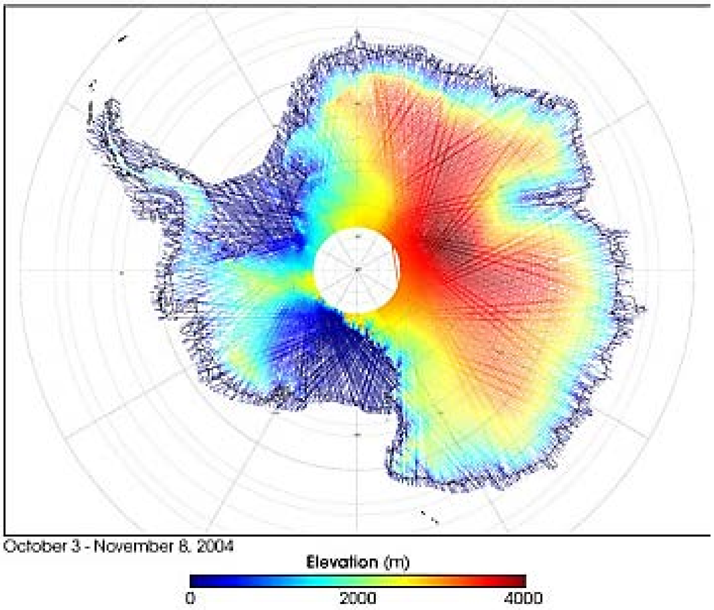

Lastly, scientific papers pertaining to vegetation structures, biomass, and cloud/ aerosol distributions (ICESat's secondary missions) are also detailed and extensive. For example, Pang et al. discovered that GLAS waveform data captured during the summer and early fall seasons contributed better intensities for estimating temperate forest heights in northeastern China (Pang et al. 2008). Goetz et al. analyzed ICESat global-altimetry and land-altimetry datasets, in conjunction with Moderate Resolution Imaging Spectroradiometer (MODIS) data and information extracted from the Alaska Burned Area Database, to study disturbed forests in Alaska (Goetz et al. 2010).

Figure 26 is a vertical profile of wildfire smoke clouds in central California. The top left window box exhibits the corresponding ICESat track (green line), locations of fires (red dots), and smoke direction. In the main image, the x-axis indicates latitude and longitude, and the y-axis is cloud height in km. Density is color-coded from dark blue (ambient atmosphere) to white (dense clouds/smoke). Palm explains that the densest sections of wildfire smoke are located primarily at ground level and an altitude of about 4 km (Palm 2016).

Figure 26. Vertical Profile (Height and Density) of California Wildfire Smoke Clouds, 28 October 2003. Source: Palm (2016).

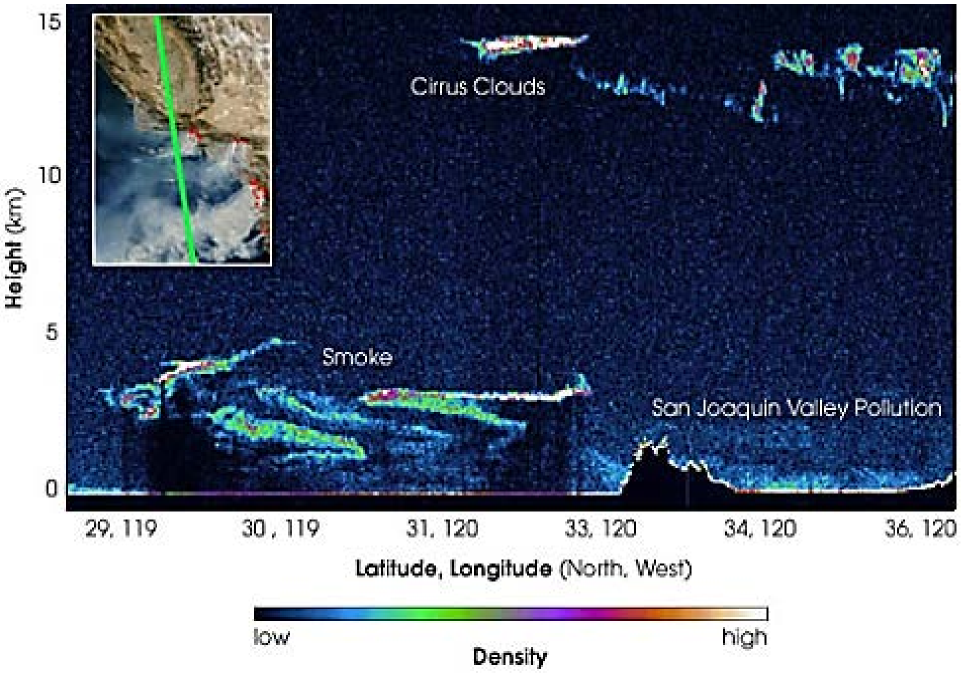

The aforementioned research publications represent just a few examples of the vast literature that stemmed from NASA’s ICESat mission. Undoubtedly, datasets from its follow-on, ICESat-2, will motivate even more cryosphere-related, atmospheric, and forestry publications, including ones that make critical comparisons between current ICESat and future ICESat-2 datasets for long-term trend analyses.

10. Mercury Surface, Space Environment, Geochemistry, and Ranging Orbiter

Abshire pointed out that “in March 2011, the Mercury Surface, Space Environment, Geochemistry, and Ranging Orbiter (MESSENGER) became the first spacecraft in history to orbit our innermost planet” (Abshire 2011, 41). He added that the instrument suite underneath the probe contained a magnetometer; energetic particle, neutron, gamma ray, x-ray, atmospheric, surface, and plasma spectrometers; a dual wide- and narrow-angle imaging system; and the Mercury Laser Altimeter (MLA) (Abshire 2011). MESSENGER’s magnetometer occupies the position at the tip of the extended pole in Figure 27, and the MLA sits about midway on the underside of the spacecraft’s main body.

Figure 27. Artist Impression of MESSENGER Orbiting Mercury. Source: Hopkins University Applied Physics Lab/Carnegie Institution (2016).

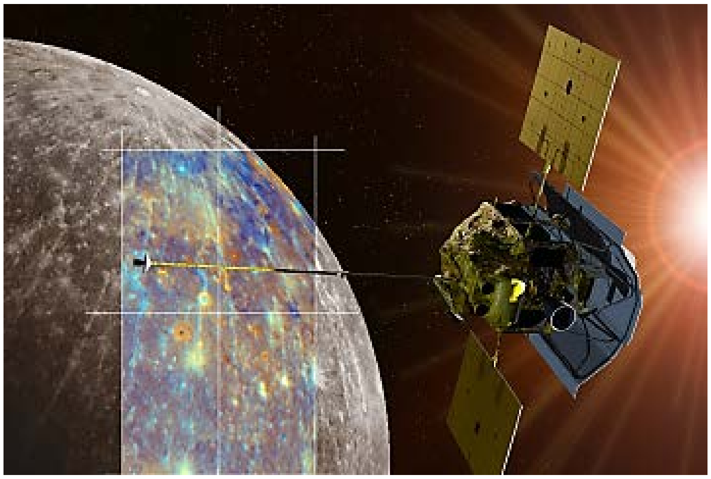

Enhanced color photograph overlay taken near Hokusai Crater.

Cavanaugh et al. processed MLA’s range calculations and boresight pointing angles, in conjunction with spacecraft orbital data, to precisely characterize Mercury’s surface topography (Cavanaugh et al. 2007). Additionally, Neumann's analysis of surface reflectance measurements led to the theory that anomalous bright and dark spots on Mercury's northern facing slopes indicated the possible presence of subsurface water-ice insulated by organic volatiles, both deposited by foreign bodies after impact with the planet (Neumann et al. 2012).

Figure 28 is a MLA-derived topographic map of Mercury from 4° South to 90° North on a cylindrical projection with resolution at 1 km per pixel (NASA/John Hopkins University/Carnegie Institute 2016). On the elevation scale to the right, dark blue denotes the lowest regions (-5 to -3 km) and brown denotes the highest points (2.5+ km), also: light blue (-2 km); green (-1 km); yellow (~0 km); orange (1 km); and red (2 km).

Figure 28. Topography Map of Mercury's Northern Hemisphere. Source: NASA/ Johns Hopkins University/Carnegie Institution (2016).

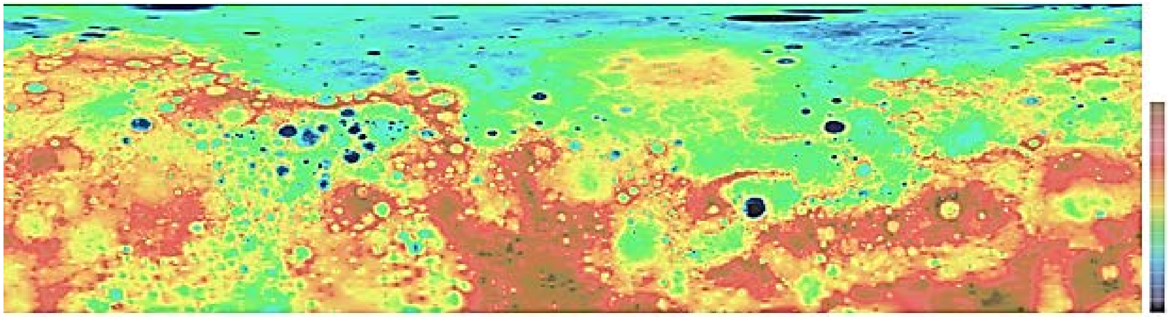

MLA had an 8 Hz, two-stage, Nd:YAG laser transmitter that produced a 1064 nm (infrared) pulse with 20 mJ of energy and a 6 ns pulse-width; it weighed 7.4 kg and required 23 watts of operating power (Abshire 2011). A rugged space-hardened LiDAR indeed, the MLA achieved more than laser altimetry and mapping of Mercury.

During a distant-Earth flyby in 2005, MLA successfully completed a two-way laser linking experiment with the NASA Goddard Geophysical and Astronomical Observatory at a range of over 23.9 million km (Smith et al. 2006). Smith et al. mentioned that MLA transmitted laser pulses to Earth during three observation periods divided across three nonconsecutive days (2006). They added that Earth received brief transmissions of 16 consecutive signals on 24 and 27 May and a transmission of about 26 consecutive signals on the 31st (the last day of testing) (2006). Meanwhile, NASA's Earth-based laser transmitted its own pulses toward MESSENGER, which the MLA detector received about 0.35 ms earlier than predicted throughout the entire testing period (2006). By comparison, transmissions from MESSENGER reached Earth approximately 0.34 ms early on the 24th/27th and 0.14 ms early on the 31st (2006). Overall, laser-acquired range measurements between the spacecraft and Earth were accurate to within ±20 cm at almost 24 million km (2006). This ground breaking asynchronous laser ranging and communications experiment "established a distance record for laser transmission and detection and accomplished a two-way laser link at interplanetary distance" (Smith et al. 2006, 53).

Once at Mercury, MESSENGER maintained a highly elliptical and nearly polar orbit with a 300 km periapsis in the northern hemisphere and a 15,000 km apoapsis in the southern hemisphere (Cavanaugh et al. 2007). Cavanaugh et al. noted that this orbit's purpose was to protect the valuable underside of the probe from the intense solar radiation (2007). Moreover, MESSENGER's orbital parameters ensured that the planet itself shielded the scientific instruments when the probe's topside solar-screen faced away from the sun (2007). Of course, the distant apoapsis explains the sparse LiDAR measurements south of the equator, since MLA's maximum operating limits were 1,200 km at nadir and 800 km at slant range (Cavanaugh et al. 2007). MESSENGER exceeded its expected mission duration by three years, ultimately crashing into Mercury's surface on 30 April 2015 (NASA/Johns Hopkins University/Carnegie Institution 2016).

11. Cloud-Aerosol LiDAR and Infrared Pathfinder Satellite Observations

Capturing first light on 7 June 2006, the Cloud-Aerosol LiDAR and Infrared Pathfinder Satellite Observations (CALIPSO) spacecraft is NASA Langley Research Center's Earth-observing and atmospheric-polarization LiDAR platform (Abshire 2011). Abshire states that CALIPSO exploits three co-aligned scientific instruments: a wide-field camera, an imaging infrared radiometer, and a polarization LiDAR (2011). He also notes that a star tracker assembly ensures accurate spacecraft and instrument pointing from CALIPSO's sun-synchronous 98.2° orbit at an altitude of 700 km (Abshire 2011).

CALIPSO currently belongs to the Afternoon Constellation (A-train) that consists of it plus the Aqua, Aura, and CloudSat satellites (Winker and Hunt 2007). Figure 29 is a rendition of CALIPSO and a diagram of its sensor payload.

Figure 29. Artist Rendition of CALIPSO On-Orbit and Diagram of Payload Optics. Adapted from NASA (2016a).

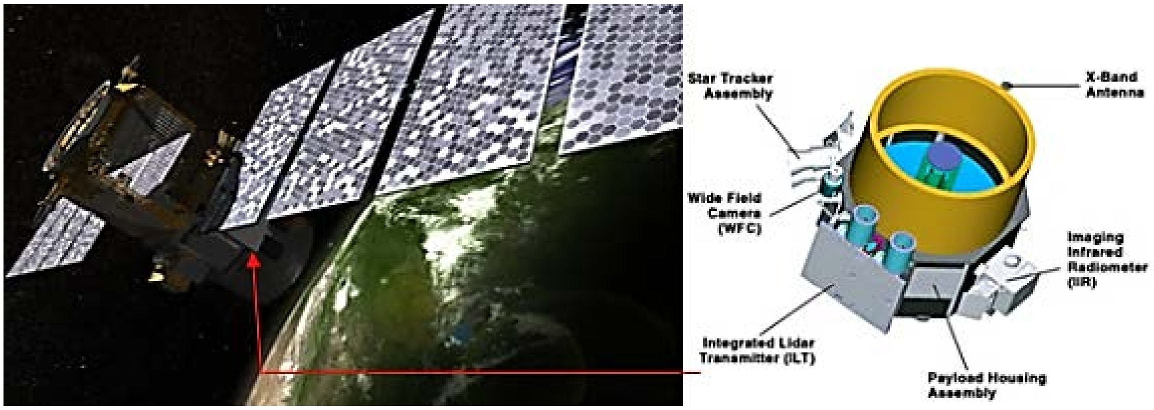

The LiDAR is officially named the Cloud-Aerosol LiDAR with Orthogonal Polarization (CALIOP); CALIOP shall not be used hereafter in this review to avoid confusion with the spacecraft's similar acronym. In short, this "first polarization LiDAR in orbit is a three-channel elastic-backscatter LiDAR optimized for aerosol and cloud profiling" (Winker and Hunt 2007, 1). Winker and Hunt discuss how CALIPSO still welds one remaining of two linear-polarizing Nd:YAG laser transmitters that produce a combined pulse of 1064 nm (infrared) and 532 nm (green) wavelengths, with a total energy of 220 mJ (2007). Furthermore, the system operates at 20 Hz with pulse-widths of 20 ns, and ground footprints are 70 m in diameter and spaced 333 m apart (2007).

The avalanche photodiode infrared detector disregards the polarization of the 1064 nm return signal (Winker and Hunt 2007). Winker and Hunt describe that the 532 nm detector employs two separate channels of photomultiplier tubes to measure the parallel and perpendicular components of polarization within the returned backscatter (2007). They go on to say that the returning wavelengths are sampled at 10 Megahertz (MHz) with an initial resolution of 15 m, then receiver electronics throttle resolution to 60 m for the infrared channel and 30 m for the parallel and perpendicular green channels

(2007). To further ease the downlink, additional data reductions are performed by onboard processors that average the top sections of the vertical LiDAR profiles to compress the data prior to transmission (Winker and Hunt 2007).

Overall, CALIPSO continues to provide researchers with highly versatile LiDAR products. For example, Hu et al. used derived sea-surface laser backscatter along with wind-speed measurements from Aqua’s Advanced Microwave Scanning Radiometer—EOS (AMSR-E) to examine global wave slope variances and near-surface wind speeds (Hu et al. 2008). Battaglia examined CALIPSO wavelength and polarization data for three areas of relatively shallow water: Kure Atoll, the Bahamas, and Sequoia National Forest (Battaglia 2010). He recognized a strong correlation between water depth and cross-polarization of the 532 nm return, enabling him to estimate water depth based on the identifiable LiDAR return signatures for shallow waters less than 20 m deep (Battaglia 2010).

Thanks to Hu, scientists are able to capitalize on a new calibration technique called *Elevation in Tail* that substantially improves the accuracy of CALIPSO laser-altimetry data (Hu 2007). *Elevation in Tail* compares the transient responses of the photomultiplier detectors to the waveform shapes of pulses returned from the surface (2007). Further processing can be applied to improve the accuracy of elevation data products from CALIPSO or a comparable LiDAR with polarization capabilities (Hu 2007).

Lastly, Figure 30 shows a CALIPSO vertical LiDAR profile of wildfire smoke clouds near Springerville, Arizona. The plumes tend to maintain an approximate altitude of 4.5 km, similar to the earlier ICESat profile of California wildfire smoke. The LiDAR profile is superimposed on a MODIS Terra image captured nine hours later by the Terra satellite’s imaging spectroradiometer (NASA 2016a). This is but one sample of the tremendous amount of useful atmospheric LiDAR data that CALIPSO has collected over the course of its mission: 10 years and counting.

Figure 30. A CALIPSO LiDAR Vertical Profile of Arizona Wildfire Smoke.
Source: NASA (2016a).

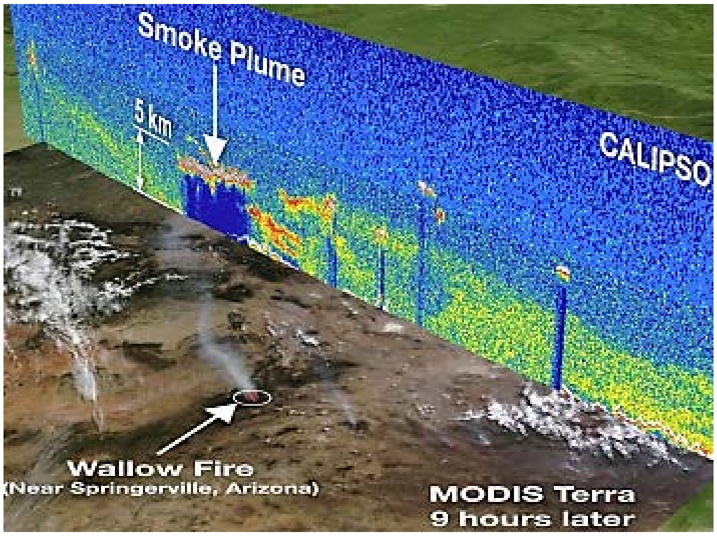

12. Lunar Reconnaissance Orbiter/Lunar Orbiter Laser Altimeter

On 23 June 2009, the Lunar Reconnaissance Orbiter (LRO) achieved its elliptical and polar orbit around the Moon, where the spacecraft maintains periselene and aposelene at 20 km and 165 km, respectively (NASA 2007a). In addition to mapping lunar topography and establishing a selenocentric coordinate system, LRO generates day and night temperature maps, captures high-quality imagery, and measures the Moon's reflectivity coefficient (albedo) (Keller, Chin, and Morgan 2007). Keller, Chin, and Morgan comment that LRO focuses specifically on the polar regions, searching for perpetually dark areas which may contain traces of water-ice (2007).

The satellite operates seven scientific instruments, of particular interest is the Lunar Orbiter Laser Altimeter (LOLA), a space LiDAR conducting a dual mission of general exploration and preliminary research in support of future robotic and manned lunar landings (Keller, Chin, and Morgan 2007). Specific tasks include "measuring potential landing site slopes and surface roughness" (NASA 2007a). Figure 31 is a rendition of LRO on orbit (left) and a LOLA-derived map of surface slopes near the lunar south pole. The slope map, with the south pole in the center, shows poleward of 75 degrees south latitude and is color-coded from no-slope (purple) to 30 degrees of slope (red). Generally, the areas of steeper slope (15°–30°) define the outlines of impact craters in this region.

Figure 31. Artist Rendition of LRO and Slope Map of the Lunar South Pole.
Source: NASA Goddard (2016b).

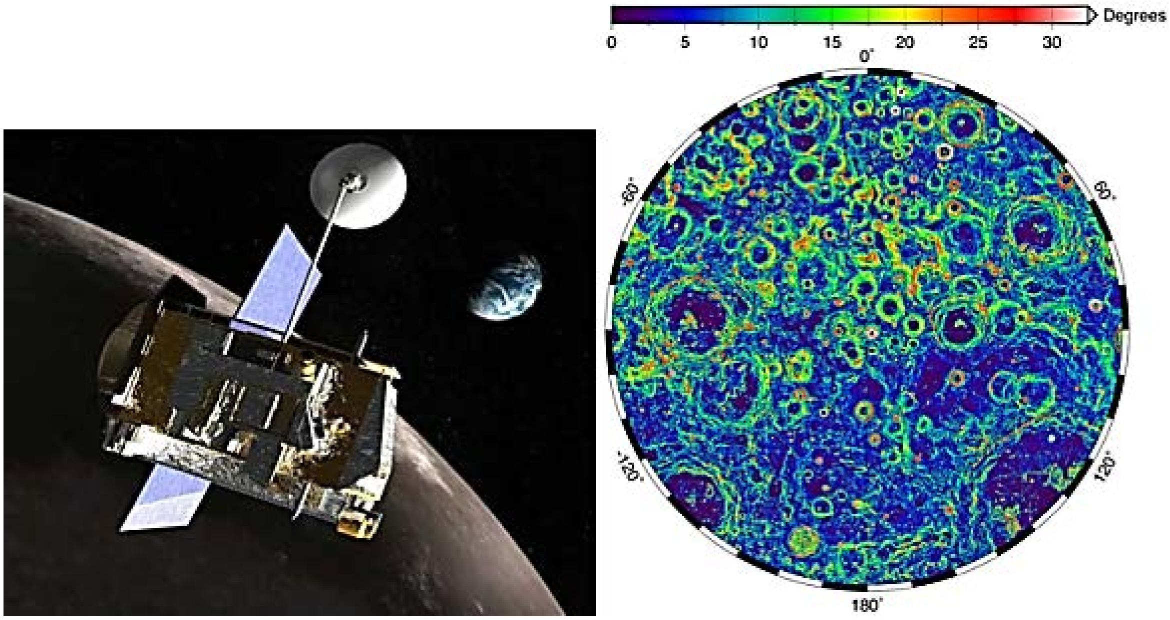

By design, this LiDAR is somewhat similar to the Mars Orbiter and Mercury Laser Altimeters, MOLA and MLA respectively (Keller, Chin, and Morgan 2007). However, LOLA does more than uphold the trend of Q-switched, diode-pumped, Nd:YAG lasers in space-based LiDAR operations. With diffractive optical elements producing five total beams, it is “the first multi-beam space LiDAR” (Abshire 2011, 38). Abshire remarks that each beam produces an individual 5 m diameter footprint, and the five footprints are spaced 25 m apart in the shape of a cross (2011). This unique feature is how LOLA can measure surface slope and elevation as it orbits the Moon (2011). More specifically, the 28 Hz LOLA functions at 1064 nm (infrared) with pulse energies of 3 mJ and a 5 ns pulse-width (2011). As the five returning laser pulses enter the 14-cm receiver telescope, an optical fiber array and timing electronics direct each to an individual silicon avalanche photodiode detector (Abshire 2011).

Figure 32 provides a LOLA-derived elevation map of the two sides of the Moon. Elevation in km is color-coded based on a mean lunar radius of 1,738 km. This image distinguishes well between the generally flatter “lowlands” of the nearside and the higher, yet heavily cratered, farside.

Figure 32. Lunar Reconnaissance Orbiter: Detailed Topography of the Moon. Adapted from NASA Goddard (2016b).

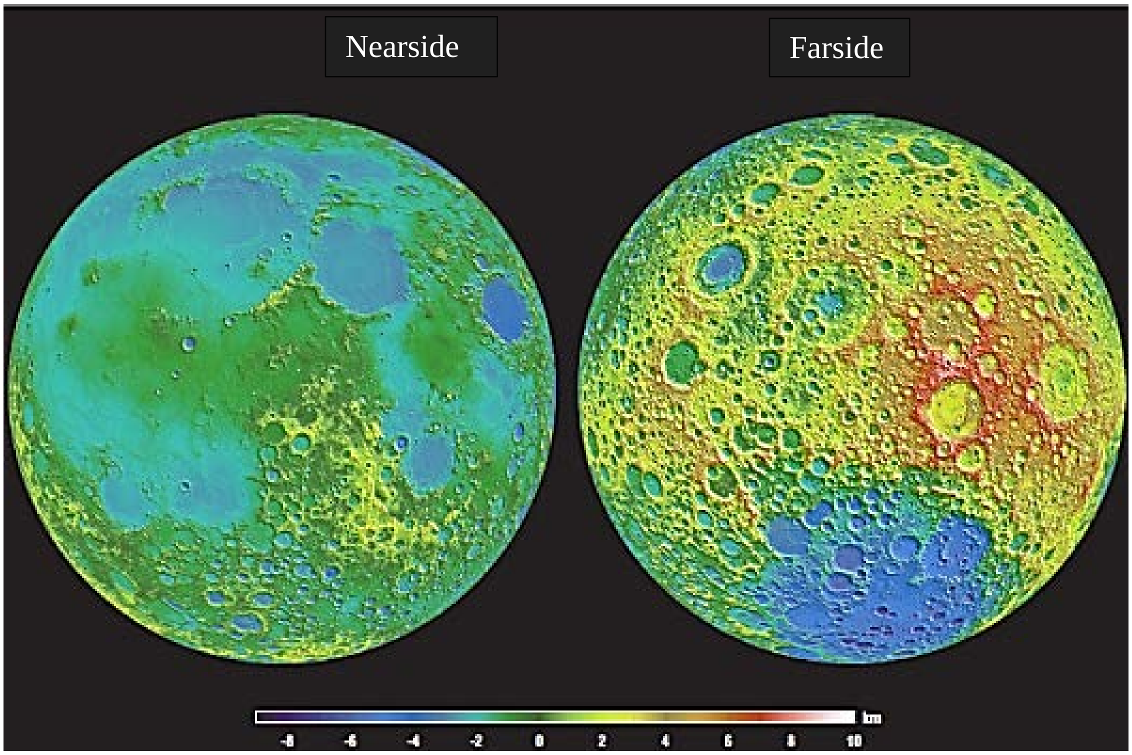

Now, one could reason that LOLA has completed the earlier works of the Apollo and Clementine laser altimeters. However, surface topography is only one capability of this built-for-space LiDAR: “Laser systems can be used to track and communicate with spacecraft in deep space to achieve better performance at lower power and with smaller size apertures than conventional microwave systems” (Sun et al. 2013, 1865) Appropriately, Sun et al. successfully demonstrated the distant-communications ability of the LOLA receiver by conducting one-way digitally modulated (4096-ary PPM) laser transmissions employing Reed Solomon coding during some of the transmissions (2013). They mentioned that after encoding, the Next Generation Satellite Laser Ranging ground station transmitted essentially error-free data at rates between 200 and 300 bits per second (2013). LRO's distance from Earth was about 380,000 km during the experiment, and the spacecraft returned accurate time tags for every laser pulse that it received (Sun et al. 2013).

Additionally, laser backscatter from LOLA offers a means to determine the albedo of various lunar surfaces (Lucey et al. 2014). Figure 33 gives the whole-surface albedo of the Moon at 1064 nm on a cylindrical projection. According to Lucey et al., the majority of the surface has an albedo of 0.29 (2014). They continue by informing us that the high of 0.33 corresponds to the farside's northern hemisphere below the pole, and the 0.24 low aligns almost completely with the segment of the nearside that directly faces Earth (Lucey et al. 2014). The LiDAR systems of this section each represent a unique and tremendous contribution to the sciences of laser detection and ranging, space systems operations, and remote sensing. Still, this review would not be complete without a look at some foreign LiDAR space platforms and a glimpse into the future.

Figure 33. The Geometric Albedo of the Moon at 1064 nm.
Source: Lucey et al. (2014, 119).

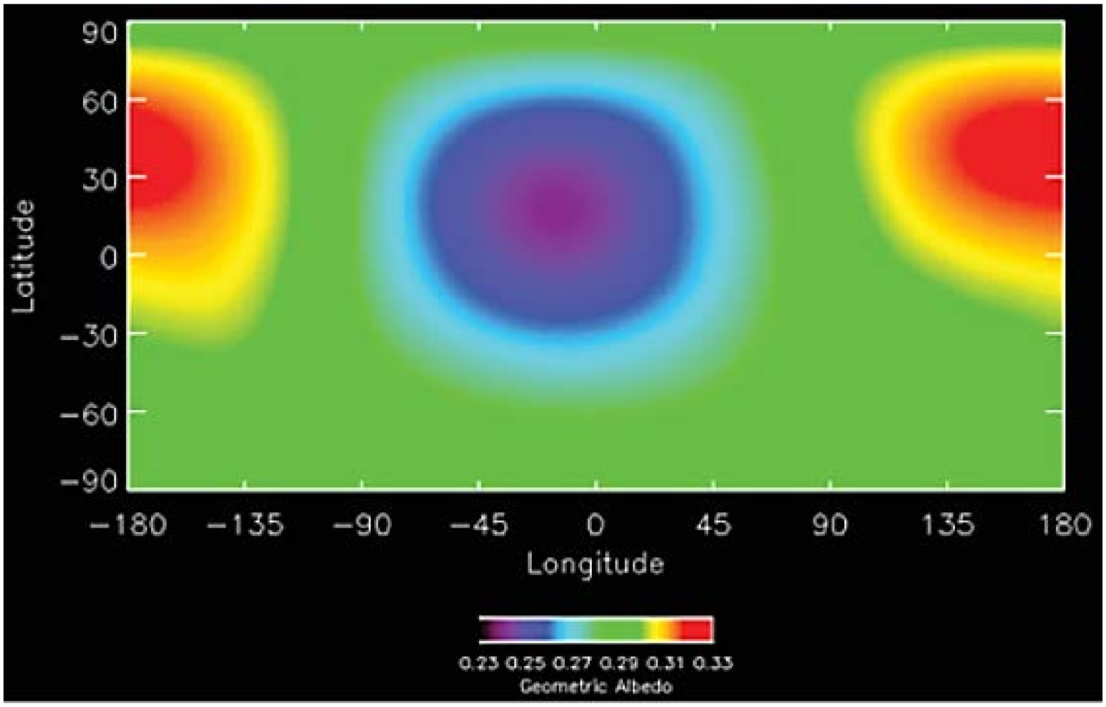

C. OTHER PLATFORMS

1. l'Atmosphere Par LiDAR Sur Saliout ("Space Station Atmospheric LiDAR")—French/Russian LiDAR on the Mir Space Station

L'atmosphere par LiDAR sur Saliout (ALISSA) was a French atmospheric LiDAR system designed by the Service d'Aéronomie and installed on the Priroda module of the Mir Space Station in 1996 (Chanin and Hauchecorne 1991). Figure 34 is a diagram of the Priroda module and its location on the Mir station. ALISSA's primary mission, as described by Chanin and Hauchecorne, was to capture detailed descriptions of the vertical structures of clouds, including the uppermost altitudes of cloud tops at a resolution of approximately 150 m (1991). They added that the LiDAR's four Nd:YAG lasers synchronized at 50 Hz to produce a combined 40 mJ, 532 nm (green) pulse; the lasers could also operate individually at 10 mJ (1991). The receiving telescope was 40 cm in diameter, and reference prisms and a secondary mirror sat in front of the telescope to correct for mechanical errors during space flight (Chanin and Hauchecorne 1991).

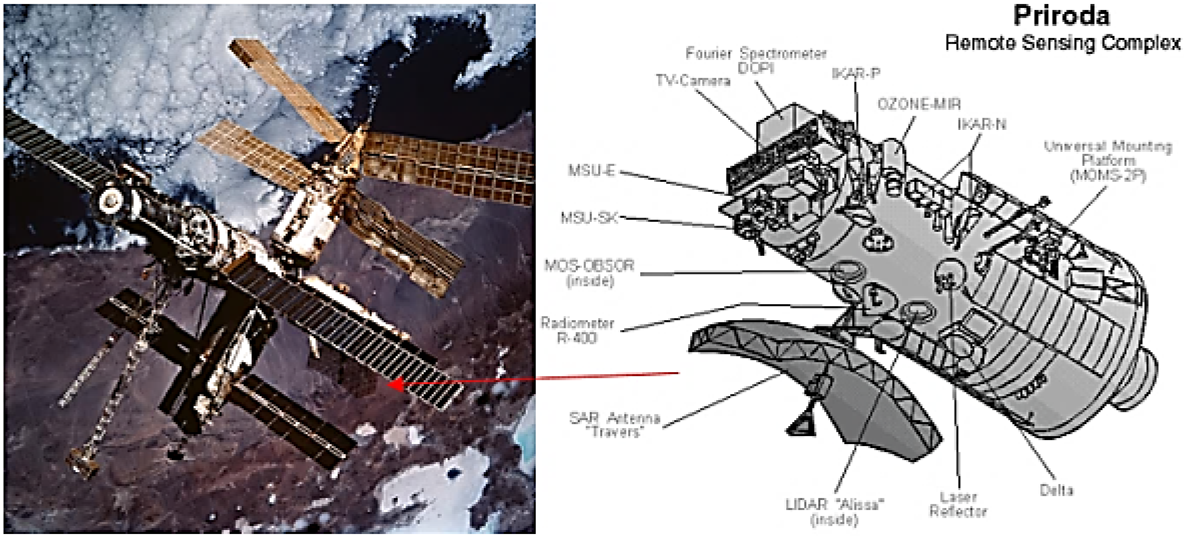

Figure 34. The Mir Space Station and the Priroda Module with the ALISSA LiDAR. Adapted from Dismukes (2013).

The Russian Institute of Applied Geophysics maintained responsibility for ALISSA (McCormick 2005). McCormick emphasized that the system's controllers only employed test mode during the first two years, then ALISSA endured a prolonged interruption in operations due to issues internal to the space station (2005). He went on to say that in 1999, ALISSA operated for approximately two months and collected 25 additional laser backscatter datasets that indicated the presence of multi-layered clouds, the boundary layer, and orographic waves (2005). In conjunction with the earlier success of LITE, ALISSA further demonstrated "that even a low power LiDAR carried on an operational satellite could provide useful information for cloud description, including the description of the aerosol boundary layer" (McCormick 2005, 381).

2. Hayabusa Asteroid Probe—Japan

In 2003, JAXA launched the Hayabusa Asteroid Explorer, code named MUSES-C, to study and return samples from asteroid 25143 Itokawa (Japan Aerospace Exploration Agency [JAXA] 2016). The mission ended successfully in 2010 when Hayabusa returned to Earth, allowing Japanese scientists to recover and authenticate the Itokawa samples (JAXA 2016). See Figure 35.

Figure 35. Hayabusa (MUSES-C) and Sample from the Itokawa Asteroid.
Source: Japan Aerospace Exploration Agency [JAXA] (2016).

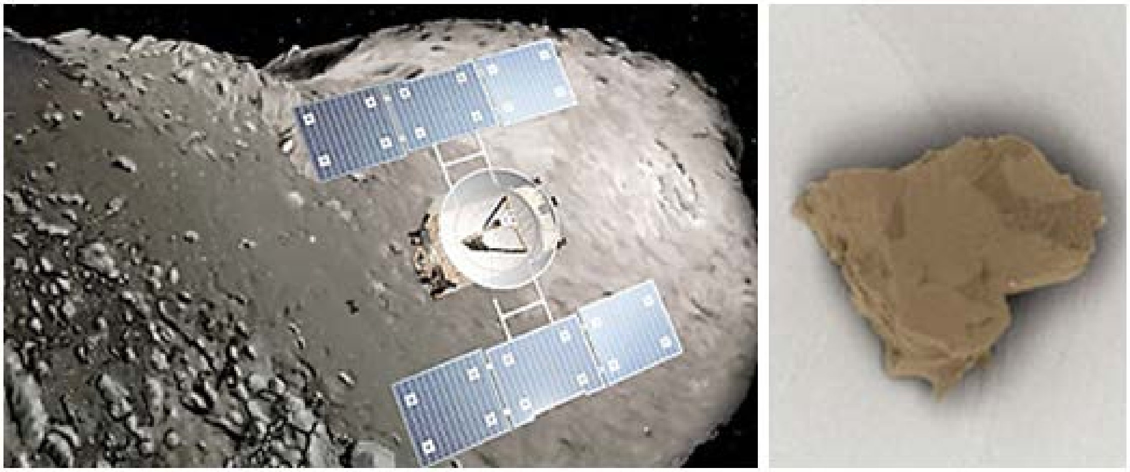

Hayabusa featured a Xenon-ion engine, a near-infrared spectrometer, a sample-collecting robot, and an autonomous navigation system (JAXA 2016). According to JAXA, this human-free navigation system incorporated an optical camera and a laser altimeter (JAXA 2016). In addition to successfully navigating the spacecraft in vicinity of the asteroid, Hayabusa's LiDAR and camera suite obtained the measurements necessary for scientists to calculate the bulk density of Itokawa (Mukai et al. 2007). The conclusions by Mukai et al. were a mass of 3.54 x 1010 kg with 6% error, a density of 1.9 g/cm-3 with 9% error, and a bulk porosity of about 40% (Mukai et al. 2007).

The Hayabusa LiDAR was a Q-switched, laser-diode, Nd:YAG transmitter that operated at 1064 nm (infrared) (JAXA 2016). During testing, the actual wavelength produced varied by about 0.3 nm per degree of temperature change, so the developers installed a thermostat and heater specifically for the LiDAR's transmitter (Mukai et al. 2007). Mukai et al. mentioned that frequent temperature fluctuations still affected the laser during spaceflight which resulted in intensity variations among the outgoing pulses (2007).

The Hayabusa LiDAR's minimum range was 50 m due to a small angular offset between the laser transmitter and receiver (Abe et al. 2006). Abe et al. remarked that the predicted maximum range was 50 km, and the first mission-recorded laser return occurred at a spacecraft distance of 49 km from the asteroid (2006). They described how a timing clock frequency of 75 MHz afforded approximately 1 m accuracy at the minimum operating range of 50 m; laser accuracy was 2 m at slightly over 3 km (2006). Abe et al. admitted that Hayabusa's LiDAR detected 1,665,548 of the 4,107,104 transmitted pulses, about 41%, during the asteroid-orbiting and pre-landing phase from 10 September to 25 November 2005 (2006). Unfortunately, spacecraft pointing accuracy, and with it the number of returned laser pulses, decreased substantially after 2 October due to a major attitude control failure: two of three reaction wheels (Abe et al. 2006).

D. THE WAY AHEAD FOR LiDAR IN SPACE

1. NASA—Next Generation Spacecraft Landing Integrated LiDAR

Space Shuttle precision docking using TriDAR represented a major leap forward in automated rendezvous technology. Building on this success, NASA continues the development of a multi-LiDAR spacecraft landing system for future space exploration missions (Amzajerdian et al. 2015). Amzajerdian et al. state that the Autonomous

Landing and Hazard Avoidance Technology Project (ALHAT) endeavors to successfully integrate its chosen trio: an advanced laser altimeter, a Doppler LiDAR, and a 3D Flash Imaging LiDAR (2015). Once installed onboard future spacecraft, these systems will work together to achieve "autonomous precision landing and hazard avoidance capabilities" through highly accurate and simultaneous measurements of spacecraft altitude, relative velocity, orientation, and proximity to terrain and other navigational hazards (Amzajerdian et al. 2015, 1).

In 2014, the ALHAT integrated LiDAR system demonstrated itself on the underside of a Huey helicopter and on the rocket-powered Morpheus unmanned test vehicle, as shown in Figure 36. The continuous-wave Navigation Doppler LiDAR uses frequency-modulated laser pulses segmented into up-ramp chirp, constant frequency, and down-ramp chirp to determine accurate ranges and relative velocities (Amzajerdian et al. 2015). This report comments that the pre-modulated signal is a single 1.55 micron (infrared) pulse that is split after modulation and transmitted simultaneously in three separate directions (2015). It also notes that the Doppler velocity during craft movement is determined through a comparison of the up-ramp and down-ramp chirp frequencies; the constant (center) frequency is used to confirm the calculated Doppler velocities, helping the system disregard erroneous measurements (2015). Next, a field-programmable gate array applies fast Fourier transforms to the different frequency components of all three return signals in order to calculate actual spacecraft range and line-of-sight velocity (2015). Additional statistics for the Doppler LiDAR are as follows: velocity resolution of 0.2 cm/sec, line-of-sight resolution of 17 cm, maximum range of 2,200 m, and a data rate of 20 Hz (Amzajerdian et al. 2015).

Figure 36. Testing of Integrated LiDAR Landing Systems on a Morpheus Vehicle. Source: Amzajerdian et al. (2015, 9).

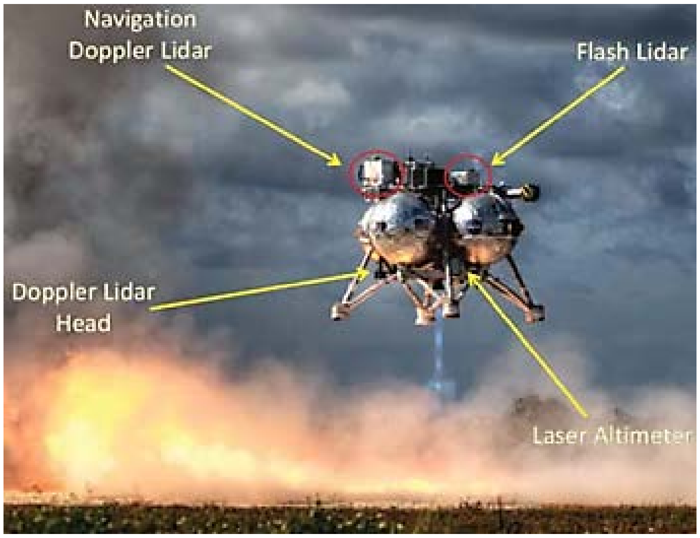

The long-range laser altimeter will complement the Doppler LiDAR at ranges less than 2 km, but it will function exclusively at greater distances (Amzajerdian et al. 2015). Amzajerdian et al. describe that this multi-return, automatic threshold detection, laser altimeter operates at 1.57 microns (infrared), and it is capable of providing 0.5 m precision at altitudes above 20 km to correct for inertial measurement unit drift during the approach phase of a landing (2015). Furthermore, they report that close-up range resolution is on the order of 5 cm, and the data rate frequency is 30 Hz (2015). The laser altimeter supplies accurate terrain contours that will enable successful terrain-relative navigation with no human inputs (Amzajerdian et al. 2015).

Lastly, the 3D Flash Imaging LiDAR is designed for object recognition of hazards greater than 29 cm at a maximum slant range of 2 km; each return of the 1.06 micron (infrared) pulse is measured individually by a Readout Integrate Circuit at the detector (Amzajerdian et al. 2015). Amzajerdian et al. contend that this is a tremendous improvement over traditional laser-imaging object-recognition technologies which employ a single detector and scan using a raster pattern (2015). Here, the 128 x 128 pixel detector array achieves an imaging rate of 30 frames per second (2015). Additional statistics for the 3D Flash Imaging LiDAR are as follows: 50 mJ pulse energy, 8 ns pulse-width, 100 mm receiver aperture, 1,800 m range at nadir, and 8 cm range precision (Amzajerdian et al. 2015).

2. NASA—Advanced Topographic Laser Altimeter System and Swath Imaging Multi-polarization Photon-counting LiDAR

NASA's ICESat-2 will "continue polar ice topography measurements with improved precision laser-ranging techniques" as a follow-on to the success of ICESat (Troupaki et al. 2015, 1). Troupaki et al. explain that the Advanced Topographic Laser Altimeter System (ATLAS) comprises ICESat-2's entire scientific instrument loadout (2015). They believe that the micro-pulsed, multi-beam, ATLAS will deliver a significant improvement over ICESat's single-beam GLAS LiDAR (2015). Troupaki et al. mention that this LiDAR will work at 532 nm (green) and 10 Kilohertz (KHz), splitting each pulse into six individual beams, as seen in Figure 37 (2015). Originating as a 16-beam concept, the ATLAS design subsequently dropped to nine and, then, to its current six-beam configuration due to changing mission requirements (2015). The full-width half-maximum pulse duration is less than 1.5 ns, and full output power exceeds 9 watts (Troupaki et al. 2015).

Figure 37. Drawing of ICESat-2 and its Six-beam ATLAS LiDAR. Source: NASA Goddard (2016a).

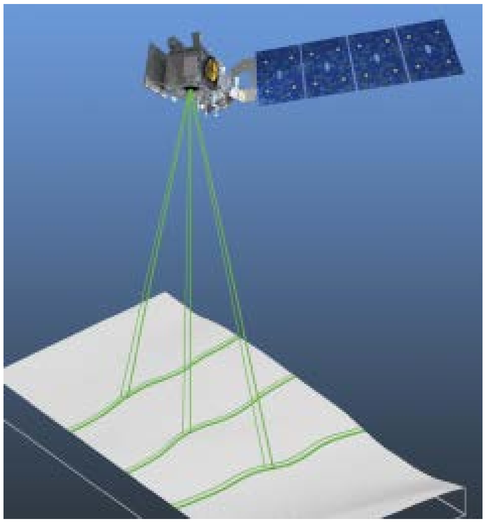

Beam pair spacing is 3.3 km (NASA Goddard 2016a).

Fibertek's photon-counting ATLAS overcomes the complications of orbital altitude versus laser power through low-photon detection *(6 beams = 1/6 of the total power each, about 1.5 watts)* (Troupaki et al. 2015). Troupaki et al. state that an Optical Filter Assembly is included to mitigate the increased detection of solar noise inherent to photon-sensitive LiDAR systems (2015). LRO/LOLA broke the decades-long tradition of spacecraft welding single-beam laser altimeters. ATLAS follows in the footsteps of LOLA by ushering in a new era of space-borne LiDAR: a metamorphosis toward advanced multi-beam systems with photon-counting capabilities (Yu, Stephen et al. 2010).

ICESat-2 and ATLAS are part of NASA's organizational trend toward wide-swath photon-counting LiDARs for space-based topography and atmospheric-sensing missions (Yu, Stephen et al. 2010). SIMPL is a theoretical satellite laser-imaging concept predicated upon the actual Airborne Instrument Development Incubator program named Slope Imaging Multi-polarization Photon-counting LiDAR (same acronym). The airborne SIMPL program arose from NASA's desire to "advance key technologies and mitigate some of the risk associated with the LiDAR Surface Topography (LIST) mission" (Yu, Krainak et al. 2010, 1). Furthermore, NASA's aerial-SIMPL analyses of forest canopy structure and available biomass were successful due to the high resolution, dual wavelength, and polarization properties of the airborne SIMPL LiDAR (Yu, Krainak et al. 2010). Results from the airborne SIMPL experiment have generated a tremendous anticipation for future ICESat-2 data (Harding, Dabney, and Valett 2011).

Figure 38 shows point clouds for the four polarization channels (Green Parallel, Green Perpendicular, NIR Parallel, NIR Perpendicular) of SIMPL beam three of four during a Learjet overflight of Lake Erie in winter 2009 (NASA 2016b). Per NASA, the segment is an approximately 260 m long strip across an area with heavy, yet young, sea-ice coverage (2016b). Additionally, a video frame composite, taken during flight, provides a visual representation of the segment (2016b). The four general types of sea-ice present in the data are labeled by letters: (A) dark nilas ice, (B, E) fresh gray-white ice, (C) skim ice over water, and (D) fractures/leads of open water within the ice sheet

(2016b). The perceived slope exhibited by the laser points stems from uncorrected roll bias during flight and not from the actual topography of the study area (NASA 2016b).

Figure 38. Data Segment of Beam #3 Collected During Airborne SIMPL Flight Over Lake Erie, 25 February 2009. Source: NASA (2016b).

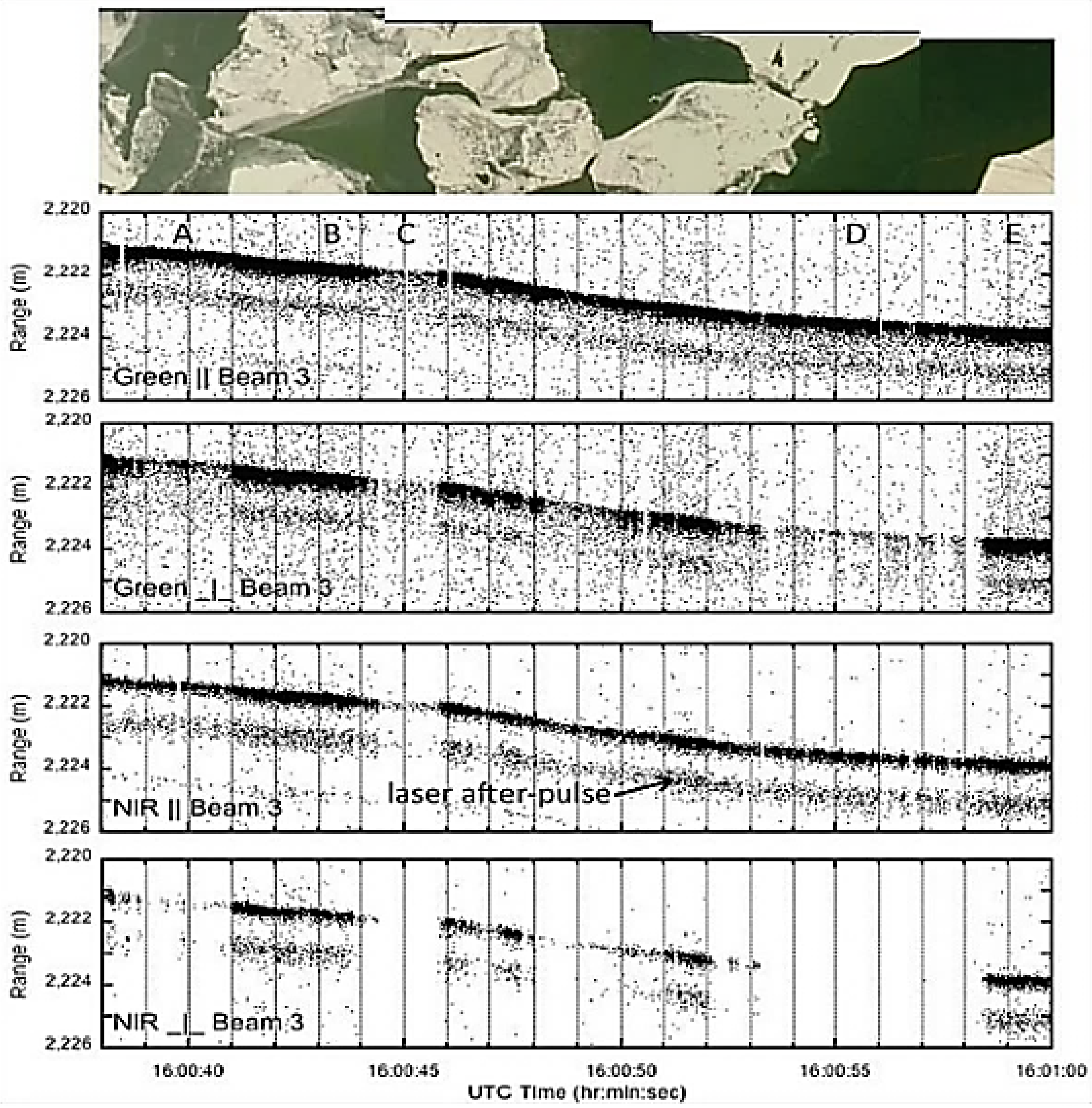

Although it will lack the polarization aspect of SIMPL, ICESat-2 is an attempt at laser imaging an ever-larger swath from space that intends to satisfy at least some of LIST's mission requirements and NASA's expectations:

> (1) A medium cost mission to be launched by NASA between 2016–2020; (2) a single-instrument payload carrying an imaging lidar at low Earth orbit; (3) one-time global mapping of land, ice sheet and glacier topography and vegetation structure through the duration of the mission; (4) observe topography and vegetation structure change through time in selected areas; and (5) achieve five meter horizontal resolution, 0.1 m vertical precision, and absolute vertical accuracy for ground surface topography including where covered by vegetation. (Yu, Krainak et al. 2010, 1)

Figure 39 is a diagram of the conceptual principles behind a space-based Swath Imaging Multi-polarization Photon-counting LiDAR platform. Numerous fiber lasers and single-photon sensitive detectors are integrated with advanced timing electronics to generate enhanced measurements of surface topography and reflectance (Harding et al. 2007). The theoretical SIMPL space-LiDAR will simultaneously transmit laser wavelengths of 532 nm (green) and 1064 nm (infrared), and the received backscatter will be depolarized into components parallel and perpendicular to the original pulse in order to determine surface type and roughness based on photon scattering due to wavelength and polarization (Harding et al. 2007).

Figure 39. Satellite SIMPL Push-Broom Laser Altimeter Measurement Approach. Source: Harding et al. (2007, 1–2).

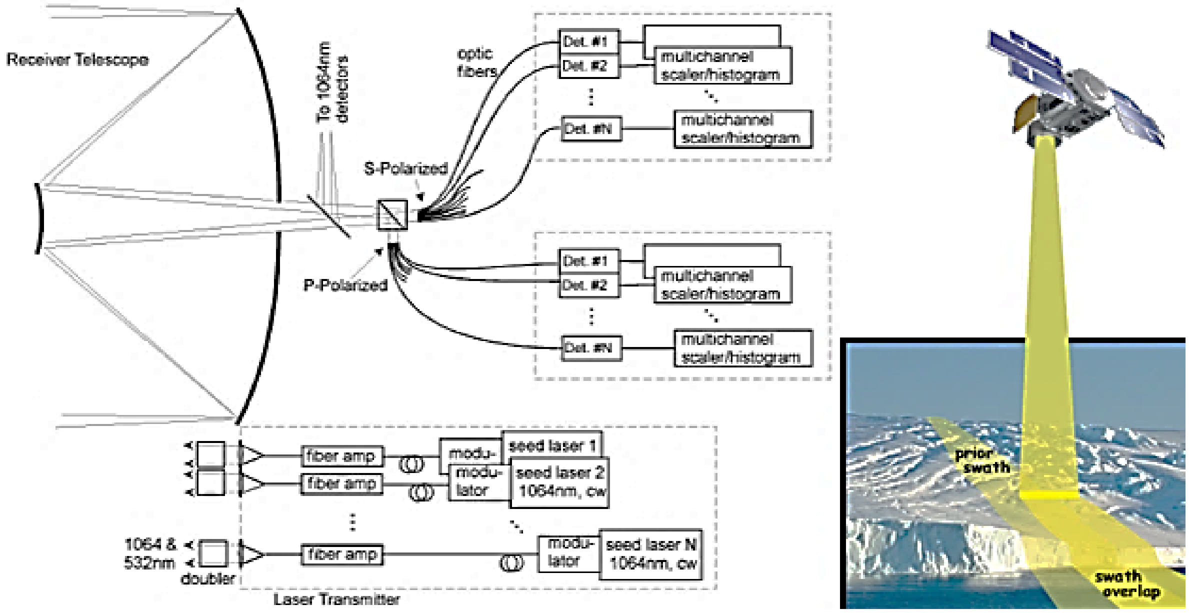

3. NASA—Global Ecosystem Dynamics Investigation LiDAR

In 2018, NASA intends to end the almost 17-year absence of a space station–based LiDAR which began in 2001 when Mir, with ALISSA onboard, reentered the Earth's atmosphere. The plan is to install a laser system that will measure the biomass of the Earth's forests from the ISS, as it orbits at approximately 410 km with 51.65 degrees of inclination (NASA Science Missions 2015). NASA's Global Ecosystem Dynamics Investigation LiDAR (GEDI) is specifically designed to measure the heights of trees (to within 1 m accuracy) and the amount of carbon stored within them and other vegetation (2015). The data will be analyzed to generate a better understanding of available forest biomass and habitat quality (NASA Science Missions 2015).

Probable reasons for the chosen host platform are the operational and size requirements of the 14-pulse system, also the majority of the world's critical forests lie between 51° north and south latitudes. The ISS is the ideal, and possibly the only, space platform that can currently support the GEDI. According to NASA, the GEDI's mass, power requirement, and operating wavelength are 230 kg, 516 watts, and 1064 nm, respectively (2015). NASA intends to park the GEDI at the exposed facility of the Japanese Experiment Module, red circle in Figure 40 (NASA Science Missions 2015). Figure 41 is a simple diagram of the system.

Figure 40. ISS and Future Location of GEDI. Source: Dubayah (2014).

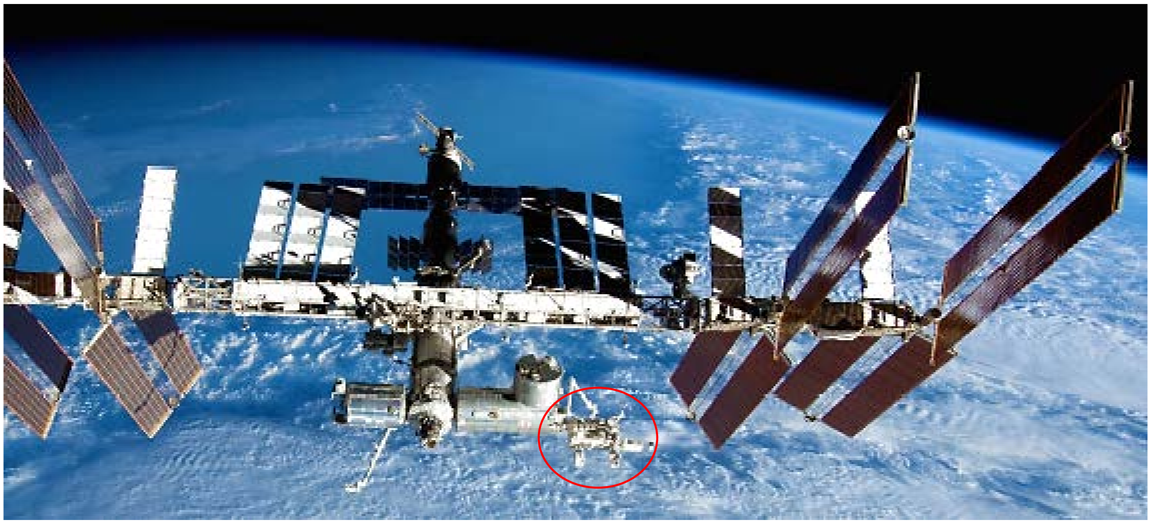

Figure 41. Diagram of the GEDI. Source: Dubayah (2014).

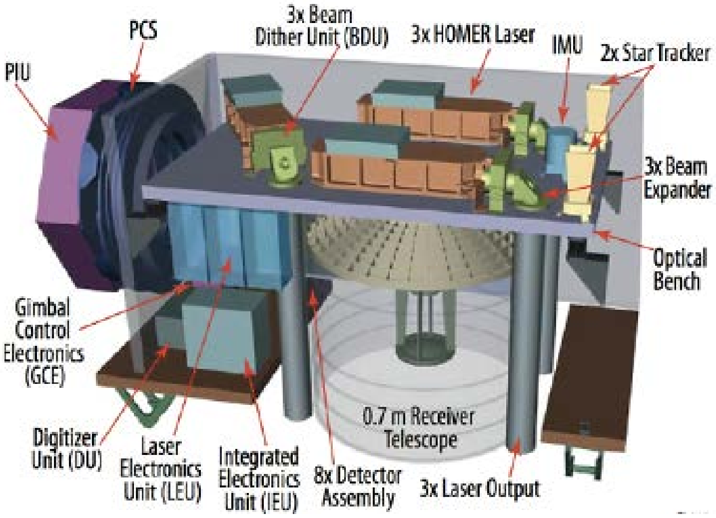

Yearly, the GEDI system will collect over 15 billion laser waveform profiles; gridded estimates of biomass have a predicted resolution of 500 m (Dubayah 2014). GEDI data will be analyzed to identify and describe the changes in forest biomass due to prolonged stressors, such as climate change, drought, forestry, and other human interactions (NASA Science Missions 2015). Three laser transmitters and splitting optics will produce the GEDI’s 14 parallel beams, and individual laser ground spots will measure approximately 25 m in diameter, with 60 m along-track and 500 m across-track spacing (creating a 60 m X 6.5 km swath) (Dubayah 2014). This is illustrated in Figure 42. Notice that the middle, nadir-facing, laser will operate at full power and has a narrower across-track swath for stronger signal returns. Conversely, the two outer lasers trade power for wider coverage, so they will collect more, lower-amplitude, waveform profiles.

Figure 42. GEDI’s Three-sectioned, 14-Beam, Swath. Source: Dubayah (2014).

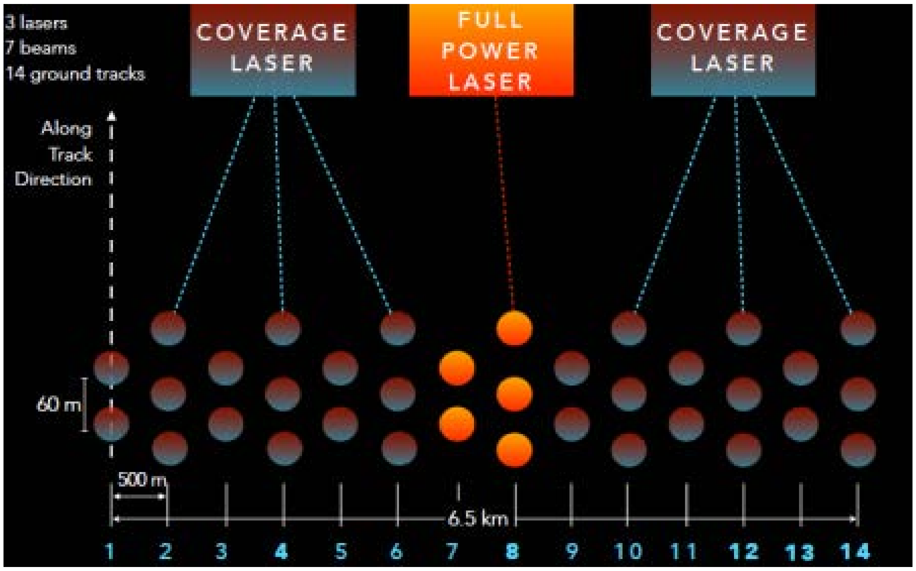

4. Sigma Space—Single Photon-counting 3D LiDAR

Sigma Space Corporation is striving to push the advantages and the altitude of single photon detection ever higher. Two of its recently developed 3D-imaging LiDARs appear promising for future space-based laser altimetry and topographic applications: the High Resolution Quantum LiDAR System (HRQLS) and the High Altitude LiDAR (HAL). The medium-altitude HRQLS can detect single photons at an altitude of over 5 km, and the HAL can currently operate at slightly above 8.5 km (Degnan et al. 2013). The idea behind both systems is to “provide contiguous few decimeter resolution topographic coverage on a single overflight at aircraft speeds up to about 220 knots (407 km/hr)” (Degnan et al. 2013, 3).

Instead of single- or even multi-pulse lasers, these systems emit hundreds of pulselets at frequencies up to 32 KHz with a dedicated timing mechanism for each pulselet (Degnan et al. 2013). Degnan’s pulse-widths are in picoseconds and the imaging rate is millions of 3D pixels a second (2013). Figure 43 shows the large-area DEM from a 12-hour airborne HRQLS survey of a rugged and densely forested 1,700 km^2 section of Garrett County, Maryland. Degnan et al. disclose the survey parameters: 2 km flight altitude, 0.81 km single flight line width, and an average aircraft velocity of 278 km/hr (Degnan et al. 2013).

Figure 43. HRQLS Airborne LiDAR Survey of Garrett County, Maryland Imposed on a Google Earth Map. Source: Degnan et al. (2013, 4).

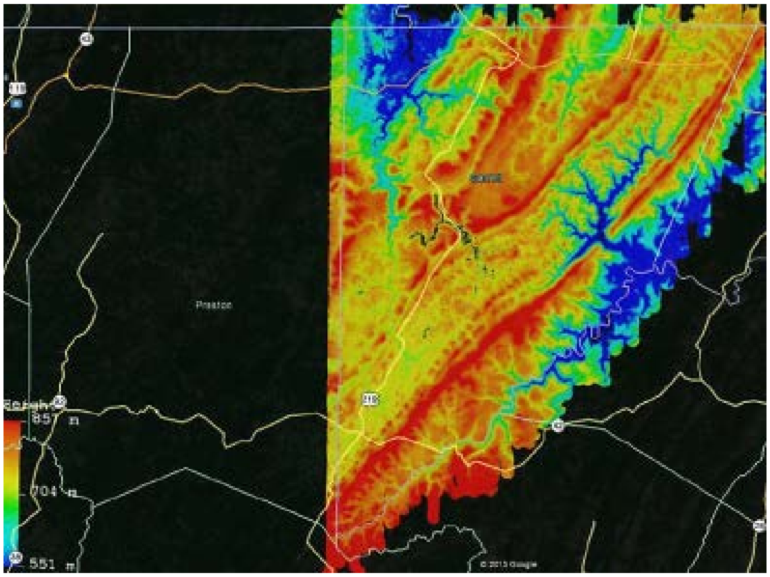

The pulselet concept applied by Sigma Space LiDAR technologies stems from Degnan's first-generation research at the NASA Goddard Space Flight Center just prior to his retirement from NASA in 2003 (Degnan 2002). Degnan concludes that for a particular telescope aperture and a set level of transmitter power, traditional high-energy low-frequency laser pulses perform significantly worse for laser-altimetry sampling than a series of low-energy high-frequency pulses used in conjunction with advanced timing receivers and photon-counting detectors (2002). In the same report, Degnan affirms that employing small receiver telescopes improves the system's ability to distinguish between legitimate ground returns and noise from other photon sources, primarily the Sun (Degnan 2002). Under his direction as Chief Scientist, Sigma Space continues to improve on these 3D photon-counting LiDAR systems.

All things considered, Sigma Space's next generation of single photon-counting LiDAR is designed with future space operations in mind. With single photon sensitivity, "contiguous, high resolution topographic mapping and surveying on a single overflight becomes possible with very modest laser powers and telescope apertures—even from orbital altitudes" (Degnan et al. 2013, 1). According to Degnan et al., these systems will possess the higher spatial resolutions and wider swath coverages required to expedite large-scale extraterrestrial topography missions without overly sacrificing precision and accuracy (2013). They also offer the improved foliage, water, and atmospheric penetration critical for Earth-targeted forestry, bathymetry, climate/pollution monitoring, and meteorology operations from orbiting satellites (Degnan et al. 2013).

5. Multi-wavelength LiDAR for Terrain Classification

Although multi-wavelength LiDAR technology remains primarily restricted to low-flying airborne platforms, it represents a growing field of interest and capability. The predominance of LiDAR-in-space has been monochromatic, with exceptions mainly for atmospheric purposes: Shuttle LITE, Phoenix Mars Lander, ICESat, CALIPSO, and ALISSA. Spaceborne spectral LiDAR systems may one day collect new information on extraterrestrial landscapes that thus far have only been visited by single-wavelength platforms: Mercury, Mars, the Moon, and near-Earth asteroids. Understandably, the ground work must occur first, which means spectral classification studies on the unique features of our Earth, including manmade objects and vegetation.

Fernandez-Diaz et al. recently published a paper titled "Capability Assessment and Performance Metrics for the Titan Multispectral Mapping Lidar." The paper discusses two years of Optech Titan testing and mapping campaigns that "demonstrate capabilities to classify land covers in urban environments with an accuracy of 90%, map bathymetry under more than 15 m of water, and map thick vegetation canopies at sub-meter vertical resolutions" (Fernandez-Diaz et al. 2016, 8). Also, Morsy et al. have obtained classification accuracies of 92.51% using three normalized difference feature indexes (NDFI) for separate land/water and vegetation/built-up area analyses (Morsy et al. 2016). Their $\text{NDFI}_{\text{Green-NIR}}$, $\text{NDFI}_{\text{Green-MIR}}$, and $\text{NDFI}_{\text{NIR-MIR}}$ indexes are calculated from the spectral intensity values of a Titan dataset collected at two locations in Ontario, Canada (2016). Morsy et al. convert the 3D point cloud into a raster with grids of 1 m cell size, assigning each grid a mean intensity value before calculating the indexes (2016).

They conclude that $\text{NDFI}_{\text{Green-MIR}}$ is better for distinguishing vegetation, whereas $\text{NDFI}_{\text{NIR-MIR}}$ is better for built-up (urban) areas (2016). All three of their NDFIs perform poorly (32.19%–40.31%) at separating land from water, unless the points are restricted by “number of returns” (2016). Inclusion of the “number of returns” attribute significantly reduces the misclassification of water points as vegetation, increasing success to approximately 97% (Morsy et al. 2016).

In his thesis, Judson Thomas applies a new spectral LiDAR technique for terrain classification using the ENvironment for Visualizing Images’ (ENVI) “n-Dimensional Visualizer” (N-D VIS) tool (Thomas 2015). Thomas’ data are not rasterized, and he does not average the intensities; the individual spectral returns for the green, NIR, and MWIR channels are preserved for analysis (2015). His primary focus centers on manmade surfaces in a suburb of Toronto, Canada: various pavements, roofing materials, road paint, and railway tracks (Thomas 2015). This thesis will apply a similar process in an effort to spectrally subclassify ground and roofing materials on the campus of the Naval Postgraduate School, where accurate ground truth is readily accessible.

III. DATASET AND PREPARATIONS

A. INSTRUMENT

1. Optech Titan Multispectral LiDAR

The Optech Titan multispectral sensor collected the aerial LiDAR data for this thesis. Titan employs three independent lasers with a combined ground-sampling rate of approximately 1 MHz (Teledyne Optech 2015). It expands on the traditional spatial applications of LiDAR by introducing multispectral sensing. According to the manufacturer, the Titan system "offers improved performance for 3D land cover classification, vegetation mapping, shallow bathymetry, and dense topography" (Teledyne Optech 2015, 3). This thesis strives to support that claim, primarily for ground types and roofing materials. Table 3 lists relevant information about the sensor, and Figure 44 is a drawing of the laser component from the specifications brochure.

Table 3. Some Applicable Titan Attributes. Adapted from Teledyne Optech (2015).

	Wavelength	Offset	Beam Divergence
Channel 1	1550 nm (SWIR)	3.5º Forward	0.35 mrad
Channel 2	1064 nm (NIR)	0 º (Nadir)	0.35 mrad
Channel 3	532 nm (Vis–Green)	7 º Forward	0.7 mrad

Figure 44. Titan Laser Drawing. Source: Teledyne Optech (2015).

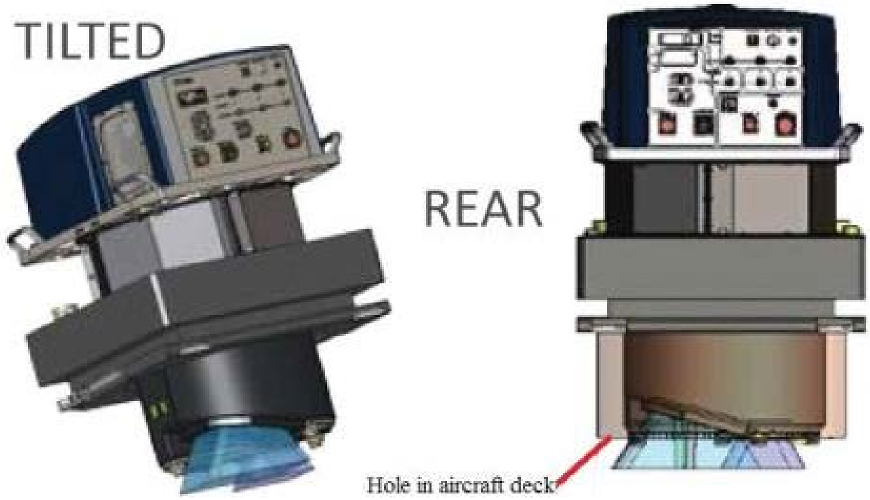

2. Dataset Collection

In May 2016, the National Center for Airborne Laser Mapping (NCALM), based at the University of Houston, flew the Optech Titan sensor over Monterey, California. NCALM collected multi-wavelength and waveform LiDAR data for the Remote Sensing Center at the Naval Postgraduate School (NPS). The complete spectral dataset has 23 flight lines, mostly north-south tracks, spanning from the Monterey Regional Airport to the city of Pacific Grove. There are three laser format (LAS) files per flight line, corresponding to the individual 532 nm, 1064 nm, and 1550 nm channels. For this effort, the four north-south flight lines (12 LAS files total) that overlap the NPS campus are selected: FL 10, FL 12, FL 13, and FL 15, as shown in Figure 45.

Figure 45. Titan Monterey Dataset—Four-Selected Flight Lines and Overlap.

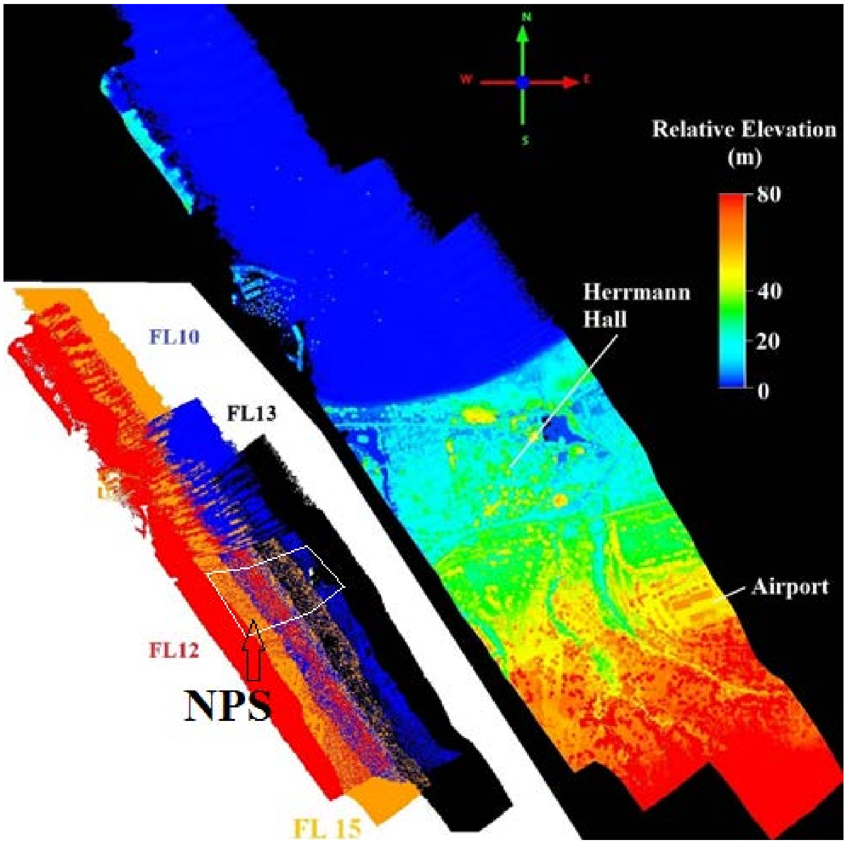

FL’s 10 and 15 correspond to the central campus, and FL’s 12 and 13 correspond to the western and eastern areas, respectively. As a reference, Figure 45 provides an overhead view of the four-selected flight lines, colored by relative height, and the flight line overlap. The dataset corresponds to terrain located in Universal Transverse Mercator (UTM) zone 10N, and it is referenced using the North American Datum of 1983 (NAD83) and the North American Vertical Datum of 1988 (NAVD 88).

B. DATA PREPARATION

1. Flight Line Channel Merging, Boundary, and Noise Removal

Figure 57 offers an overall roadmap of data preparation and processing, and all of Section B is summarized in the left hand column. The first preparation step uses a set of locally developed ArcGIS scripts (Titan Toolbox) to merge the three channels of each flight line into one LAS file and, then, clip all of the flight line boundaries. The LAS "point source id" field retains the original channel/flight line information for each point. The Titan_boundary_clip script is essential, because the laser points become overly spread out toward the edges of a flight line—where the laser optic's scan angle is greatest, up to 60º off-nadir (Teledyne Optech 2015). Leaving the edge points will cause discrepancies during the upcoming nearest neighbor algorithm. The data loss due to clipping is insignificant, as the edges occur within the areas of flight line overlap and at the absolute boundaries of the point cloud (See Figure 46).

Figure 46. Example Titan Monterey Flight Line After Boundary Clip.

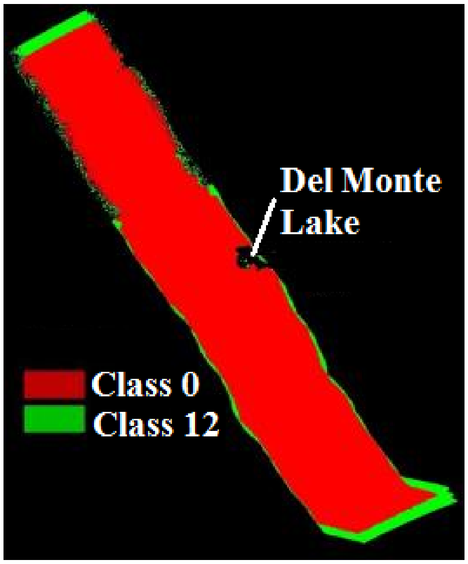

Figure 46 is an example of a flight line after running the Titan_boundary_clip script. The points with classification “0” *(red)* will be retained during the upcoming LASground script, however the edge points (classification “12’–*green*) will be discarded. Next, it is necessary to remove noise points before proceeding to spatially classify the point cloud. Martin Isenburg’s LAStools software suite includes a script that automatically removes point cloud noise. However, the raw Monterey dataset is relatively noise free. The manual removal of noise points from all four flight lines took less than 30 minutes total using Applied Imagery’s Quick Terrain Modeler (QTM) software.

2. Standard Ground, Building, and Vegetation Classification—Spatial Geometry Only (LASclassify)

The basic classification process begins with establishing the ground level using LASground, another LAStools’ script. The following input parameters produce the best ground result for the NPS campus: -city mode, -offset 12, -fine. “City mode” applies a step height of 35 m to help distinguish flat rooftops from the ground. “Offset 12” includes all points 12 cm above the initial estimate as ground. “Fine mode” uses a greater number of points to create the initial ground estimate. After LASground, all of the points are classified as either “class 1–unclassified” *(red points)* or “class 2–ground” *(green points)*. Figure 47 is a screenshot of the results of LASground near the quad and Herrmann Hall.

Figure 47. LASground Results for a Small Section of the NPS Campus.

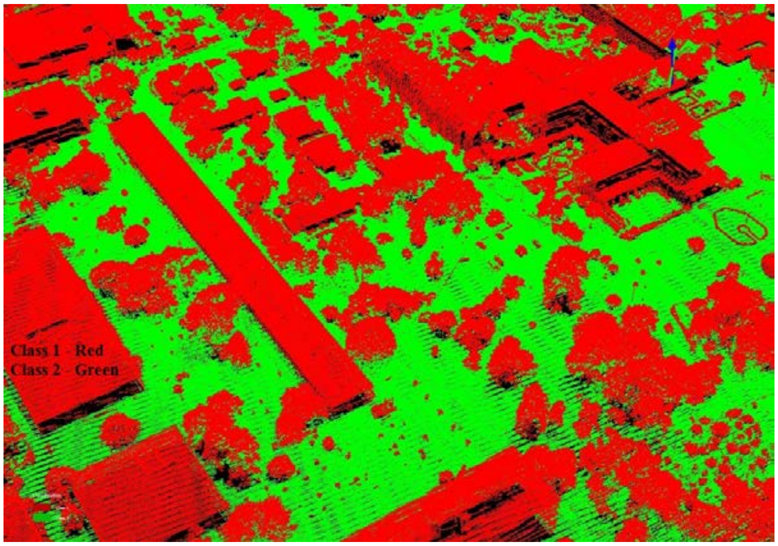

Next, the above ground level (AGL) metric is calculated via the LASheight script in order to determine the height above ground for each laser point. AGL is a critical metric that will be relied on heavily by the upcoming spectral analysis and the ENVI classifiers. After running LASheight, the point cloud is ready for the LASclassify script, which will separate the unclassified points that correspond to buildings and vegetation. LASclassify analyzes neighboring points to identify planar structures (buildings) and rough surfaces (vegetation). The result is a point cloud now with four basic classifications: red–unclassified (1), green–ground (2), dark blue–vegetation (5), and cyan–buildings (6). Note that this autonomous, spatial-only, classifier is limited and does result in discrepancies. For example, in Figure 48 the rough clay-tiled roof and the walls of Herrmann Hall are misclassified as vegetation in some areas or left unclassified.

Figure 48. Raw Results of the LASclassify Script.

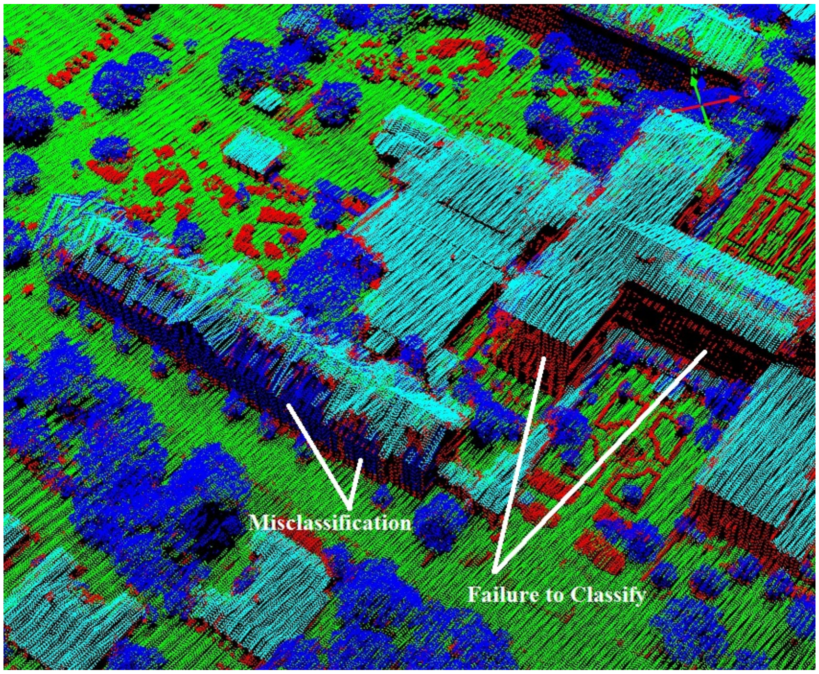

Thomas' statement is still true: "To provide increased fidelity to the follow on spectral classification, the results of automatic classification tool, LASclassify, require manual correction" (Thomas, 2015, 25). Here, the primary focus of manual correction is to fix the portions of buildings previously misclassified as vegetation. Also, we classify as many unclassified *(red)* points as possible into either the vegetation or building categories. This will allow our spectral analysis to focus directly on the subclassification of specific ground types and manmade materials, instead of trying to separate out misclassified roofing materials from the vegetation class. No new classifications are established manually, this is for correction only. Figure 49 is the same area as Figure 48 after manual correction. Manual correction is accomplished in Quick Terrain Modeler by highlighting a region with the polygon selection tool and using the "set classification in area" option.

Figure 49. Corrected Results of the LASclassify Script.

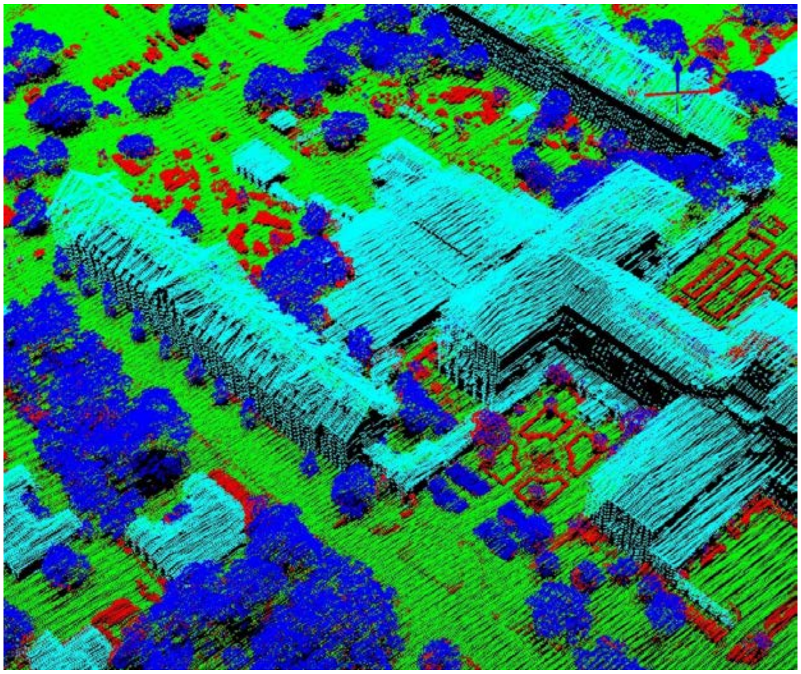

Before proceeding to the nearest neighbor script, the analysis area is chipped out from the four full-length flight lines. The analysis area contains the NPS campus, a section of Monterey Beach, and a buffer zone. The buffer zone includes CA Highway 1 to the south, the ocean to the north, and the two side-streets to the east and west of the campus. Figure 50 is a Google Earth view of the analysis area outlined in red. And, Figure 51 displays the analogous point cloud in QTM, colored by classification. Lastly, Table 4 break downs the number of points per classification within the analysis area.

Figure 50. NPS Subset in Google Earth. Adapted from Google Earth (2016).

Figure 51. NPS Subset Colored by Classification—Post LASclassify.

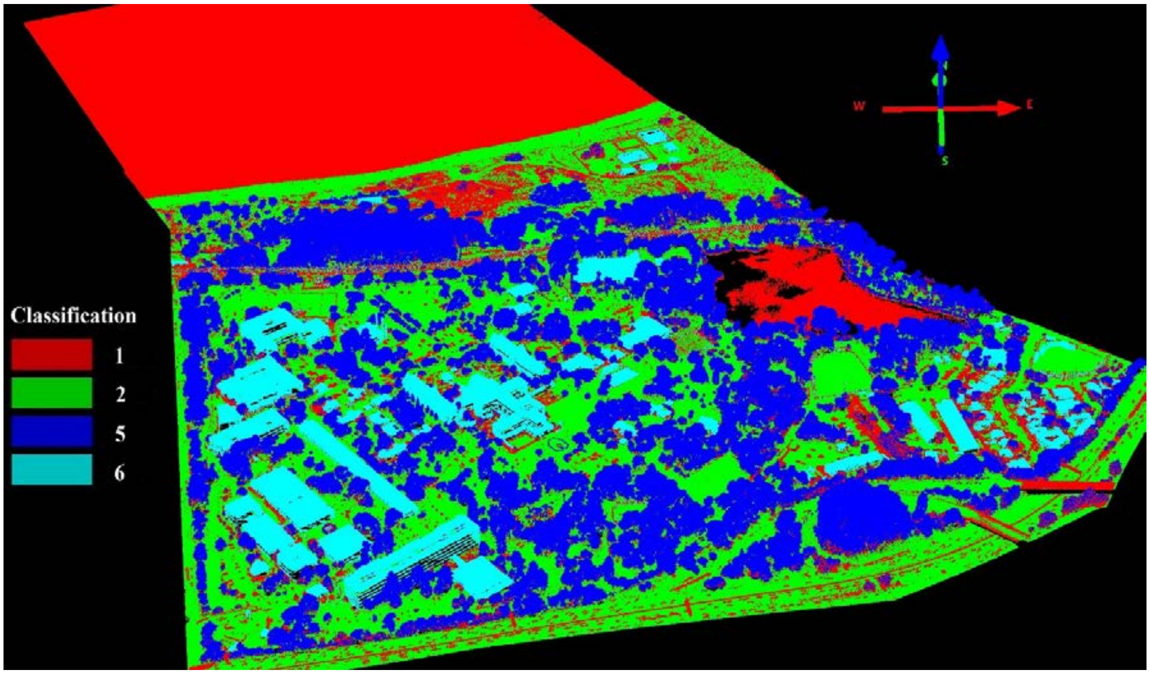

Table 4. Point Classification Breakdown—Post LASclassify.

Classification	Color	No. of Points	% of Total
1—Unclassified	Red	3,401,822	22.64
2—Ground	Green	6,826,990	45.45
5—Vegetation	Dark Blue	3,970,153	26.43
6—Buildings	Cyan	823,837	5.48
		15,022,802	100

Overall accuracy is 77.36% (the total percentage of points that are not unclassified).

3. Nearest Neighbor—RGB and Conversion from LAS to ASCII Files

A local Matrix Laboratory (MATLAB) script employs the OpenTSTOOL's nearest neighbor algorithm for the process of spectral incorporation. This is the principle step of data processing, and it makes future spectral analysis possible. First, each flight line file is divided back into three separate LAS files, one for each channel: C1–1550 nm, C2–1064 nm, and C3–532 nm. Then, for all of the laser points in each channel, the neighboring intensities from the other two channels are located. The two results are saved in the LAS "Red-Green-Blue" (RGB) attributes of the original point according to the following assignments: The nearest 1550 nm intensity is stored as the "Blue" field. The nearest 1064 nm intensity is stored as the "Red" field. And, the nearest 532 nm intensity is stored as the "Green" field. Of course, each point duplicates its own intensity into the appropriate RGB field before the remaining two fields are populated by the intensity values from the other wavelengths. Figure 52 illustrates this process.

With a spatial point density of approximately 10–15 points per square meter, the spectral incorporation via nearest neighbor is occurring with nearly coincident points (spatially and temporally), so discrepancies from this process are negligible. Additionally, the nearest neighbor injection of spectral returns into the LAS "RGB" attributes produces a false-color point cloud that can be rasterized, if desired, into a multiband image. Figure 53 is this point cloud in QTM colored by "RGB." Roads, buildings, and other manmade objects appear close to true color, and vegetation appears in varying shades of red and pink (higher 1064 nm returns). Areas of water, such as the ocean, appear mostly dark due to weak signal returns in all channels. The coastal surf and the shallow NPS reflecting pool appear green, indicating stronger 532 nm returns.

Figure 52. Nearest Neighbor Spectral Incorporation. Source: Miller et al. (2016).

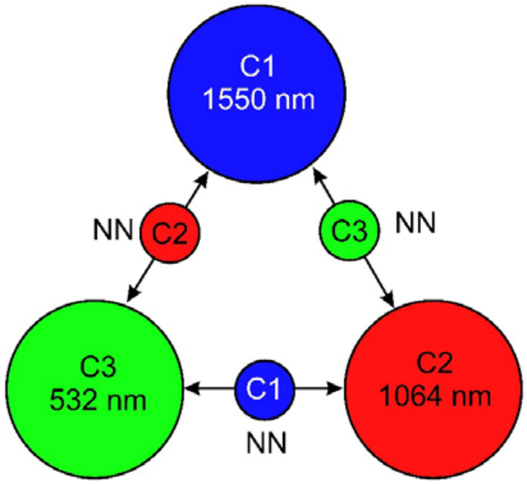

"For every point in each channel, find the nearest neighbor intensities from the other 2 channels and store in the RGB fields" (Miller et al. 2016, 14).

Figure 53. NPS Point Cloud in False Color RGB—Post Nearest Neighbor.

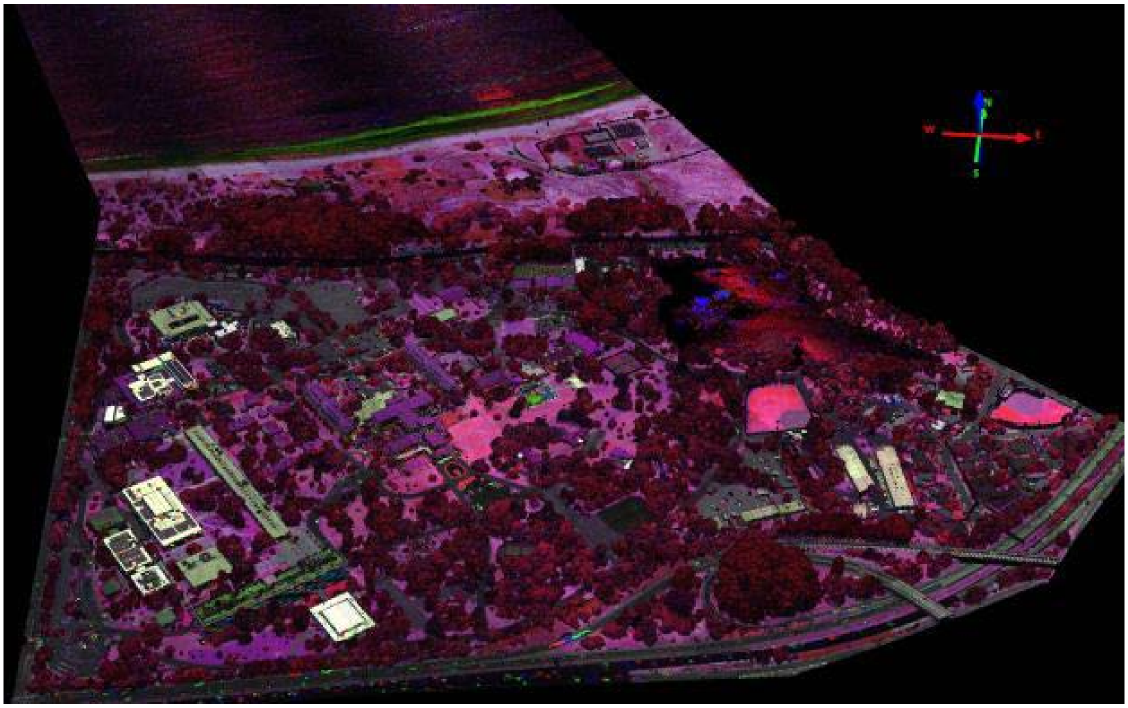

4. Final ASCII Preparations and Calculation of Vegetation Indices

In addition to LAS files, the nearest neighbor script outputs the point cloud as text files, one per flight line. These ASCII files provide the input to the final script of the data preparation process. This is necessary for two reasons: 1). The ASCII_prep_pro script must append several more attributes for each data point, however the LAS file structure cannot accommodate the additional fields. 2) There is no direct conversion from LAS to ENVI standard format; LAS to ASCII to ENVI format is the only way to get the data into ENVI's N-D VIS tool.

ASCII_prep_pro is a locally developed Interactive Data Language (IDL) program designed to merge the separate ASCII flight line files into a collective array of data points, complete several additional processing steps, and output the result as a single ENVI file set (.dat, .hdr, and .roi files). The intermediate ASCII_prep_pro steps are as follows: flag a 5% subset of points, calculate vegetation indices, and append a manual classification attribute. A reduction factor of 20 is applied via random-sampling code to flag a 5% subset of the data points evenly throughout the entire scene. The remaining 95% of the points are maintained, however the reduction flag allows them to be separated out during spectral analysis in N-D VIS. This permits the analyst to spectrally classify only the 5% subset and, then, test the abilities of various ENVI classifiers on the remaining 95% (e.g., K-means, Maximum Likelihood, or Spectral Angle Mapper). The reduction flag is appended to the data array as attribute #21 for each point: A value of "0" means that point is part of the 95%. A value of "1" means part of the 5% training subset. Figure 54 indicates how the data points will be separated by visualizing attribute #21 in N-D VIS; the upper line is comprised of all points with a reduction flag value of "1," and the lower line contains all points with a value of "0."

Next, ASCII_prep_pro calculates three vegetation indices and appends them to the data array as attributes #18, #19, and #20. The vegetation indices will assist us in differentiating points as either vegetation or non-vegetation in areas where it is otherwise unclear. Since Titan does not carry a visible-red laser, the three available vegetation indices (Table 5) are the Green Normalized Difference Vegetation Index (GNDVI), Green Difference Vegetation Index (GDVI), and Green Ratio Vegetation Index (GRVI).

Table 5. Vegetation Indices. Adapted from Richards (2013).

Green Normalized Difference Vegetation Index	GNDVI	= (NIR - Green)/(NIR + Green)
Green Difference Vegetation Index	GDVI	= NIR - Green
Green Ratio Vegetation Index	GRVI	= NIR/Green

All three are calculated for each point: Green is the 532nm intensity value—stored in the "G" field of a point's RGB. NIR is the 1064 nm intensity value—stored in the "R" field.

Appending the manual classification attribute is an optional step. In order to make use of this attribute, one must first export the LAS files from QTM as "XYZ" ASCII files. The ASCII_prep_pro script prompts for these input "XYZ" files after it asks for the post-nearest neighbor files. The classification of each point in the "XYZ" files is copied over to the matching point in the data array and saved as attribute #17. This step contributes a potential method of ground-truth comparison, if one is willing to manually classify the entire point cloud. Again, we added no new classifications to the base four during the earlier manual correction, making attribute #17 not applicable to this work.

Lastly, ASCII_prep_pro formats the ASCII data into an array of the following dimensions: (1 x # of points x # of attributes). The array for the NPS analysis area is (1 x 15,022,802 points x 21 attributes). The 21 attributes for each point are outlined in Table 6. The array is automatically exported as an ENVI .dat file with accompanying header (.hdr) and region of interest (ROI) files.

Table 6. ASCII Attributes. Adapted from Miller et al. (2016).

Field #	Attribute	Field #	Attribute
1	X (UTM—meters)	12	Point Source ID
2	Y (UTM—meters)	13	Time (GPS Tag)
3	Z (meters)	14	Red
4	Original Intensity	15	Green
5	Return Number	16	Blue
6	Number of Returns	17	Manual Classification
7	Scan Direction	18	GNDVI
8	Edge of Flight Line	19	GDVI
9	Classification (Initial)	20	GRVI
10	Scan Angle Rank	21	Reduction Flag
11	Height (AGL)—8 bit relative scale from 0 *(ground)* to 255		

5. Input to ENVI's N-Dimension Visualizer (N-D VIS)

The ENVI files are brought into the N-D VIS tool for spectral analysis by selecting the "visualize with new data" option. N-D VIS allows an "n" number of dimensions to be visualized at one time in the display window. N-D VIS is designed for traditional multi- and hyperspectral imagery, where an image's wavelength bands are the dimensions for visualizing its pixels. Here, we have adapted N-D VIS to our LiDAR data currently in ENVI file format, where we will instead represent the 21 attributes as the dimensions and visualize laser points in this n-dimensional space. Each laser point is treated as an "image pixel" in our data array of 15,022,802 lines ("rows"—one per point) and 21 samples ("the attribute columns" of Table 6):

> Use the n-D Visualizer to locate, identify, and cluster the purest pixels and the most extreme spectral responses (endmembers) in a dataset in n-dimensional space. The n-D Visualizer was designed to help you visualize the shape of a data cloud that results from plotting image data in spectral space (with image bands as plot axes)...When using the n-D Visualizer, you can interactively rotate data in n-D space, select groups of pixels into classes, and collapse classes to make additional class selections easier. You can export the selected classes to ROIs and use them as input into classification techniques. (Harris Geospatial Solutions 2017c)

The "n-D Controls" window gives us the ability to select which of the 21 attributes from Table 6 to study at any one time. Hereafter, we generally use the term bands instead of attributes to maintain consistency with ENVI and N-D VIS terminology. The goal of our spectral analysis, in Chapter IV, is to view the RGB spectral values (Bands 14, 15, and 16) of all points to identify and reclassify point clusters that correspond to specific ground types, vegetation, and manmade impervious surfaces. This represents a unique capability that is not possible with geometric classifiers, such as LASclassify. Additionally, spatial attributes will be exploited as necessary to assist the spectral classification process. For example, the AGL "height" (Band 11) will be utilized to separate the ocean's surface and the seafloor and to distinguish between ground and roofing concretes.

Two steps remain before the spectral subclassification can begin. First, data reduction is accomplished by selecting X (Band 1) and Reduction Flag (Band 21) in the "n-D Controls" window. In Figure 54, the random subset of points appears as the upper line (Band 21 value = "1") and is selected by circling it with the cursor. ENVI Classifiers will exploit the user-classified 5% subset as a training region for classifying the remaining 95% of points (The lower line in Figure 54: Band 21 value = "0").

Figure 54. N-D VIS Data Reduction Via Reduction Flag (Band 21).

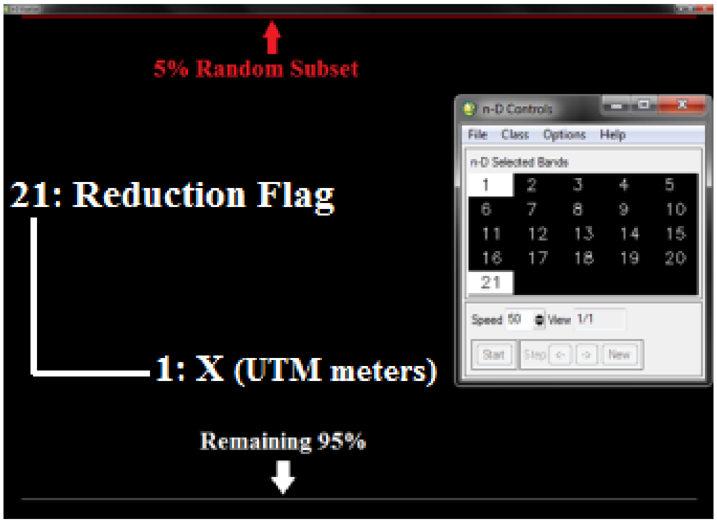

X (Band 1) and Classification (Band 9) are selected to assign colors in accordance with the original classification outputs from the LASclassify script. The red, green, dark blue, and cyan scheme is temporarily preserved to maintain consistency. Classification colors are assigned by selecting the appropriate color in the "n-D Class Controls" window and circling the correct line of points according to Figure 55. Remember, LASclassify assigns its output classes a number designator (See Table 4). Here, our choice of Band 1 and Band 9 presents the points of each numbered class as lines in ascending order: unclassified (0), ground (2), vegetation (5), and buildings (6). If the user has altered any of the LASclassify number designators or manually created new classes with a different numbering scheme, N-D VIS would still display those classes in their numerically ascending order. It is important to note the minimum number of dimensions that N-D VIS can display is two, which is why X (Band 1) is also selected in Figures 54 and 55. Again, the lines are actually groups of points separated by Reduction Flag (Band 21) in Figure 54 and by Classification (Band 9) in Figure 55.

Figure 55. N-D VIS Point Clusters by Initial Spatial Classification (Band 9).

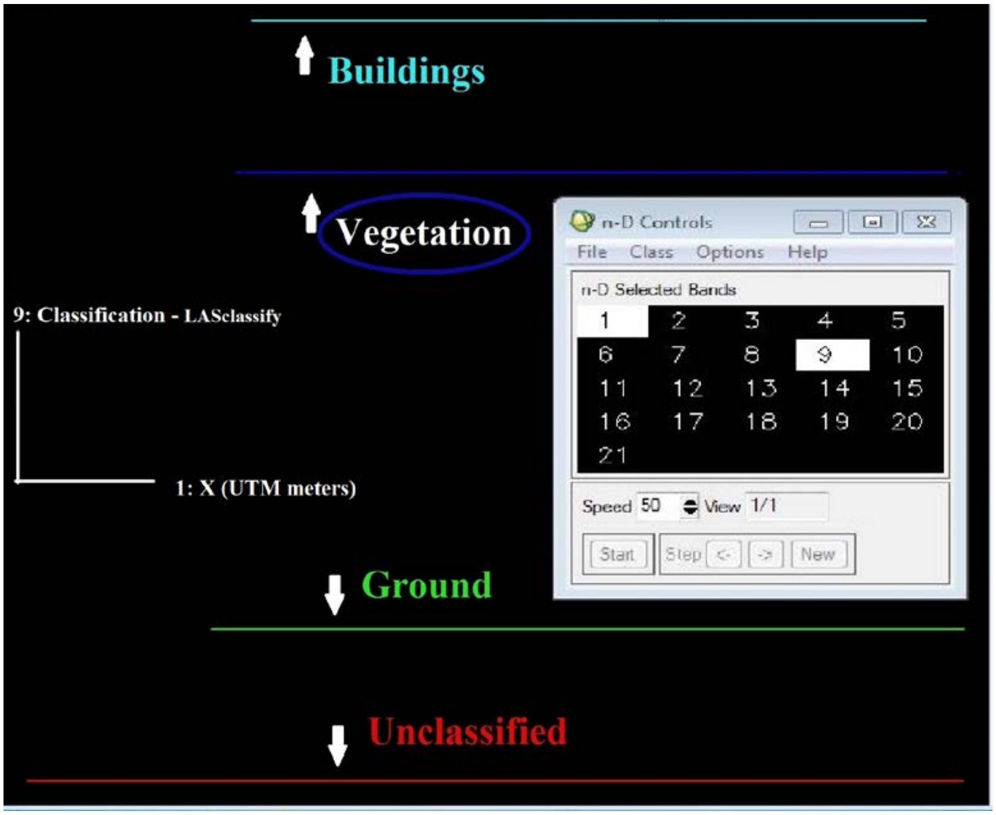

After applying the classification colors, the elements of the point cloud become distinguishable in XYZ space, band selections: X (Band 1), Y (Band 2), and Z (Band 3). XYZ space is now the base state for viewing the entire point cloud spatially in N-D VIS. Figure 56 shows the same data points as seen in Figures 54 and 55, now displayed in their normal x, y, and z positions instead of by classification, reduction flag value, or any of the other bands (dimensions). It provides a recognizable overhead view of the campus, similar to Figure 51. At this point, the N-D VIS session is saved as a .ndv file to establish a quick restoration point. This is the best way to save and restore N-D VIS work-in-progress, so that it does not have to be exported back into ENVI or ASCII files until after we have run the ENVI classifiers in Chapter V.

Figure 56. NPS Campus in N-D VIS XYZ Space.

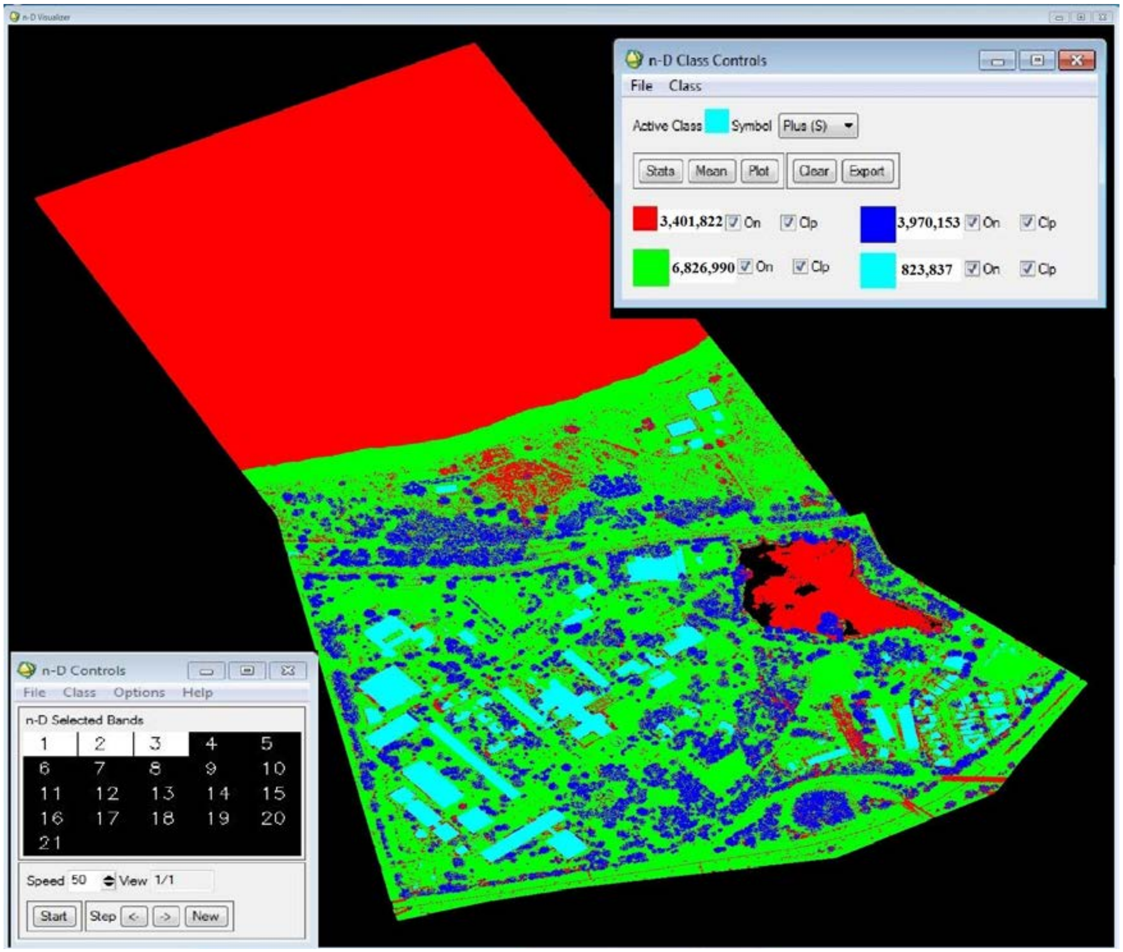

Active Class 🟦 Symbol Plus (S)

🟥 3,401,822 ☑ On ☑ Clp
🟦 3,970,153 ☑ On ☑ Clp
🟩 6,826,990 ☑ On ☑ Clp
🟦 823,837 ☑ On ☑ Clp

Speed 50 View 1/1

THIS PAGE INTENTIONALLY LEFT BLANK

IV. PROCESSING APPROACH

A. ANALYSIS WORKFLOW

Analytical software tools for the terrain classification of spectral LiDAR datasets remain virtually non-existent. The Optech Titan multispectral LiDAR is still a relatively new and unique system. Accordingly, this thesis continues the use of ENVI’s N-D VIS tool to identify and define spectral subclasses from three-wavelength Optech Titan point clouds. Chapter III details the conversion of the four-chosen flight lines from traditional LAS file format to ENVI file format. Figure 57 is the analysis workflow that covers the contents of Chapters III, IV, and V: data preparations, spectral analysis and processing approach (i.e., the definition of training regions), and classification results using ENVI classifiers.

There are four principle software tools that make this research effort possible. The LAStools suite contributes the critical preparation steps of ground determination, height calculation, and initial spatial classification. Quick Terrain Modeler and Cloud Compare (CC) provide LiDAR point cloud viewing and modeling in 3D plus the ability to view, filter, and analyze various data attributes, such as intensity, RGB, scan angle, GPS time, return number, and point source id. The ENVI software suite contributes the N-D VIS tool for spatial and spectral analysis, as well as the necessary built-in classifiers. ENVI’s IDL interface allows for the quick conversion between the ASCII and ENVI file formats. This gives us the ability to export the completely classified point cloud from N-D VIS back to QTM or CC for viewing.

Figure 57. Analysis Workflow for Spectral LiDAR Data.

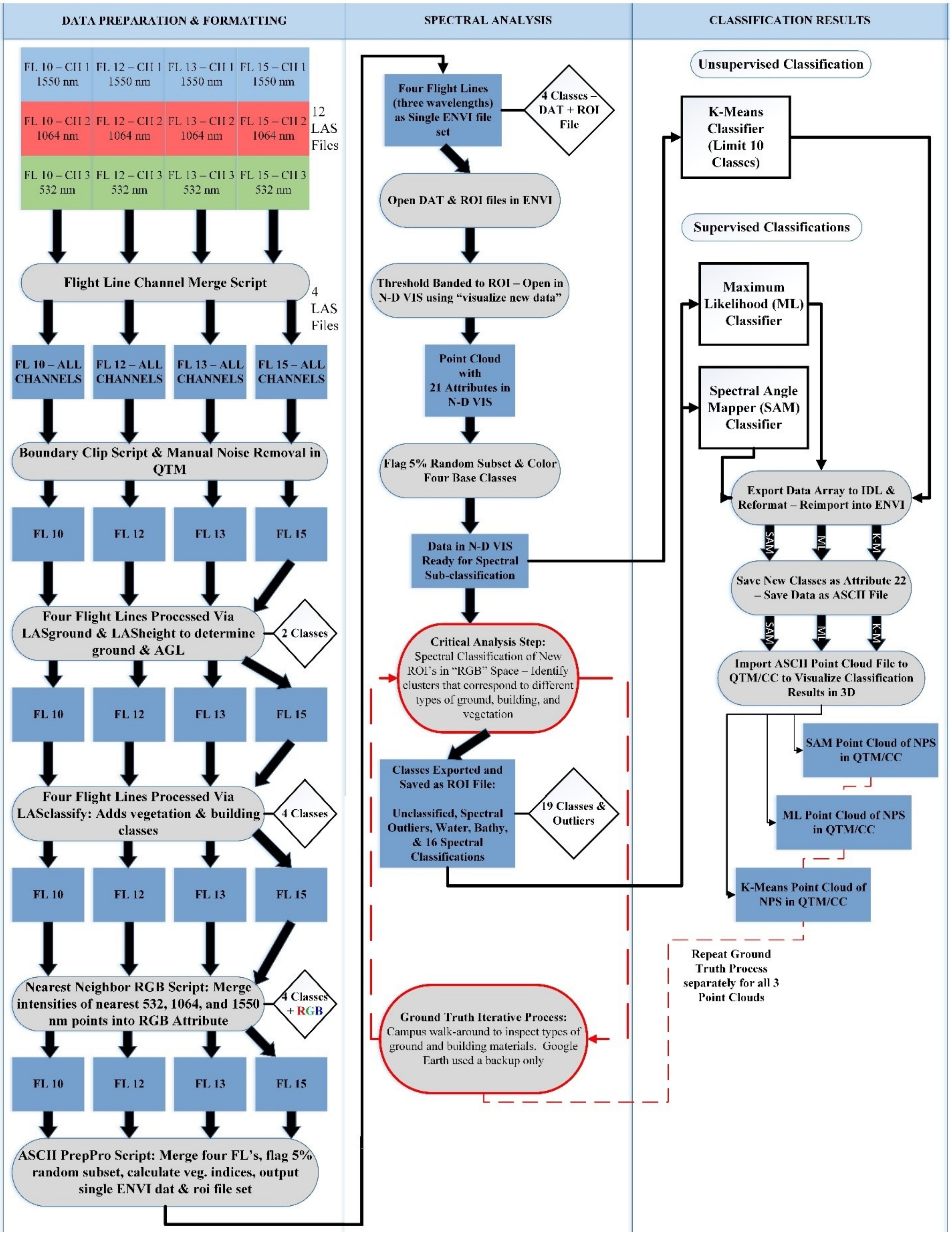

B. SPECTRAL CLUSTERING IN N-D VIS USING A 5% RANDOM SUBSET

1. Establishing the Land, Water, and Bathymetry Interfaces

First, we establish an intuitive color scheme in N-D VIS: Ground points are set to sienna, buildings to yellow, and vegetation to a medium green. Dark blue and cyan are used to represent water and bathymetry (ocean bottom measurements), respectively. The 95% of points not flagged as part of the 5% training subset are considered unclassified and colored white. The unclassified points are hidden from view for the duration of analysis by unchecking the white class in the "n-D VIS Class Controls" window. This ensures that the upcoming spectral-clustering process is not obstructed by the disproportionately large number of unclassified points (14+ million).

Identifying spectral clusters (subclasses) that correspond to specific types of ground, building materials, and vegetation takes place primarily in RGB space: Red (Band 14), Green (Band 15), and Blue (Band 16). Nevertheless, we distinguish the water and bathymetry subclasses using Z (Band 3), original Intensity (Band 4), and AGL (Band 11). Figure 58 is a N-D VIS screenshot showing the distinctive land, water, and bathymetry interfaces. Here, the wide range of intensity values exhibited by the water points aids our subclassification process. The two upward spikes on the intensity axis correspond to the ocean and the lake.

Figure 58. Water and Bathymetry Distinguished by Z, Intensity, and Height.

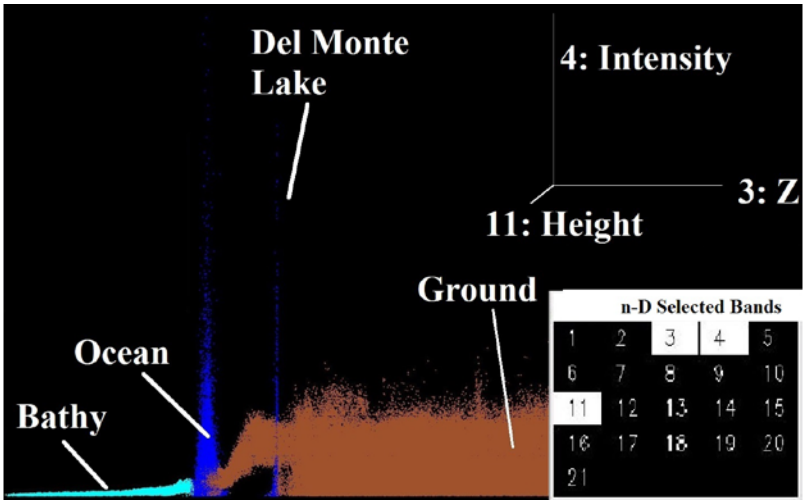

Alternately, the water and bathymetry subclasses can be selected by visualizing two-purely spatial attributes: Y (Band 2) and Z (Band 3) creates the pseudo-side view of the analysis area as seen in Figure 59. The two bodies of water occupy distinct and narrow ranges of Z values—the surface of calm water is essentially flat. This is also apparent in Figure 58. The bathymetry points appear in Figure 59 as a slope below the ocean level. Vegetation and buildings are temporarily unchecked in the "Class Controls" window, so that they are hidden to avoid confusion.

Figure 59. Water and Bathymetry Distinguished Spatially in N-D VIS in YZ Coordinates.

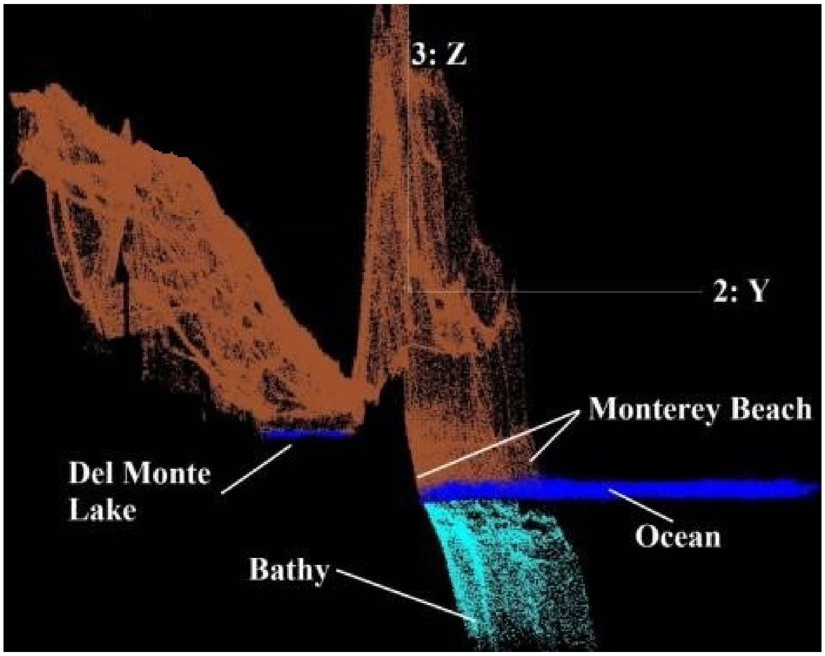

We switch back to XYZ space (Bands 1, 2, 3) to view the land, water, and bathymetry interfaces before proceeding to subclassify the ground, vegetation, and building classes. Figure 60 presents five of our six classes in XYZ space. The unclassified 95% (white) remains hidden from view. The ability to turn classes on or off as needed is another extremely useful attribute of the N-D VIS tool. Again, dark blue is the water, cyan is the bathymetry, yellow is the buildings class, green is the vegetation class, and sienna is the ground class. Since we are working with only the 5% subset of points, Figure 60 appears less dense than the comparable Figure 56.

Figure 60. NPS Campus in XYZ Space, Now with Water and Bathymetry Classes.

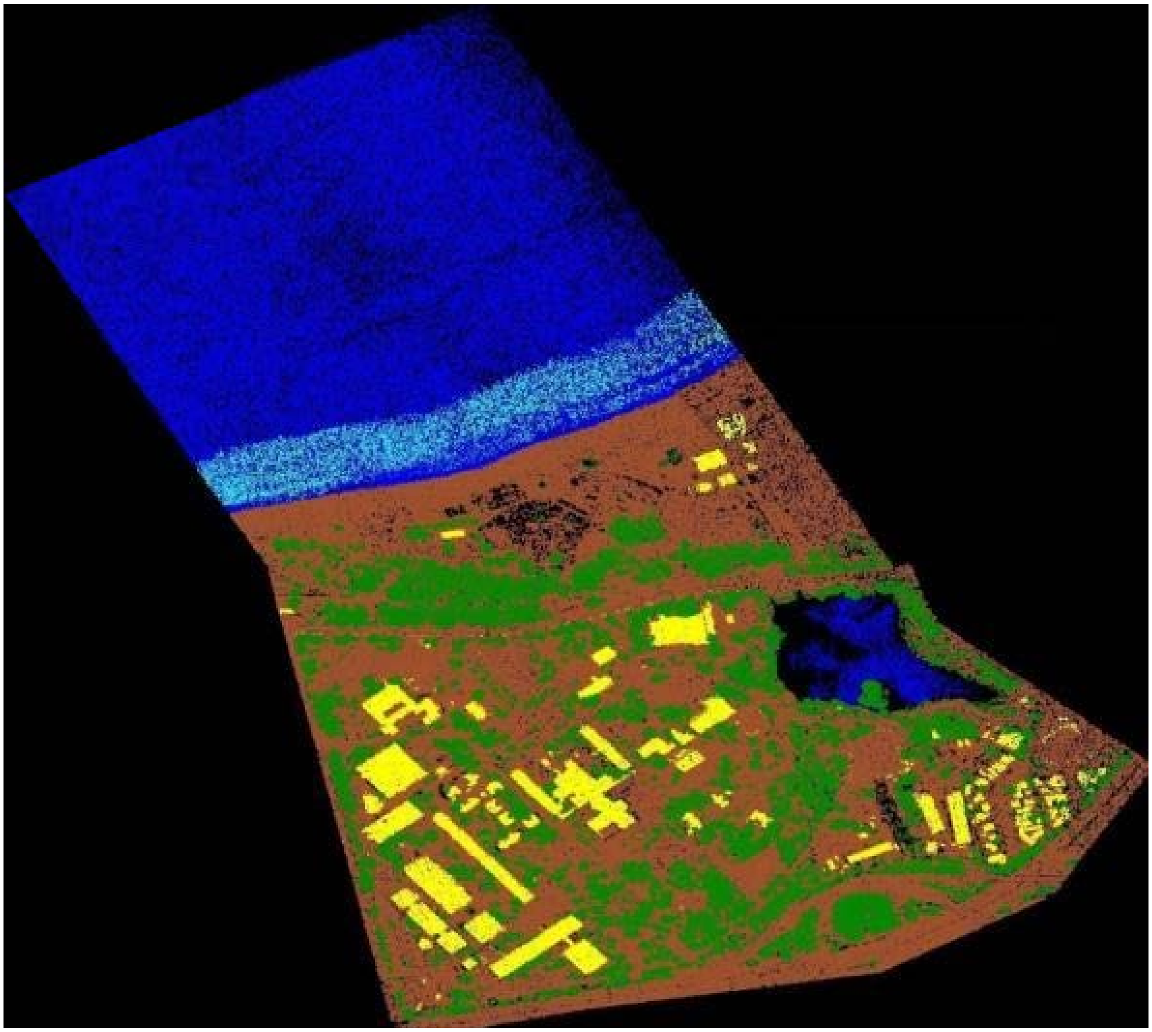

2. Spectral Subclassification—Ground Points

Next, ground points (sienna) are isolated in order to identify terrain categories in RGB space, also referred to as spectral space. Figure 61 shows the ground points only in XYZ space, approximately 341,300 points. Figure 62 is the corresponding spectral space. The data points are now represented in a format that resembles a 3D scatterplot. The visualizer can animate forward or backward through the various plot orientations, or one can use the “3D Drive Axis” option to manually maneuver the display. In Figure 61, the silhouettes of the Del Monte Lake and several campus buildings are labelled to provide a sense of orientation about the scene.

Figure 61. Ground Points Only in XYZ Space, Prior to Subclassification.

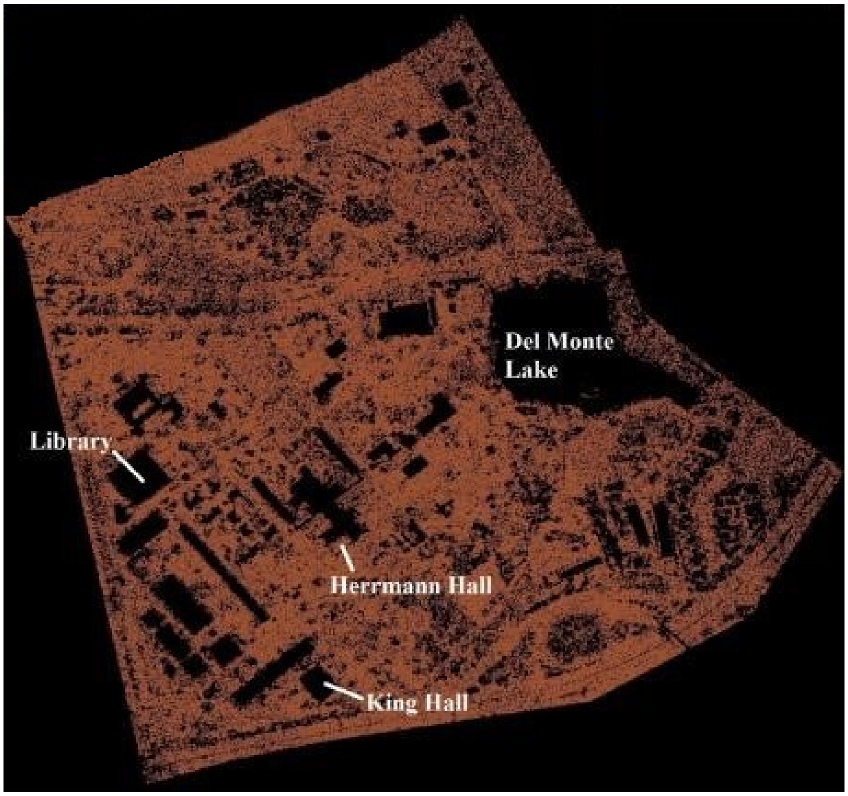

Figure 62. Ground Points Only in RGB Space, Prior to Subclassification.

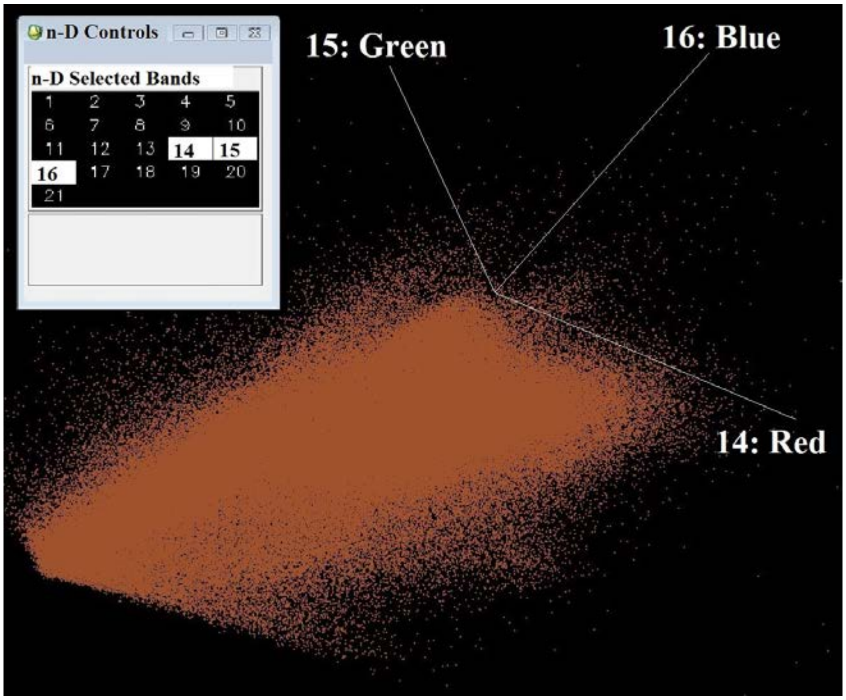

The spectral analysis proceeds systematically through the data in RGB space by visualizing the points from various perspectives. First, the extreme outliers are removed to ease access to the bulk of the points; they are intentionally absent from Figure 62. Next, points which appear to form clusters are selected and assigned to a new class (color). The screen is then switched back to XYZ space to inspect and correct the selection as necessary. This process is applied iteratively until all of the ground points have been reviewed and subclassified. Figure 63 displays the largest four of the newly defined ground subclasses. The most appropriate colors available in ENVI are assigned to the new subclasses.

Figure 63. Ground Subclasses in N-D VIS: Dirt, Grass, Concrete, and Asphalt.

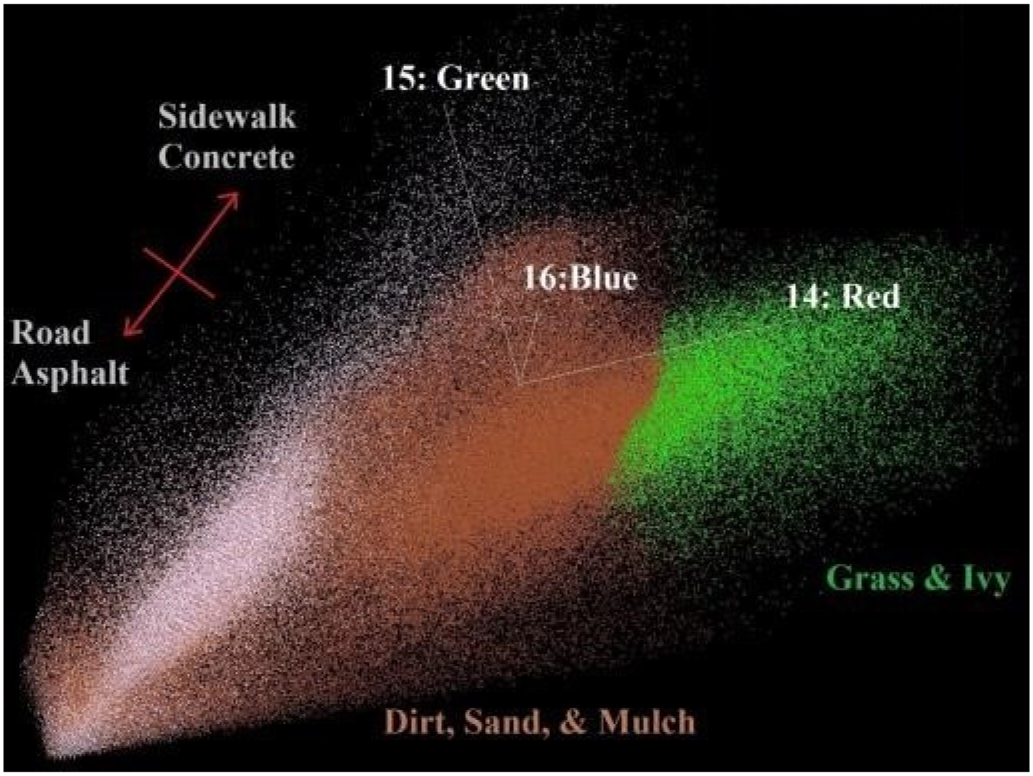

The grass/ivy (bright green) points have strong spectral returns in the red band (1064 nm). Thus, they occupy the highest values on axis 14. The sidewalk concrete (thistle—gray) is relatively bright and nearly even in the red, green (532 nm), and blue (1550 nm) bands. Comparatively, road asphalt (thistle 1) appears dark in all three bands.

The remaining sienna-colored points correspond to areas of dirt, sand, and mulch, which seem to be spectrally indistinguishable in the three available wavelengths. Additionally, two smaller ground subclasses are identified in Figure 64. The turf (fake grass) near the NPS flagpole (colored sea green) and the encompassing red-brick (red 3) traffic circle are the two smallest subclasses distinguishable in RGB space. In Figure 64, the grass/ivy subclass remains displayed as a reference, but it is necessary to hide the dirt, concrete, and asphalt subclasses to view the turf and brick spectral clusters.

Figure 64. Ground Subclasses in N-D VIS: Grass, Red Brick, and Turf.

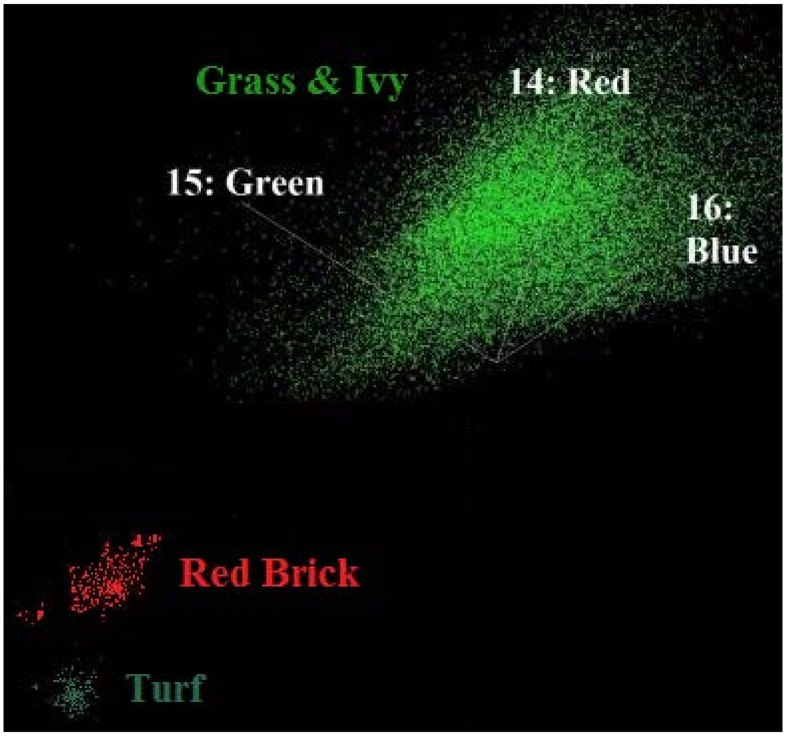

The ground class is now divided into six spectrally defined subclasses: dirt/sand/mulch, grass/ivy, sidewalk concrete, road asphalt, red brick, and turf. Figure 65 is a spectral plot of these ground subclasses created using the average (mean) RGB values of each cluster. The x-axis is comprised of the three wavelengths: 532 nm, 1064 nm, and 1550 nm. The y-axis is return intensity in arbitrary units; intensities are represented as a 12-bit relative scale from 0 to 4096 (2 raised to the 12th power). None of the mean intensities for the ground subclasses exceed 2,500. From the 3-band spectral plot, the red brick and the dark road asphalt are the two most similar spectra. Also, note the vast differences between grass and green turf, especially in the red (1064 nm) and blue (1550 nm) bands. Concrete and road asphalt have similarly shaped profiles; however, the concrete is nearly twice as bright in all bands. This corresponds with the locations of the concrete and asphalt clusters in RGB space (Figure 63).

Figure 65. Spectral Plot of Ground Subclasses from Mean RGB Intensities.

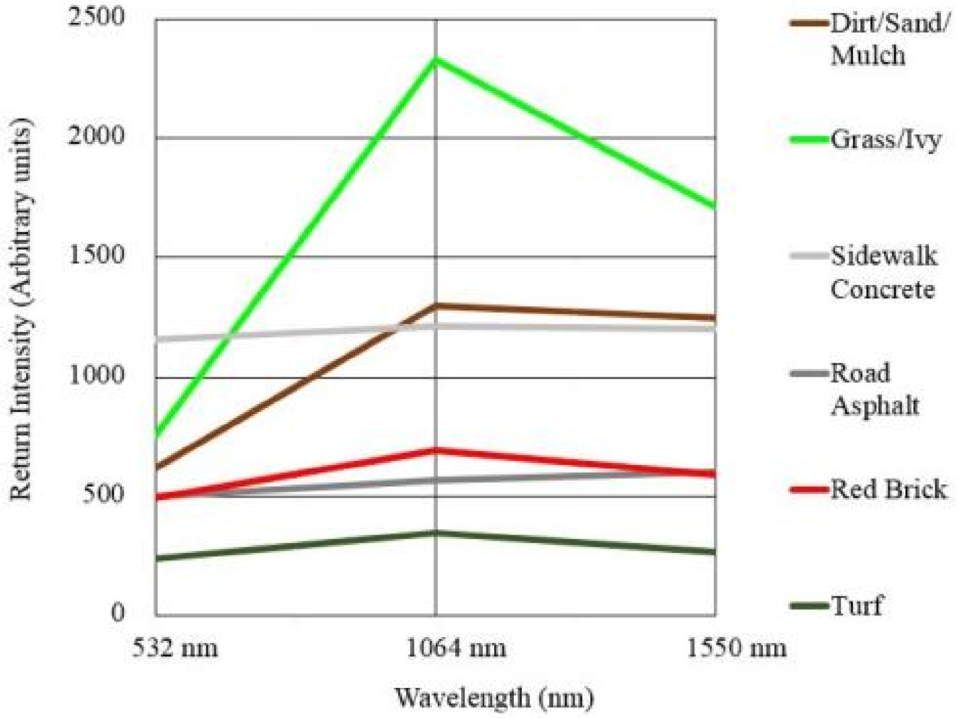

The AGL for all ground points is 0.

Before proceeding to subclassify the vegetation and buildings, the newly defined ground types are reviewed altogether in XYZ space. The analysis is temporarily paused here to permit a ground truth walk-around of the NPS campus. This occurred in late October 2016, approximately five months after data collection. There was no noticeable change in any of the areas of concrete, asphalt, turf, or the red brick traffic circle. Due to a couple of recent rains and gardening, some of the real-world areas of grass appear larger and lusher than in the dataset. Thus, Google Earth imagery from April 2016 (about one month before the LiDAR collect) is used as a backup means of ground-truth comparison for grass versus dirt areas. Refer to Figure 50.

Figure 66 displays the six ground subclasses in XYZ space. Again, several landmark features and building silhouettes are labelled as a guide. Since N-D VIS only offers three shades of thistle (gray), the boundaries between sidewalk concrete and asphalt are difficult to discern in the image. During analysis, this is overcome by selecting only one class to view at a time by means of the control panel. Lastly, it is readily apparent that the grass on the softball fields and around the front of Herrmann Hall is the healthiest and densest on campus.

Figure 66. Ground Points Only in XYZ Space, Post-Spectral Subclassification.

3. Spectral Subclassification—Vegetation Points

The primary intent of this thesis is to spectrally distinguish specific ground and building materials. Therefore, the vegetation class received the least amount of analysis. A brief look at the vegetation points in RGB space reveals two large clusters. The spectral cluster with the greater intensities in all bands roughly corresponds to shrubs, shorter cacti, and succulents. The other cluster, with lower RGB intensities, represents taller bushes and trees.

Figure 67 displays the two newly defined vegetation subclasses in RGB space. Shrubs are colored using "green 2" and trees are the slightly darker "green 3." Although grass technically belongs to the ground subclasses, it is included in Figure 67 to show that it has stronger returns in the red band (1064 nm) than the taller vegetation. The red lines are dividers among the three classes, not axes.

Figure 67. Vegetation Subclasses Compared to Grass in N-D VIS.

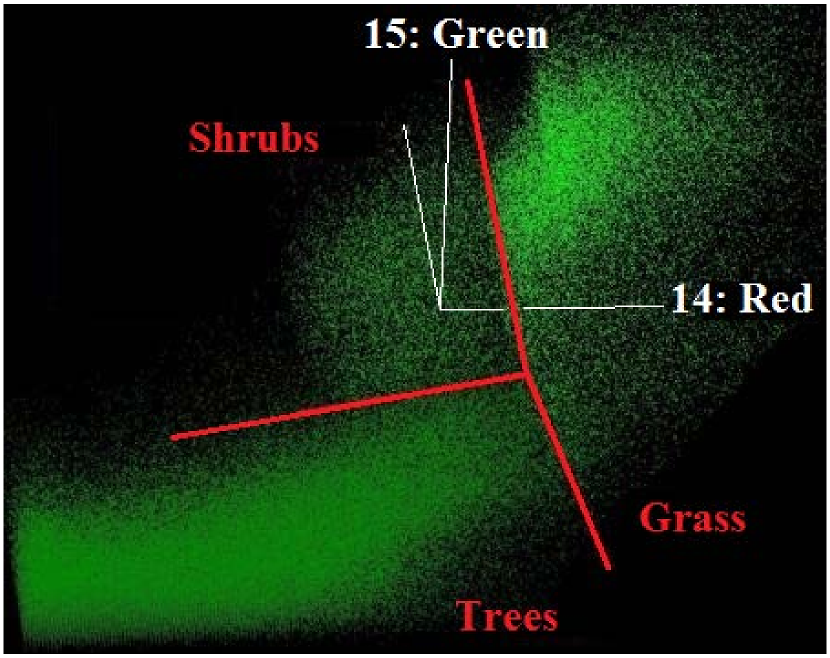

We failed to discover any distinctive clusters corresponding to specific species of trees or shrubs. There does not appear to be enough information with only three spectral bands to distinguish between deciduous or evergreen plants, so separating vegetation at the species level seems even less likely. For this reason, a spectra plot is not included for the vegetation subclasses, and the analysis moves forward to the last category: building materials and powerlines.

Figure 68 highlights the two new vegetation subclasses alone in XYZ space. Trees are the darker green and generally appear denser than the shrubbery. The grass subclass is now hidden to prevent confusion, because the shades of green in N-D VIS are quite similar. Several noteworthy features are labelled, such as the NPS Arizona Cactus Garden and the hedges surrounding the flagpole in front of Herrmann Hall.

Figure 68. Vegetation Points Only in XYZ Space, Post-Spectral Subclassification.

Mean AGL for shrubs is 16.5. Mean AGL for trees is 127.6.

4. Spectral Subclassification—Building Points

Lastly, this analysis will apply the N-D VIS spectral-clustering technique to the campus buildings and powerlines. Figure 69 exhibits the starting point for buildings in XYZ space (left) and the corresponding RGB space (right). Several features are labelled in the XYZ image, including the powerlines that run along Del Monte Avenue just outside of the campus fence. Clusters of points are more apparent in the starting RGB image for buildings than they were for the ground and vegetation classes. This proved beneficial, because the subclassification process for buildings took approximately half the time as compared to the work on the ground points. Additionally, buildings are successfully subclassified into eight categories, as compared to the six for ground and two for vegetation. Building points that cannot be spectrally identified as a specific type of material are retained in the general building (yellow) subclass.

Figure 69. NPS Buildings in XYZ and RGB Space,
Prior to Spectral Subclassification.

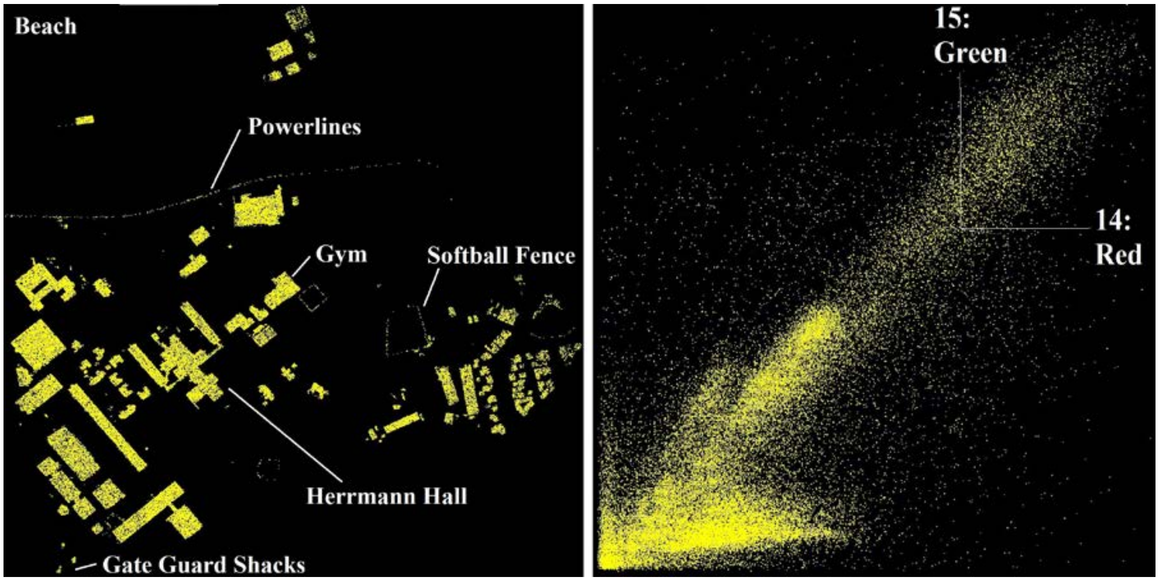

The first building materials that we identify from Figure 69 are two types of concrete: light and dark. Light concrete (thistle 2) is the brightest material in all three spectral bands, and it appears to also include white-plaster surfaces. Dark concrete (yellow 3—“gold”) has a similar RGB proportionality to light concrete, but it maintains lower intensities across the board. See Figure 71.

Clay-tile roofing shingles (coral—color, not the organism) are approximately twice as bright in the red (1064 nm—NIR) and blue (1550 nm—SWIR) bands as they are in the green (532 nm—visible green). Accordingly, they are almost as readily identifiable as the light concrete. Once the clay shingles subclass is separated out, it is possible to distinguish another type of roofing material that is spectrally similar: red lava rocks and red basalt-felt shingles (orange 3). This cluster sits just below the clay shingles in RGB space, because it is slightly dimmer in all three bands. Red lava rocks and red basalt-felt composite shingles are incorporated into one class, since they are similar in both color and volcanic origin.

Three final material clusters are identified with relatively low RGB intensities. These are “darker” than all of the aforementioned building subclasses. Tan/gray roofing shingles (maroon 2—”magenta”), dark asphalt shingles (purple 3), and powerlines (orchid—”light pink”) represent the least-sampled building subclasses in the dataset.

Figure 70 provides two N-D VIS screenshots of the new building spectral subclasses in RGB space. In the right image, the dark concrete, clay shingles, and tan/gray shingles subclasses have been disabled in order to expose the smaller clusters for dark asphalt shingles and red basalt/lava rock. Figure 71 is the corresponding spectral plot with the three wavelengths on the x-axis and return intensities on the y-axis. Y-axis values are the mean RGB intensities, in arbitrary units, for each subclass. The general building (yellow) subclass is included in the plot, but would be distracting in Figure 70.

Figure 70. New Building Clusters in N-D VIS, Less the General Building Subclass.

Figure 71. Spectral Plot of Building Subclasses from Mean RGB Intensities and Average AGLs.

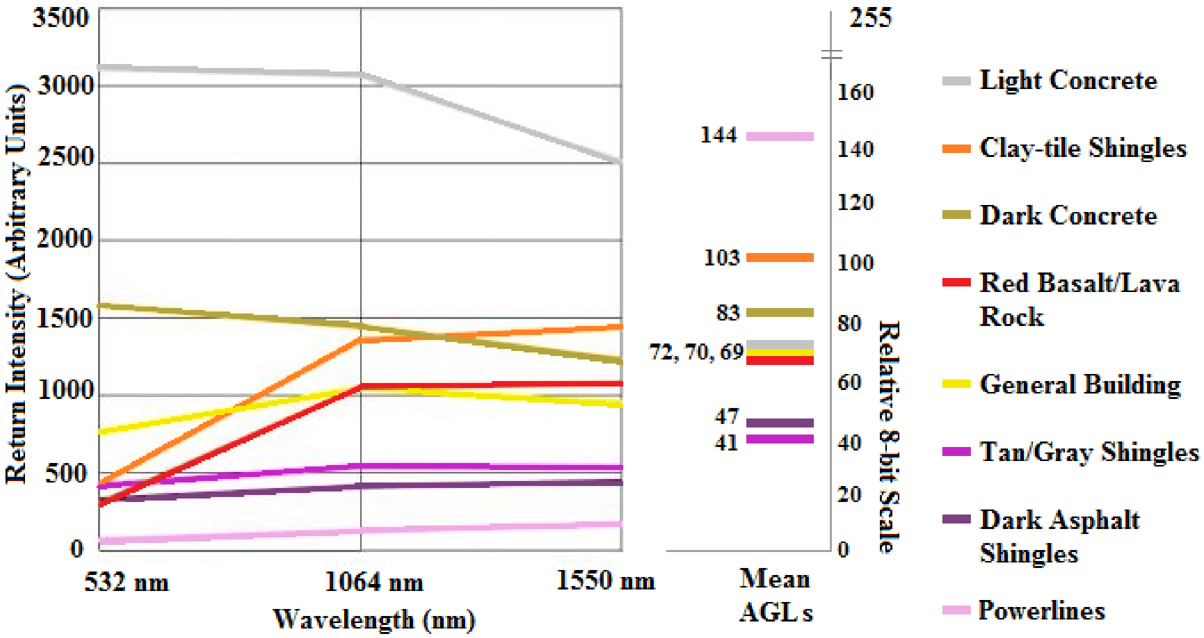

Figure 72 presents the new building subclasses in XYZ space. The primary members of the new light concrete (thistle 2) subclass are King Hall, Glasgow East, Halligan Hall, most of Watkins Hall, some of the library roof, and the plastered walls of Herrmann Hall. Darker concrete (yellow 3) occupies the rooftops of Bullard Hall, Spanagel Hall, main Glasgow Hall, and the flat section of the Naval Exchange (NEX). Clay-tile shingles (coral) top Herrmann Hall, the adjacent small houses, the peaked section of the gym roof, and the guard shacks at the two campus entrances.

Red basalt/lava rock (orange 3) roof coverings are present on Ingersoll Hall, part of the library, the flat section of the gym, and the U.S. Post Office. Tan/gray shingles (maroon 2) can be found on a structure attached to the backside of Herrmann Hall near the loading dock and in a neighborhood to the east of campus. Dark asphalt shingles (purple 3) are present on one house (#283) near the library and Root Hall and in the same neighborhood to the east.

Figure 72. Building Points Only in XYZ Space, Post-Spectral Subclassification.

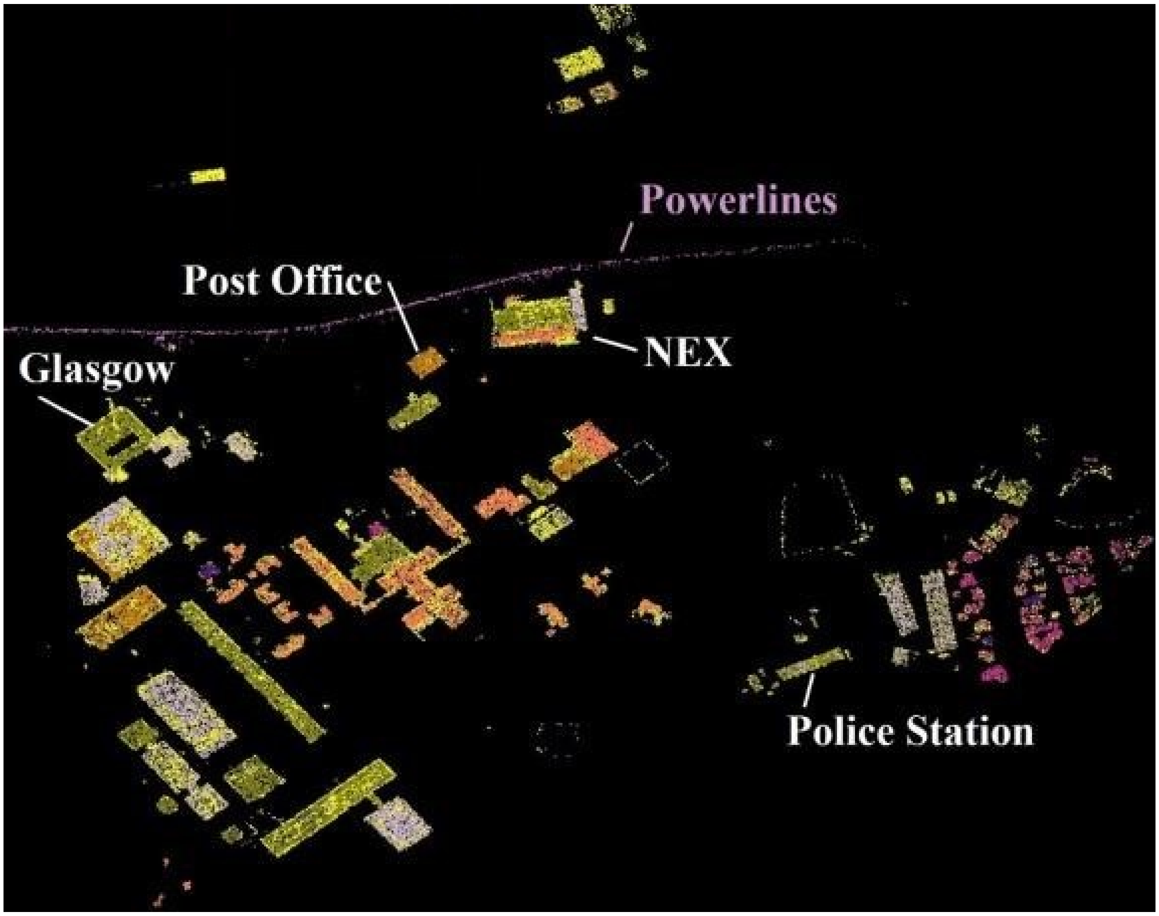

Ground truth involved accessing the upper balconies of Herrmann Hall and the rooftops of Spanagel and Ingersoll Halls with binoculars to determine the composition of the other rooftops not visible from the ground. Since the neighborhood to the east of campus is not within the primary area of concern, Google Earth is used to approximate the colors and types of roofing shingles. The points remaining in the general building (yellow) subclass appear to be mostly metal, wood, and concrete outliers that do not fall into the dark or light concrete subclasses. Metal surfaces, such as the rooftop over the NEX gas pumps, have a wide variance of intensity values and do not form distinct clusters in RGB space. This phenomenon is likewise exhibited on a grander scale by the water points, and it is why water requires subclassification using spatial attributes in addition to intensity (Figure 58). In Figure 73, the general building subclass is hidden from display. This allows for a better view of the primary material(s) on each roof. Also, Figure 73 exclusively shows the NPS campus.

Figure 73. Roofing Materials of the NPS Campus.

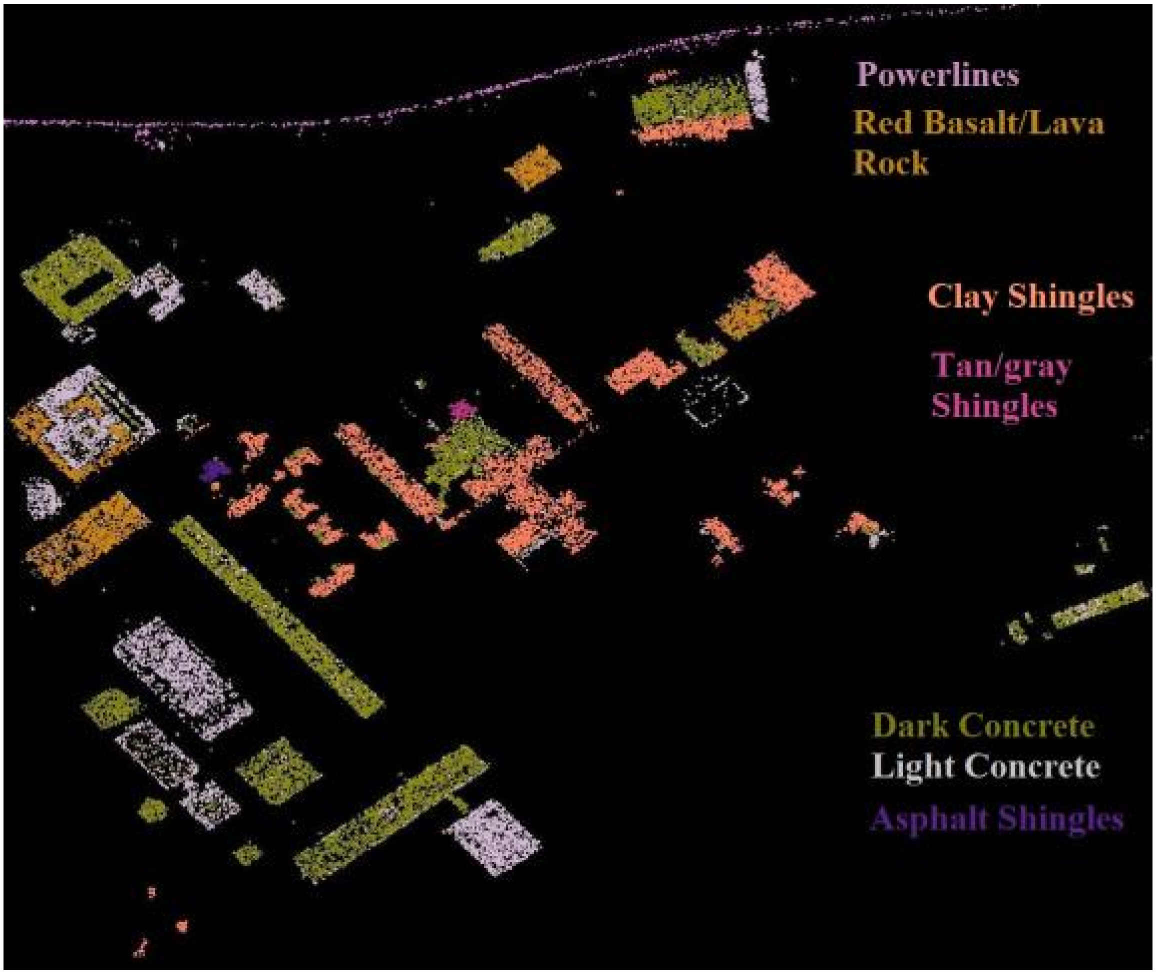

5. Summary of New Spectral Classifications

By combining spatial and spectral attributes in N-D VIS, this analysis session produces 19 pertinent classes and one discarded class of extreme spectral outliers. The 19 classes include the bulk 95% (unclassified points) and the new ground, vegetation, and building subclasses. These classes are exported from N-D VIS as regions of interest (ROIs) and are ready to be utilized as inputs for the ENVI classifiers described in Chapter V. Figure 74 is a screenshot of the newly classified 5% training subset in XYZ space. The shrubs subclass is included, but not labeled in the key. This is because the large extent of Figure 74 makes them difficult to discern from the similarly colored and more-important grass. Also, Figure 74 does not display the unclassified 95% or the extreme spectral outliers. Table 7 provides summary information to accompany Figure 74; it includes the unclassified points and the outlier class for a general comparison.

Figure 74. End of Spectral Analysis in N-D VIS—New Subclasses in XYZ Space.

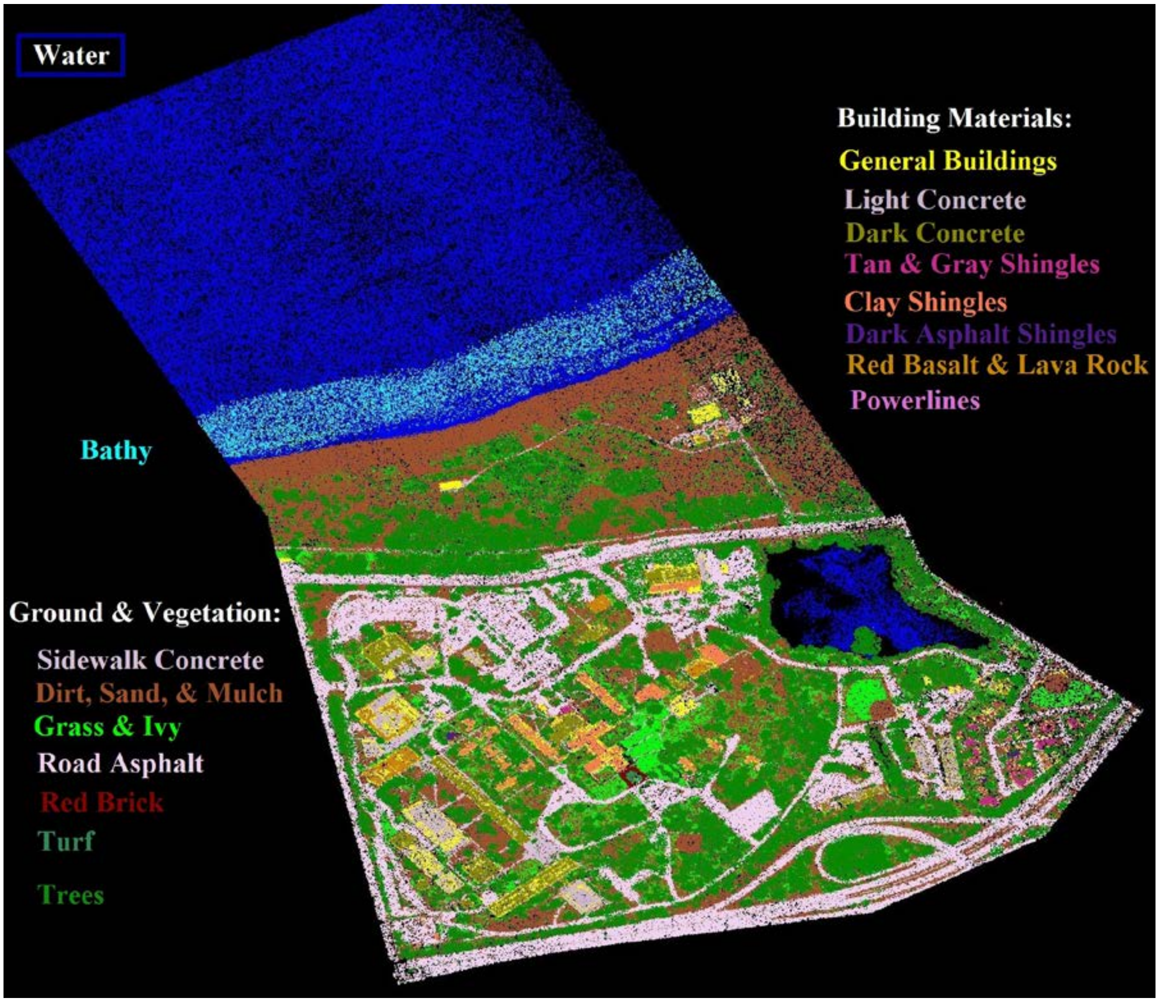

Table 7. List of Spectral Subclasses Generated Using the 5% Random Subset.

Subclass	**Assigned Color**	**Previous Class—Pre N-D VIS**	**Number of Points**
Unclassified	White	All—Randomly Sampled as described in CH III	14,338,344
Extreme Outliers	Orange 1	All	4,603
Water	Blue	Unclassified (1)	107,059
Bathymetry	Cyan	Unclassified (1)	11,750
Dirt, Mulch, & Sand*	Sienna	Ground (2)	196,044
Grass & Ivy	Green	Ground (2)	26,204
Sidewalk Concrete	Thistle	Ground (2)	31,872
Road Asphalt	Thistle 1	Ground (2)	72,356
Red Brick	Red 3	Ground (2)	298
Turf	Sea Green	Ground (2)	122
Shrubs	Green 2	Vegetation (5)	5,995
Trees	Green 3	Vegetation (5)	190,083
General Building	Yellow	Building (6)	7,025
Light Concrete	Thistle 2	Building (6)	6,835
Dark Concrete	Yellow 3	Building (6)	12,078
Powerlines	Orchid	Unclassified (1) & Building (6)	615
Clay Shingles	Coral	Building (6)	6,799
Tan & Gray Shingles	Maroon 2	Building (6)	1,313
Dark Asphalt Shingles	Purple 3	Building (6)	819
Red Basalt & Lava Rock	Orange 3	Building (6)	2,588

*Note: After the completion of this chapter, we realized that sand could be separated in RGB space from the larger dirt, mulch, and sand subclass. The coastal sand of Monterey Beach forms a spectral cluster of 14,179 points; this leaves the dirt and mulch subclass at 181,865 points. The sand subclass is not shown in Figure 74, however it will be incorporated into the classifiers and displayed in Chapter V.

V. CLASSIFICATION ANALYSIS AND RESULTS

A. GENERAL PARAMETERS AND UNSUCCESSFUL CLASSIFIERS

Before displaying the classification results, it is necessary to explain the methodologies and input parameters applicable to all of the ENVI classifiers demonstrated in this chapter. Additionally, we will briefly discuss the classifiers that fail to produce acceptable results. Section B continues with the somewhat-successful K-means unsupervised classifier, and Section C describes the more-successful Maximum Likelihood (ML) supervised classifier. Lastly, Section D illustrates limited post-processing (clean-up) applied to the ML results.

First, we consider an important question: How do the results differ if a classifier is run on just a single flight line versus the four-combined flight lines of the entire NPS campus? To answer, we always run two concurrent instances of each classifier with identical input parameters—one instance classifies only a single flight line, and the other instance classifies the entire NPS campus. We choose flight line 10 for all single flight line instances, because it offers the longest north-south run down the center of the campus. Flight lines 12 and 13 are heavily cropped and exclude Herrmann Hall, and flight line 15 is essentially identical to 10.

Second, we discover early in the classifier experiments that the wide range of intensity values exhibited by water points feeds excessive noise into the process. Water points are heavily misclassified as vegetation and, to a lesser extent, light building concrete. To circumvent this problem, we need an ENVI mask file that forces the classifiers to ignore the water and bathymetry points, both as ROIs (input classes) and as points to classify. So, we turn on the unclassified (white) class in N-D VIS and manually select all water and bathymetry points via the manner displayed in Figure 58. Then, we build a mask that will exclude the water (blue) and bathymetry (cyan) classes by choosing the “select areas off” option in the ENVI “Mask Builder” tool. These masked points will be exported as a combined, yet otherwise unaltered, class ignored by all of the upcoming classifiers.

Next, we experiment with various K-means and ML spectral input bands in addition to the height above ground (AGL) and Red-Green-Blue (RGB). GNDVI and the other vegetation indices do not contribute a noticeable improvement to the results of any classifier. Including the “number of returns” metric has no impact on K-means, but it does alter the ML output. For ML, the “number of returns” metric improves the results for some classes, primarily single-return-only classes (e.g., rooftop materials, turf, red brick, road asphalt, and sidewalk concrete). However, it significantly degrades the results for multi-return classes, such as shrubs and trees. ENVI classifiers are programmed to calculate statistics on continuous variables with expansive ranges (e.g., AGL [8-bit range] and RGB [12-bit range]), but number of returns is technically a discrete variable with a finite set of possible values: 1, 2, 3, or 4. Later, we will make use of the “number of returns” metric with Quick Terrain Modeler’s “Multivariate Filtering” tool, where we can selectively apply filtering by number of returns to only the classes that will benefit—as opposed to the classifiers which apply it indiscriminately. This is the post-processing technique discussed in Section D, the only post-processing that we perform on the data.

Lastly, the Spectral Angle Mapper (SAM) and Spectral Information Divergence (SID) supervised classifiers produce extremely poor results. Like ML, SAM and SID generate an output class for all input classes from the 5% training subset, however there is no correlation: All of the SAM/SID output classes contain points randomly dispersed throughout the scene that in no way resemble the input classes. The SAM classifier defines classes according to n-dimensional spectral angles, and three wavelengths does not appear to be enough for SAM to function properly. The SID classifier works based on n-dimensional spectral divergence, similar to SAM’s spectral angles. SID is also hindered by only three input bands. Moreover, SAM and SID have no capacity to consider the AGL or any spatial attribute; they are strictly spectral (RGB only for this data) classifiers. The point clouds classified by SAM and SID are unsalvageable and receive no further attention.

B. K-MEANS UNSUPERVISED CLASSIFICATION

Since K-means is an unsupervised classification technique, it disregards the 5% training subset. Instead, K-means classifies the data into its own algorithm-defined classes up to a user-specified maximum. This classifier begins by assuming that all class means within the data space are distributed evenly, then pixels are grouped into the class with the nearest mean via a minimum distance approach (Harris Geospatial Solutions 2017a; Tou and Gonzalez 1974). This is an iterative process that recalculates class means and regroups pixels until the algorithm reaches the user-set maximum number of iterations or the overall change in pixel reclassification reaches a minimum limit (default setting is < 5%) (Harris Geospatial Solutions 2017a).

We include K-means in this work primarily to show the limits of autonomous spectral classification—similar to how we described the limits of autonomous spatial-only classification in Chapter III. Although there exists no quantitative method to compare the unsupervised results of K-means to the supervised results of ML, it is clear that ML is the better classifier for our spectral LiDAR dataset. This justifies the time and effort spent on the spectral training work in Chapter IV. Still, the K-means classifier performs better than expected for both a single flight line and the combined flight lines of the entire campus. The following represent our best K-means results, with these parameters: maximum class limit of nine (arbitrarily chosen as a balance between LASclassify's four spatial and ML's 15+ spectral output classes); input bands 11 (AGL), 14 (Red), 15 (Green), and 16 (Blue); maximum number of iterations 20 (no improvement beyond this value); and the default change threshold percentage of < 5%.

Table 8 is the point classification breakdown of K-means results for the single flight line and entire campus instances. It provides the class names and color-codes applicable to all upcoming K-means figures. The two instances of K-means produce the same 10 classes: the nine defined by K-means and the masked water/bathymetry class. However, the individual point classifications differ between the two K-means point clouds, especially at the flight line edges.

Table 8. K-means Point Classification Breakdown and Approximate Percentages.

K-means Class (Number and Color)	Name* and Description	Single Flight Line	Entire Campus
1—Dark Green	Trees: canopy bottoms and other dark vegetation	1,955,053 *(33.3%)*	4,975,598 *(33.1%)*
2—Dark Green	Trees: inner canopies	133,748 *(2.3%)*	312,953 *(2.1%)*
3—Dark Gray	Road Asphalt	561,741 *(9.6%)*	1,478,834 *(9.8%)*
4—Light Gray	Semi-dark Concrete and concrete/asphalt mix	530,138 *(9%)*	1,368,249 *(9.1%)*
5—Middle Green	Shrubs and many tree tops	397,829 *(6.7%)*	1,035,129 *(6.9%)*
6—Gold/Gray	Darker Concrete: building and ground	216,092 *(3.7%)*	495,133 *(3.3%)*
7—Brown	Dirt, Mulch, Sand, Clay	655,211 *(11.2%)*	1,754,284 *(11.7%)*
8—Bright Green	Grass and ivy	442,472 *(7.5%)*	1,084,551 *(7.2%)*
9—Off White	Light Concrete	26,916 *(0.45%)*	78,452 *(0.5%)*
0—Blue	Water and Bathymetry (masked points)	950,638 *(16%)*	2,439,619 *(16.2%)*
Total Point Count		5,869,838	15,022,802

* Capitalized words in the name and description column are the assigned class names.

1. K-means Single Flight Line—Central Campus

Figure 75 is a wide-area screenshot of the K-means classifier results for the single flight line instance. It shows all of the classes in Table 8 other than the water/bathymetry class. Again, Figure 75 is the central campus (FL 10 only). Several areas are labelled to provide a sense of orientation.

Figure 75. K-means Single Flight Line—All Classes but Water.

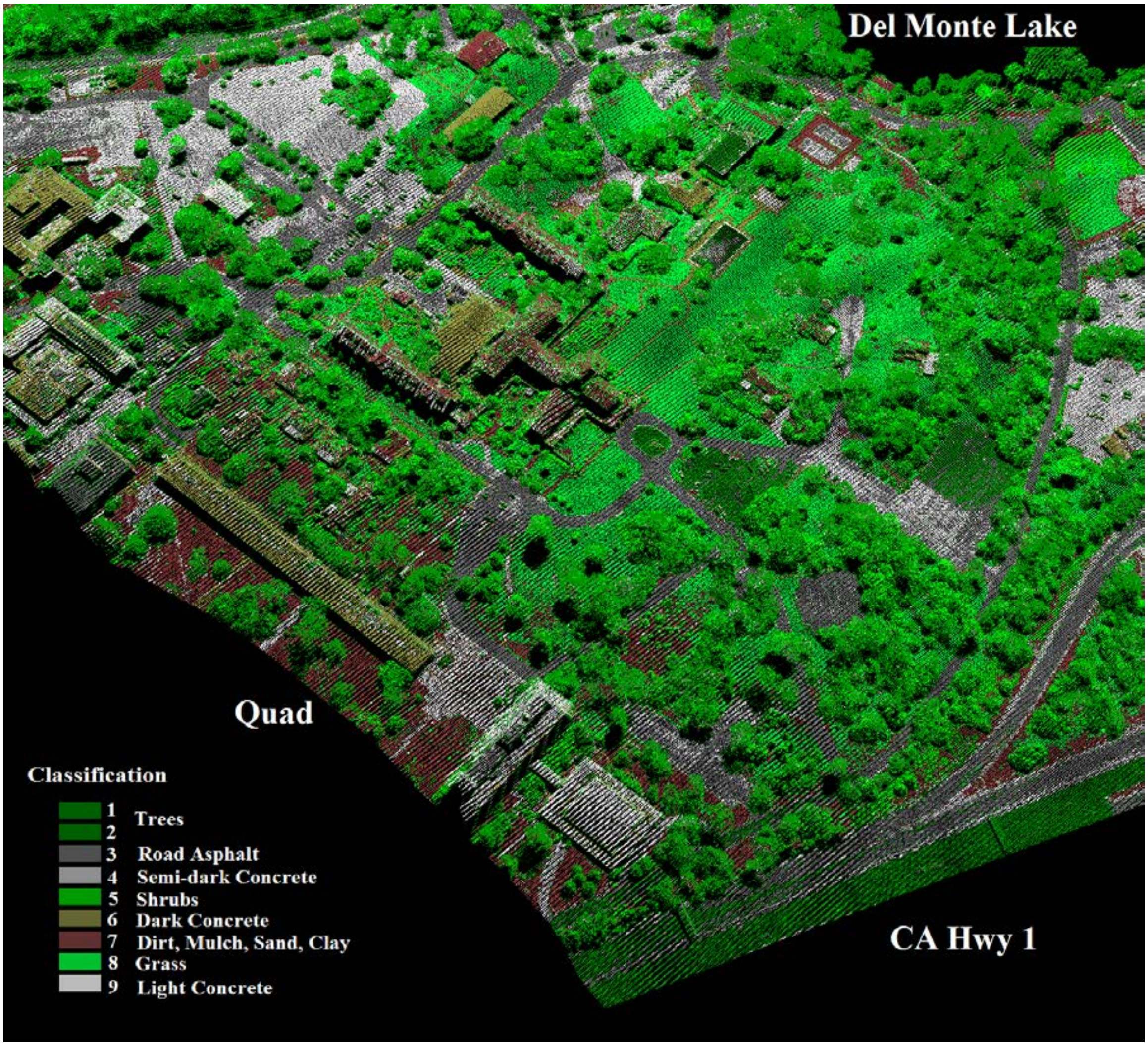

From Figure 75, it is obvious that K-means demonstrates more weaknesses than strengths when classifying spectral LiDAR data. Remember, this unsupervised classifier does not use the 5% training classes from N-D VIS. Figure 76 shows the individual K-means classes that we loosely place into the strengths category for the single flight line point cloud. Quick Terrain Modeler's "QTA Discrete Attribute Analysis" tool allows one to view or hide points by classification, AGL, or any other individual attribute from Table 6.

Figure 76. K-means Single Flight Line Strengths.

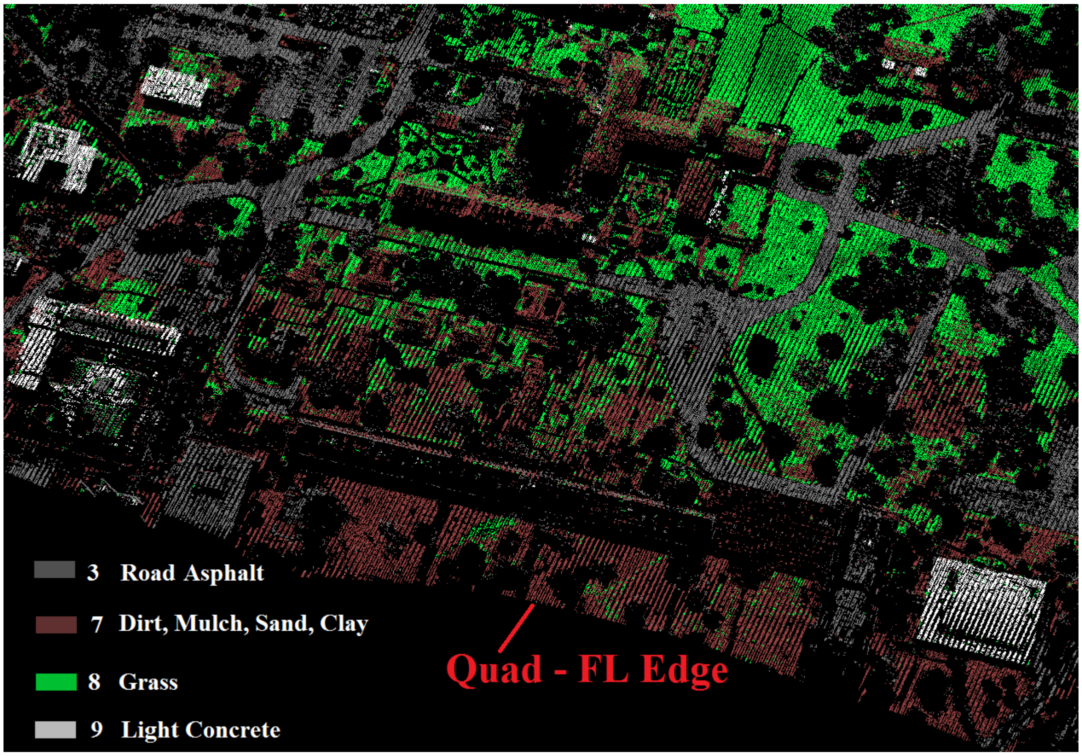

The correct classification of ground points along the flight line edge represents the primary benefit of running the K-means classifier on a single flight line vice combined flight lines. The majority of the NPS Quad in Figure 76 is correctly classified into the dirt, mulch, sand, and clay class. Additionally, K-means does a decent job distinguishing the interfaces among the road asphalt, grass, and dirt/mulch/sand/clay classes: notice the sharp definition of the roads around Herrmann Hall and the Arizona Cactus Garden’s clear borders between dirt/sand and grass. Lastly, the light building concrete class is defined well by the K-means classifier, especially on the rooftop of King Hall. This is not considered the primary strength for single flight line K-means, because the combined flight line K-means and the ML classifiers also define the light building concrete class with exceptional distinction.

Nevertheless, the K-means classification process generates serious problems, as seen in Figures 77 and 78. In Figure 77, the turf around the NPS flagpole and the adjacent asphalt parking lot are misclassified as trees. Turf and areas of darker asphalt have low spectral intensities for all three wavelengths, similar to tall and dense vegetation which also experiences weak signal returns. In contrast, tree tops are often misclassified as shrubs due to the brighter returns from that part of the canopy. Next, the rooftops with clay-tile shingles (e.g., Herrmann Hall) demonstrate gross misclassifications. Despite having AGL as an input metric, the K-means classifier cannot separate dirt, mulch, sand, and clay on the ground from the clay shingles at much greater heights. Also, a substantial amount of points on the clay-tile roofs are misclassified as semi-dark concrete and some are even included in the tree classes. Furthermore, K-means sometimes has difficulty distinguishing between sand and concrete, especially for large areas of sand (e.g., Monterey Beach—not shown).

Figure 77. K-means Single Flight Line Weaknesses.

Figure 78 shows another K-means AGL-related discrepancy, similar to the aforementioned problem of ground dirt, mulch, sand, and clay versus the clay-tile shingles. The darker concrete (gold) points on the rooftop of Root Hall are grouped into the same class as some of the adjacent ground concrete. In Figure 78, the trees (classes 1 and 2) and shrubs (class 7) are hidden, creating the apparent black holes in the image. Also, the entire rooftop of Ingersoll Hall is classified as road asphalt, however it is mainly comprised of red lava rocks—a material class unidentified by K-means.

Figure 78. K-means Single Flight Line Weaknesses Continued.

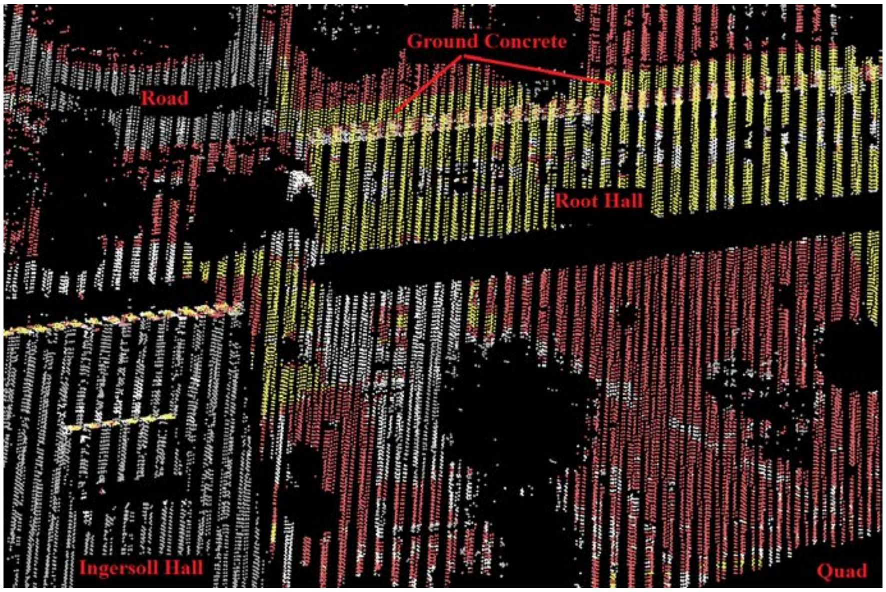

2. K-means Combined Flight Lines—Entire Campus

Running the K-means classifier on the entire NPS point cloud (four-combined flight lines) generates no significant improvements over the single flight line instance. There is slightly less confusion between sand and concrete in the combined point cloud. Moreover, the combined flight lines K-means demonstrates all of the serious weaknesses of the single flight line instance, plus an additional issue in the areas of flight line overlap. The NPS Quad in Figure 79 is comprised of points from three flight lines (10, 12, and 15), in contrast to the single flight line portion of the Quad in Figure 76. Due to variations in aircraft altitude, speed, and other factors during the flight campaign, the points of different flight lines have a slight vertical offset (3-5 cm). This becomes a problem in the areas where two or more flight lines overlap. K-means interprets many of these offset points as grass, as seen in the majority of the Quad in Figure 79.

Figure 79. K-means Combined Flight Lines—Additional Weakness.

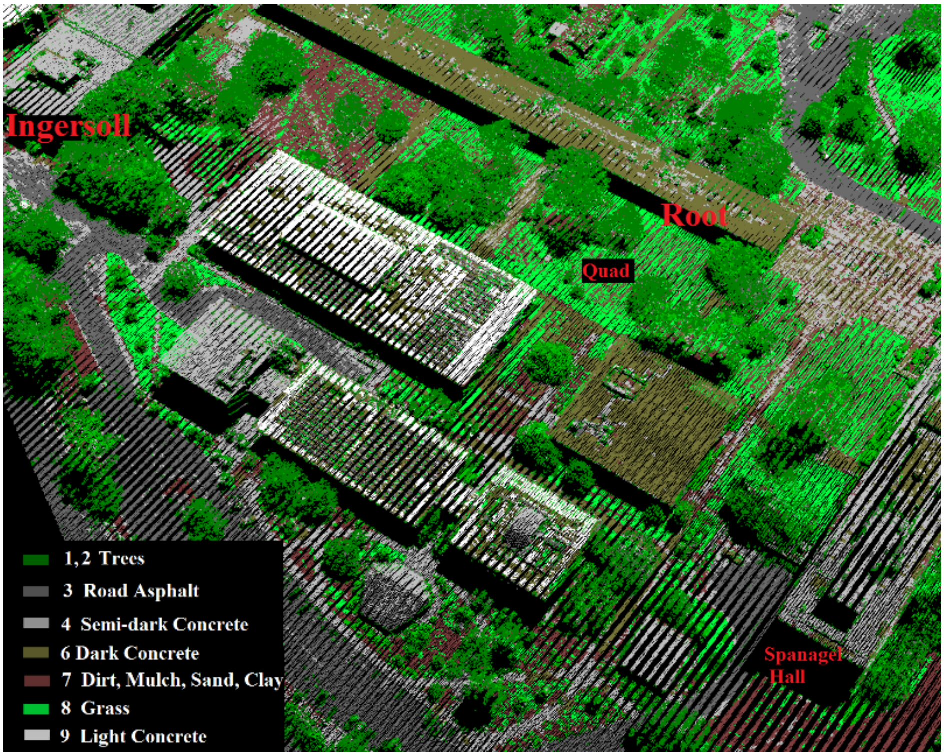

Overall, K-means performs better than initially expected. Yet, it is insufficient for both single flight line and combined flight line classification. Even with the AGL metric, the K-means classifier fails to separate similar ground and building materials: clay-tile vs. dirt, sand vs. concrete, and sidewalk vs. building concretes. The autonomous K-means classifier also struggles with spectrally dark materials, including trees, turf, and asphalt. Now, we will demonstrate how the spectral classification process is improved by a supervised classifier that operates based on input classes from the 5% training subset.

C. MAXIMUM LIKELIHOOD SUPERVISED CLASSIFICATION

ML is the best classification method for extrapolating the N-D VIS spectral processing approach, demonstrated in Chapter IV, to the remaining unclassified points. First, the ML classifier creates a unique rule image for each of the selected input classes. Every pixel (laser data point) is represented in each rule image and assigned class-probability values based on normally distributed class statistics (Harris Geospatial Solutions 2017b). The ML algorithm then builds one classification image from the separate rule images. In the classification image, every laser data point is assigned a classification that corresponds to the rule image with the highest probability value for that point (2017). Afterward, the rule images are discarded unless the user chooses to save them. According to Harris, ENVI applies the discriminate ML formula described in Figure 80 (Harris Geospatial Solutions 2017b).

Figure 80. ML Probability Equation. Adapted from Richards (2013, 251).

$$g_i(x) = 1\text{n}\, p(\omega_i) - {}^{1}\!/_{2}\, 1\text{n}\, |\Sigma_i| - {}^{1}\!/_{2}(x - m_i)^T \Sigma_i^{-1} (x - m_i)$$

$g_i(x)$ = probability that data point ‘x’ belongs to class ‘i’

i = class

x = n-dimensional data (where n is the number of bands)

$p(\omega_i)$ = probability that class ω_i occurs in the image and is assumed the same for all classes

$|\Sigma_i|$ = determinant of the covariance matrix of the data in class ω_i

Σ_i^{-1} = inverse of the data covariance matrix

m_i = mean vector

Figure 81 is the probability graph for the concrete-class rule image. It somewhat resembles a fat-tailed log-normal distribution, albeit with heavy skew. ENVI applies a logarithmic scale to the probabilities on the x-axis. The probability of a point being concrete is zero on the right edge of the graph and increases toward one moving to the left. The green and red lines in Figure 81 correspond to the colored areas in Figure 82. This shows the points most likely to be classified as concrete when the classification image is constructed from the rule images. The points that remain colored white in Figure 82 are less likely to be classified as concrete.

Figure 81. ML Probability Graph for Concrete-Class Rule Image.

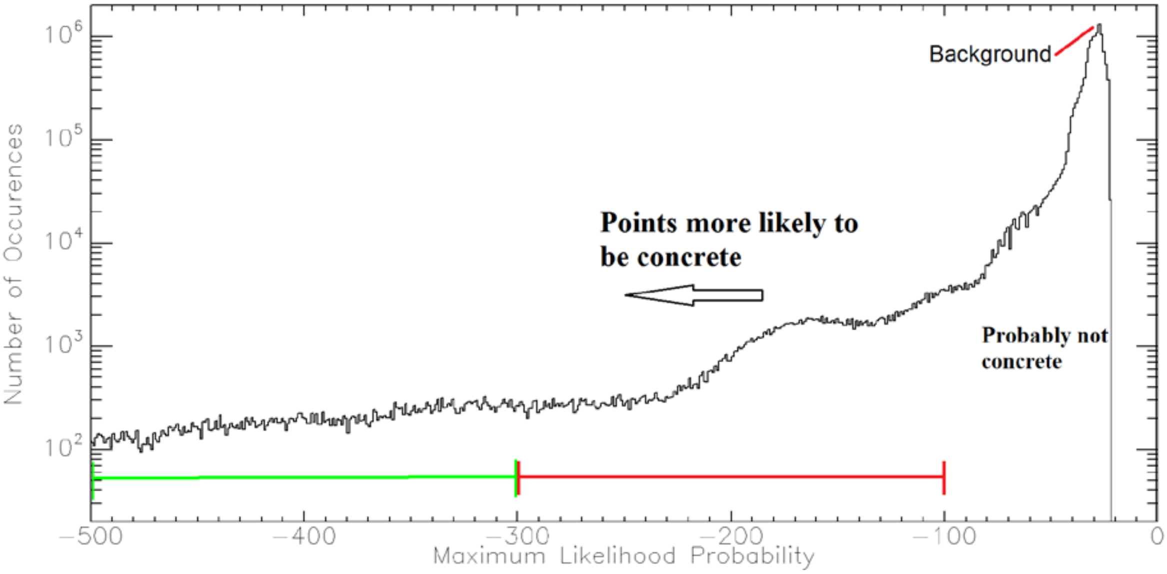

Figure 82. ML Points Colored According to Rule Graph for Concrete Class.

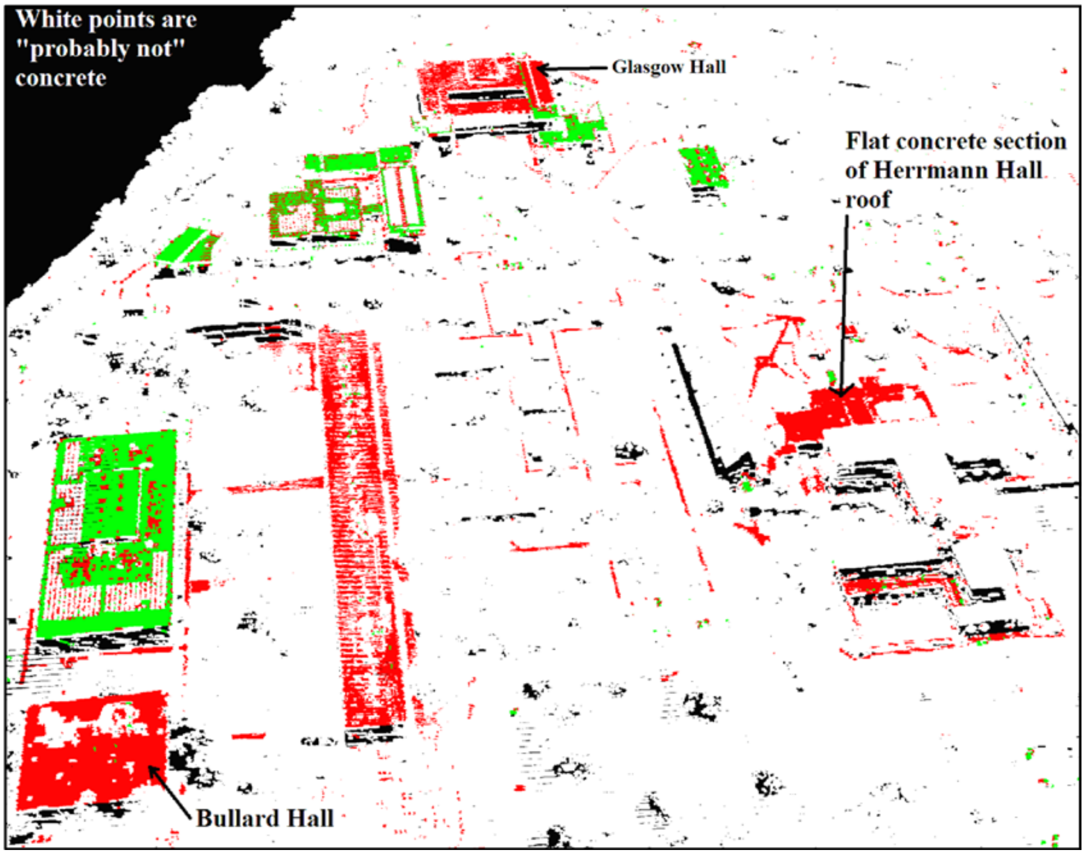

The ML probability threshold is an input parameter that can be set either universally for all classes or individually for each. While it does not factor into the ML equation, the probability threshold will prevent a point from being classified into the most-likely class if that point does not meet the minimum probability requirement. For example, an arbitrary point has the following rule image probabilities: 0.1 for trees, 0.2 for asphalt, 0.5 for grass, and 0.1 for turf. Normally, this point will get classified as grass in the classification image. However, if the probability threshold for the grass class is set to 0.75, then this point does not meet the threshold and remains unclassified—it is not reviewed again for inclusion into any other class, even the next most likely.

We experiment with different probability thresholds to see if this factor can improve the results. We expect that selecting "no probability threshold" across-the-board will result in a point cloud with many errors of commission (e.g., numerous points will be classified as, say, concrete that are not actually concrete). Indeed, this is true. So, will making the classifier more discriminate, by increasing the probability thresholds, result in fewer errors of commission and more distinctly defined classes? The answer: yes, there will be fewer errors of commission, however the cost is an increase in errors of omission (e.g., some of the points that truly are concrete will remain unclassified). Figure 83 is a comparison of ML results for the clay-tile shingles class at no probability threshold (left) and 50% probability threshold (right).

Figure 83. Clay-tile Shingles Class Probability Thresholds—Errors of Commission vs. Omission.

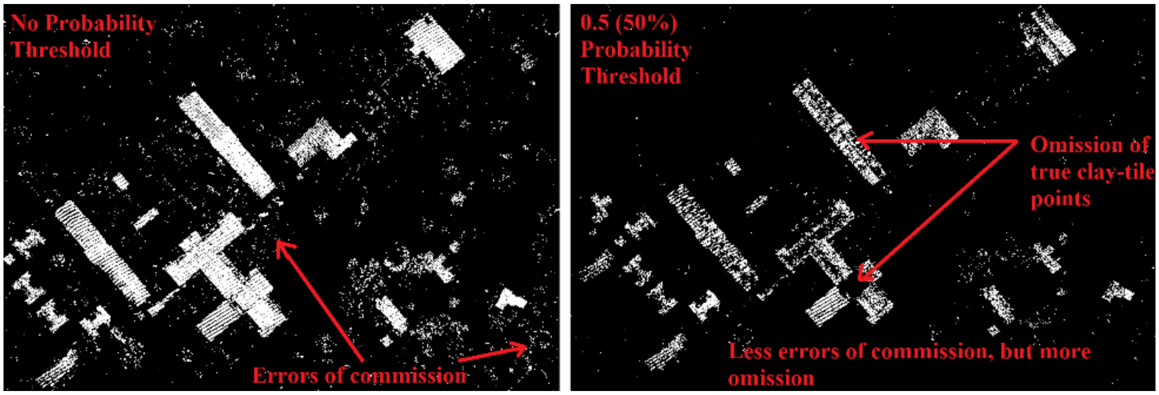

Table 9 is the point classification breakdown for the four runs of the ML classifier: zero and 0.5 probability thresholds for both a single flight line (FL 10) and the four-combined flight lines of the entire campus. Approximate percentages are provided for a comparison. A 0.5 probability threshold results in 34% of the point cloud remaining unclassified—millions of points! Instead of attempting to find a threshold balance between zero and 0.5, we proceed with no probability threshold and apply the post-processing technique in Section D. Post-processing by multivariate filtering offers the advantage of removing errors of commission without introducing errors of omission, unlike what happens by simply increasing the probability threshold of the ML classifier.

Table 9. ML Point Breakdown by Class and Probability Threshold.

	ML Single Flight Line		**ML Combined Flight Lines**	
Class	No Threshold	50% Threshold	No Threshold	50% Threshold
0—Unclassified	—	1,966,674 ***(34%)***	—	5,095,287 ***(34%)***
1—Grass	347,778 *(6%)*	204,170 *(3.4%)*	881,438 *(5.9%)*	491,714 *(3.3%)*
2—Turf	70,032 *(1.2%)*	22,359 *(0.4%)*	177,813 *(1.2%)*	57,020 *(0.38%)*
3—Clay-tile Shingles	104,500 *(1.8%)*	31,788 *(0.5%)*	254,587 *(1.7%)*	72,451 *(0.48%)*
4—Dirt and Mulch	999,086 *(17%)*	734,721 *(12.4%)*	2,594,605 *(17.3%)*	1,880,332 *(12.5%)*
5—Sidewalk Concrete	160,455 *(2.7%)*	95,650 *(1.6%)*	438,732 *(2.9%)*	255,037 *(1.7%)*
6—Red Brick	247,467 *(4.2%)*	138,904 *(2.4%)*	620,056 *(4.1%)*	347,399 *(2.3%)*
7—Shrubs	488,686 *(8.3%)*	278,069 *(4.6%)*	1,258,132 *(8%)*	737,906 (4.9%)
8—Trees	1,263,462 *(21.5%)*	756,061 *(12.9%)*	3,178,190 *(21.2%)*	1,900,236 *(12.6%)*
9—Dark Bldg Concrete	132,314 *(2.3%)*	70,869 *(1.1%)*	332,166 *(2.2%)*	165,446 *(1.1%)*
10—Tan/Gray Shingles	42,053 *(0.7%)*	6,042 *(0.1%)*	104,734 *(0.7%)*	17,830 *(0.1%)*
11—Asphalt Shingles	81,462 *(1.4%)*	9,570 *(0.2%)*	191,858 *(1.3%)*	17,209 *(0.1%)*
12—Red Basalt/Lava Rock	60,666 *(1%)*	16,725 *(0.3%)*	161,088 *(1%)*	49,104 *(0.3%)*
13—Sand	208,664 *(3.6%)*	138,864 *(2.4%)*	544,199 *(3.6%)*	353,910 *(2.4%)*
14—Road Asphalt	640,412 *(11%)*	404,635 *(6.9%)*	1,622,459 *(10.7%)*	1,026,055 *(6.8%)*
15—Light Bldg Concrete	72,163 *(1.2%)*	44,099 *(0.8%)*	223,126 *(1.5%)*	116,247 *(0.8%)*
16—Water/Bathy	950,638 *(16%)*	950,638 *(16%)*	2,439,619 *(16.2%)*	2,439,619 *(16.2%)*
Total Point Count	5,869,838		15,022,802	

1. ML Single Flight Line—Central Campus

After a few practice runs of the ML classifier, it became apparent that some of the training classes in Table 7 must be excluded from the process. The general building class is too spectrally diverse; it causes an excessive misclassification of vegetation points as general building. Powerlines have extremely low intensities in all three wavelengths (see Figure 71). Consequently, there is excessive confusion between true powerlines and the similarly dark inner tree canopies. Henceforth, the pertinent ML input/output classes are grass (1), turf (2), clay-tile shingles (3), dirt and mulch (4), sidewalk concrete (5), red brick (6), shrubs (7), trees (8), dark building concrete (9), tan/gray shingles (10), asphalt shingles (11), red basalt/lava rock (12), sand (13), road asphalt (14), and light building concrete (15). Again, water and bathymetry points (16) are carried over to the classified point cloud via masking. The following bands are selected as input metrics for the ML classifier: AGL (Band 11), Red (Band 14), Green (Band 15), and Blue (Band 16). Classification results are not noticeably improved by including the vegetation indices: GNDVI (Band 18), GDVI (Band 19), and GRVI (Band 20).

Figure 84 shows the results of the ML classifier for a region near Herrmann Hall. This is the single flight line instance (FL 10), and the figure key includes only the classes that exist in the chosen area. The advantages of ML over K-means are readily apparent: The majority of rooftop points on Herrmann Hall are correctly classified as clay-tile shingles, not as dirt/mulch or concrete. There exists minor confusion between clay-tile shingles and trees—some points on the clay-tiled roof are misclassified as trees, and some points in the nearby tree canopies are misclassified as clay-tile shingles.

Similar to K-means, ML does well in distinguishing the interfaces among dirt/mulch, sidewalk concrete and road asphalt, grass, red brick, and turf. Nevertheless, the red brick and turf classes demonstrate minor confusion. In Figure 84, small sections of the asphalt parking lot in front of Herrmann Hall are misclassified as turf. Additionally, it appears that some sections of sidewalk concrete and the majority of road paint (white-, red-, and yellow-painted lines) are confused with red brick. We were unable to separate road paints from the road asphalt in N-D VIS (Chapter IV). While it is reasonable to assume that road paint is spectrally closer to red brick than to dark asphalt, the process is complicated by the narrow margin of spectral separation between these two classes (Refer to red brick and asphalt in the ground materials spectral plot—Figure 65). Therefore, we attribute this problem to the analysist's inability to distinguish a road paint training class, rather than to the ML classifier. Lastly, many of the parked cars (also undefined in the training subset) are misclassified as shrubs—the reason is unknown, but cars are within the same AGL range as shrubs (0-17), far below the mean AGL of trees (127).

Figure 84. Screenshot of Single Flight Line ML Results Near Herrmann Hall.

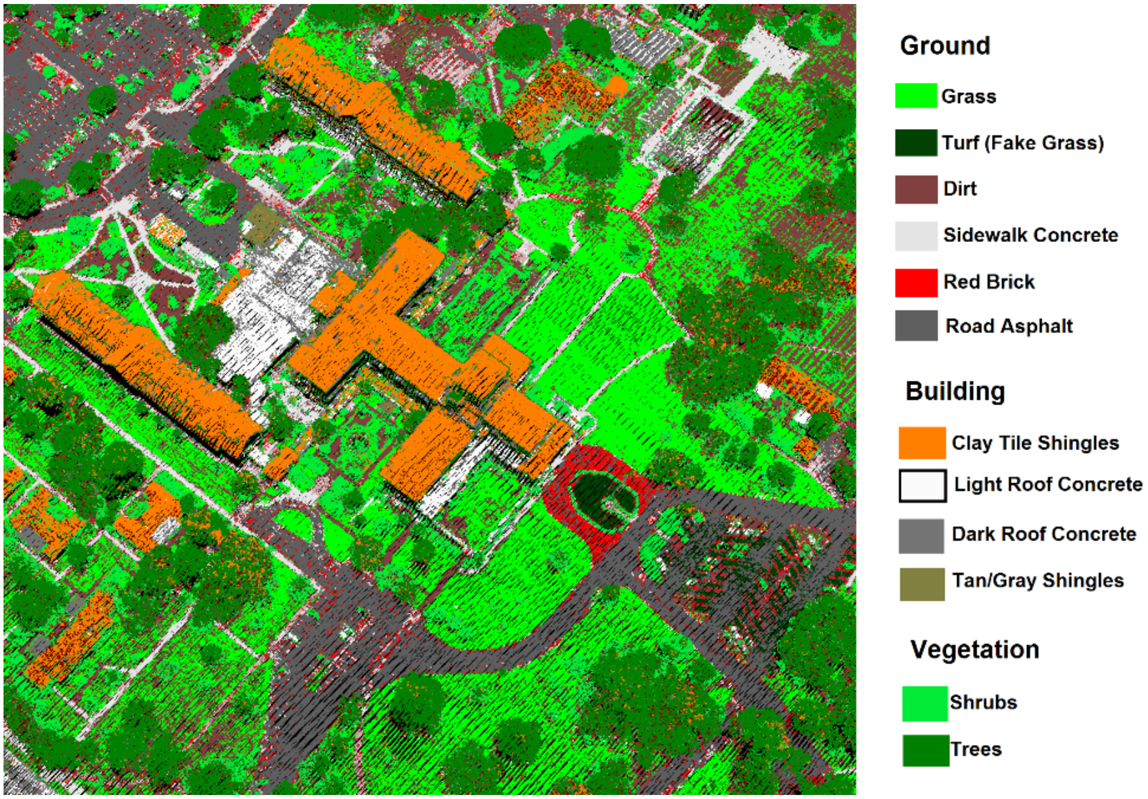

2. ML Combined Flight Lines—Entire Campus

The input classes and spectral bands (AGL and RGB) for the combined flight lines instance of ML are identical to those of the single flight line instance. The strengths and weaknesses described previously for the single flight line point cloud are reproduced in the combined flight lines point cloud. Unlike K-means, ML does not breakdown in the areas of flight line overlap. Notice the Quad in Figure 85; the ground points are correctly classified as dirt/mulch, not as the grass seen in Figure 79. ML keeps the points classified as trees in a single class, as opposed to the three K-means classes that contain various parts of the canopies (see Table 8). Still, some should-be tree points are misclassified as clay-tile shingles or red basalt/lava rock. Also, the beach sand directly touching the ocean is often misclassified as red brick or asphalt—wet sand is spectrally darker than dry sand. Similarly, the concrete of Spanagel Hall is darker in color than many of the other buildings, exhibiting a higher degree of misclassification as trees.

Figure 85. Raw ML Results for the Entire NPS Campus—
Four Combined Flight Lines.

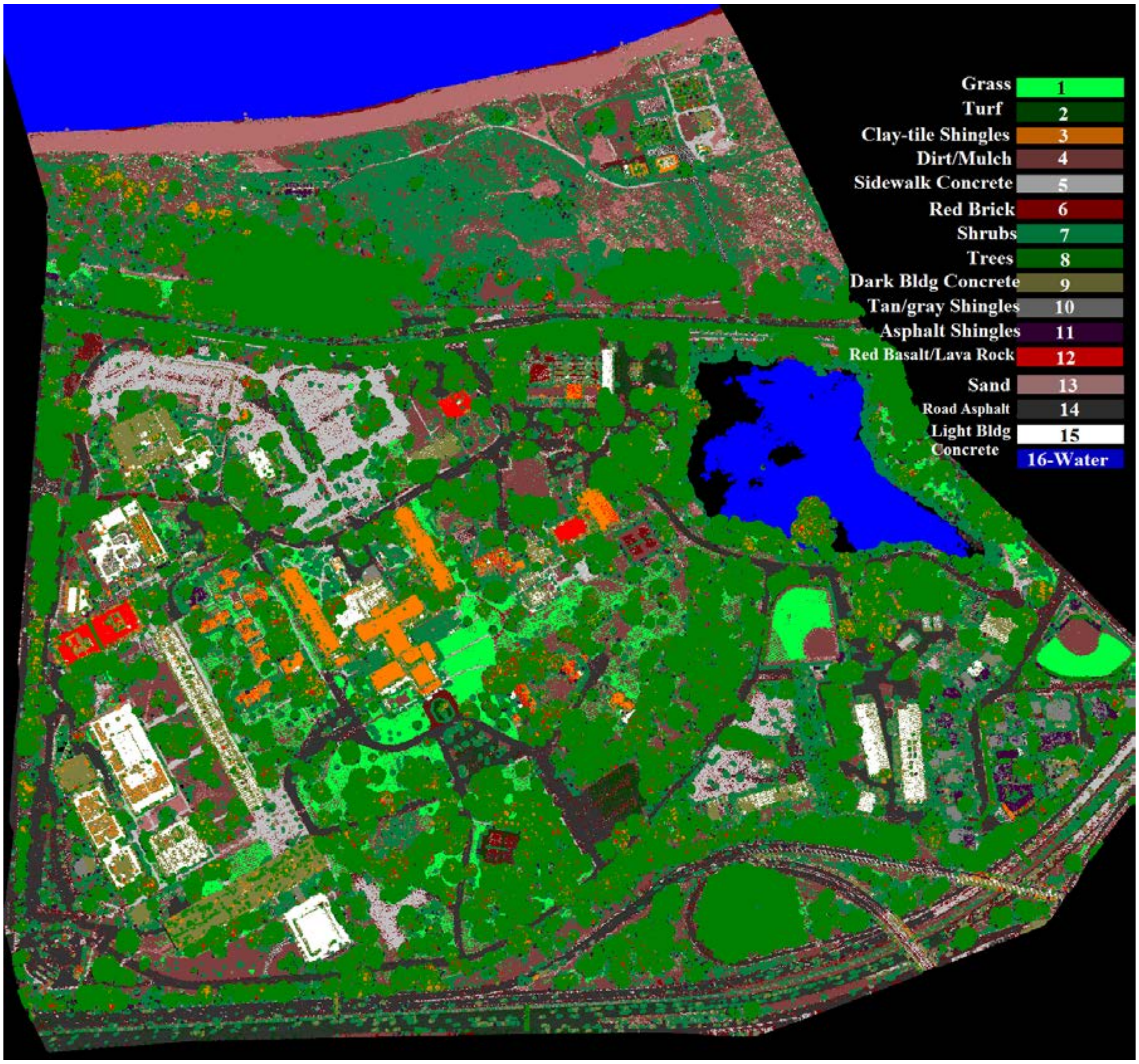

Overall, the ML classifier performs significantly better than the K-means classifier. ML successfully uses the AGL metric to distinguish between ground and roofing concretes and between dirt/mulch and clay-tile shingles. By comparison, the K-means classifier seems to ignore the AGL input metric, frequently mixing similar-composition ground and building points into the same output classes. Section D will apply post-processing to the point cloud in Figure 85; compare this figure to the refined Figure 91. Look specifically at the trees, the roofs of Herrmann and Spanagel Halls, the library, and the NEX.

Table 10 is the confusion matrix for the entire campus point cloud, classified by ML with no probability threshold. It compares the points in the 5% training subset before and after classification. Each class' greatest misclassification (confusion) is in red text. The bold-type along the diagonal highlights individual class accuracies—i.e., points mapped from a particular training class in Table 7 to the correct ML output class in Table 9. Bold-type class names have an accuracy of 70% or better.

Table 11 provides a quick summary for the confusion matrix in Table 10. Again, these results are only for the ML combined flight lines instance with no probability threshold. Classes are listed by descending order of accuracy in Table 11. Potential reasons are given for each class' most frequent misclassification(s). Overall classification accuracy is 75%, with 10 of the 14 classes demonstrating individual accuracies above 70%. The grass and turf classes outperform the others with accuracies of 99.9% and 95%, respectively. The worst performer is sidewalk concrete at 46% due to a high degree of confusion with similar ground types: sand, older faded asphalt roads, and roads paved with a lighter-color asphalt/concrete mixture (i.e., not fresh or dark black asphalt). Lastly, approximately half of the classes fall into the range of moderate success: 75–89%.

THIS PAGE INTENTIONALLY LEFT BLANK

Table 10. Confusion Matrix—Raw ML Results vs. the 5% Training Subset.

	Grass	Turf	Clay-tile	Dirt/ Mulch	Sidewalk Concrete	Red Brick	Shrubs	Trees	Dark Bldg Concrete	Tan/gray Shingles	Asphalt Shingles	Red Basalt Lava Rock	Sand	Road Asphalt	Light Bldg Concrete
Grass (26,204)	**26,181 (99.9%)**	0	0	23	0	0	0	0	0	0	0	0	0	0	0
Turf (122)	1	**116 (95%)**	0	0	0	1	0	0	0	0	0	0	0	4	0
Clay-tile Shingles (6,799)	3	0	**5,202 (77%)**	346	1	13	282	48	36	130	0	734	0	2	2
Dirt/Mulch (181,865)	16,293	4,262	0	**120,466 (66%)**	4,417	17,258	0	0	1	0	0	0	6,504	12,664	0
Sidewalk Concrete (31,872)	56	14	0	1,443	**14,657 (46%)**	3,770	0	0	0	0	0	0	7,300	4,632	0
Red Brick (298)	2	0	0	1	9	**204 (68%)**	0	0	0	0	0	0	0	82	0
Shrubs (5,995)	18	3	106	36	0	28	**5,108 (85%)**	301	50	58	178	94	0	7	8
Trees (190,083)	0	0	2,902	1	0	0	21,551	**151,666 (80%)**	1,283	1,729	6,978	3,950	0	0	23
Dark Bldg Concrete (12,078)	2	6	212	347	248	841	177	25	**7,521 (62%)**	453	10	27	56	150	2,003
Tan/gray Shingles (1,313)	0	0	9	0	0	0	15	0	8	**1,098 (84%)**	181	2	0	0	0
Asphalt Shingles (819)	0	0	0	0	0	0	16	3	1	32	**767 (94%)**	0	0	0	0
Red Basalt Lava Rock (2,588)	0	0	114	470	0	3	29	15	0	22	0	**1,935 (75%)**	0	0	0
Sand (14,179)	0	0	0	228	496	716	0	0	0	0	0	0	**12,441 (88%)**	298	0
Road Asphalt (72,356)	0	4,066	0	526	915	5,844	0	0	0	0	0	0	130	**60,875 (84%)**	0
Light Bldg Concrete (6,835)	2	0	1	5	37	0	0	0	724	0	0	0	0	0	**6,066 (89%)**
Total Accuracy		414,303 of 553,406 points			**75%**										

THIS PAGE INTENTIONALLY LEFT BLANK

Table 11. Accuracy Summary for Raw ML Confusion Matrix.

Class Name (#)	Accuracy (%)	Primary Misclassification	Suspected Reasons for Confusion
Grass (1)	99.9	Dirt/Mulch	These two classes naturally exist in extremely close proximity. (Possibly some subpixel mixing).
Turf (2)	95	Road Asphalt	Dark in all spectral bands; both are ground materials (AGL = 0).
Asphalt Shingles (11)	94	Tan/gray Shingles	Gray and black asphalt shingles are often interspersed on the same roof.
Light Building Concrete (15)	89	Dark Building Concrete	There are several middle shades of concrete on various roofs that are not separated in N-D VIS.
Sand (13)	88	Red Brick, Sidewalk Concrete	There are many areas with a thin layer of sand over a concrete path (especially near the beach). Some areas of wet sand are spectrally darker, resembling red brick.
Shrubs (7)	85	Trees	There is greater confusion for vegetation points around the cutoff AGL between shrubs and trees. (AGL = ~16).
Road Asphalt (14)	84	Red Brick, Turf	All are spectrally dark. Road paint left unseparated from the asphalt in N-D VIS—gets placed into red brick class.
Tan/Gray Shingles (10)	84	Asphalt Shingles	Same reason as asphalt shingles (above).
Trees (8)	80	Shrubs, Asphalt Shingles	Spectrally dark and many tree points are at similar AGLs to the asphalt rooftops.
Clay-tile Shingles (3)	77	Red Basalt/Lava Rock	Similar in color; no visible-red laser to help distinguish.
Red Basalt Lava Rock (12)	75	Dirt/Mulch, Clay-tile Shingles	Same as previous reason for confusion with clay shingles. Confusion with dirt/mulch is due to a sub-area of corrupt AGLs (described later).
Red Brick (6)	68	Road Asphalt	No visible-red laser; both are spectrally dark. Almost all the road paint within the asphalt class is classified as red brick.
Dirt/Mulch (4)	66	All other ground classes, especially Red Brick	Large and disperse class in N-D VIS
Dark Building Concrete (9)	62	Light Building Concrete, Red Brick	Middle shades of concrete are not distinguishable in N-D VIS, getting lumped into the dark concrete class. Unsure on the confusion with red brick.
Sidewalk Concrete (5)	46	Sand, Road Asphalt	Concrete is made from sand, and all three classes have AGL = 0 for all points. Many of the campus roads are more of a lighter concrete/asphalt mixture.

D. POST-PROCESSING: REFINEMENT BY MULTIVARIATE FILTERING

Quick Terrain Modeler's "Multivariate Filtering" tool applies simple logical operators to filter points. An example is illustrated in Figure 86 for the sidewalk concrete class, filtered by number of returns. Most areas of true sidewalk concrete have only one return, whereas the majority of sidewalk concrete points with more than one return are actually dirt or sand under vegetation (red points in Figure 86). Of course, this method will incorrectly filter some true-class points, however the tradeoff is a substantial improvement over the raw ML results without the introduction of a significant amount of errors of omission. In Figure 86, the 23,250 filtered points are colored red, but this tool also allows the user to hide, cut, or reclassify the selected points.

Figure 86. Illustration of the Multivariate Filtering Process for Sidewalk Concrete.

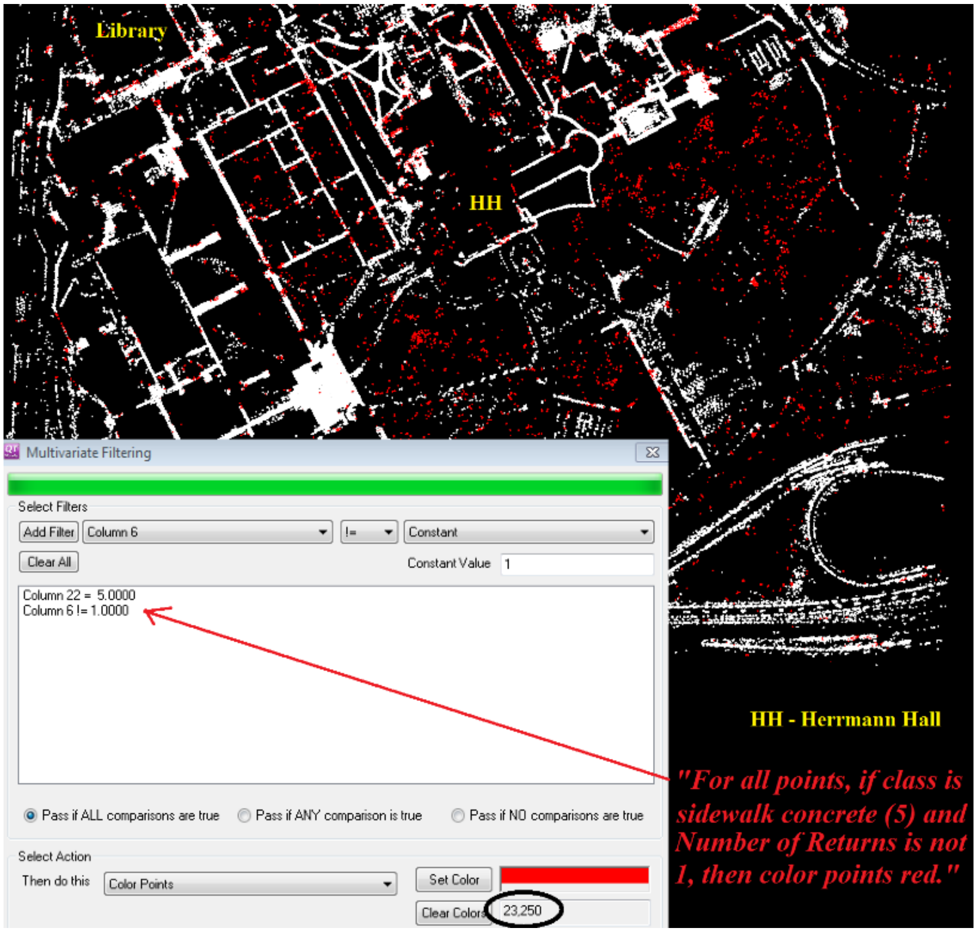

Column 6 != Constant

Constant Value 1

Column 22 = 5.0000
Column 6 != 1.0000

● Pass if ALL comparisons are true ○ Pass if ANY comparison is true ○ Pass if NO comparisons are true

Then do this Color Points

23,250

"For all points, if class is sidewalk concrete (5) and Number of Returns is not 1, then color points red."

We can apply multivariate filtering for individual attributes or any combination of attributes from Table 6. For this effort, we post-process only the ML entire campus point cloud, limited to the single most-beneficial filtering attribute: number of returns (#6). The grass class is not post-processed due to its raw classification accuracy of 99.9%. For the other 14 (non-water) classes, number-of-returns filtering is applied in a logical manner that errs on the side of caution: under correction is preferred to over correction. E.g., this method can decrease the confusion between single-return building materials and multi-return vegetation classes, however it cannot be used to correct the confusion between shrubs and trees (both multi-return classes) or between asphalt shingles and dark building concrete (both single-return classes).

1. Select Before-and-After Figures

The upcoming figures compare the ML results before and after post-processing for two ground classes and all six building classes. Figures 87 and 88 respectively represent the before and after for turf (2) and road asphalt (14). Figures 89 and 90 are the before and after for clay-tile shingles (3), dark building concrete (9), tan/gray shingles (10), asphalt shingles (11), red basalt/lava rock (12), and light building concrete (15).

Figure 87. Turf and Road Asphalt Before Filtering by Number of Returns.

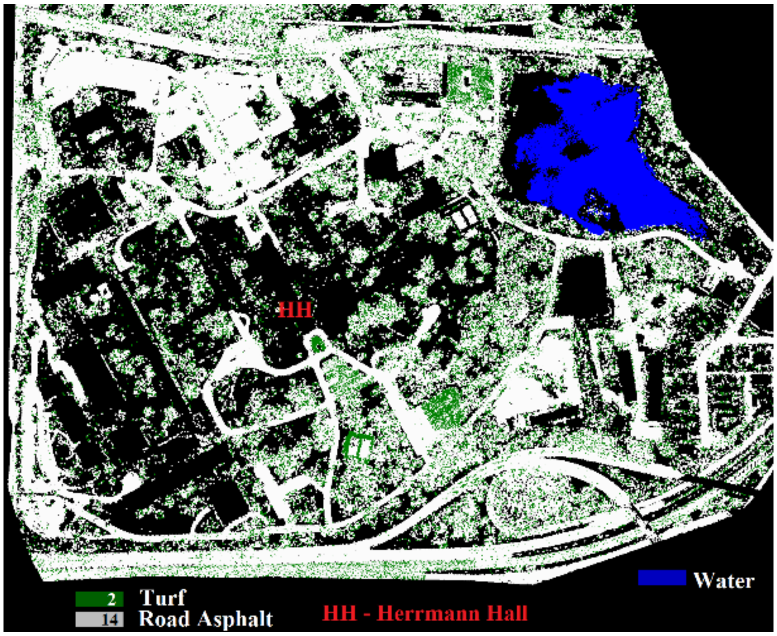

Figure 88. Turf and Road Asphalt After Filtering by Number of Returns.

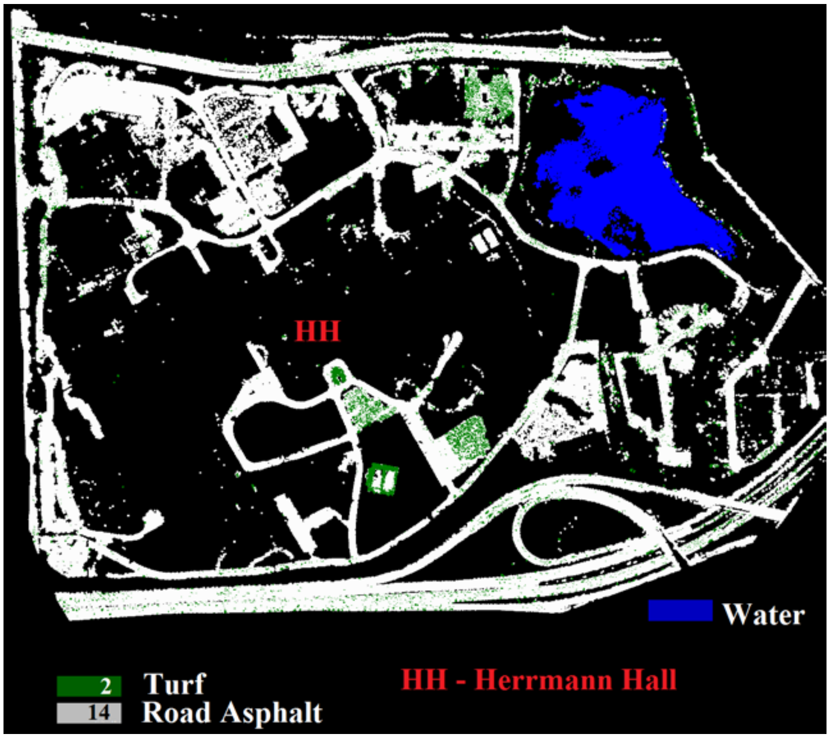

Figure 89. Building Materials Before Filtering by Number of Returns.

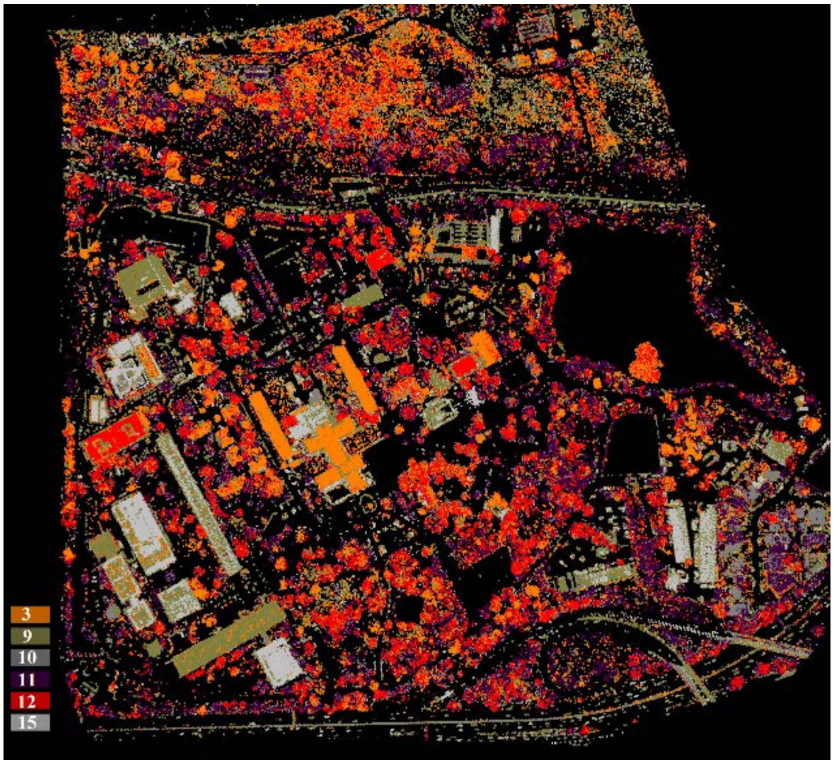

Figure 90. Building Materials After Filtering by Number of Returns.

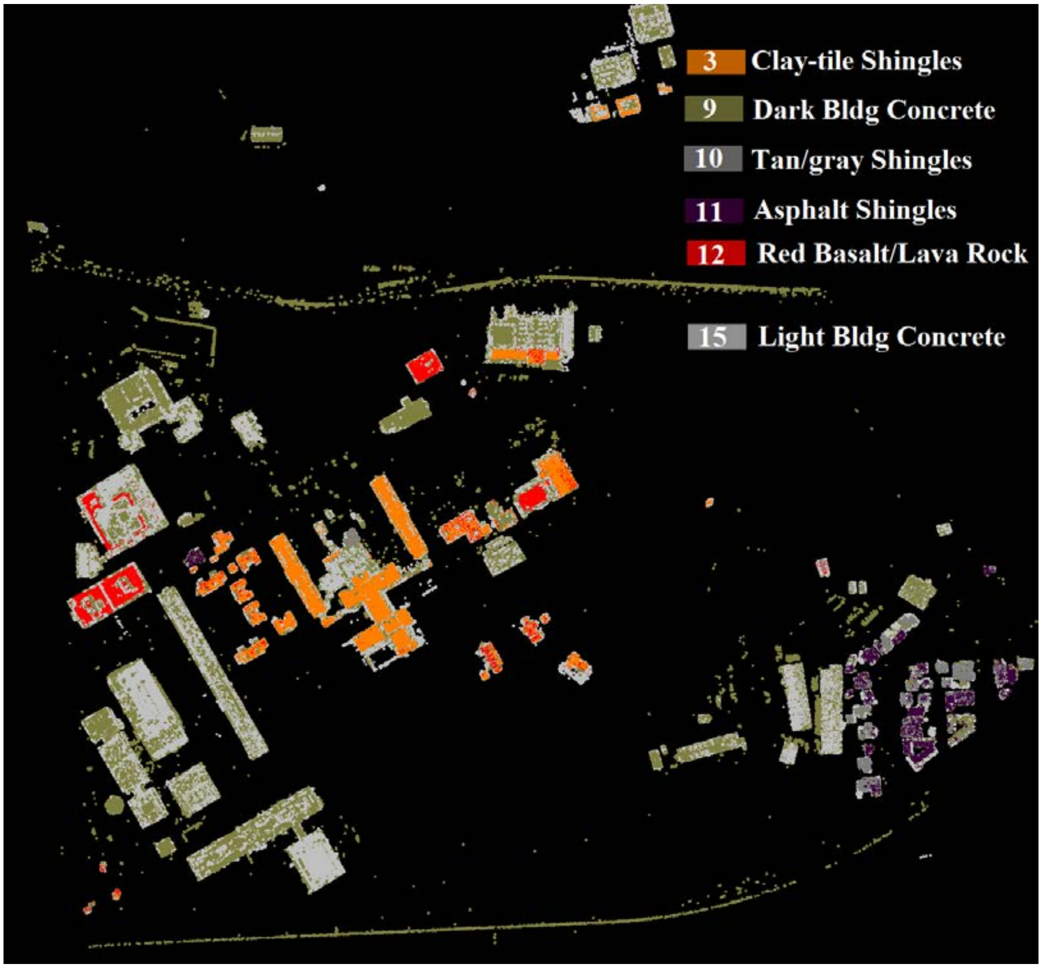

2. NPS Campus Refined by Number of Returns

In both before-and-after examples, filtering by number of returns greatly improves class definition by removing the majority of errors of commission without introducing too many errors of omission. Figure 91 is the refined entire campus point cloud. A significant change can be seen in the trees and on the building rooftops. During the multivariate filtering process, two major rooftop misclassifications are discovered and corrected: On the NEX, many of the clay-tile shingles and some areas of the flat concrete roof are misclassified as dirt/mulch. Likewise, the red lava rock section of the library roof is misclassified as dirt/mulch. It appears that these areas incorrectly received an AGL value of zero during the LASheight script. Accordingly, ML classifies them into the most-appropriate ground class (dirt/mulch)—we manually correct only these specific errors (and absolutely no others), since the fault is not attributable to the classifier.

Figure 91. Post-Processed ML Point Cloud—Entire NPS Campus (Four Combined Flight Lines).

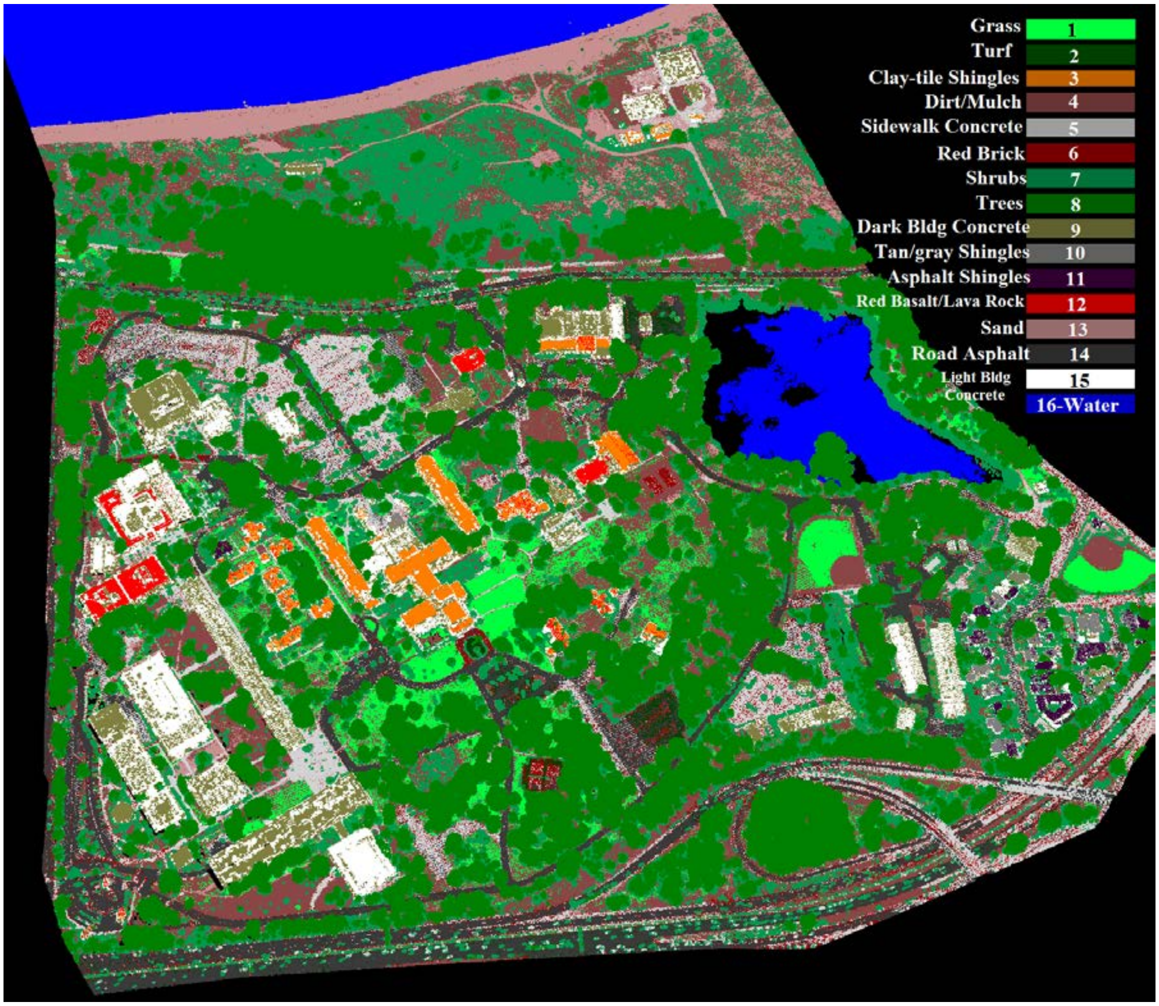

Table 12 is the confusion matrix for the post-processed results compared to the original 5% training subset. The gray-shade cells indicate changes from the raw ML confusion matrix in Table 10. A red-text entry represents each class' greatest misclassification after refinement. Additionally, a summary chart for the post-processing confusion matrix is provided in Table 13, listing each class' individual improvement and the overall improvement.

Table 12. Confusion Matrix—ML Post-Processed by Number of Returns vs. the 5% Training Subset.

	Grass	Turf	Clay-tile	Dirt/Mulch	Sidewalk Concrete	Red Brick	Shrubs	Trees	Dark Bldg Concrete	Tan/gray Shingles	Asphalt Shingles	Red Basalt Lava Rock	Sand	Road Asphalt	Light Bldg Concrete
Grass (26,204)	**26,181 (99.9%)**	0	0	23	0	0	0	0	0	0	0	0	0	0	0
Turf (122)	1	**116 (95%)**	0	0	0	1	0	0	0	0	0	0	0	4	0
Clay-tile Shingles (6,799)	3	0	**5,839 (86%)**	3	1	11	24	14	36	130	0	734	0	2	2
Dirt/Mulch (181,865)	16,293	615	0	**146,132 (80%)**	3,784	5,786	0	0	1	0	0	0	6,504	2,750	0
Sidewalk Concrete (31,872)	56	7	0	1,450	**14,806 (46%)**	3,621	0	0	0	0	0	0	7,300	4,632	0
Red Brick (298)	2	0	0	1	9	**204 (68%)**	0	0	0	0	0	0	0	82	0
Shrubs (5,995)	18	1	99	24	0	10	**5,390 (90%)**	301	36	18	2	85	0	3	8
Trees (190,083)	0	0	2,229	1	0	0	21,551	**164,405 (86%)**	102	208	82	1,487	0	0	18
Dark Bldg Concrete (12,078)	2	4	212	286	244	810	66	21	**7,934 (66%)**	453	10	27	0	6	2,003
Tan/gray Shingles (1,313)	0	0	9	0	0	0	3	0	8	**1,110 (85%)**	181	2	0	0	0
Asphalt Shingles (819)	0	0	0	0	0	0	11	1	1	32	**774 (95%)**	0	0	0	0
Red Basalt Lava Rock (2,588)	0	0	114	3	0	2	9	2	0	22	0	**2,436 (94%)**	0	0	0
Sand (14,179)	0	0	0	228	496	0	0	0	0	0	0	0	**13,455 (95%)**	0	0
Road Asphalt (72,356)	0	3,719	0	873	915	5,844	0	0	0	0	0	0	130	**60,875 (84%)**	0
Light Bldg Concrete (6,835)	2	0	1	5	37	0	0	0	724	0	0	0	0	0	**6,066 (89%)**
Total Accuracy		455,723 of 553,406 points			**82%**										

THIS PAGE INTENTIONALLY LEFT BLANK

Table 13. Accuracy Summary for Post-Processing ML Confusion Matrix.

Class Name (#)	Raw ML Accuracy (%) from Table 11	Accuracy After Post-Processing (%)	Rate of Improvement (%)
Grass (1)	99.9	N/A	N/A
Turf (2)	95	95	-
Asphalt Shingles (11)	94	95	+1
Light Building Concrete (15)	89	89	-
Sand (13)	88	**95**	**+7**
Shrubs (7)	85	**90**	**+5**
Road Asphalt (14)	84	84	-
Tan/Gray Shingles (10)	84	85	+1
Trees (8)	80	**86**	**+6**
Clay-tile Shingles (3)	77	**86**	**+9**
Red Basalt Lava Rock (12)	75	**94**	**+19**
Red Brick (6)	68	68	-
Dirt/Mulch (4)	66	**80**	**+14**
Dark Building Concrete (9)	62	66	+4
Sidewalk Concrete (5)	46	46	-
Overall	75	82	+7

Considerable individual class improvements are in bold type.

Post-processing by number of returns increases overall classification accuracy to 82%. The dirt/mulch and red basalt/lava rock classes demonstrate the greatest progress of +14% and +19%, respectively. Areas of dirt and mulch now exhibit better distinction from turf and the impervious surfaces, primarily road asphalt and red brick. The improvement in the red basalt/lava rock class is mostly attributable to the aforementioned correction of the library roof—misclassified as dirt/mulch due to false AGL values. Had this error not occurred, we would expect red basalt/lava rocks to demonstrate approximately 90% or better classification accuracy. Some confusion persists among clay-tile and red basalt/lava rock roofs, which is uncorrectable without analyzing other attributes besides number of returns (or outright manual correction).

Figure 92 is the area near Herrmann Hall previously displayed in Figure 84, but now post-processed by number of returns. Notice the sharper class definitions, especially on the rooftop; there remains no noticeable confusion among the building materials and vegetation classes. The misclassifications of road paint as red brick, asphalt as turf, and cars as shrubs remain the three apparent discrepancies in the scene, however these are considered minor—and uncorrectable without additional post-processing. Figure 92, *refined spectral LiDAR classification*, should also be compared to Figure 49, *the best of spatial-only (traditional) classification plus manual correction*. The increased accuracy and diversity in terrain, building, and vegetation classification due to the spectral component is evident: 82% (minimally refined spectral accuracy) vs. 77.36% (heavily refined spatial accuracy—from Table 4) and 16 classes vs. four.

Figure 92. Post-Processed ML Results Near Herrmann Hall.

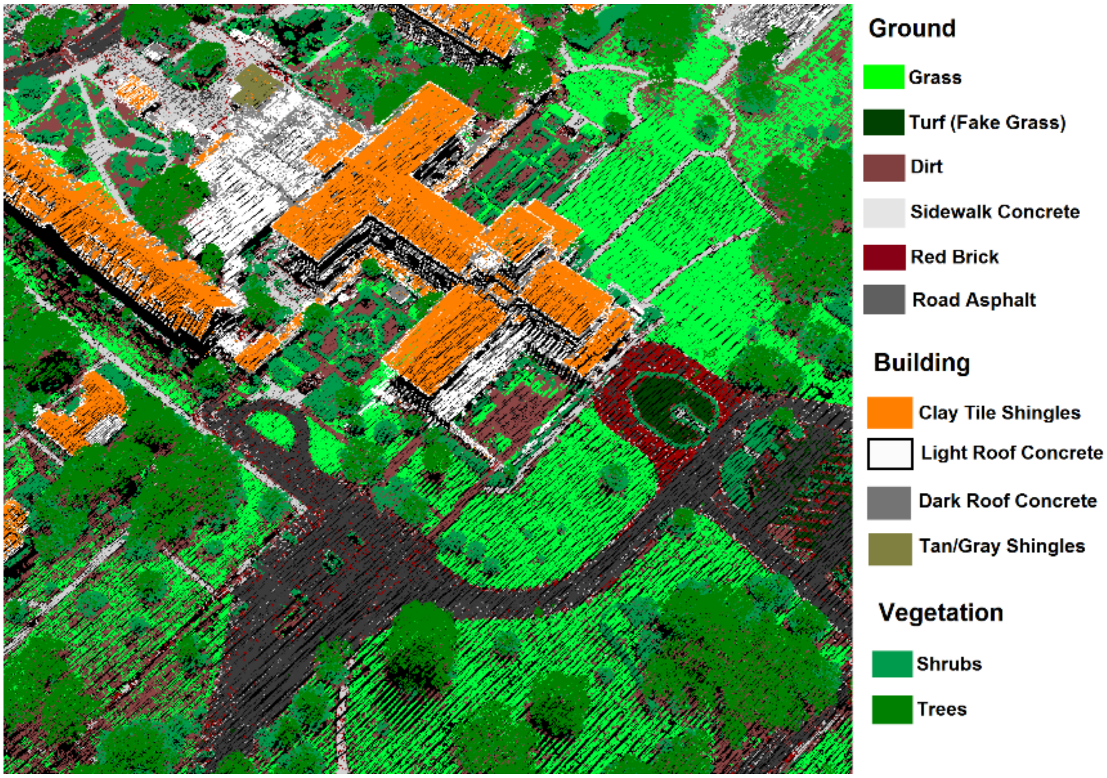

After multivariate filtering, the tree and shrub classes are unconfused with the building materials, as seen in Figures 91 and 92. Less noticeable is the 7% improvement for sand, primarily from the de-confliction of wet beach sand with asphalt and red brick. Eight of the 14 classes maintain essentially the same self-mapping accuracies: grass (not post-processed), turf, asphalt shingles, light building concrete, road asphalt, tan/gray shingles, red brick, and sidewalk concrete (still the worst at 46%). For these classes, any improvement in class distinction comes primarily from the de-confliction of true-class points with the dirt/mulch and vegetation classes, as exemplified in the before-and-after figures for turf and road asphalt (Figures 87 and 88). Altogether, post-processing by number of returns makes a worthwhile contribution to the spectral LiDAR terrain classification process. Additional filtering attributes that may further refine the results are the vegetation indices (GNDVI, GDVI, and GRVI), AGL, and possibly RGB. We leave this as future work for the next analyst.

THIS PAGE INTENTIONALLY LEFT BLANK

VI. CONCLUSION

A. APPLICABILITY TO SPACE AND MILITARY OPERATIONS

LiDAR technologies continue to climb increasingly upward in operational altitude. Eventually, a narrow-beam multi-wavelength LiDAR system will become an important remote-sensing satellite payload. The analysis techniques applied herein represent a demonstration-of-concept that multi-wavelength LiDAR systems improve upon terrain classification by adding a spectral component. Furthermore, ENVI’s n-Dimension Visualizer has successfully exhibited the capacity to adapt to LiDAR data. This powerful tool can, in theory, support spectral LiDAR data of up to “n” wavelengths (i.e., a hyperspectral LiDAR—currently an infant laboratory technology). With a greater number of available dimensions (wavelengths), class clusters will become even more recognizable and easier to distinguish in spectral space.

As demonstrated, spectral LiDAR imaging allows us to analyze 3D spatial and spectral attributes simultaneously. This may provide significant advantages for identifying adversarial deception tactics, such as camouflage. By analyzing both the spatial dimensions and the spectral returns of a scene, camouflage is more likely to become distinguishable from real vegetation. Analysis techniques for multispectral and hyperspectral electro-optical (EO) imagery also possess the capacity to separate fake from actual vegetation, however LiDAR is an active remote-sensing method that can be employed at night. Moreover, it offers high-resolution 3D data products that compliment traditional, lower-resolution and 2D, multi- and hyperspectral imagery.

In the military space domain, technological innovation, evolution, and adaptability permit us to remain ahead of our advancing adversaries. Considerable effort should remain devoted to the evolution of spectral LiDAR systems and the maturation of accompanying data-analysis techniques. This technology may prove tremendously beneficial if it becomes available from space over areas denied even to airborne intelligence, surveillance, and reconnaissance (ISR) platforms.

B. FUTURE WORK IN SPECTRAL LIDAR

One potential avenue of future work is to analyze the spectral RGB attributes in Cloud Compare as XYZ to identify class clusters. Once the flight line LAS files are converted into ASCII files via the nearest neighbor script, the RGB attributes can be imported into Cloud Compare software as x, y, and z values. This creates a 3D scatterplot similar to viewing the RGB in N-D VIS. Spectral class clusters are selected and exported as new data classifications. A future effort can conduct the spectral analysis using Cloud Compare and then compare the output to the results from N-D VIS for the same scene.

Additionally, an effort should be made to consolidate the data preparations process, discussed in Chapter III, into a single script. This script can streamline the process by taking in the full-flight line LAS files (as-received from NCALM) and outputting the data in ENVI file format ready for immediate analysis in N-D VIS. Alternately, the consolidated script can generate all of the intermediate outputs, so that the analyst may still review the direct outputs of LASground, LASheight, LASclassify, and nearest neighbor.

Finally, the analyst should setup various camouflaged targets in the scene of a future Optech Titan flight campaign. Ideally, military-grade camouflage should be used if available. The N-D VIS technique can then be applied to spectrally separate the camouflage from the true vegetation. This effort would have the potential to demonstrate the advantages of spectral-LiDAR classification over traditional geometric-based (purely spatial) classifiers in a military-relevant scenario.

APPENDIX. FOUNDATIONAL DATA PROCESSING: NASA DATASET DERIVED GRAPHS, POINT CLOUDS, AND DIGITAL ELEVATION MODELS

The purposes of this appendix are to outline preliminary work with laser point cloud modeling and processing software (Sections B and C) and to illustrate that multi-wavelength LiDAR, whether for topographic or atmospheric purposes, provides more information than monochromatic LiDAR alone (Section A). This represents important groundwork for the spectral LiDAR classification techniques demonstrated in Chapters III–V. Quick Terrain Modeler (QTM) and Cloud Compare (CC) are utilized to develop conventional LiDAR datasets (in ASCII and LAS formats) from two archived NASA laser altimetry data records: the Mars Orbiter Laser Altimeter (MOLA) and the Clementine Lunar Probe. Additionally, atmospheric graphs are produced for a single mission day of the Phoenix Mars Lander’s meteorological LiDAR station.

The MOLA and Clementine datasets are converted into spreadsheet format for preparatory work in Microsoft Excel, then imported into QTM and CC to create two-dimensional (2D) and three-dimensional (3D) point clouds of Mars and the Moon. For the MOLA dataset, some additional orbital graphs are made in Excel. The exact processes are described thoroughly in Section B for MOLA and Section C for Clementine. Figure 93 is a general workflow diagram for both datasets.

The Phoenix work in Section A does not follow Figure 93, as it is constructed using Excel alone. The Phoenix atmospheric graphs reveal how the combination of 532 nm and 1064 nm laser information generates a greater amount of understanding about the composition of the Martian atmosphere. Although the bulk of this appendix involves single-, not multi-wavelength, LiDAR, it stands as a necessary learning experience and foundation for the main thesis effort.

Figure 93. Workflow Diagram for NASA Laser Altimetry Datasets.

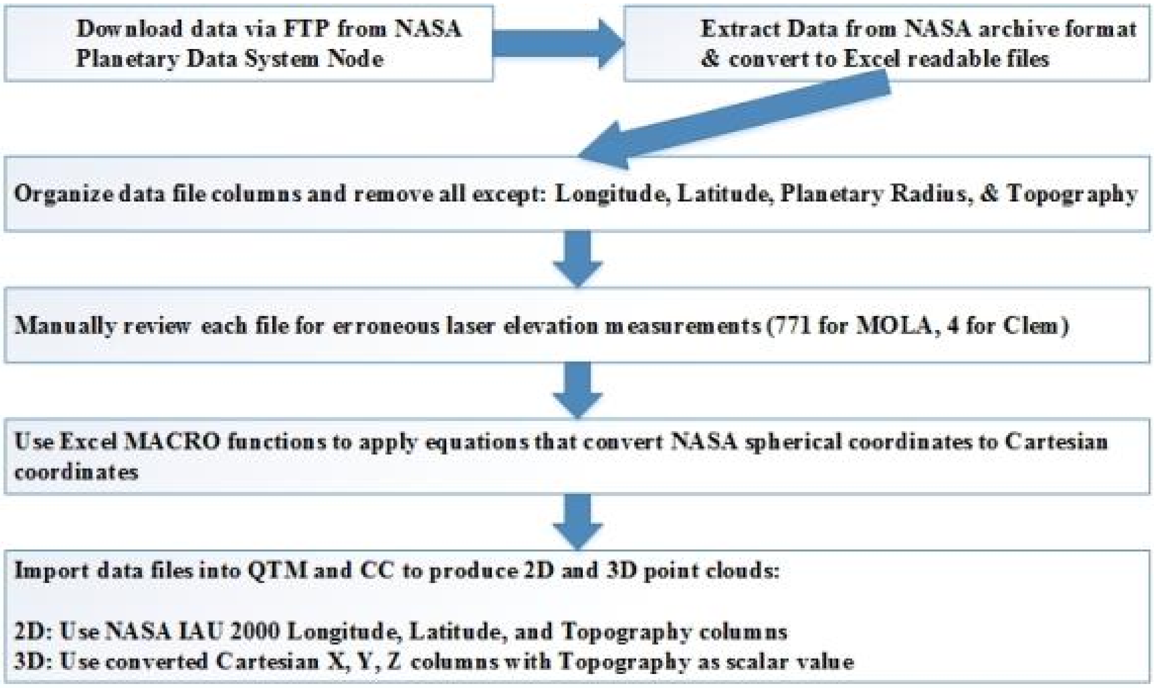

A. PHOENIX MARS LANDER “PHX-M-MET-3-L-RDR-V1.0”

The NASA higher-level Reduced Data Record (RDR) is selected over the raw dataset, the Experiment Data Record (EDR), to create graphs from Phoenix atmospheric LiDAR data. The RDR has a more intuitive data format than the EDR. For example, the RDR gives 532 nm and 1064 nm analog return signals in volts, whereas the EDR’s LiDAR return signals are in the form of digital numbers that would require a conversion to volts. This dataset is available via file transfer protocol (FTP) download from the Washington University (St. Louis, Missouri) Node of the NASA Planetary Data System (PDS), http://pds-geosciences.wustl.edu/default.htm.

1. Martian Atmospheric Graphs for Sol 100 (05 Sep 2008)

For this effort, a one day subset of Phoenix Lander data is selected to explain the concept that multi-wavelength LiDAR provides additional useful information, even for places without vegetation, buildings, or large lifeforms (i.e., Mars). The lander’s meteorological station collected the LiDAR data for Sol 100 over a period of approximately one hour, from 23:52 on 5 September 2008 to 00:52 on 6 September 2008.

The aforementioned are the local mean solar times at the lander's location near the Martian north pole: 68.218º north latitude, 234.248º east longitude.

The following graphs are Martian atmospheric profiles as a function of return signal voltage for two distinct moments in time: the first and last cycles of the Sol 100 measurement period. For laser backscatter measurements below 10 km, Phoenix uses analog detection for both wavelengths: 532 nm and 1064 nm (Dickinson et al. 2008). Photon counting is employed for 532 nm backscatter detection from between 10 km and 20 km; no method exists on Phoenix for 1064 nm backscatter detection from altitudes above 10 km (Dickinson et al. 2008). Here, only the analog signals for backscatter returns below 10 km are graphed. Figure 94 corresponds to the 1064 nm (infrared) return signal, and Figure 95 corresponds to the 532 nm (green) return signal.

Figure 94. Phoenix Mars Lander, Sol 100: 1064 nm LiDAR Backscatter vs. Altitude. Adapted from Dickinson et al. (2008).

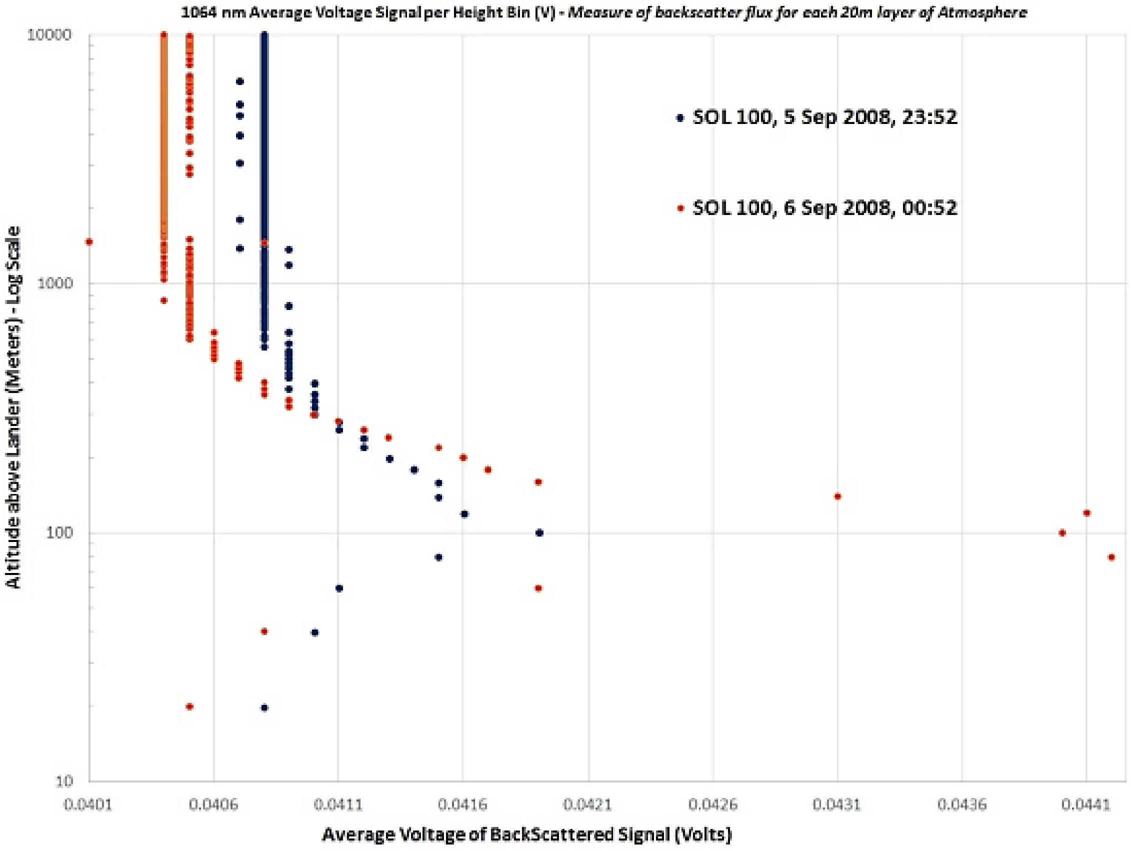

In both figures, the y-axes display a logarithmic scale of the altitude above the Phoenix Lander, from 0 m to 10,000 m. The x-axes are ranges for average return signal voltage (due to backscatter from the atmosphere). LiDAR backscatter voltage is recorded in vertical bins of 20 m, so a data point exists for every 20 m of altitude. Due to the logarithmic scale of the y-axes, the data points above 1,000 m converge to resemble a solid line.

Figure 95. Phoenix Mars Lander, Sol 100: 532 nm LiDAR Backscatter vs. Altitude. Adapted from Dickinson et al. (2008).

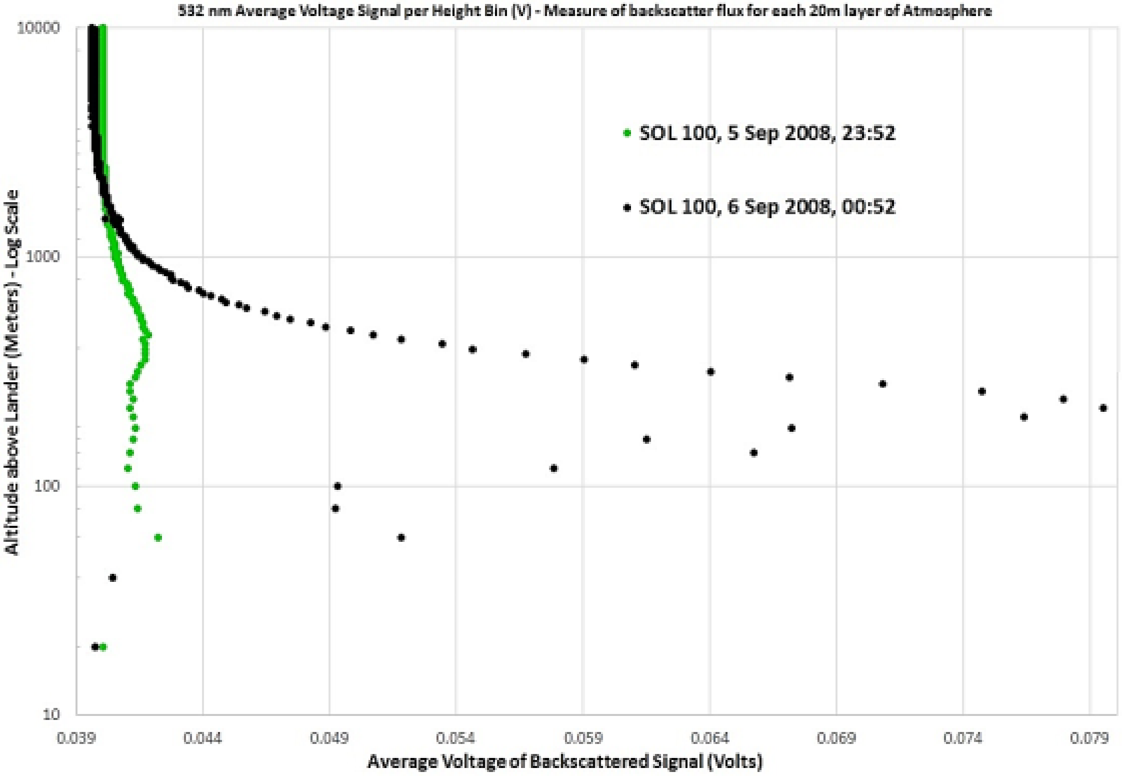

The depicted Sol 100 profiles suggest concentrations of atmospheric dust between the altitudes of 100 m and 800 m, with the overall volume of dust increasing from 23:52 to 00:52. On this night, it seems that no Martian clouds exist above the dust layer, as indicated by the straight vertical lines from approximately 1 km to 10 km. This conclusion of an increase in atmospheric dust over the hour is further supported by the greater backscatter of the 532 nm signal at 00:52, as compared to the 1064 nm return signal at the same time. The shorter wavelength makes the 532 nm photons more susceptible to backscattering from atmospheric dust particles. Here, multi-wavelength LiDAR offers us more information about the Martian atmosphere than monochromatic LiDAR alone. In “Clouds and Precipitation at the Phoenix Mars Lander Site,” Dickson et al. describe Sol 100 as “dust only: exhibiting a smooth profile of extinction coefficients” (Dickson et al. 2012, 1).

B. MARS ORBITER LASER ALTIMETER “PRECISION EXPERIMENT DATA RECORD”

The NASA Precision Experiment Data Records (PEDRs) are selected over the Aggregated Experiment Data Records (AEDR) to save time in the production of high quality 2D and 3D terrestrial LiDAR products of Mars. The PEDR dataset, officially identified as “MGS-M-MOLA-3-PEDR-L1A-V1.0,” is the result of precision orbital, geometric, and equipment calibration corrections applied by NASA to the raw AEDR files (Smith et al. 1999). Released in 1999, the dataset is available via FTP from the Washington University (St. Louis, Missouri) Geosciences Node of the NASA PDS, http://pds-geosciences.wustl.edu/default.htm.

Initially, the 771 PEDR files are downloaded as compressed binary files (e.g., “ap01578l.b”). The number within each filename roughly corresponds to the beginning orbit of the file. Each PEDR binary file contains data for several MOLA orbits, approximately 500,000 to 750,000 laser shots per file. The NASA-programmed command-line script “PEDR2TAB” is used to extract the data as TAB files, viewable in Microsoft Excel. This program is courtesy of MOLA Team’s Gregory Neumann, and it includes a version for Windows, MAC OS, and Sun. The accompanying FORTRAN source code file “PEDR2TAB.PRM” contains several lines of data extraction options. A text editor places a “T” on each line desired for output to the TAB file. For this effort, PEDR2TAB.PRM line option “1” and “ground returns only” are selected to extract the following attributes for each laser point: IAU 2000 longitude (east positive), IAU 2000 latitude (north positive), topography (planetary radius minus areoid), MOLA range, planetary radius, trigger channel, attitude flag, shot number, packet sequence number, and orbit number. Figure 96, shows a portion of an extracted PEDR file.

Figure 96. Sample from Extracted MOLA PEDR File.
Source: Smith et al. (1999).

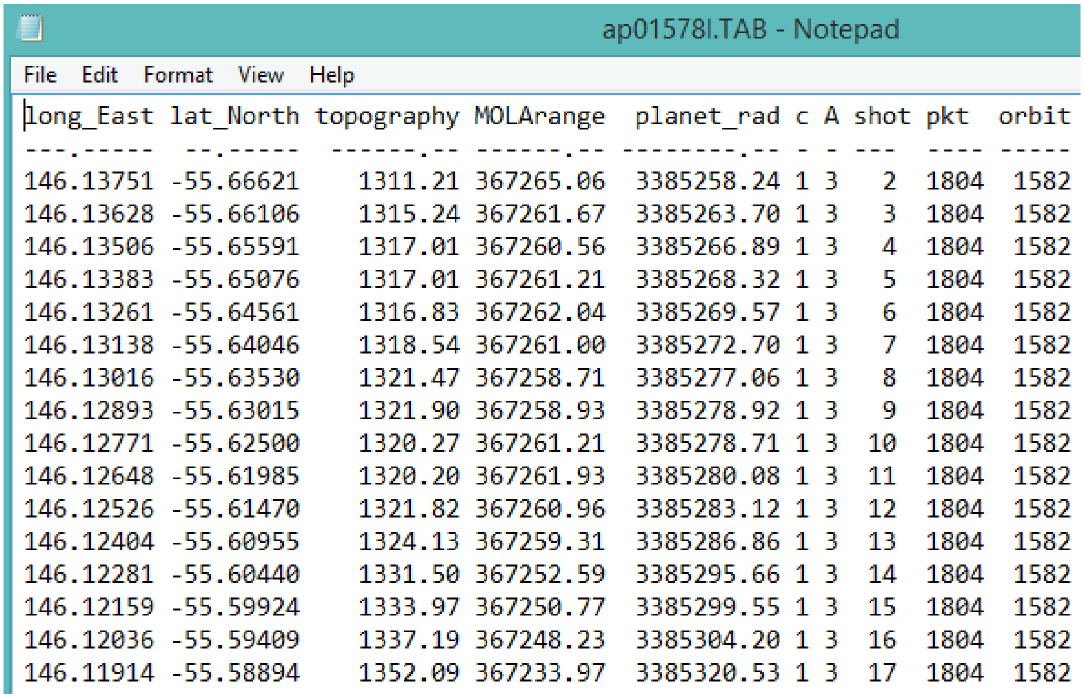

```
long_East lat_North topography MOLArange  planet_rad c A shot pkt  orbit
---.----- --.----- ------.-- ------.-- --------.-- - - ---  ---- -----
146.13751 -55.66621   1311.21 367265.06  3385258.24 1 3   2 1804  1582
146.13628 -55.66106   1315.24 367261.67  3385263.70 1 3   3 1804  1582
146.13506 -55.65591   1317.01 367260.56  3385266.89 1 3   4 1804  1582
146.13383 -55.65076   1317.01 367261.21  3385268.32 1 3   5 1804  1582
146.13261 -55.64561   1316.83 367262.04  3385269.57 1 3   6 1804  1582
146.13138 -55.64046   1318.54 367261.00  3385272.70 1 3   7 1804  1582
146.13016 -55.63530   1321.47 367258.71  3385277.06 1 3   8 1804  1582
146.12893 -55.63015   1321.90 367258.93  3385278.92 1 3   9 1804  1582
146.12771 -55.62500   1320.27 367261.21  3385278.71 1 3  10 1804  1582
146.12648 -55.61985   1320.20 367261.93  3385280.08 1 3  11 1804  1582
146.12526 -55.61470   1321.82 367260.96  3385283.12 1 3  12 1804  1582
146.12404 -55.60955   1324.13 367259.31  3385286.86 1 3  13 1804  1582
146.12281 -55.60440   1331.50 367252.59  3385295.66 1 3  14 1804  1582
146.12159 -55.59924   1333.97 367250.77  3385299.55 1 3  15 1804  1582
146.12036 -55.59409   1337.19 367248.23  3385304.20 1 3  16 1804  1582
146.11914 -55.58894   1352.09 367233.97  3385320.53 1 3  17 1804  1582
```

1. Processing of MOLA PEDR Files to Create Data Products

To improve compatibility with Cloud Compare “3D point cloud and mesh processing software,” all of the 771 MOLA TAB files are opened individually in Microsoft Excel and converted into comma delimited text format (.csv). Additionally, the non-essential data columns are removed from each file (see Figure 96) in order to reduce the size of the final dataset.

After initial processing, each .csv file contains four columns of data: longitude, latitude, planetary radius, and topography. Longitudes and latitudes are in IAU 2000 format; planetary radii and topographies are in meters. Planetary radii represent the distances from the NASA-determined gravitational center of Mars to the location of the MOLA laser hit on the surface. The dataset documentation explains that NASA calculates planetary radii from an areoid of stable rotational and gravitational potential, based on the Goddard Mars Gravity Model: mgm 1025 (Smith et al., 1999 and 2003).

2. 2D Process and Results—IAU 2000 (Lat/Long) Coordinates

a. MOLA Topography Graphs for Orbit # 20328

First, two graphs are produced from the .csv file containing data for orbit number 20,328. Figure 97 is a single-orbit representation of the Mars Global Surveyors' ground track derived from actual MOLA ground returns. The x-axis is in IAU 2000 longitude (0–360º East), and the y-axis is in IAU 2000 latitude (-90–90º North). The large gap at approximately 170º East most likely results from the decision to extract only valid ground returns via the aforementioned PEDR2TAB option: "1—Ground Returns Only.'

Additionally, the longitudes and the corresponding topography values are combined in Figure 98 to make an Apollo-style topography graph (See Figure 2) for Mars. Several prominent Martian landscape features are identified in red with the longitude and latitude coordinates in parenthesis. Again, the vertical line at 170º East corresponds to the gap in valid ground hits also seen in Figure 97.

Figure 97. Orbit Track Based on MOLA Ground Hits—Orbit 20,328. Adapted from Smith et al. (1999).

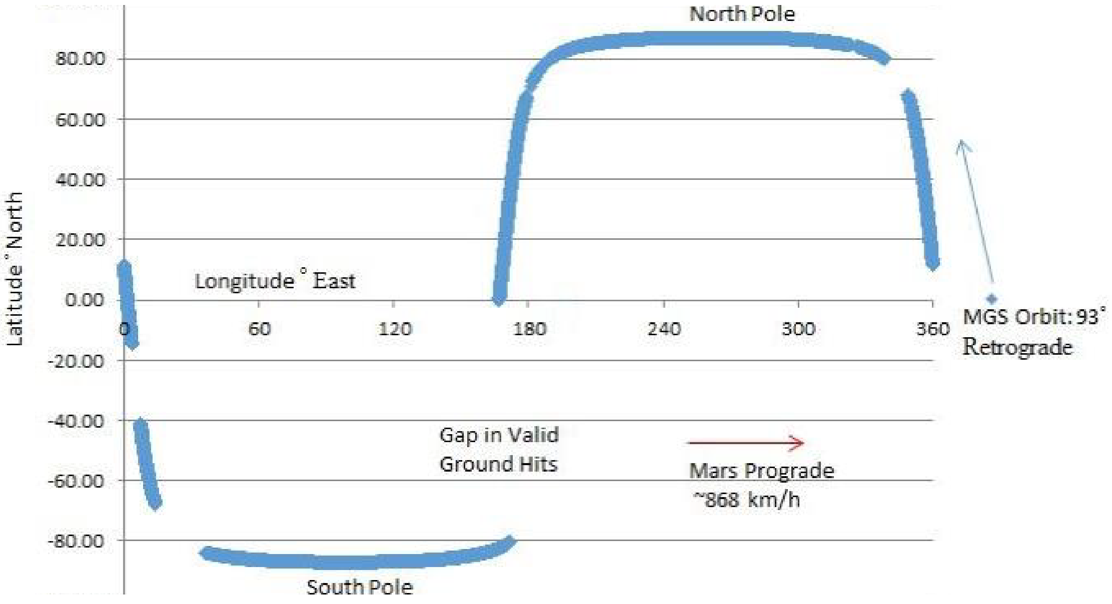

Figure 98. MOLA Topography Above Mean Radius—Orbit 20,328. Adapted from Smith et al. (1999).

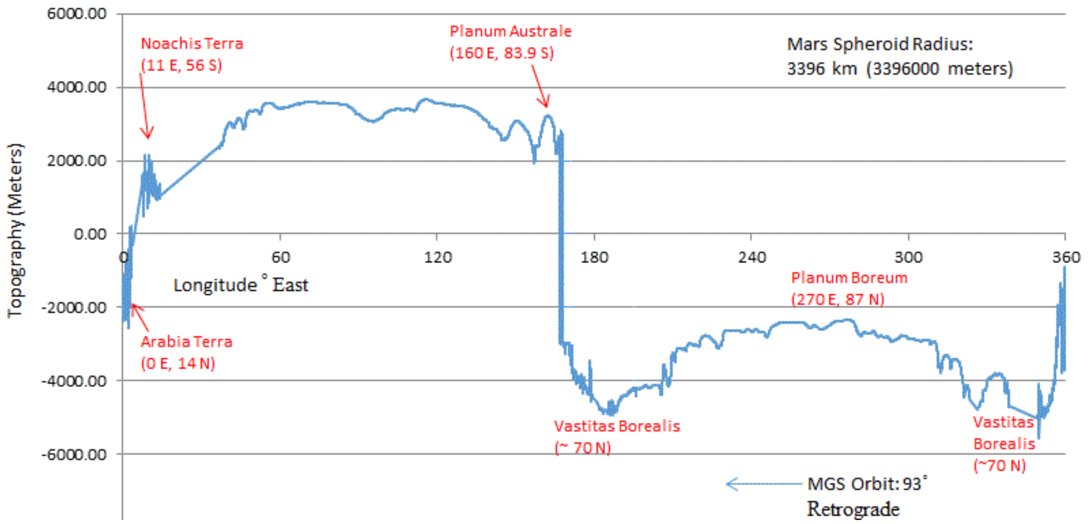

b. 2D Maps and DEM

All of the 771 .csv files are loaded in succession into Cloud Compare v2.6.0 using longitudes as the x-values, latitudes as the y-values, and topographies as the z-values. Next, the minimum and maximum z-values for the 771 Cloud Compare entities are inspected to remove values outside of valid Martian topographies: -9,200 m to 21,274 m. “Ap18004.csv” is discarded entirely, because it contains a large number of invalid topography values. A few additional .csv files contained one or two invalid topographies; we found and removed these errors quickly via basic Excel sort and filter functions. Seven hundred seventy files are then reloaded into Cloud Compare. These entities are now ready for merging.

The Cloud Compare “Merge Multiple Clouds” function compiles the 770 separate point clouds into one entity of approximately 590 million points. We export this to ASCII immediately. The resulting combined point cloud, “MOLA 2D ASCII.txt,” occupies 29.7 gigabytes of disk space. Figure 99 is a screenshot of the MOLA 2D point cloud opened in Quick Terrain Modeler v8.0.5.2 with elevations above areoid displayed in grayscale.

Figure 99. Ungridded MOLA 2D Point Cloud (QTM)—
Topography in Grayscale.

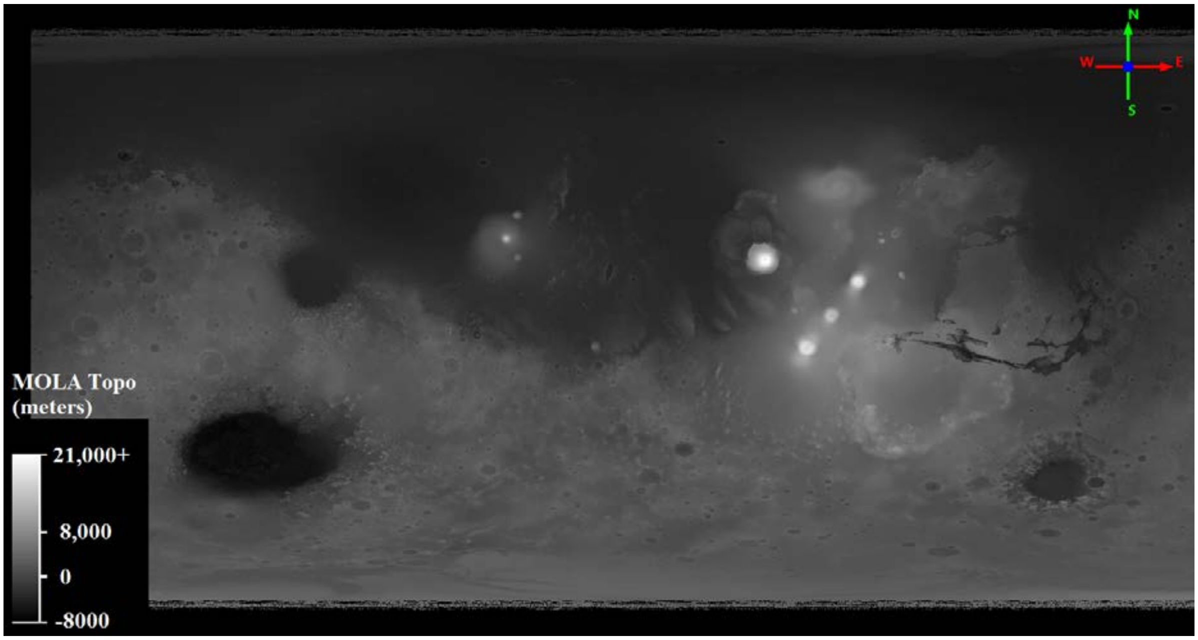

A generic geodetic coordinate system is necessary in QTM to view the point cloud properly in the 3D viewer mode, because degrees of longitude and latitude are the x- and y-values, respectively. The default Cartesian coordinate system projects the map (Figure 99) properly in the 2D viewer mode, but not in the 3D mode.

To produce the complete planetary DEM in Figure 100, the point cloud is converted to a QTT (Quick Terrain Modeler Gridded Surface) using the “Convert Model Type Function.” We accept the following default options: grid sampling at ~0.01, adaptive triangulation fill, and max z algorithm. Larger grid-sampling settings result in a gridded surface that distorts the planet’s natural features, and settings less than 0.01 result in program crashes due to the large data size of the point cloud. Based on the good result from the default options (Figure 100) and our disappointing tests with different grid sampling values, we decided not to experiment with altering the other parameters.

Figure 100. MOLA Digital Elevation Model of Mars (QTM)—
Topography in Color.

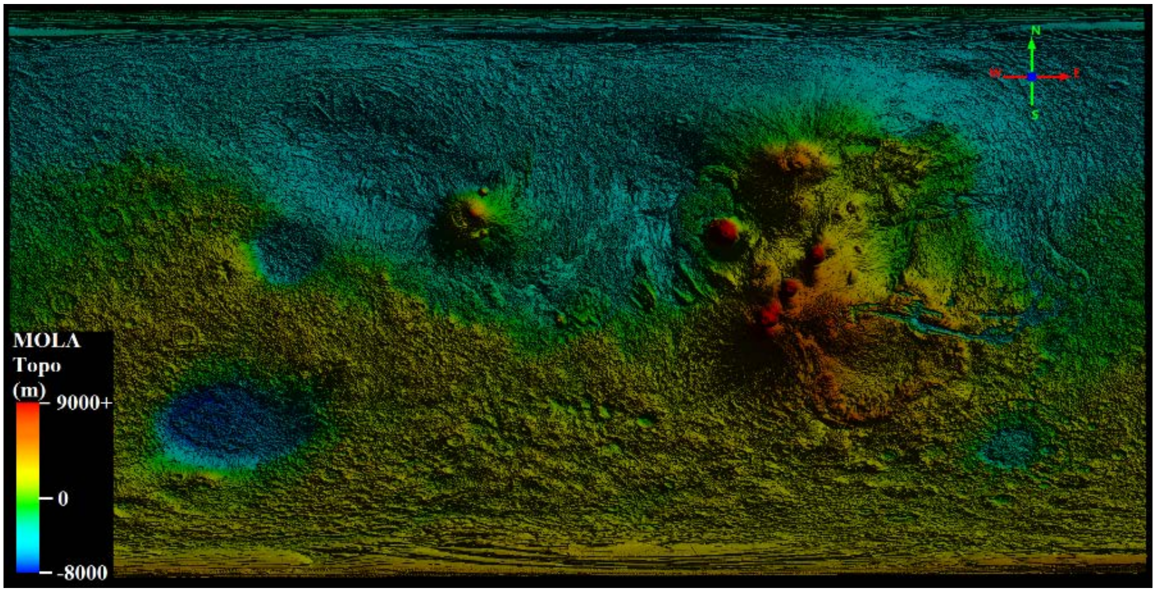

Figures 99 and 100 maintain the IAU 2000 coordinate system and display it in a cylindrical projection. Zero degrees longitude corresponds to the left map edge, and 359 degrees longitude corresponds to the right edge. NASA-produced DEMs, included in the Mission Experiment Gridded Data Records (MEGR), have resolutions of approximately 128 pixels per degree of longitude at the equator and mid-latitudes and 512 pixels per degree at the poles—pixel size is approximately 0.463 km/pixel (Smith et al. 2003). The resolutions of the figures in this section exhibit negligible degradation from the NASA products, even with the one discarded file, “ap18004.csv.” The data loss is approximately 700,000 of 590,000,000 points (0.0012%).

The complete-planetary ASCII file loads slowly, and it is difficult to navigate and analyze on a computer with limited RAM (<12 gigabytes). Thirty two gigabytes or greater RAM should alleviate this problem. Quick Terrain Modeler’s “rectangular selection” tool allows one to select and export a subset of data points in laser file format (.las). This permits closer terrain analysis without lengthy screen refresh delays due to the large data file. The area selected for “MOLA Portion.las” includes prominent Martian terrain features in the western hemisphere, such as Olympus Mons, the other Tharsis volcanoes, and Valles Marineris.

Figure 101 is the un-gridded point cloud for the “MOLA Portion” subset. It shows the Mars Global Surveyor’s numerous orbital ground tracks across the landscape. Figure 102 is the same scene in gridded format. Again, the default QTM “Convert Model Type” options are selected to generate the rasterized surface model. Remember, a geodetic coordinate system is required to properly view the point cloud in the 3D viewer mode of QTM with IAU 2000 coordinates as x- and y-values. QTM offers a coordinate conversion utility that is straightforward.

Figure 101. MOLA Subset Point Cloud (QTM)—Topography in Color.

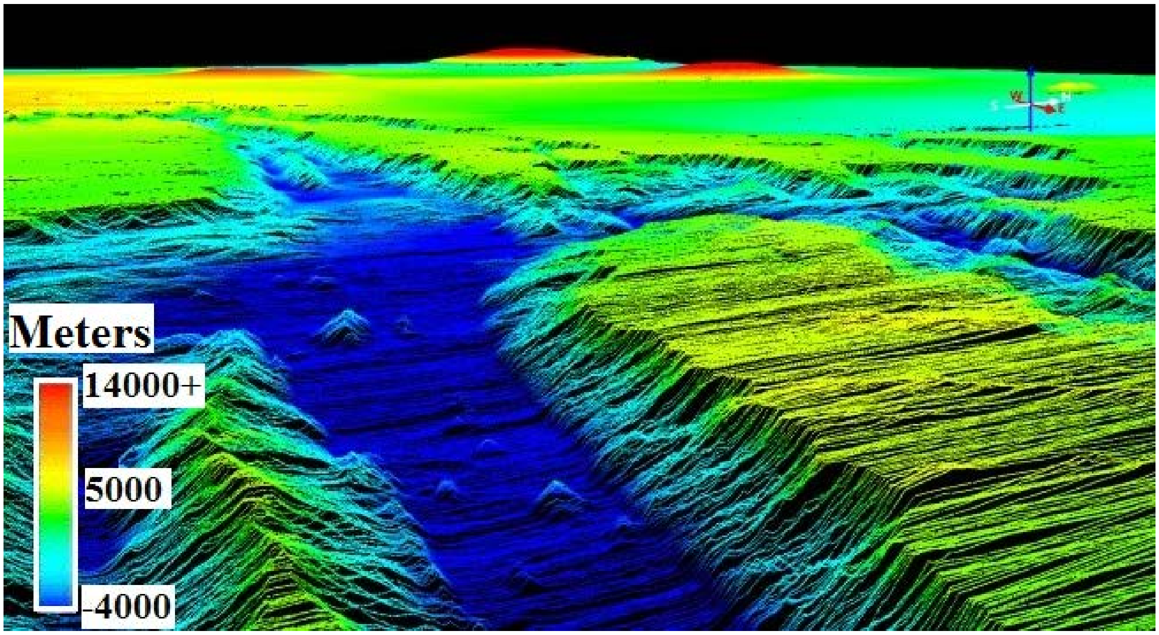

Figure 102. MOLA Subset DEM (QTM)—Topography in Color.

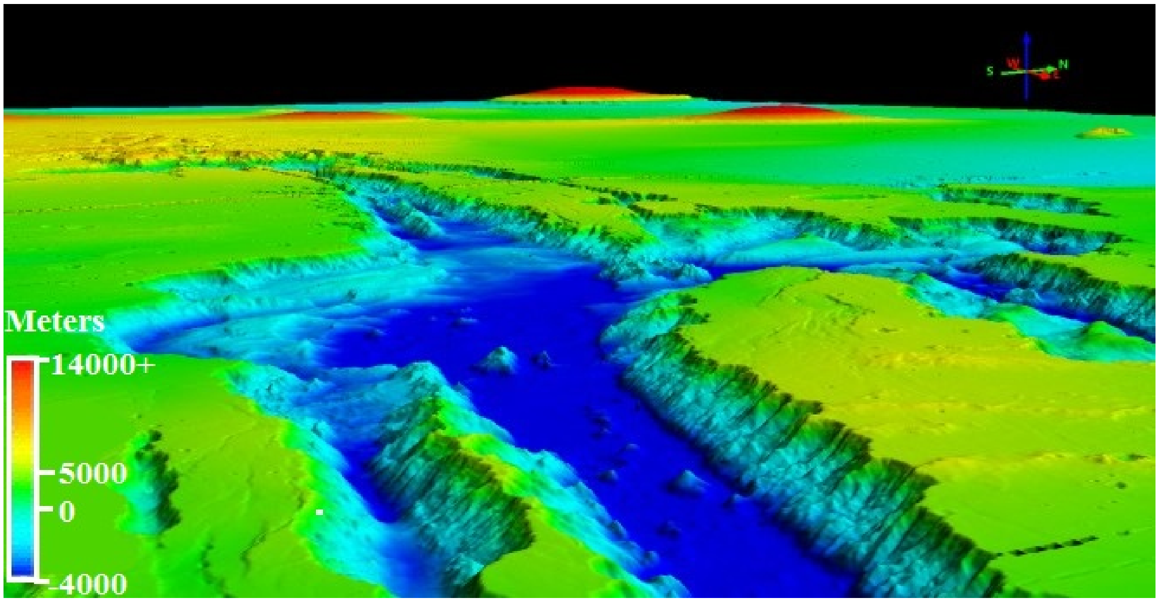

3. 3D Conversion and Results—IAU 2000 to Cartesian Coordinates

Unfortunately, no Cloud Compare or Quick Terrain Modeler functions exist that can directly convert the complete 2D point cloud (Figure 99) into a spherical representation of Mars. Nevertheless, it is possible to derive the 3D Cartesian coordinates for each laser point from the NASA-provided spherical coordinates: longitude, latitude, and planetary radius. Table 14 lists the parameters and formulas for the spherical-to-Cartesian conversion, applied individually for each MOLA point in all 770 .csv files. MACRO functions in Excel are used to rapidly apply the three formulas to each line item (laser point), on average 500,000 to 750,000 lines per file. To verify that each file is processed correctly via the MACROs, no batch processing is implemented: all 770 files are opened, processed, inspected, and saved individually.

Table 14. Generic Mathematical Formulas for Converting Each MOLA Point.

Spherical Coordinates	
Polar Angle (θ)	= (90 degrees - IAU2000 Latitude)
Azimuth Angle (φ)	= IAU2000 Longitude
r (meters)	= Planetary Radius
Derived Cartesians	
X (meters)	= $\cos(\varphi) \times \sin(\theta) \times r$
Y (meters)	= $\sin(\varphi) \times \sin(\theta) \times r$
Z (meters)	= $\cos(\theta) \times r$

Now, each MOLA .csv file contains seven columns: IAU 2000 longitude, IAU 2000 latitude, planetary radius, Cartesian x, Cartesian y, Cartesian z, and topography. The 770 files are imported into Cloud Compare using the Cartesian coordinates with topography as a scalar value. The separate point clouds are merged into one entity, and the result is saved as “MOLA 3D.csv” (36.2 gigabytes).

For viewing the 3D point cloud in QTM, it is essential to import the topographies as the “alpha” values and to set the height scale to “color by alpha.” Also, the 3D point cloud must be viewed in a Cartesian coordinate system, unlike the 2D cloud that requires a geodetic system. Lastly, QTM gridding cannot successfully produce a 3D (spherical) raster of Mars—the attempt resulted in a complete failure which resembled an accordion ball. However, the spatial point density of the un-gridded cloud is sufficient to project the appearance of a complete surface, unless the viewer examines extremely close to the planet—where you will see ground tracks similar to Figure 101.

Again, resolution is approximately 128 pixels/degree of longitude at the equator and 512 pixels/degree at the poles. When the display screen is zoomed in close to the planet’s surface, the satellite’s ground tracks (represented by crisscrossing lines of laser points) are significantly closer together at the poles than at the equator. Figures 103, 104, 105, and 106 are select screenshots of the 3D MOLA point cloud in Cloud Compare and

Quick Terrain Modeler. The initials of the respective program are indicated in parentheses in the figure titles. Additionally, each image is color-scaled differently to best highlight the topographic features of the particular region in view.

Figure 103. MOLA 3D North Pole—Topography in Color (CC).

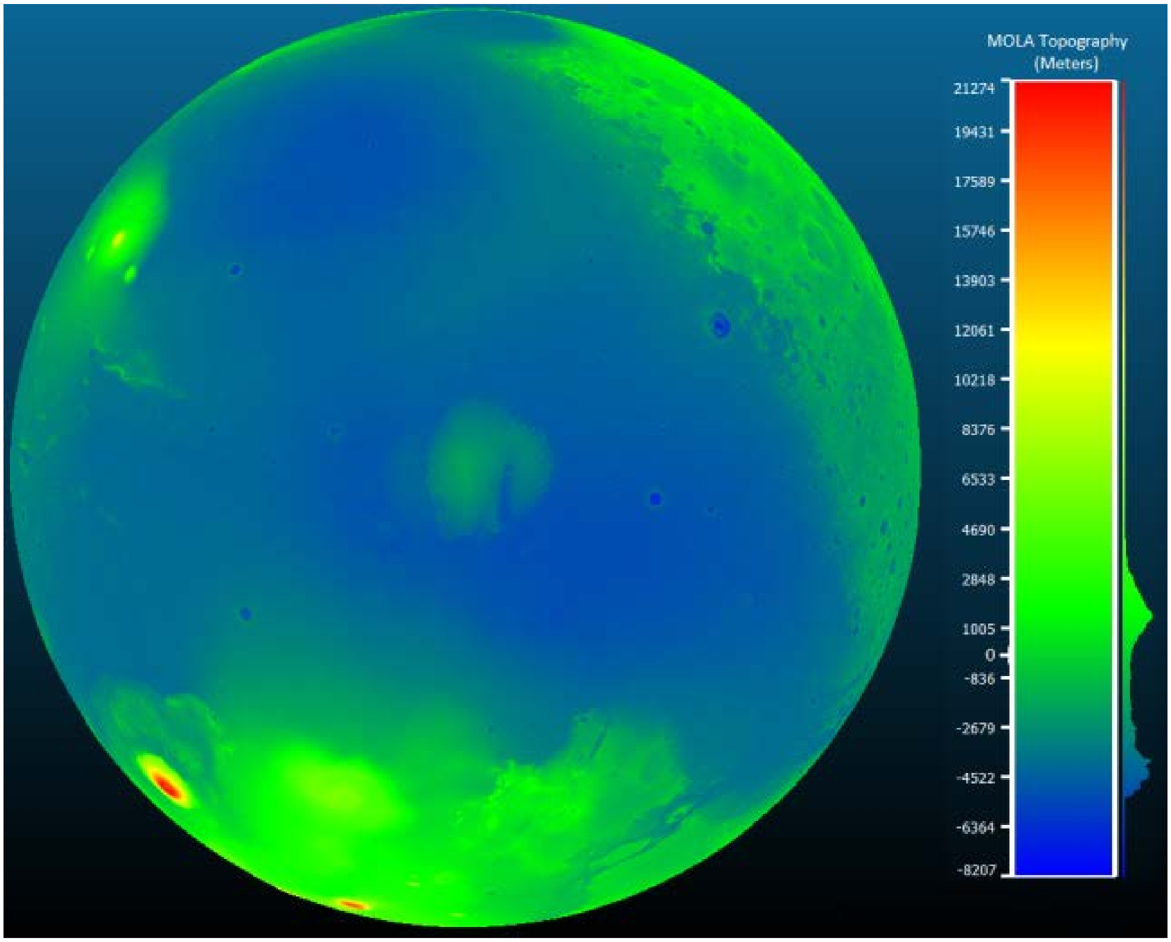

Figure 104. MOLA 3D South Pole—Color (QTM).

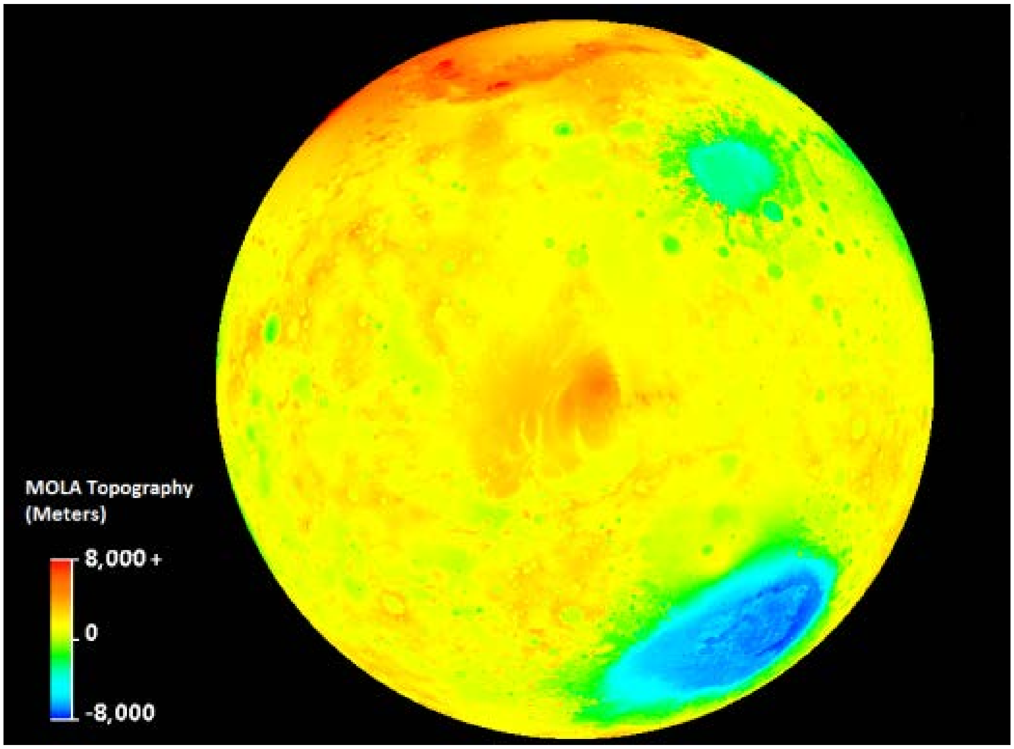

Figure 105. MOLA 3D Eastern Hemisphere—Grayscale (QTM).

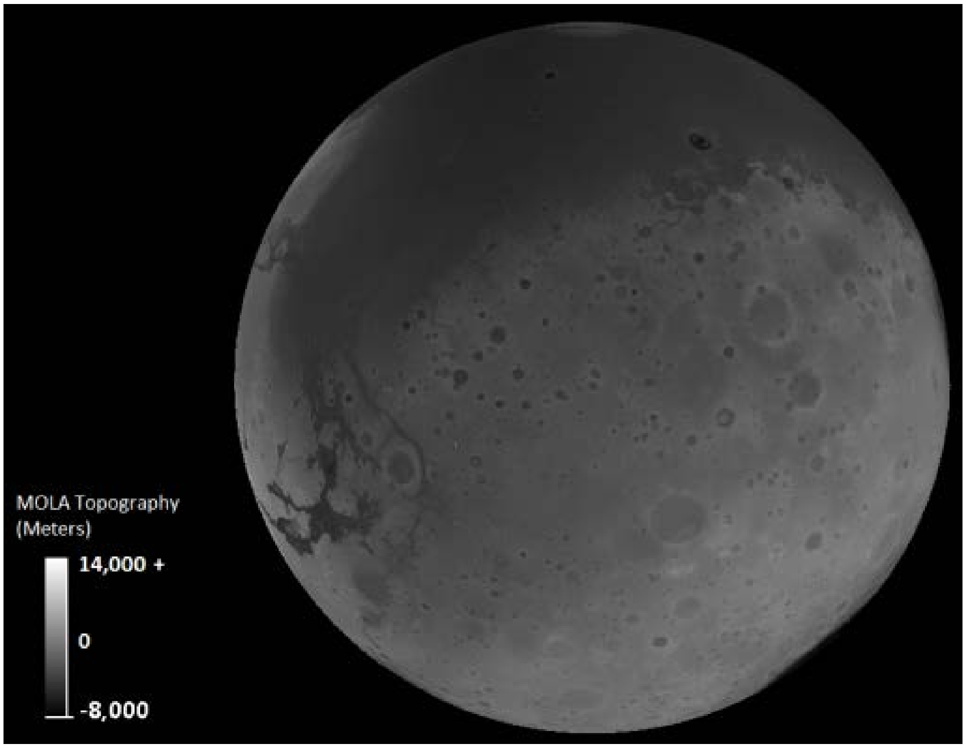

Figure 106. MOLA 3D Western Hemisphere Topography in Grayscale (QTM).

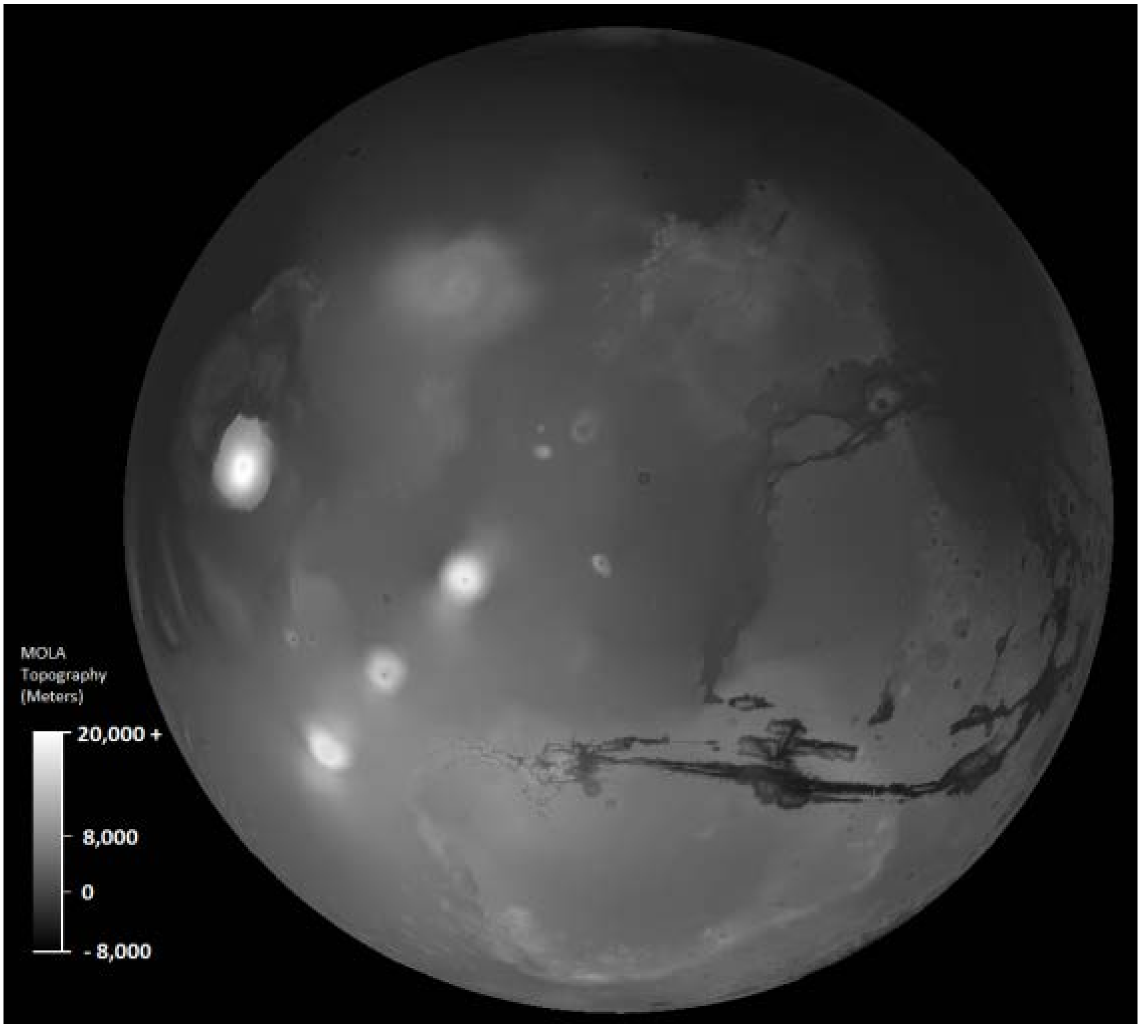

C. CLEMENTINE LUNAR PROBE “CLEM1-L-LIDAR-3-TOPO-V1.0”

To produce a Clementine-data point cloud of the Moon, the “CLEM1-L-LIDAR-3-TOPO-V1.0” dataset is downloaded via FTP from the PDS Geosciences Node, Washington University (St. Louis, Missouri). The dataset includes four TAB files plus the associated label files, each containing data for approximately 100 orbits: r009_099.tab, r100_199.tab, r200_299.tab, and r300_346.tab. These files are combined into one .csv file of over 100,000 laser data points. Next, each line item is compared to the lunar topography values contained in the higher-level data product “CLEM1-L-LIDAR-5-TOPO-V1.0” and to the Clementine Topography Map of the Moon (Figure 6) to determine erroneous laser measurements. The resulting lunar point cloud of valid topography values contains approximately 73,000 points.

Figure 107 superimposes the Clementine-derived 2D point cloud, exported from Cloud Compare, onto a cylindrical lunar map with a resolution of 64 pixels/degree. The underlying lunar mosaic is one of the wide-angle-camera global morphological maps included in the "Lunar Reconnaissance Orbiter Camera Reduced Data Record," courtesy of NASA/GSFC/Arizona State University. The image is centered at zero degrees north latitude and 180 degrees east longitude, corresponding to the farside of the Moon. Topography values are in meters above a lunar spheroid with an equatorial radius of 1,738 km.

Figure 107. Clementine LiDAR Topographic Point Cloud. Adapted from Berwick et al. (2007) and Robinson (2010).

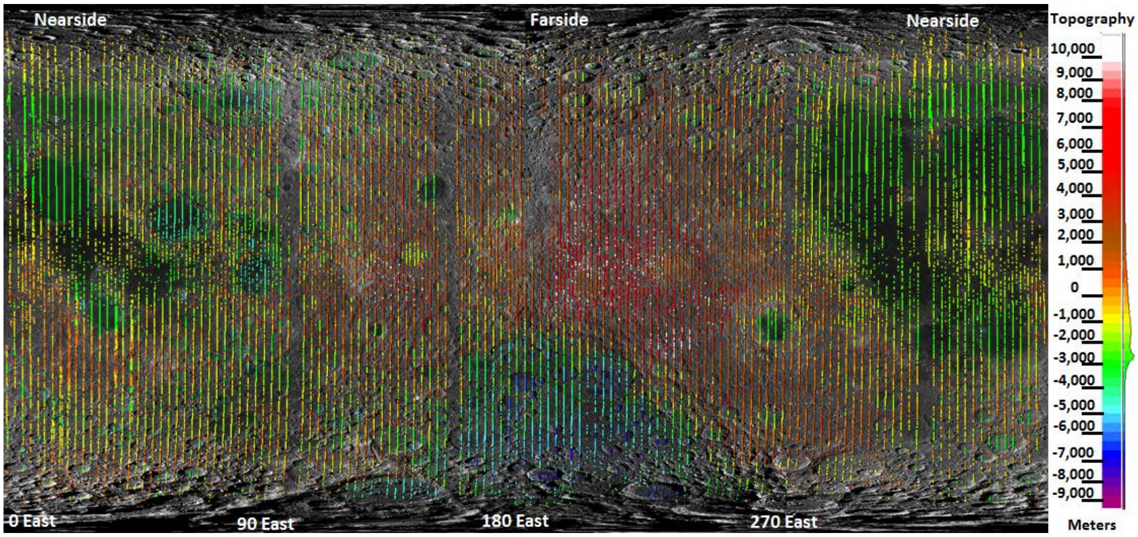

Next, we convert the Clementine point cloud from IAU 2000 longitude/latitude coordinates to Cartesian coordinates, in accordance with Table 14, to produce a 3D lunar point cloud. Unfortunately, the point total of the Clementine data (~73,000 points) is far below that of the MOLA data (~590,000,000 points). Thus, the resulting Clementine 3D point cloud has insufficient point density to convey a complete spherical representation of the lunar surface, unless the view screen is zoomed out substantially. Despite the poor resolution, the lower-quality 3D point clouds are shown in Figure 108.

Figure 108. Clementine LiDAR Point Cloud in 3D—Various Perspectives.

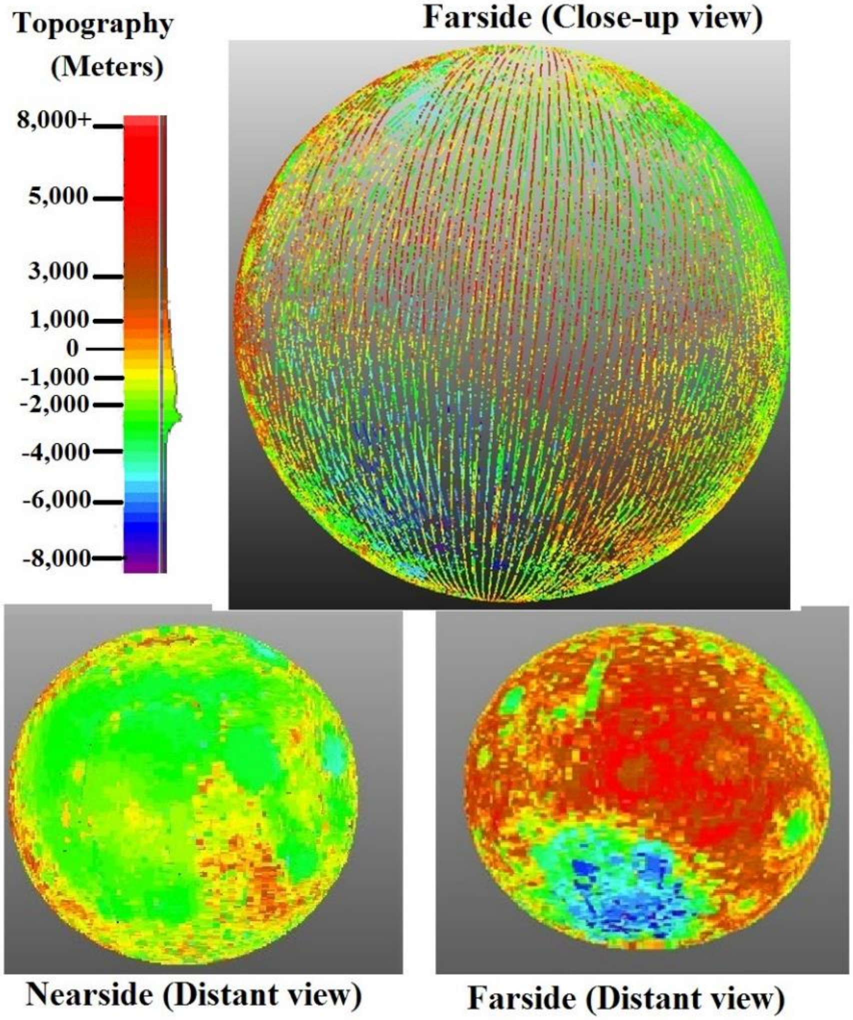

From Figure 107 and the "farside (close-up view)" in Figure 108, we see that Clementine's approximately 350 mapping orbits did not provide complete coverage of the Moon's surface. Future work could apply this process to Lunar Reconnaissance Orbiter (LRO) data collected by its LiDAR, the Lunar Orbiter Laser Altimeter (LOLA). LOLA 2D and 3D point clouds can then be compared to those from Clementine. LOLA datasets are also available from the NASA Planetary Data System.

LIST OF REFERENCES

Abe, Shinsuke, Tadashi Mukai, Nura Hirata, Olivier S. Barnouin-Jha, Andrew F. Cheng, Hirohide Demura, Robert W. Gaskell, Tatsuaki Hashimoto, Kensuke Hiraoka, Takayuki Honda, Takashi Kubota, Masatoshi Matsuoka, Takahide Mizuno, Ryosuke Nakamura, Daniel J. Scheeres, and Makoto Yoshikawa. 2006. "Mass and Local Topography Measurements of Itokawa by Hayabusa." *Science* 312: 1344–1347, 2 June.

Abshire, James B. 2011. "NASA's Space Lidar Measurements of the Earth and Planets: A Brief Overview." National Aeronautics and Space Administration (NASA) Goddard Space Flight Center (GSFC). Paper presented at Institute of Electrical and Electronics Engineers (IEEE) Photonics Society Meeting, University of Maryland, College Park, Maryland, 5 April.

Amzajerdian, Farzin, Glenn D. Hines, Vincent E. Roback, Larry B. Petway, Bruce W. Barnes, Paul F. Brewster, Diego F. Pierrottet, and Alexander Bulyshev. 2015. "Advancing Lidar Sensors Technologies for Next Generation Landing Missions." Paper presented at American Institute of Aeronautics and Astronautics (AIAA) Guidance, Navigation, and Control Conference, AIAA SciTech Forum, (AIAA 2015–0329), 29 March. doi:10.2514/6.2015-0329.

Baldwin, Richard R. 1972. *NASA: Apollo 15 Preliminary Science Report*. Washington, D.C.: Scientific and Technical Information Office.

Battaglia, Neal. 2010. "Utility of Satellite Waveform Data in Shallow Water." Master's thesis, Naval Postgraduate School.

Behn, Mark D., and Maria T. Zuber. 2000. "A Comparison of Ocean Topography Derived from the Shuttle Laser Altimeter-01 and TOPEX/POSEIDON." *IEEE Transactions on Geoscience and Remote Sensing* 38(3):1425–1438, May.

Berwick, Meredith, Susan Slavney, and Jenn Ward. 2007. "CLEM1-L-LIDAR-3-TOPO-V1.0" and "CLEM1-L-LIDAR-5-TOPO-V1.0." Planetary Data System Geosciences Node. Washington University, St. Louis, Missouri. Accessed 31 May. http://pds-geosciences.wustl.edu/missions/clementine/default.htm.

Bufton, Jack, Bryan Blair, John Cavanaugh, James Garvin, David Harding, Dan Hopf, Ken Kirks, David Rabine, and Nita Walsh. 1995. "Shuttle Laser Altimeter (SLA): A Pathfinder for Space-Based Laser Altimetry & Lidar." Laboratory for Terrestrial Physics Goddard Space Flight Center. *The 1995 Shuttle Small Payloads Symposium*: 83–90, 1 September.

Carabajal, Claudia C., David J. Harding, Scott B. Luthcke, Waipang Fong, Shelley C. Rowton, and James J. Frawley. 2000. “Processing of Shuttle Laser Altimeter Range and Return Pulse Data in Support of SLA-02.” p.2. *International Archives of Photogrammetry and Remote Sensing*.

Cavanaugh, John F., James C. Smith, Xiaoli Sun, Arlin E. Bartels, Luis Ramos-Izquierdo, Danny J. Krebs, Jan F. McGarry, Raymond Trunzo, Anne Marie Novo-Gradac, Jamie L. Britt, Jerry Karsh, Richard B. Katz, Alan T. Lukemire, Richard Szymkiewicz, Daniel L. Berry, Joseph P. Swinski, Gregory A. Neumann, Maria T. Zuber, and David E. Smith. 2007. “The Mercury Laser Altimeter Instrument for the MESSENGER Mission.” *Space Science Reviews (2007)* 131:451–479, 9 November. doi:10.1007/s11214-007-9273-4.

Chanin, Marie-Lise, and Alain Hauchcorne. 1991. “Le LiDAR Spatial ALISSA Embarque sur la Plateforme Sovietique Mir.” Service d’Aéronomie du CNRS BP 3–91371. Paper presented at International Conference on Space Optics 91, Toulouse, France, 25–27 September.

Christian, John, and Scott Cryan. 2013. “A Survey of LiDAR Technology and Its Use in Spacecraft Relative Navigation.” Paper presented at AIAA Guidance, Navigation, and Control (GNC) Conference, Guidance, Navigation, and Control and Co-located Conferences, (AIAA 2013–4641), 19–22 August. doi:10.2514/6.2013-4641.

Cole, Timothy D. 1998. “NEAR Laser Rangefinder: A Tool for the Mapping and Topologic Study of Asteroid 433 Eros.” *Johns Hopkins APL Technical Digest* 19(2):143–145, June.

Degnan, John J. 2002. “Photon-Counting Multikilohertz Microlaser Altimeters for Airborne and Spaceborne Topographic Measurements.” *Journal of Geodynamics 2002* 34:503–549.

———. 2014. “A Celebration of Fifty Years of Satellite Laser Ranging.” Sigma Space. Paper presented at Joint Science/Engineering Colloquium 19th International Workshop on Laser Ranging, Goddard Space Flight Center, Greenbelt, Maryland, 19 October.

Degnan, John J., Christopher Field, Roman Machan, Ed Leventhal, David Lawrence, Yunhui Zheng, Robert Upton, Jose Tillard, Spencer Disque, and Sean Howell. 2013. “Recent Advances in Photon-Counting, 3D Imaging Lidars.” Sigma Space Corporation. Paper presented at Eighteenth International Workshop on Laser Ranging Instrumentation, Session 12, Fujiyoshida, Japan, 11–15 November.

Dickinson, Cameron, Allan Carswell, Thomas Duck, David Fisher, Laurent Huber, Carlos Lange, James Murphy, Peter Taylor, and James Whiteway. 2008. "PHX METEOROLOGICAL DATA V1.0" Dataset. Washington University (St. Louis, Missouri) Node of the NASA Planetary Data System (PDS). http://pds-geosciences.wustl.edu/default.htm.

Dickinson, Cameron, Leonce Komguem, and James Whiteway. 2012. "Clouds and Precipitation at the Phoenix Mars Lander Site." Paper presented at the 43rd Lunar Planetary Science Conference, The Woodlands, Texas, 19–23 March.

Dismukes, Kim. 2013. NASA Spaceflight. "Shuttle-Mir History website." Last modified August 23. http://spaceflight.nasa.gov/history/shuttle-mir/spacecraft/s-mir.htm.

Dubayah, Ralph. 2014. "GEDI LiDAR: Global Ecosystem Dynamics Investigation." Paper presented at American Geophysical Union, Fall Meeting 2014, abstract #U14A-07, San Francisco, California, 15–19 December.

Duong, Hieu van. 2010. "Processing and Application of ICESat Large Footprint Full Waveform Laser Range Data." Doctoral thesis, Delft University of Technology, Netherlands.

Fernandez-Diaz, Juan Carlos, William E. Carter, Craig Glennie, Ramesh L. Shrestha, Zhigang Pan, Nima Ekhtari, Abhinav Singhania, Darren Hauser, and Michael Sartori. 2016. "Capability Assessment and Performance Metrics for the Titan Multispectral Mapping Lidar." *Journal of Remote Sensing* 8(936). doi:10.3390/rs8110936.

Goetz, Scott J., Mei Sun, Alessandro Baccini, and Pieter S. A. Beck. 2010. "Synergistic Use of Spaceborne Lidar and Optical Imagery for Assessing Forest Disturbance: An Alaska Case Study." *Journal of Geophysical Research* 115, G00E07. doi:10.1029/2008JG000898.

Google Earth. 2016. "Naval Postgraduate School, Monterey, CA." 36º35'49.57" North and 121º52'27.47" West. Imagery Date: 13 April 2015. Accessed 1 September.

Harding, David J., James B. Abshire, Phillip W. Dabney, Ted A. Scambos, Antonios A. Seas, Christopher A. Shuman, and Xiaoli Sun. 2007. "The Swath Imaging Multi-polarization Photon-counting Lidar (SIMPL): A Technology Demonstration for Space-based Laser Altimeter Swath Mapping." Paper presented at the 2007 NASA Science Technology Conference (NSTC2007), University of Maryland, 19–21 June.

Harding, David J., Philip W. Dabneya, and Susan Valetta. 2011. "Polarimetric, Two-color, Photon-counting Laser Altimeter Measurements of Forest Canopy Structure." Paper presented at the International Symposium on Lidar and Radar Mapping 2011: Technologies and Applications, 828629, 24 October. doi:10.1117/12.913960.

Harding, David J., Dean B. Gesch, Claudia C. Carabajal, and Scott B. Luthcke. 1998. “Application of the Shuttle Laser Altimeter in an Accuracy Assessment of Global 1-Kilometer Digital Elevation Data.” Paper presented at 1998 Fall Meeting of the American Geophysical Union, San Francisco, California, 1 December.

Harris Geospatial Solutions. 2017a. “K-Means.” Accessed 1 March. http://www.harrisgeospatial.com/docs/KMeansClassification.html.

———. 2017b. “Maximum Likelihood.” Accessed 5 March. http://www.harrisgeospatial.com/docs/MaximumLikelihood.html.

———. 2017c. “The n-D Visualizer.” Accessed 10 February. http://www.harrisgeospatial.com/docs/nDimensionalVisualizer.html.

Howat, Ian M., Claire Porter, Myoung-Jong Noh, Ben Smith, and Seongsu Jeong. 2015. “Brief Communication: Sudden Drainage of a Subglacial Lake Beneath the Greenland Ice Sheet.” *The Cryosphere* 9:103–108, 15 January. doi:10.5194/tc-9-103-2015.

Hu, Yongxiang, Kathy Powell, Mark Vaughan, Charles Tepte, Carl Weimer, Mike Beherenfeld, Stuart Young, David Winker, Chris Hostetler, William Hunt, Ralph Kuehn, David Flittner, Mike Cisewski, Gary Gibson, Bing Lin, and David MacDonnell. 2007. “Elevation Information in Tail (EIT) Technique for Lidar Altimetry.” *Optics Express* 15(22):14504–14515, 19 October.

Hu, Yongxiang, Knut Stamnes, Mark Vaughan, Jacques Pelon, Carl Weimer, Dongxiao Wu, Mike Cisewski, Wenlu Sun, Ping Yang, Bing Lin, Ali Omar, David Flittner, Chris Hostetler, Charles Trepte, David Winker, Gary Gibson, and Maria Santa-Maria. 2008. “Sea Surface Wind Speed Estimation from Space-based Lidar Measurements.” *Atmospheric Chemistry and Physics* 8:3593–3601, 8 July.

Japan Aerospace Exploration Agency (JAXA). 2016. “Satellites and Spacecraft: Asteroid Explorer ‘HAYABUSA’ (MUSES-C).” Accessed 20 February. http://global.jaxa.jp/projects/sat/muses_c/.

Kaula, William M., Gerald Schubert, Richard E. Lingenfelter, William L. Sjogren, and Wilber R. Wollenhaupt. 1974. “Apollo Laser Altimetry and Inferences as to Lunar Surface Structure.” *Proceedings of the Fifth Lunar Science Conference* 3:3049–3058. http://adsabs.harvard.edu/full/1974LPSC....5.3049K.

Keller, John, Gordon Chin, and Thomas Morgan. 2007. “Lunar Reconnaissance Orbiter: Instrument Suite and Objectives.” IAC-07-A3.6.A.03. NASA GSFC. 25 September.

Kurtz, Nathan, Thorsten Markus, Sinead Farrell, Denise Worthen, and Linette Boisvert. 2011. “Observations of Recent Arctic Sea Ice Volume Loss and its Impact on Ocean-atmosphere Energy Exchange and Ice Production.” *Journal of Geophysical Research* 116, C04015. doi:10.1029/2010JC006235.

Lucey, Paul G., Gregory A. Neumann, Miriam A. Riner, Erwan Mazarico, David E. Smith, Maria T. Zuber, David A. Paige, Ben Bussey, Joshua T. Cahill, Andy McGovern, Peter Isaacson, Laura M. Corley, Mark H. Torrence, Jay Melosh, James W. Head, and Eugenie Song. 2014. “The Global Albedo of the Moon at 1064 nm from LOLA.” *Journal of Geophysical Research Planets*:119, 1 July. doi:10.1002/2013JE004592.

Lunar and Planetary Institute. 2016. “Clementine Explores the Moon.” Accessed 2 April. http://www.lpi.usra.edu/publications/slidesets/clem2nd/clementine_index.shtml.

Lunar and Planetary Institute and Universities Space Research Association. 2016. “Apollo 17 Mission Page.” Accessed 15 February. http://www.lpi.usra.edu/lunar/missions/apollo/apollo_17/experiments/.

McCormick, Patrick. 2005. “Airborne and Spaceborne LiDAR.” In *Range-Resolved Optical Remote Sensing of the Atmosphere*, edited by Claus Weitkamp, 355–397. New York: Springer-Verlag.

McCormick, Patrick, David M. Winker, Edward V. Browell, James Coakley, Chet S. Gardner, Ray M. Hoff, Geoffrey S. Kent, Harvey Melfi, Robert T. Menzies, Martin R. Platt, David Randall, and John Regan. 1994. “LITE: Measuring the Atmosphere with Laser Precision.” NASA Fact Sheet (NF230). Langley Research Center. 1 August. http://www.nasa.gov/centers/langley/news/factsheets/LITE.html.

Miller, Chad, Judson Thomas, Angela Kim, Jeremy Metcalf, and Richard Olsen. 2016. “Application of Image Classification Techniques to Multispectral LiDAR Point Cloud Data.” Science Applications International Corporation/Naval Postgraduate School Physics Dept. and Remote Sensing Center. Paper presented at Society of Photographic Instrumentation Engineers (SPIE) Defense Security and Sensing (DSS), Baltimore, Maryland, 17–21 April.

Morsy, Salem, Ahmed Shaker, Ahmed El-Rabbany, and Paul E. LaRocque. 2016. “Airborne Multispectral LiDAR Data for Land-cover Classification and Land/water Mapping Using Different Spectral Indexes.” *ISPRS Annals of the Photogrammetry, Remote Sensing and Spatial Information Sciences* III-3.

Mukai, Tadashi, Shinsuke Abe, Naru Hirata, Ryosuke Nakamura, Olivier S. Barnouin-Jha, Andrew F. Cheng, Takahide Mizuno, Kensuke Hiraoka, Takayuki Honda, Hirohide Demura, Robert W. Gaskell, Tatsuaki Hashimoto, Takashi Kubota, Masatoshi Matsuoka, Daniel J. Scheeres, and Makoto Yoshikawa. 2007. "An Overview of the LiDAR Observations of Asteroid 25143 Itokawa." *ScienceDirect, Advances in Space Research* 40:187–192, 20 April.

NASA. 1971. *Apollo 15 Mission Report*. Houston, Texas: Manned Spacecraft Center.

———. 2007a. "Lunar Reconnaissance Orbiter Fact Sheet." FS-2007-11-098-GSFC. Greenbelt, Maryland: Goddard Space Flight Center. https://lunar.gsfc.nasa.gov/images/LRO-Fact-Sheet.pdf.

———. 2007b. *Mars Global Surveyor (MGS) Spacecraft Loss Report*. Washington, DC: NASA Headquarters. 13 April. https://www.nasa.gov/pdf/174244main_mgs_white_paper_20070413.pdf.

———. 2008. "Phoenix Landing Mission to the Martian Polar North: Press Kit." Washington, DC: NASA Headquarters. 8 May. https://www.jpl.nasa.gov/news/press_kits/phoenix-landing.pdf.

———. 2015. "Phoenix Lander Mission Page." Last modified 30 July. https://www.nasa.gov/mission_pages/phoenix/images/index.html.

———. 2016a. "CALIPSO Mission Page." Accessed 8 March. http://www.nasa.gov/mission_pages/calipso/spacecraft/index.html. http://www.nasa.gov/mission_pages/calipso/mission/5years.html.

———. 2016b. "SIMPL (Slope Imaging Multi-polarization Photon-counting Lidar)." Accessed 13 April. https://directory.eoportal.org/web/eoportal/airborne-sensors/simpl.

NASA Goddard Space Flight Center. 2015. ICESat Cryospheric Sciences Lab. Last modified 14 April. http://icesat.gsfc.nasa.gov/icesat/.

———. 2016a. "ICESat-2 Instrument." Last modified 22 February. http://icesat.gsfc.nasa.gov/icesat2/instrument.php.

———. 2016b. "Lunar Reconnaissance Orbiter Images and Multimedia." Accessed 1 March. http://lunar.gsfc.nasa.gov/imagesandmultimedia.html.

NASA Human Space Flight. 2014. "STS-131 Mission Imagery." Last modified 11 August. http://www.spaceflight.nasa.gov/gallery/.

NASA Jet Propulsion Laboratory (JPL)/California Institute of Technology (Caltech). 2012. "Mars Global Surveyor." Last modified 28 July. http://mars.jpl.nasa.gov/mgs/.

———. "MGS Mission Images." Accessed 20 February. http://mars.jpl.nasa.gov/mgs/mission/images/PIA02820_mola.jpg.

NASA JPL/Caltech/University of Arizona/Canadian Space Agency. 2016. "Phoenix Mission Pages." Accessed 20 February. http://www.nasa.gov/mission_pages/phoenix/images/index.html.

NASA/Johns Hopkins University Applied Physics Laboratory/Carnegie Institution of Washington. 2016. Accessed 5 April. http://messenger.jhuapl.edu/the_mission/.

NASA Science Missions. 2015. "GEDI." Last modified 14 December. http://science.nasa.gov/missions/gedi/.

NASA Space Science Data Coordinated Archive (NSSDCA). 2016a. "Apollo 16 Laser Altimeter." Last modified 12 February. http://nssdc.gsfc.nasa.gov/nmc/experimentDisplay.do?id=1972-031A-05.

———. 2016b. "BE-B." Last modified 12 February. http://nssdc.gsfc.nasa.gov/nmc/spacecraftDisplay.do?id=1964-064A.

National Space Science Data Center (NSSDC). 1994. "Clementine Spacecraft Details." NSSDC ID: 1994–004A.

———. 2003. "ICESat Spacecraft Details." 2003–002A.

Neumann, Gregory A. 2001. "Some Aspects of Processing Extraterrestrial LiDAR Data: Clementine, NEAR, MOLA." *International Archives of Photogrammetry and Remote Sensing* XXXIV-3/W4:73–80.

Palm, Steve. 2016. "Vertical Profile of the Smoke off California: Image of the Day." NASA Goddard Space Flight Center. Accessed 20 February. https://earthobservatory.nasa.gov/IOTD//view.php?id=3918.

Pang, Yong, Michael Lefsky, Guoqing Sun, Mary Ellen Miller, and Zengyuan Li. 2008. "Temperate Forest Height Estimation Performance Using ICESat GLAS Data from Different Observation Periods." *The International Archives of the Photogrammetry, Remote Sensing and Spatial Information Sciences* XXXVII(B7), Beijing:777–782.

Richards, John A. 2013. *Remote Sensing Digital Image Analysis: An Introduction*. Berlin Heidelberg: Springer-Verlag.

Roberson, Floyd I., and William M. Kaula. 1972. *NASA: Apollo 15 Preliminary Science Report*. Washington, DC: Scientific and Technical Information Office.

Robinson, Mark S. 2010. “Lunar Reconnaissance Orbiter Camera Reduced Data Record.” Wide-Angle-Camera (WAC) Global Morphologic Map (WAC_GLOBAL_E0_00N1800_064P.IMG). NASA Planetary Data System. NASA/GSFC/Arizona State University. http://wms.lroc.asu.edu/lroc/view_rdr/WAC_GLOBAL.

Ruel, Stephane, Tim Luu, and Andrew Berube. 2010. “On-Orbit Testing of Target-less TriDAR 3D Rendezvous and Docking Sensor.” Paper presented at International Symposium on Artificial Intelligence, Robotics and Automation in Space (i-SAIRAS 2010), Sapporo, Japan, 29 August to 1 September.

Shuman, Christopher. 2016. “Antarctica's Land and Ice Elevation: Image of the Day.” NASA Goddard Space Flight Center. Accessed 20 February. https://earthobservatory.nasa.gov/IOTD/view.php?id=5081.

Smith, David. 1996. “Mars Orbiter Laser Altimeter (MOLA).” NASA Space Science Data Coordinated Archive: Goddard Space Flight Center. https://nssdc.gsfc.nasa.gov/nmc/masterCatalog.do?sc=1996-062A&ex=03.

Smith, David, and Maria Zuber. NASA Goddard Space Flight Center. 2007 “About MOLA.” Last modified 19 January. http://mola.gsfc.nasa.gov/about.html.

Smith, David, Maria Zuber, Herbert V. Frey, James B. Garvin, James W. Head, Duane O. Muhleman, Gordon H. Pettengill, Roger J. Phillips, Sean C. Solomon, H. Jay Zwally, W. Bruce Banerdt, Thomas C. Duxbury, Matthew P. Golombek, Frank G. Lemoine, Gregory A. Neumann, David D. Rowlands, Oded Aharonson, Peter G. Ford, Anton B. Ivanov, Catherine L. Johnson, Patrick J. McGovern, James B. Abshire, Robert S. Afzal, and Xiaoli Sun. 2001. “Mars Orbiter Laser Altimeter: Experiment Summary After the First Year of Global Mapping of Mars.” *Journal of Geophysical Research* 106(E10):23,689–23,722, 25 October.

Smith, David, Maria Zuber, Xiaoli Sun, Gregory Neumann, John Cavanaugh, Jan McGarry, and Thomas Zagwodzki. 2006. “Two-Way Laser Link Over Interplanetary Distance.” *Science* 311:53, 6 January.

Smith, David, Gregory Neumann, Raymond E. Arvidson, Ed A. Guinness, and Susan Slavney. 2003. “Mars Global Surveyor Laser Altimeter Mission Experiment Gridded Data Record.” MGS-M-MOLA-5-MEGDR-L3-V1.0. NASA Planetary Data System.

Smith, David, Gregory Neumann, Peter Ford, Raymond E. Arvidson, Ed A. Guinness, and Susan Slavney. 1999. “Mars Global Surveyor Laser Altimeter Precision Experiment Data Record.” MGS-M-MOLA-3-PEDR-L1A-V1.0. NASA Planetary Data System.

Sørensen, Louise S., Sebastian B. Simonsen, Karina Nielsen, Philippe Lucas-Picher, Giorgio Spada, Gudfinna Adalgeirsdottir, Rene Forsberg, and Christian S. Hvidberg. 2011. "Mass Balance of the Greenland Ice Sheet (2003–2008) from ICESat Data—The Impact of Interpolation, Sampling and Firn Density." *The Cryosphere* 5:173–186, 9 March. doi:10.5194/tc-5-173-2011.

Sun, Gui-Quan, Kenneth J. Ranson, Viacheslav I. Kharuk, and Katalin Kovacs. 2003. "Validation of Surface Height from Radar Topography Mission Using Shuttle Laser Altimeter." *Remote Sensing of Environment* 88:401–411, 3 September.

Sun, Xiaoli, David R. Skillman, Evan D. Hoffman, Dandan Mao, Jan F. McGarry, Leva McIntire, Ronald S. Zellar, Frederic M. Davidson, Wai H. Fong, Michael A. Krainak, Gregory A. Neumann, Maria T. Zuber, and David E. Smith. 2013. "Free Space Laser Communication Experiments from Earth to the Lunar Reconnaissance Orbiter in Lunar Orbit." *Optics Express* 21(2):1865–1857, 28 January.

Teledyne Optech. 2015. "Optech Titan Multispectral Lidar System Spec Sheet." Toronto, Canada. 15 May.

Thomas, Judson. 2015. "Terrain Classification Using Multi-Wavelength LiDAR Data." Master's thesis, Naval Postgraduate School.

Tou, Julius and Rafael Gonzalez. 1974. *Pattern Recognition Principles*. Reading, MA: Addison-Wesley Publishing Company.

Troupaki, Elisavet, Zachary H. Denny, Stewart Wu, Heather N. Bradshaw, Kevin A. Smith, Judy A. Hults, Luis A. Ramos-Izquierdo, and William B. Cook. 2015. "Space Qualification of the Optical Filter Assemblies for the ICESat-2/ATLAS Instrument." NASA Goddard Space Flight Center. Science Systems and Applications (SSAI) Inc. Orbital Sciences Corps. 7 February.

Whiteway, James, Michael Daly, Allan Carswell, Thomas Duck, Cameron Dickinson, Leonce Komguem, and Clive Cook. 2008. "Lidar on the Phoenix Mission to Mars." *Journal of Geophysical Research*:113, E00A08. doi:10.1029/2007JE003002.

Williams, David R. 2011. "Clementine Project Information." National Space Science Data Center (NSSDC). NASA Goddard Space Flight Center. Last modified 7 November. http://nssdc.gsfc.nasa.gov/planetary/clementine.html.

Winker, David M., Richard H. Couch, and Patrick McCormick. 1996. "An Overview of LITE: NASA's LiDAR In-space Technology Experiment." *Proceedings of the IEEE* 84(2):164–180.

Winker, David M., and Bill Hunt. 2007. "First Results from CALIOP." Third Symposium on LIDAR Atmospheric Applications, Session 3. 17 January.

Yu, Anthony W., Mark A. Stephen, Steve X. Li, George B. Shaw, Antonios Seas, Edward Dowdye, Elisavet Troupaki, Peter Liiva, Demetrios Poulios, and Kathy Mascetti. 2010. “Space Laser Transmitter Development for ICESat-2 Mission.” Proceedings of the SPIE 7578:757809-1 to 757809-11.

Yu, Anthony W., Michael A. Krainak, David J. Harding, James B. Abshire, Xiaoli Sun, Jonh Cavanaugh, and Susan Valett. 2010. “Efficient Swath Mapping Laser Altimetry Demonstration Instrument Incubator Program.” NASA Goddard Flight Center.

Yadav, Girish Kumar. 2010. “Simulation of ICESat/GLAS Full-Waveform Over Highly Rugged Terrain.” Netherlands: Geo-information Science and Earth Observation and Indian Institute of Remote Sensing.

Zuber, Maria T., David E. Smith, Andrew F. Cheng, James B. Garvin, Oded Aharonson, Timothy D. Cole, Peter J. Dunn, Yanping Guo, Frank G. Lemoine, Gregory A. Neumann, David D. Rowlands, and Mark H. Torrence. 2000. “The Shape of 433 Eros from the NEAR-Shoemaker Laser Rangefinder.” *Science* 289, 22 September.

Zubritsky, Elizabeth. 2014. “How Satellite Laser Ranging Got its Start 50 Years Ago.” NASA Goddard Space Flight Center. 13 November. http://www.nasa.gov/content/goddard/laser-ranging-50-years/#.Vtsy4ua1joU.

Zwally, Jay, Bob Schutz, Waleed Abdalati, James Abshire, Charles Bentley, Anita Brenner, Jack Bufton, Joe Dezio, David Hancock, David Harding, Thomas Herring, Jean-Bernard Minster, Katherine Quinn, Steve Palm, James Spinhirne, and Robert Thomas. 2002. “ICESat’s Laser Measurements of Polar Ice, Atmosphere, Ocean, and Land.” *Journal of Geodynamics* 34:405–445, October–November.

INITIAL DISTRIBUTION LIST

1. Defense Technical Information Center
   Ft. Belvoir, Virginia

2. Dudley Knox Library
   Naval Postgraduate School
   Monterey, California